Semiconductors, Vol. 34, No. 10, 2000, pp. 1103–1108. Translated from Fizika i Tekhnika Poluprovodnikov, Vol. 34, No. 10, 2000, pp. 1153–1158.

ATOMIC STRUCTURE AND NONELECTRONIC PROPERTIES OF SEMICONDUCTORS

Evaluation of Compositional Intermixing at Interfaces in Si(Ge)/$Si_{1-x}Ge_x$ Heteroepitaxial Structures Grown by Molecular Beam Epitaxy with Combined Sources of Si and GeH_4

L. K. Orlov*, N. L. Ivina, and A. V. Potapov

Nizhni Novgorod State University, pr. Gagarina 23, Nizhni Novgorod, 603600 Russia

Institute of Physics of Microstructures, Russian Academy of Sciences, Nizhni Novgorod, 603600 Russia

** e-mail: orlov@ipm.sci-nnov.ru*

Submitted March 21, 2000; accepted for publication March 30, 2000

Abstract—The main causes of the diffusion spreading of a solid-solution composition near the boundaries of the Si transport channel in a Si/$Si_{1-x}Ge_x$ heterostructure grown by molecular-beam epitaxy combined with solid (Si) and gaseous (GeH_4) sources are considered. For the grown structures, the contributions from various mechanisms involved in forming the profile of the metallurgical boundary of the layer are compared and the effect of channel boundary spreading on the mobility of a two-dimensional electron gas in the channel is evaluated. *© 2000 MAIK "Nauka/Interperiodica".*

Recently, the requirements for the technological procedures used to fabricate heterostructures with nanolayers have become much more stringent in view of the widespread introduction of these heterostructures into semiconductor engineering. In addition to conventional molecular-beam epitaxy employing solid sources of silicon and germanium, methods of gaseous epitaxy with high-purity hydrides under both lowered [1] and atmospheric pressure [2] in a reactor are widely used to fabricate Si–Ge structures. Combined epitaxial techniques, with a combination of various sources of atomic and molecular fluxes (solid, liquid, gaseous, and plasmachemical), are being tested. The sources used in epitaxy produce molecular fluxes with molecular dissociation times that are fairly long, compared with the characteristic times of atom incorporation into a growing layer. This draws close attention to the kinetics of processes occurring on the growth surface in order to find the optimal conditions for growing nanolayers with extremely abrupt planar heteroboundaries.

The stringent requirements on the quality of the boundaries in pseudomorphic heterostructures are most frequently imposed in those cases where acceptable electrical characteristics of charge carriers in two-dimensional (2D) transport channels must be obtained. This may be necessary both for the observation of a number of unique phenomena in a 2D charge-carrier gas (e.g., the effects of liquid-type interactions in a system of 2D electrons etc.) and for applications of these structures in devices (e.g., for fabricating high-frequency field-effect transistors, lasers relying on electron heating effects, etc.). Moreover, when most of the existing technological procedures are used, the effect of compositional intermixing in the vicinity of heteroboundaries leads to severe difficulties in creating a new class of materials of the Si_nGe_m type, which combine monolayers within an individual unit cell of a single crystal. In connection with this, there is an urgent need to analyze the possibilities of various techniques that can be used to grow planar heterostructures with extremely abrupt boundaries and to determine the main causes of compositional intermixing at nanolayer boundaries in order to eliminate this effect, if possible. Substantial compositional intermixing and spreading at nanolayer boundaries can lead to the following. First, the potential profile in the well can be markedly distorted by a significant background of an isovalent impurity created in the 2D channel. Second, the boundary roughness may become more pronounced owing to composition fluctuations in the heteroboundary plane, enhanced by the effects of elastic strain and by the accelerated diffusion of alloy components.

The aim of this study was to determine (by means of a theoretical analysis based on our nonsteady kinetic model of layer growth [3] and the experimental material accumulated so far [4, 5]) the most important real causes of compositional intermixing near heteroboundaries in Ge(Si)/$Si_{1-x}Ge_x$ heterostructures grown by MBE with a combined solid source of silicon and gaseous chemical source of germanium: (Si–GeH_4)-MBE [5, 6].

We have previously shown [3, 4] for the given combined epitaxial technique that GeH_4 molecule pyrolysis, both on a substrate and on a sublimating silicon slab placed in the reactor, can successfully solve the problem of controlling fluxes of Si and Ge atoms and ger-

1063-7826/00/3410-1103$20.00 © 2000 MAIK "Nauka/Interperiodica"

mane molecules toward the substrate. This simultaneously stabilizes the growth rate in a wide range. In addition, an unconventional model that describes the growth kinetics of $Si_{1-x}Ge_x$ solid solution layers from an atomic beam of silicon, and a molecular flux of germane in vacuum, has been developed for this epitaxial process. This was done in order to study in detail the pyrolysis of germane molecules on the surface of the growing layer and the effect of this process on the rate of epitaxy [7]. Numerical simulation data were compared with the experimentally established dependences. In this way, the steady-state kinetics of $Si_{1-x}Ge_x$ layer growth were studied and a comparative analysis was made of the efficiency of incorporating Ge and Si atoms into the growing layer, both with and without Si and Ge atom fluxes in the reactor [8].

In this study, we attempted to establish a relationship between the effective heteroboundary broadening and the basic parameters of $Si_{1-x}Ge_x$ layer growth in the (Si–GeH_4)-MBE method, i.e., the temperature and rate, and the gas pressure in the reactor. For different growth conditions employing combinations of atomic and molecular beams in the reactor, various mechanisms that govern heteroboundary abruptness in the layer are compared. The following mechanisms can be assigned to this category: a finite rate of material delivery to the substrate surface; a finite rate of Ge and Si atom incorporation into the growing layer; a finite dissociation rate of hydride molecules, which, generally speaking, is determined by the different pyrolysis pathways on the growth surface; accelerated diffusion over the surface due to elastic strain effects; surface segregation; and the dependence of Si and Ge atom incorporation factors on surface bond filling, which include hydrogen. The results are used to evaluate the composition profile in Ge(Si) layers that form potential wells; these served as transport channels for holes (electrons) in the $Si_{1-x}Ge_x$ matrix in structures grown in our previous work [9] by the given epitaxy technique. Recommendations are provided for selecting the growth conditions, under which factors that severely impair the transport characteristics of the structures can be eliminated or their influence significantly diminished. A computer model based on these selected parameters, can reproduce the compositional profile of a grown structure with high reliability.

We analyze the causes and efficiency of compositional intermixing near the heteroboundaries of a multilayer Si(Ge)–$Si_{1-x}Ge_x$ structure grown by the (Si–GeH_4)-MBE method by examining the main nonsteady physicochemical processes on the $Si_{1-x}Ge_x$ layer growth surface. The validity of the mathematical model employed in the analysis relies upon the consistency of steady-state characteristics obtained from it with the experimentally observed dependences (e.g., the dependence of the growth rate on the film growth temperature and atomic and molecular fluxes) [10]. The system of time-dependent kinetic equations for dimensionless mean surface concentrations of GeH_3 molecules and H, Ge, and Si atoms corresponding to the chosen model has the form

$$\begin{aligned} d\theta_{GeH_3}/dt &= 2(S_{GeH_4}F_{GeH_4}/n_s)\theta_{nbl}^2 - 24\nu_{GeH_3}\theta_{GeH_3}\theta_{fr}^3, \\ d\theta_H/dt &= 2(S_{GeH_4}F_{GeH_4}/n_s)\theta_{nbl}^2 \\ &\quad + 24\nu_{GeH_3}\theta_{GeH_3}\theta_{fr}^3 - \nu_H(x)\theta_H, \\ d\theta_{Ge}/dt &= g(S_{GeH_4}F_{GeH_4}/n_s)\theta_{fr} + 24\nu_{GeH_3}\theta_{GeH_3}\theta_{fr}^3 \\ &\quad - (\nu_{Ge} + r_{Ge})\theta_{Ge}, \\ d\theta_{Si}/dt &= (S_{Si}F_{Si}/n_s)\theta_{fr} - (\nu_{Si} + r_{Si})\theta_{Ge}. \end{aligned} \tag{1}$$

In Eqs. (1), S_{GeH_4} is the capture coefficient of a GeH_4 molecule by a free surface, $F_{GeH_4(Ge,\,Si)}$ is the molecular (atomic) flux, $\nu_{GeH_3}[s^{-1}] = \nu_0\exp(-E_{act}/kT) = 0.5\exp(-0.4/kT\,[eV])$ is the effective decomposition rate of a GeH_3 molecule for a specific technological process, ν_H is the rate of hydrogen-atom desorption from the surface of the growing layer, $\nu_{Ge(Si)}$ is the desorption rate of Ge(Si) atoms, and $r_{Ge(Si)}$ is the crystallization rate of Ge(Si) atoms. The transfer coefficient g accounts for the specific features of the experimental installation, including the geometric dimensions of the Si source, its temperature, distance from the source to the substrate, and their mutual orientation.

The physicotechnological model of $Si_{1-x}Ge_x$ layer growth proposed for the given method of epitaxy with combined atomic and gas fluxes is based on the reactions

$$\begin{gathered} GeH_4(gas) + \underline{2} \longrightarrow \underline{Ge}H_3 + \underline{H}, \\ \underline{Ge}H_3 + \underline{3} \longrightarrow \underline{Ge} + 3\underline{H}, \\ Ge,\ Si + \underline{1} \longrightarrow \underline{Ge,\ Si}, \quad \underline{Ge,\ Si} \longrightarrow Ge,\ Si(crystal), \\ \underline{Ge,\ Si} \longrightarrow Ge,\ Si(gas), \quad 2\underline{H} \longrightarrow H_2(gas), \end{gathered} \tag{2}$$

which rely on the following assumptions: (i) monomolecular adsorption takes place in the system, (ii) there is no interaction between the particles being adsorbed, (iii) atomic fluxes have no effect on chemisorption and pyrolysis of GeH_4 molecules; and (iv) each GeH_3 molecule blocks three free adsorption centers, (v) hydride atoms are delivered to the growth surface only by germane molecules. Germane decomposition and the formation of additional Ge atomic fluxes in a hybrid (Si–GeH_4)-MBE system may proceed on a hot solid source of Si vapor. The underlining in (2) indicates an atom bound to the surface.

For monomolecular adsorption, we also assume that the following condition is satisfied:

$$\theta_{Si} + \theta_{Ge} + \theta_H + \theta_{GeH_3} + \theta_{fr} = 1, \tag{3}$$

the concentrations θ_{bl} and θ_{nbl} of free surface bonds blocked and nonblocked by GeH_3 molecules satisfy the relations

$$\theta_{fr} = \theta_{bl} + \theta_{nbl}, \quad \theta_{bl} = 3\theta_{GeH_3}. \tag{4}$$

Equations (1)–(4) form a general system of equations for determining the dimensionless concentrations θ_i. With a knowledge of θ_i, the film growth rate V_{gr} and Ge content in the epitaxial layer can be readily calculated

$$\begin{aligned} V_{gr} &= (r_{Si}\theta_{Si} + r_{Ge}\theta_{Ge})n_s/n_0, \\ x &= r_{Ge}\theta_{Ge}/(r_{Si}\theta_{Si} + r_{Ge}\theta_{Ge}). \end{aligned} \tag{5}$$

Numerically solving the system of equations (1) allows the investigation of both the steady and nonsteady processes in the growth system. The time-independent relations, readily found in each particular case from experiment, can be used to determine the unknown parameters of the model [7, 8].

To study transient processes in the growth system, we used a rectangular pulse of germane pressure (silicon flux) at a constant flux of Si atoms (constant pressure of germane in the reactor) [11]. The characteristic curves describing the time dependence of the surface concentrations of GeH_3, Ge, H, and Si and the growth rate in a $Si/Si_{1-x}Ge_x/Si$ structure, calculated for some parameter values, were reported previously [10, 12]. In this study, we only pay attention to the effective compositional intermixing near heteroboundaries. The intermixing is determined by the distance L at which the Ge concentration in the $Si_{1-x}Ge_x$ alloy decreases by two orders of magnitude to $0.01x$ (for a given x) when one of the fluxes is abruptly switched off. Apparently, if the abruptness of the lower boundary of a $Si_{1-x}Ge_x$ layer is determined mainly by the rate of surface coverage by germyl molecules when the pulsed gas flux is switched on ($t = t_0$), i.e., it is proportional to $\exp\{(F_{GeH_3}/n_s)(t - t_0)\}$, then spreading of the upper boundary is associated exclusively with relaxation processes governed both by the rate of atom incorporation into the growing layer and by the rate of pyrolysis of germane molecules. However, the question remains open as to what range of parameters will be dominated by the process determining the effective boundary broadening and background doping of the adjacent silicon layer. Figure 1 illustrates the specificity of physicochemical processes, occurring at the surface and affecting the abruptness of the boundaries, by the example of the composition profiles near heteroboundaries forming a $Si_{1-x}Ge_x$ layer that acts as a barrier to electrons (Fig. 1a) and, correspondingly, a quantum well (QW) in the Si layer (Fig. 1b). Numerical calculations using the above formulas were performed for a growth temperature $T_{gr} = 500°C$, which is sufficiently low for the effects of surface segregation to be disregarded, for the values $r_{Ge} = r_{Si} = r = 3.1$, $x = 0.35$ (prescribed composition) at various germane pressures

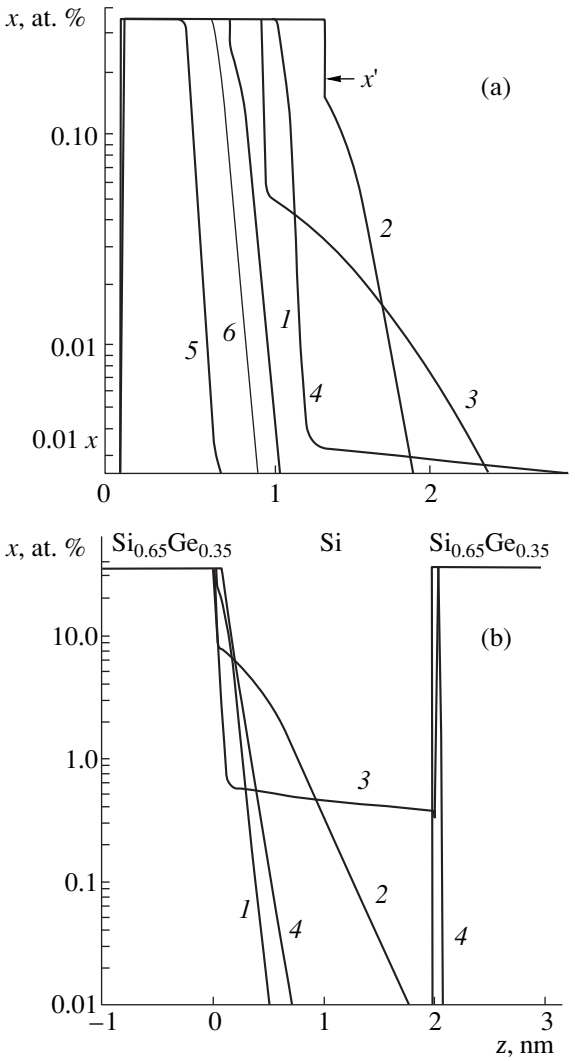

Fig. 1. Germanium distribution along the z coordinate in (a) $Si_{1-x}Ge_x$ and (b) Si layers in a $Si_{1-x}Ge_x$–Si heterostructure grown by the (Si–GeH_4)-MBE technique at T = 500°C, x = 0.35, $r_{Ge} = r_{Si} = r$ = 3.1, and g = 0.037. (a) P_{GeH_4}/F_{Si} = (*1*) 0.011/0.01, (*2*) 0.042/0.02, (*3*) 0.168/0.06, (*4*) 0.187/0.6, (*5*) 3.15/1, and (*6*) 6.3/2 mTorr/(10^{15} cm^2/s). (b) P_{GeH_4}/F_{Si} = (*1*) 0.011/0.01, (*2*) 0.104/0.04, (*3*) 1.24/0.4, and (*4*) 12.5/4 mTorr/(10^{15} cm^2/s).

P_{GeH_4} and silicon atom fluxes. Figures 1a and 1b clearly demonstrate the asymmetry of the lower and upper layer boundaries; the latter is characterized by the presence of at least two regions in which the compositional intermixing due to relaxation processes occurs at two different rates. It also follows from Fig. 1b that in a specific range of germane pressures in the reactor (incidentally, the range most frequently used in the experiment) the residual concentration of the isovalent germanium impurity in the thin (2–3 nm) silicon transport channel may be as high as several

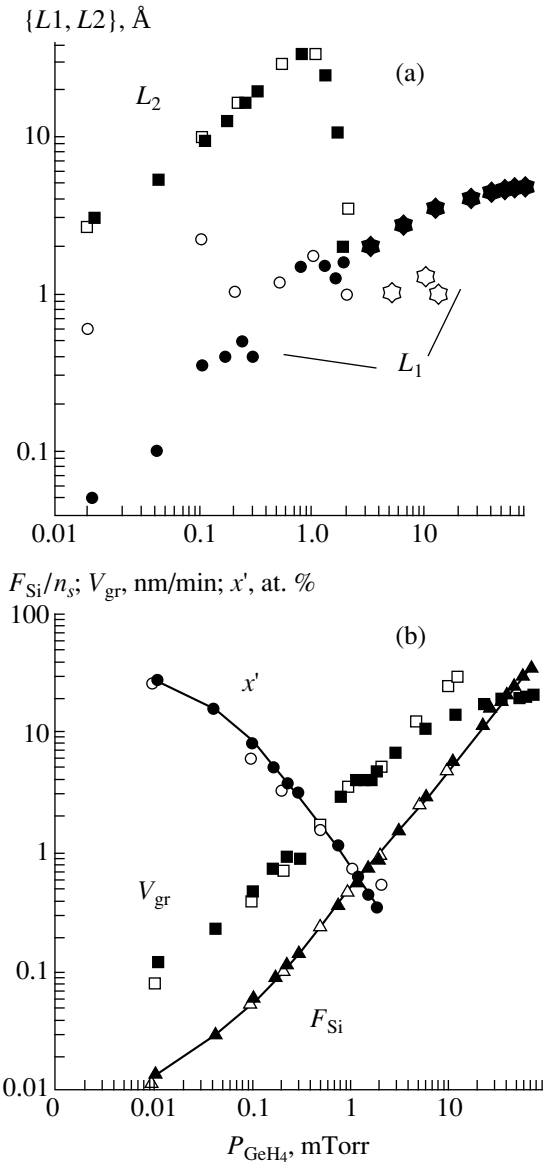

Fig. 2. (a) Dependences of the characteristic parameters $L1$ and $L2$ of the compositional intermixing near the upper heteroboundary of the $Si_{1-x}Ge_x$ layer on the germane pressure in the reactor and (b) the atomic flux of silicon F_{Si} for a given $x = 0.35$ in the layer, growth rate V_{gr} of silicon layer at $T = 500°C$, and x' values corresponding to the onset of relaxation processes associated with pyrolysis of germane molecules on the germane pressure. Full symbols correspond to r = const, open symbols, to $r_i = r_i(\theta_i)$.

tenths of a percent, adversely affecting conduction in the 2D electron gas. In this case, the potential profile in the channel will be clearly far from rectangular.

To tackle the question as to what range of parameters is optimal for fabricating heterostructures with heteroboundaries that are as abrupt as possible, let us analyze the effective broadening of the upper boundary of the layer due to relaxation processes on the layer surface in relation to the germane pressure in the reactor. The characteristic shape of the $L(P)$ curves calculated for the same parameter values as the curves in Fig. 1 is illustrated in Fig. 2a. The quantity $L1$ is related to the finite time of Si(Ge) atom incorporation into the growing layer, and $L2$, to the finite time of germane pyrolysis on the hot surface of the epitaxial layer. The solid symbols in the figure correspond to the condition $r_{Ge} = r_{Si} = r$ = const; the blank symbols correspond to the data obtained by taking into account the dependence of the incorporation factors of atoms on their surface concentration $r_i = r_i(\theta_i)$, in accordance with [7, 10]. In Fig. 2a, the circles correspond to the values of $L1$ obtained by approximating up to the value $L1(0.01x)$ the initial portions (in the x–x' range) of the composition distribution fronts at the upper boundary of the $Si_{1-x}Ge_x$ layer, corresponding to the star-shaped symbols. The value of x', at which the relaxation mechanisms associated with germyl molecule dissociation at the surface start to be dominant, was determined from the inflection point in the $x(z)$ curve in Fig. 1a. The dependence $x'(P)$ corresponding to the curves in Fig. 2a is shown in Fig. 2b. For the chosen range of germane pressures, the silicon atom fluxes and the corresponding Si layer growth rates are also shown.

Analysis of the curves in Figs. 1 and 2 leads to somewhat interesting conclusions. First, it can be seen that, for sufficiently high gas pressures in the reactor ($P_{GeH_4} > 1$ mTorr), the growth process is dominated by atomic fluxes of silicon and germanium from the source; as a result, the rate of occurrence of the relaxation processes is determined exclusively by the rate of incorporation of the adsorbed atoms into the growing layer. The effective boundary broadening determined by this mechanism is 1–3 Å and, for r = const, decreases as the pressure in the reactor is lowered, because of the decreasing layer-growth rate (Fig. 2b). Consideration of the dependence of r_i on θ_i causes the dependence of $L1$ on P_{GeH_4} to become weaker, since, according to [10], the value of r_i increases with increasing surface coverage by adsorbed atoms. For $P_{GeH_4} <$ 1 mTorr, long-term processes associated with the dissociation of hydride molecules and radicals on the growth surface come into play. As a result, the relaxation tail of $L2$ at the boundary becomes much longer (see Figs. 1a, 2a), reaching a value of 1–3 nm in the pressure range of 0.1–1 mTorr. It should be noted that this range is most frequently used in experiments since the growth rates in this case are 0.5–5 nm/min, which is quite acceptable for epitaxy. To obtain abrupt (about one monolayer wide) fronts in the alloy composition distribution, it is necessary to use either lower or higher pressures. However, in the former case, the film growth rates become extremely low, while in the latter case, the molecular flux of the gas in the reactor may already be upset and other classical mechanisms characteristic of flow-through gas-phase systems [13] may contribute to boundary spreading.

Let us evaluate the composition profile in an actual $Si_{0.86}Ge_{0.14}$ transistor structure with a silicon transport channel, using the above analytical procedure. If we take into account only the above mechanisms of composition spreading at heteroboundaries (i.e., we assume instantaneous removal of germane from the reactor after termination of its delivery therein), then, for a growth temperature T = 700°C, germane pressure during $Si_{0.86}Ge_{0.14}$ layer growth P_{GeH_4} = 2 mTorr, and $k = r_{Si}/r_{Ge}$ = 50, we have a nearly rectangular germanium distribution profile (x) in the structure, shown by the dashed line in Fig. 3a. In an actual system, the formation of tails of the composition distribution near the transition regions may be governed not only by the natural mechanisms of diffusion broadening, but also by factors associated with the finite rate of gas evacuation. In the installation employed in this work, germane pressure decay in the reactor was described by the relation $P(t) = 2 \times 10^{-3}/\{1 + 32.8(t - t_0)\}$, where t_0 is the time (in min) of termination of germane supply into the reactor. It can be seen (Fig. 3b, solid line) that the low evacuation rate used in this study gives rise to a pronounced tail of a solid solution at the left-hand boundary of the silicon channel, forming a nearly triangular composition profile in the QW, thereby leading to low electron mobilities.

If, in order to obtain a more abrupt boundary profile, we interrupt the atomic fluxes of silicon and germanium from the source for ~2 min, and simultaneously shut off the gas supply to the reactor, a thin germanium film forms at the left-hand boundary of the Si layer (Fig. 3b). To evaluate the thickness of the Ge layer deposited onto the epitaxial $Si_{1-x}Ge_x$ layer during evacuation of germane from the reactor, it is necessary to know the effective rate of germane decomposition at the germanium surface in the absence of atomic fluxes. The effective rate can be readily determined if the germanium-film growth rate at a constant germanium pressure is known. Under conditions close to those mentioned above, the growth rate of a germanium layer in a $Ge/Si_{0.9}Ge_{0.1}$ structure is ~15 Å/min according to electron microscopy data [9]. This value, found for a temperature of 700°C, is in close agreement with results reported elsewhere [14] and corresponds to an effective rate of GeH_3 molecule dissociation of ν_0 = 6.25 at the growth surface. The germanium film thickness in Fig. 3a, corresponding to the given rate of GeH_3 molecule disintegration, is 3 nm. If the critical germanium-layer thickness is exceeded, the film grows by the Stranski–Krastanov mechanism; i.e., a system of disordered islands appears at the $Si_{1-x}Ge_x/Si$ interface. This is confirmed by scanning tunneling electron microscopy of the structure surface. Impurity gettering in the vicinity of these islands gives rise to effective scattering centers at the transport-channel boundary, thereby reducing the mobility of 2D electrons in the Si layer plane (to 4000 $cm^2/(V\ s)$ at 5 K according to our measurements). The growing germanium layer can be made thinner and the surface roughness that appears can be reduced by increasing the rate of gas evacuation from the reactor.

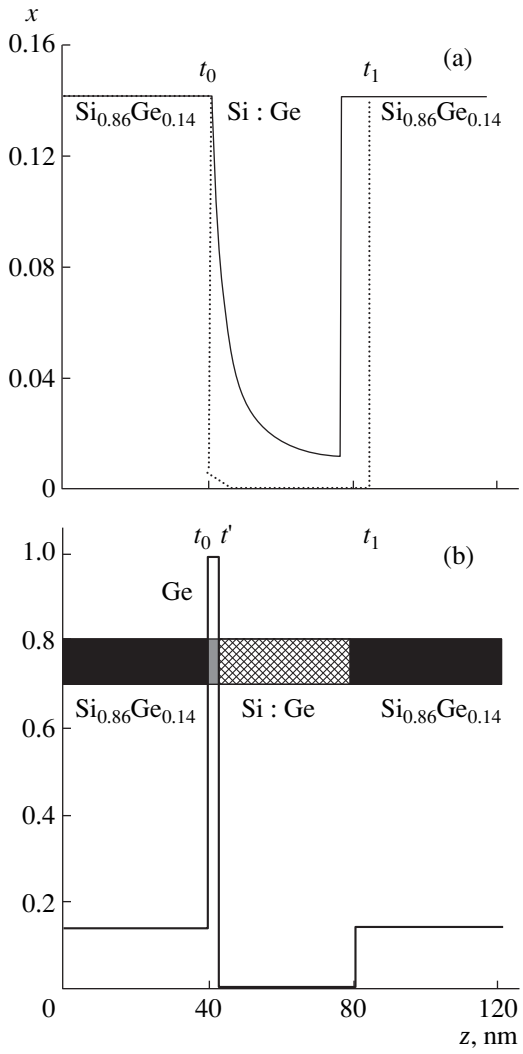

Fig. 3. Calculated distribution of germanium in a $Si_{0.96}Ge_{0.14}/Si/Si_{0.96}Ge_{0.14}$ structure grown by the ($Si–GeH_4$)-MBE technique with interruption at time t_0 of (a) molecular and (b) both molecular and atomic fluxes in the reactor. (a) $t_1 - t_0$ = 2 min and (b) $t' - t_0 = t_1 - t'$ = 2 min. The solid lines show the actually observed time dependence of germane evacuation from the growth chamber $P(t) = 2 \times 10^{-3}/\{1 + 32.8(t - t_0)\}$, dashed lines correspond to an infinite germane evacuation rate $P(GeH_4) = 2 \times 10^{-3}$ Torr at $t < t_0$, $t > t_1$ and $P(GeH_4) = 0$ at $t_0 < t < t_1$.

ACKNOWLEDGMENTS

We thank Prof. E.S. Demidov for his helpful participation in discussions of the results. The work was performed in the framework of the Russian Programs "Universities of Russia" (grant no. 99-2849) and "Phys-

ics of Solid State Nanostructures" (grant no. 97-2023) and was supported by INTAS (grant no. 96-0580).

REFERENCES

1. D. W. Greve, Mater. Sci. Eng., B **18**, 22 (1993).
2. M. G. Mil'vidskiĭ, V. I. Vdovin, L. K. Orlov, *et al.*, in *Growth of Crystals*, Ed. by E. I. Givargizov and A. M. Melnikova (Consultants Bureau, New York, 1996), Vol. 20, p. 13.
3. L. K. Orlov, V. A. Tolomasov, A. V. Potapov, and V. I. Vdovin, in *Proceedings of the 2nd Russia Symposium "Processes of Heat and Mass Transport and Growth of Single Crystals and Thin-Film Structures", Obninsk, 1998*, Ed. by V. P. Ginkin, p. 288.
4. L. K. Orlov, V. A. Tolomasov, A. V. Potapov, and V. I. Vdovin, Izv. Vyssh. Uchebn. Zaved., Ser. Mater. Élektron. Tekh. **2**, 30 (1998).
5. V. A. Tolomasov, L. K. Orlov, S. P. Svetlov, *et al.*, Kristallografiya **43**, 535 (1998) [Crystallogr. Rep. **43**, 493 (1998)].
6. T. Karasava, Y. Kunii, and M. Tabe, Jpn. J. Appl. Phys. **32**, 1039 (1993).
7. A. V. Potapov, Author's Abstract of Candidate's Dissertation (Nizhni Novgorod, 1999).
8. L. K. Orlov, A. V. Potapov, and S. V. Ivin, Zh. Tekh. Fiz. **70** (6), 102 (2000) [Tech. Phys. **45**, 770 (2000)].
9. L. K. Orlov, V. A. Tolomasov, A. V. Potapov, *et al.*, Inst. Phys. Conf. Ser. **155**, 205 (1997).
10. A. V. Potapov, L. K. Orlov, and S. V. Ivin, Thin Solid Films **336**, 191 (1998).
11. L. K. Orlov and A. V. Potapov, in *Physics, Chemistry and Application of Nanostructures Review and Short Notes to Nanomeeting'97, Minsk, 1997* (World Scientific, Singapore, 1997), p. 68.
12. L. K. Orlov, A. V. Potapov, and S. V. Ivin, Solid State Phenom. **69**/**70**, 221 (1999).
13. L. K. Orlov, A. V. Potapov, R. A. Rubtsova, and N. L. Orlova, Izv. Ross. Akad. Nauk, Ser. Fiz. **53**, 267 (1999).
14. B. Cunningham, J. O. Chu, and S. Akbar, Appl. Phys. Lett. **59**, 3574 (1991).

Translated by M. Tagirdzhanov

Semiconductors, Vol. 34, No. 10, 2000, pp. 1109–1111. Translated from Fizika i Tekhnika Poluprovodnikov, Vol. 34, No. 10, 2000, pp. 1159–1161.

ELECTRONIC AND OPTICAL PROPERTIES OF SEMICONDUCTORS

Hot-Electron Capture by Negatively Charged Centers in an Approximation of Quasi-elastic Scattering

Z. S. Kachlishvili* and N. K. Metreveli

Department of Physics, Tbilisi State University, Tbilisi, 380028 Georgia

** e-mail: faculty@tsu.ge or kzauri@altavista.com*

Submitted February 23, 2000; accepted for publication March 30, 2000

Abstract—The capture coefficient at the repulsive Coulomb centers is calculated in an explicit form within the approximation of quasi-elastic scattering in crossed strong electric and magnetic fields. It is shown that, along with the Sommerfeld factor, the capture probability must depend exponentially on the energy of an electron that has tunneled through a barrier. The dependence of the critical electric field, above which the exponential dependence should be considered, on the magnetic field and the scattering mechanism is determined. In fields lower than the critical one, the Bonch-Bruevich approximation is valid. *© 2000 MAIK "Nauka/Interperiodica".*

Hot-electron capture by negatively charged centers has been studied in numerous publications (see, for example, [1–4]). The necessity of developing the existing theories has led us to reconsider this problem. In all previous studies, including those mentioned above, electron capture has been estimated by using the expression for capture probability first obtained by Bonch-Bruevich [1]. However, as shown in [5, 6], the capture of an electron by a repulsive center should not only involve the Sommerfeld factor, but should also depend exponentially on the energy of an electron that has tunneled though a barrier:

$$P \sim \exp(-\gamma_0 x), \tag{1}$$

where $x = W/kT$, W is the electron energy, $\gamma_0 = \frac{2\tau_1}{\hbar} kT$, and τ_1 is the time of tunneling. The same authors also calculated the capture coefficient in the electron-temperature approximation and showed that consideration of electron tunneling leads to the substitution of the electron temperature by an effective electron temperature which contains a parameter of the center on the order of the inverse energy of the vibration quantum. When the electron temperature is much lower than this energy, the results obtained in [5] coincide with those obtained by Bonch-Bruevich [1].

With allowance made for expression (1), the capture coefficient was calculated under the conditions of a transverse runaway and a delta-function distribution of hot electrons [7, 8]. According to the results obtained in these studies, the effective Bonch-Bruevich cross section is a good approximation far from the runaway threshold and for a multiply charged capture center, whereas in the opposite cases it is necessary to take into account the exponential factor.

We calculated the capture coefficient in crossed strong electric and magnetic fields in an explicit form within a quasi-elastic scattering approximation. The critical electric field, above which the exponential function (1) should be considered, is determined as a function of the magnetic field and scattering mechanisms.

The nonequilibrium distribution function in a quasi-elastic-scattering approximation in crossed strong electric and magnetic fields has the form [9]

$$f_0(x) = N\exp(-ax^{\xi}), \quad \xi > 0, \tag{2}$$

where $a \equiv \frac{\eta^{\zeta}}{\alpha\xi}$, $\xi = \xi_1 = 1 - \frac{t+s}{2}$, and $\zeta = 0$ in a weak magnetic field ($\eta \ll 1$); $\xi = \xi_2 = 1 + \frac{t-s}{2}$ and $\zeta = 1$ in a strong magnetic field ($\eta \gg 1$); and t and s are the exponents in the energy dependences of the mean free paths with respect to the momentum (l) and energy ($\tilde{l}$):

$$l = l_0 x^{\frac{t+1}{2}}, \quad \tilde{l} = \tilde{l}_0 x^{\frac{s+1}{2}},$$

$$\alpha \equiv \left(\frac{E}{E_0}\right)^2, \quad \eta \equiv \left(\frac{H}{H_0}\right)^2,$$

$$E_0 \equiv \sqrt{3}\frac{k_0 T}{e(l_0\tilde{l}_0)^{1/2}}, \quad H_0 \equiv \frac{(2mc^2 k_0 T)^{1/2}}{el_0},$$

where m is the effective electron mass and c is the speed of light.

Using a conventional definition of the capture coefficient and calculating the integrals by the steepest

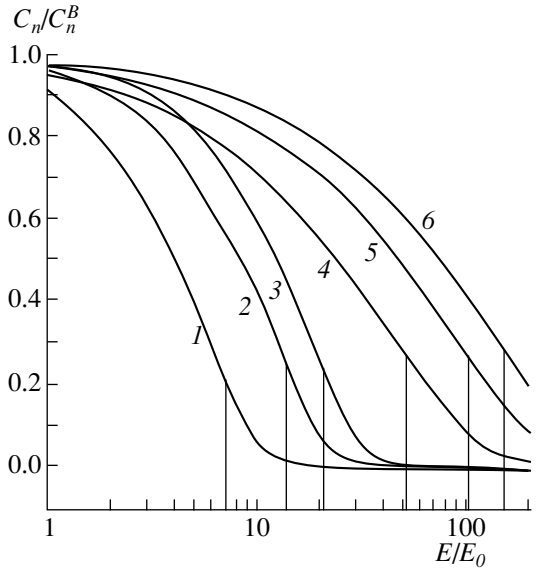

The ratio of capture coefficients as a function of the electric field. The curves correspond to (*1*) $\xi = 1$ and a weak magnetic field); (*2*) $\xi = 1$, $\eta = 4$, and a strong magnetic field; (*3*) $\xi = 1$, $\eta = 9$, and a strong magnetic field; (*4*) $\xi = 2$ and a weak magnetic field); (*5*) $\xi = 2$, $\eta = 4$, and a strong magnetic field; (*6*) $\xi = 2$, $\eta = 9$, and a strong magnetic field.

descent method, we obtain the following expression for the ratio of the capture coefficients with and without consideration of factor (1) (C_n and C_n^B, respectively) for $\xi = 1$:

$$\frac{C_n(E,H)}{C_n^B(E,H)} = \left(\frac{\eta^{\frac{\zeta}{\alpha}}}{\gamma_0 + \frac{\eta^2}{\alpha}}\right)^{\frac{5+4\nu_0}{6}} \frac{\Psi\left[\left(\frac{\gamma/2}{\gamma_0 + \frac{\eta^\zeta}{\alpha}}\right)^{2/3}\right]}{\Psi\left[\left(\frac{\gamma}{2}\frac{\alpha}{\eta^\zeta}\right)^{2/3}\right]} \times \exp\left\{-3\left(\frac{\gamma}{2}\right)^{2/3}\left[\left(\gamma_0 + \frac{\eta^\zeta}{\alpha}\right)^{1/3} - \left(\frac{\eta^\zeta}{\alpha}\right)^{1/3}\right]\right\}. \quad (3)$$

Here, Ψ is a slowly varying function, ν_0 is a parameter of the order of unity, $\gamma \equiv \frac{2\pi z e^2}{\varepsilon \hbar V_T}$, z is the charge of a repulsive center in electron charge units, ε is the dielectric constant, and V_T is the thermal velocity [1].

As was mentioned above, expression (3) is obtained for $\xi = 1$, because, in this case, a complete calculation can be performed without any approximations for the relation between α, η, γ, and γ_0. The condition $\xi = 1$ covers almost all possible mechanisms of electron and momentum scattering that may be dominant in the problem discussed. Indeed, in a weak magnetic field, $\xi = \xi_1 = 1$ if $t = +1$ and $s = -1$, or $t = -1$ and $s = +1$. In a strong magnetic field, $\xi = \xi_2 = 1$ if $t = +1$ and $s = +1$, or $t = -1$ and $s = -1$. For momentum scattering, these values of t and s correspond to the following mechanisms: scattering by dipole centers, by the piezoelectric potential of acoustic phonons (PA scattering) in a high-temperature approximation, by polar optical phonons (PO scattering), by the deformation potential of acoustic phonons (DA scattering) in a high-temperature approximation, and by the deformation potential of optical phonons (DO scattering). For energy scattering, the values of t and s correspond to the DA and PA scattering, in the high- and low-temperature approximations, and to DO scattering.

The critical magnitude of the applied electric field can be determined from expression (3) as $\alpha_{cr} \equiv \frac{\eta^\zeta}{\gamma_0}$. For the fields $\alpha \ll \alpha_{cr}$, factor (1) is insignificant and may be neglected. However, when $\alpha \geq \alpha_{cr}$, the Bonch-Bruevich approximation should be corrected by factor (1). In a strong magnetic field, the critical electric field increases directly with the magnetic field.

Now we present the results of calculating the capture-coefficient ratio for an arbitrary value of $\xi > 0$. In this case, the complete calculations can be carried out only if certain relations between the parameters α, η, γ_0, and ξ are fulfilled.

1. For

$$\gamma_0 \ll \xi\left(\frac{\eta^\zeta}{\alpha\xi}\right)^{1/\xi}\left(\frac{\Gamma\left(\frac{5}{2\xi}\right)}{\Gamma\left(\frac{3}{2\xi}\right)}\right)^{\xi-1}, \quad (4)$$

$$\frac{C_n(E,H)}{C_n^B(E,H)} = \exp\left[-\gamma_0\left(\frac{\gamma\alpha}{2\eta^\zeta}\right)^{\frac{2}{2\xi+1}}\right]. \quad (5)$$

2. For

$$\gamma_0 \gg \xi\left(\frac{\eta^\zeta}{\alpha\xi}\right)^{1/\xi}\left(\frac{\Gamma\left(\frac{5}{2\xi}\right)}{\Gamma\left(\frac{3}{2\xi}\right)}\right)^{\xi-1}, \quad (6)$$

$$\frac{C_n(E,H)}{C_n^B(E,H)} = \frac{\left(\frac{\gamma}{2\gamma_0}\right)^{\frac{2\nu_0}{3}}\Psi\left(\left(\frac{\gamma}{2\gamma_0}\right)^{2/3}\right)}{\left(\frac{\gamma\alpha}{2\eta^\zeta}\right)^{\frac{2\nu_0}{2\xi+1}}\Psi\left(\left(\frac{\gamma\alpha}{2\eta^\zeta}\right)^{\frac{2}{2\xi+1}}\right)}$$

$$\times\left(\frac{\left(2\frac{\eta^{\zeta}}{\alpha}\right)^{\frac{5}{2\xi+1}}\gamma^{\frac{2\xi-4}{2\xi+1}}(2\xi+1)}{3\frac{(2\gamma_0)^{5/3}}{\gamma^{2/3}}+4\frac{\eta^{\zeta}}{\alpha}(\xi-1)\left(\frac{\gamma}{2\gamma_0}\right)^{2(\xi-2)/3}}\right)^{1/2} \quad (7)$$

$$\times\exp\left\{-\frac{3}{2}\gamma^{2/3}(2\gamma_0)^{1/3}-\frac{\eta^{\zeta}}{\alpha\xi}\left(\frac{\gamma}{2\gamma_0}\right)^{2\xi/3}\right.$$

$$\left.+\frac{2\xi+1}{2\xi}\left(2\frac{\eta^{\zeta}}{\alpha}\right)^{\frac{1}{2\xi+1}}\gamma^{\frac{2\xi}{2\xi+1}}\right\}.$$

One can readily see that the ratio of coefficients (3) for $\xi = 1$ exactly coincides with the corresponding expressions from (5) and (7), provided inequalities (4) and (6) are valid. It is also evident that the α_{cr} can be extended to an arbitrary value of $\xi > 0$:

$$\alpha_{cr} = \xi^{(\xi-1)}\frac{\eta^{\zeta}}{\gamma_0^{\xi}}\left(\frac{\Gamma\left(\frac{5}{2\xi}\right)}{\Gamma\left(\frac{3}{2\xi}\right)}\right)^{\xi(\xi-1)}. \quad (8)$$

Thus, for the fields $\alpha \geq \alpha_{cr}$, calculation of the capture coefficients requires consideration of factor (1). For the fields $\alpha \ll \alpha_{cr}$, the Bonch-Bruevich approximation is valid.

In order to verify the precision of analytical expressions (3), (5), and (7) and for the sake of illustrating the results, we performed numerical calculations of the integrals of the general expression C_n/C_n^B for $\xi = 1$ and $\xi = 2$ at $T = 20$ K in weak and strong magnetic fields. The corresponding curves are shown in the figure. It should be noted that, for certain magnitudes of the electric field, they exactly coincide with the curves described by expressions (3), (5), and (7). The vertical lines indicate the positions of the critical electric fields. As one might expect, all the curves in a region far from the critical fields behave identically: they tend to unity in weak fields and tend to zero with increasing field strength.

REFERENCES

1. V. L. Bonch-Bruevich, Fiz. Tverd. Tela (Leningrad) **6**, 2047 (1964) [Sov. Phys. Solid State **6**, 1615 (1964)].
2. V. L. Bonch-Bruevich and S. G. Kalashnikov, Fiz. Tverd. Tela (Leningrad) **7**, 750 (1965) [Sov. Phys. Solid State **7**, 599 (1965)].
3. V. L. Bonch-Bruevich and Z. S. Kachlishvili, Vestn. Mosk. Univ., Ser. 3: Fiz., Astron. **5**, 580 (1974).
4. Kh. Z. Kachlishvili and A. G. Mironov, Tr. Tbilis. Univ. **291**, 37 (1989).
5. V. N. Abakumov, V. Karpus, V. I. Perel', and I. N. Yassievich, Fiz. Tekh. Poluprovodn. (Leningrad) **22**, 262 (1988) [Sov. Phys. Semicond. **22**, 159 (1988)].
6. V. N. Abakumov, V. I. Perel', and I. N. Yassievich, *Nonradiative Recombination in Semiconductors* (S.-Peterburgskiĭ Inst. Yadernoĭ Fiziki Ross. Akad. Nauk, St. Petersburg, 1997), p. 140.
7. Z. S. Kachlishvili, Kh. Z. Kachlishvili, and F. G. Chumburidze, Fiz. Tekh. Poluprovodn. (St. Petersburg) **31**, 204 (1997) [Semiconductors **31**, 161 (1997)].
8. Z. S. Kachlishvili, Kh. Z. Kachlishvili, and F. G. Chumburidze, Fiz. Tekh. Poluprovodn. (St. Petersburg) **31**, 944 (1997) [Semiconductors **31**, 804 (1997)].
9. Z. S. Kachlishvili, Phys. Status Solidi A **33**, 15 (1976).

Translated by A. Zalesskiĭ

Semiconductors, Vol. 34, No. 10, 2000, pp. 1112–1115. Translated from Fizika i Tekhnika Poluprovodnikov, Vol. 34, No. 10, 2000, pp. 1162–1165.

ELECTRONIC AND OPTICAL PROPERTIES OF SEMICONDUCTORS

A Verification of the Applicability of the Monovalent-Defect Model to the Description of Properties of the Vacancy–Oxygen Complex in Silicon

L. F. Makarenko

Belarussian State University, ul. Leningradskaya 14, Minsk, 220080 Belarus

e-mail: makarenko@fpm.bsu.minsk.by

Submitted February 9, 2000; accepted for publication March 30, 2000

Abstract—Temperature dependences of the charge-carrier concentration in Czochralski-grown *n*-Si crystals irradiated with ^{60}Co gamma-quanta are studied. The applicability of a model of the monovalent defect with a level at about $E_c - 0.17$ eV to the description of the *A*-center properties in *n*-Si crystals is analyzed. It is shown that the model is not consistent with available experimental data. It is suggested that the *A*-center introduces two levels into the upper half of the band gap: an acceptor level in the vicinity of $E_c - 0.16$ eV and a donor level near $E_c - 0.20$ eV. This assumption is consistent with the data obtained by magnetic spectroscopy. © *2000 MAIK "Nauka/Interperiodica".*

The structure of the oxygen–vacancy complex (the *A*-center) in silicon has long been known [1]; however, many of its properties have not been explained satisfactorily. One of these properties is the extremely high recombination activity of the *A*-centers, which is caused by a very large capture cross section for both electrons (σ_n) and holes (σ_p) [2]. According to [2, 3], the theory of multiphonon transitions cannot account for such large values of cross sections for charge-carrier capture by the *A*-center acceptor state (at least for σ_p). The causes of such a discrepancy between the theory and experiment are not yet clear. One of these causes may consist in the inapplicability of the multiphonon-transition theory to the vacancy centers [2]. However, it is possible that the discrepancy is caused by the fact that the current concepts of the *A*-center in *n*-Si as a simple monovalent defect are unrealistic.

These concepts have primarily come into existence on the basis of results of Hall measurements that indicated that the *A*-center had an acceptor level $E_A(-/0) \approx E_c - 0.17$ eV [4, 5]. Most commonly (see [16]), the ionization energy obtained by Wertheim [4] is cited: $\Delta E_A = 0.160 + 1.1 \times 10^{-4}$ T (in eV), where, as usual, $\Delta E_A = E_c - E_A(-/0)$. The data of the Hall measurements were analyzed in more detail elsewhere [5]. It was found that the values of enthalpy (ΔH_A) and entropy (ΔS_A) that correspond to *A*-center ionization and are obtained for materials with various ratios between the concentrations of donors and compensating radiation defects may differ considerably. Therefore, it is desirable, in addition to the determination of ΔH_A and ΔS_A, to somehow assess whether the description of experimental data in terms of the occupancy function used is adequate. Unfortunately, such an assessment was not performed fully either in the above cited or in the subsequent publications devoted to studying the *A*-center with the use of the Hall effect.

The results of capacitance-related studies of radiation defects in silicon also give no way of judging the adequacy of the monovalent-defect model. The *A*-center parameters determined by different researchers feature a wide scatter, which, in our opinion, exceeds what might be expected. Thus, the value of $\Delta H_A = 0.15$ eV was reported previously [7], whereas $\Delta H_A = 0.19$ eV is typical of detector-grade silicon [8]. In addition, the influence of the electric field of the *p–n* junction on the emission rate of electrons from the *A*-center acceptor level [9, 10] hampers the interpretation of data obtained in studying the barrier structures with differing impurity concentrations.

Thus, the available experimental data give no way of stating that the monovalent-defect model is adequate to describe the *A*-center occupancy function in *n*-Si. Consequently, this model should be regarded as a mere hypothesis that requires testing. It is such a test that constitutes the subject of this study.

We studied a Czochralski-grown single-crystal *n*-Si with a resistivity of 20 Ω cm and concentrations of oxygen $[O] = 0.9 \times 10^{18}$ cm^{-3} and carbon $[C] = 5 \times 10^{16}$ cm^{-3}. Temperature (T = 78–320 K) dependences of the Hall coefficient R_H were measured. The charge-carrier concentration n was calculated with the conventional formula $n = A_H(T)/eR_H$, where $A_H(T)$ is the Hall factor. The temperature dependence $A_H(T)$ was approximated by a polynomial, much the same as was done previously [5, 11].

1063-7826/00/3410-1112$20.00 © 2000 MAIK "Nauka/Interperiodica"

In order to introduce the *A*-centers, we irradiated the samples with ^{60}Co gamma-quanta. The irradiation dose was chosen in accordance with the condition for slight compensation, so that the *A*-center concentration (N_A) would be lower than the phosphorus-dopant concentration (N_P). According to numerous experimental data [2, 12–14], in Czochralski-grown lightly doped ($n < 10^{16}$ cm^{-3}) *n*-Si crystals irradiated with ^{60}Co gamma-quanta, the *A*-center is the prevalent type of electrically active defects, whereas the concentration of other centers with levels in the upper half of the band gap is negligibly low.

Figure 1 shows the temperature dependences of electron concentration $n(T)$ for one of the studied samples; these dependences were measured both immediately after irradiation and after several stages of isothermal annealing at 352°C. As a result of irradiation, a radiation defect with the level in the vicinity of $E_c - 0.18$ eV is introduced; henceforth, this defect is designated as $E(0.18)$. The simplest method for identifying a defect from the Hall data consists in determining its level from the position of the Fermi level ($F_{1/2}$) at a temperature for which the occupancy function is equal to 1/2 and, consequently, corresponds to the electron concentration $n = (N_{net} - N_{low})/2$ (the quantities N_{net} and N_{low} are indicated in Fig. 1). For all crystals, the value of $F_{1/2} = E_c$–0.183 eV for $E(0.18)$ was obtained, which is consistent with the data reported previously [4, 11]. The temperature and the time constant of annealing for the $E(0.18)$ centers are also consistent with the results obtained in studying the *A*-centers by electron spin resonance (ESR) and infrared (IR) spectroscopy [15, 16], which serve as additional verification when identifying the center in question with the oxygen–vacancy complex.

First, we analyze the adequacy of the single-level model using the differential method [17]. According to [17], the parameters of a defect may be determined from the Fermi-level (F) dependence of the quantity

$$D_H = \frac{4}{N_A} kT \frac{dn}{dF}. \quad (1)$$

We approximated numerically the quantity D_H as

$$\Delta_H = \frac{2}{N_A} kT_i \left[\frac{\Delta n_i}{\Delta F_i} + \frac{\Delta n_{i+1}}{\Delta F_{i+1}} \right]. \quad (2)$$

Here, $\Delta n_i = n_{exp}(T_i) - n_{exp}(T_{i-1})$ and $\Delta F_i = F_{exp}(T_i) - F_{exp}(T_{i-1})$, where $n_{exp}(T_i)$ and $F_{exp}(T_i)$ are the experimentally determined values of the electron concentration and the Fermi-level position, respectively. Such an approximation makes it possible to partly smooth the oscillations in Δ_H, which emerge owing to random errors in the measurements.

The maximal value of Δ_H for a monovalent defect with $\Delta S_A = 0$ should be virtually equal to unity [17, 18]. However, the maximal value of Δ_H is significantly smaller than unity for the *A*-center (see Fig. 2). This may indicate that $\Delta S < 0$ [18]. In fact, the dependence $\Delta_H(F)$ calculated for the values of ΔH_A and ΔS_A reported previously [4] is in much better accord with experimental data than the similar dependence calculated for $\Delta H_A = F_{1/2}$ and $\Delta S_A = 0$ (see Fig. 2). However, neither of the curves calculated on the basis of the single-level model can satisfactorily describe the experimental data in the entire temperature range under consideration. Thus, for example, curve *A* (Fig. 2) adequately describes the high-temperature portion of experimental dependence, whereas curve *B* adequately describes only the low-temperature portion.

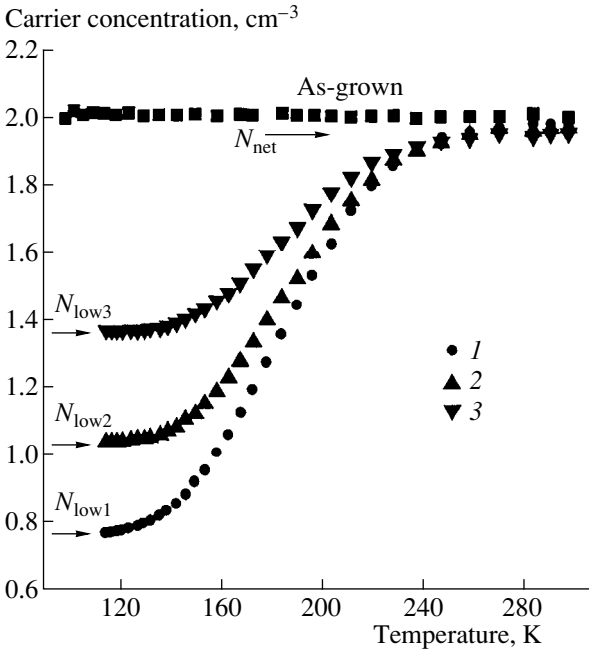

Fig. 1. Temperature dependences of the charge-carrier concentration in silicon crystal (*1*) immediately after irradiation with ^{60}Co gamma-quanta to a dose of $\Phi = 2.5 \times 10^{17}$ cm^{-3} and after subsequent annealing at 352°C for (*2*) 15 and (*3*) 40 min.

The cause of the discrepancy between the calculated and experimental dependences $\Delta_H(T)$ becomes clear if we consider the temperature variations of the quantity

$$\varepsilon(T) = kT \ln \frac{N_c}{n} \frac{N_{net} - n}{n - N_{low}}, \quad (3)$$

where N_c is the effective density of states in the valence band. According to [19], $\varepsilon(T) = \Delta E(T) = \Delta H_A - T\Delta S_A$ for a monovalent defect. If we are not dealing with very low temperatures and if the starting and final temperatures in the experiments differ by no more than a factor of 2–3, the quantities ΔH_A and ΔS_A may be regarded as virtually constant and the dependence $\Delta E(T)$ is linear [20]. This assumption is typically postulated and can be used as the applicability criterion for the single-level model.

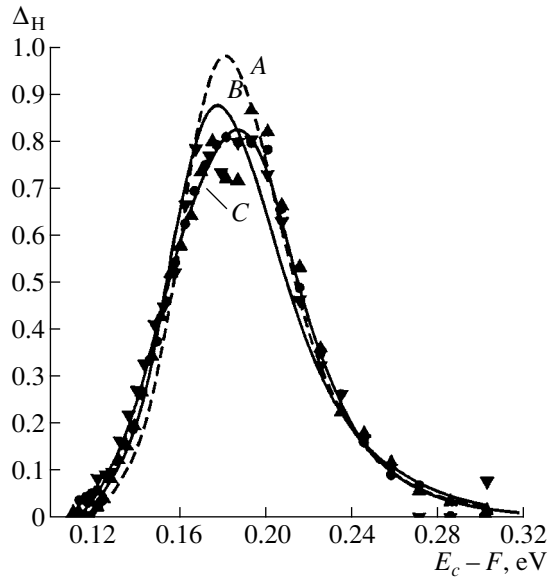

Fig. 2. Dependences of the quantity Δ_H on the distance between the conduction-band bottom (E_c) and the Fermi level (F). The symbols used to designate the experimental data are the same as in Fig. 1. Calculated curves Δ_H were computed on the basis of the electroneutrality equation according to the single-level model for the values of (*A*) ΔH_A = 0.183 eV and ΔS_A = 0; (*B*) ΔH_A = 0.160 eV and $\Delta S_A = -1.25k$ eV/K (taken from [4]); and also (*C*) according to the divalent-center model with the following parameters taken from [21]: ΔH_1 = 0.158 eV, $\Delta S_1 = -0.5k$ eV/K, ΔH_2 = 0.205 eV, and $\Delta S_2 = 0.4k$ eV/K.

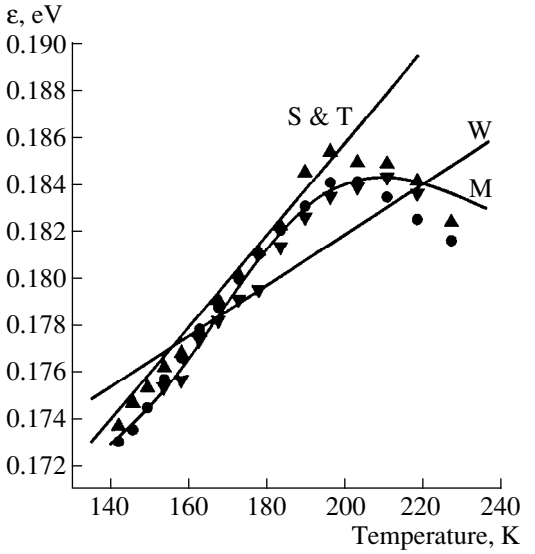

Fig. 3. Temperature dependences $\varepsilon(T)$. The symbols used to designate the experimental data are the same as in Fig. 1. The straight lines represent the dependences $\Delta E_A(T)$ plotted on the basis of the results reported in [4] (W) (ΔH_A = 0.160 eV and $\Delta S_A = -1.25k$ eV/K) and in [5] (S & T) (ΔH_A = 0.146 eV and $\Delta S_A = -2.3k$ eV/K); the curve M was calculated on the basis of the divalent-center model with the following parameters taken from [21]: ΔH_1 = 0.158 eV, $\Delta S_1 = -0.5k$ eV/K, ΔH_2 = 0.205 eV, and $\Delta S_2 = 0.4k$ eV/K.

Experimental curves $\varepsilon_{exp}(T)$ are shown in Fig. 3. The dependences $\Delta E_A(T)$ obtained by Wertheim (W) [4] and Sonder and Templeton (S & T) [5] are also plotted. As can be seen, the curve derived by Wertheim [4] is a linear approximation of the dependence $\varepsilon_{exp}(T)$ in the entire temperature range under consideration, whereas the straight line plotted according to the data obtained by Sonder and Templeton [5] is a good approximation of only the low-temperature portion of the experimental curve. However, it can be seen that the experimental curves $\varepsilon_{exp}(T)$ cannot be described by a linear dependence. Consequently, in order to interpret the experimental data of the Hall measurements, we have to assume that either the *A*-center ionization energy features an anomalous nonlinear temperature dependence or the model used to describe the *A*-center properties is inapplicable. The first assumption is apparently unlikely from the standpoint of the physical significance of the quantities ΔH_A and ΔS_A [20]. It follows from the second assumption that it is necessary to use a more sophisticated model for describing the *A*-center occupancy function.

Recently [21], a new model was suggested; according to this model, the *A*-center is regarded as an amphoteric defect with an acceptor level near $E_c - 0.16$ eV and a donor level in the vicinity of $E_c - 0.20$ eV. As can be seen from Figs. 2 and 3, this model adequately accounts for the features of the dependences $\Delta_H(F)$ and $\varepsilon(T)$. The model also makes it possible to explain the data of the Hall measurements in Si crystals irradiated with large doses of gamma-quanta [22], in which case a large spread (from 0.16 to 0.20 eV) is observed for the *A*-center activation energy. In addition, the above assumption is also consistent with the data obtained by other methods.

The simplest test for the applicability of the bivalent model to the *A*-center is apparently related to the data of ESR spectroscopy. The *A*-center is paramagnetic only in the negatively charged state (the Si-B1 center) [1]. In this case, according to this model, the concentration of Si-B1 centers in the Czochralski-grown silicon crystals should be equal to $(N_{net} - N_{low})/2$. At the same time, it follows from Fig. 1 that a decrease in the concentration of phosphorus-impurity atoms in the paramagnetic state would be proportional to $N_{net} - N_{low}$. Thus, it should be expected that an increase in the amplitude of the ESR signal related to Si-B1 would amount to only half of a decrease of the signal related to phosphorus donors, which agrees well with experimental data [23].

If the *A*-center has a donor level, the value of N_{net} should increase after irradiation to $N_{net}^{irr} = N_P + N_A$, and, after termination of the *A*-center ionization, we would observe an increase in the charge-carrier concentration by a value of N_A compared to the initial phosphorus concentration. Since such an increase is not observed, we should assume that, simultaneously with the *A*-centers, other acceptor defects with virtually the same

introduction rate are produced under irradiation. Moreover, as follows from Fig. 1, this acceptor center should be annealed in exactly the same way as the *A*-center. Although, at first glance, such a correlation appears to be unlikely, it can be logically expected for generically related radiation defects. Moreover, it was such behavior that was revealed from the DLTS data for $E(0.18)$ and the hole trap $H(0.42)$ [12].

It is assumed that the $H(0.42)$ center is related to the complex C_iO_i [23–25]. In turn, a correlation between the spatial distributions of the *A*-center and C_iO_i is consistent with the data reported [26] and related to electron transitions between these centers in irradiated silicon. It is the result of the effect of this interimpurity recombination mechanism that may account for the anomalously high recombination activity of the oxygen–vacancy complex in silicon.

Thus, we have shown that the assumption that the *A*-center in silicon is a defect that introduces a single acceptor level into the upper half of the band gap is inconsistent with experimental data of the Hall coefficient measurements. The model according to which the *A*-center in silicon has an acceptor level near $E_c - 0.16$ eV and a donor level in the vicinity of $E_c - 0.20$ eV is more satisfactory.

REFERENCES

1. G. D. Watkins and J. W. Corbett, Phys. Rev. **121**, 1001 (1961).
2. A. S. Zubrilov and S. V. Koveshnikov, Fiz. Tekh. Poluprovodn. (Leningrad) **25**, 1332 (1991) [Sov. Phys. Semicond. **25**, 804 (1991)].
3. S. M. Dikman, Fiz. Tekh. Poluprovodn. (St. Petersburg) **26**, 1427 (1992) [Sov. Phys. Semicond. **26**, 801 (1992)].
4. G. K. Wertheim, Phys. Rev. **106**, 1272 (1958).
5. E. Sonder and L. C. Templeton, J. Appl. Phys. **31**, 1279 (1960).
6. V. V. Emtsev and T. V. Mashovets, *Point Defects in Semiconductors* (Radio i Svyaz', Moscow, 1980).
7. C. A. Londos, Phys. Status Solidi A **113**, 503 (1989).
8. E. M. Verbitskaya, V. K. Eremin, A. M. Ivanov, and N. B. Strokan, Fiz. Tekh. Poluprovodn. (St. Petersburg) **27**, 1113 (1993) [Semiconductors **27**, 612 (1993)].
9. B. A. Komarov and V. I. Sopryakov, Phys. Status Solidi A **66**, 783 (1981).
10. K. Irmscher, H. Klose, and K. Maass, Phys. Status Solidi A **75**, K25 (1983).
11. H. J. Stein and F. L. Vook, Phys. Rev. **163**, 790 (1967).
12. L. C. Kimerling, in *Radiation Defects in Semiconductors*, Ed. by N. B. Urli and J. W. Corbett (Inst. of Physics and Physical Society, London, 1977), p. 221.
13. S. D. Brotherton and P. J. Bradley, J. Appl. Phys. **53**, 5720 (1982).
14. L. S. Berman, V. B. Voronkov, A. D. Remenyuk, and M. G. Tolstobrov, Fiz. Tekh. Poluprovodn. (Leningrad) **21**, 140 (1987) [Sov. Phys. Semicond. **21**, 84 (1987)].
15. J. W. Corbett and G. D. Watkins, Phys. Rev. A **135**, 1381 (1964).
16. B. G. Svensson and J. L. Lindström, Phys. Rev. B **34**, 8709 (1986).
17. H-J. Hoffmann, Appl. Phys. **19**, 307 (1979).
18. L. F. Makarenko, V. P. Markevich, and L. I. Murin, Fiz. Tekh. Poluprovodn. (Leningrad) **19**, 1935 (1985) [Sov. Phys. Semicond. **19**, 1192 (1985)].
19. V. L. Bonch-Bruevich and S. G. Kalashnikov, in *The Physics of Semiconductors* (Nauka, Moscow, 1977), Chap. 5.
20. J. A. van Vechten and C. D. Thurmond, Phys. Rev. B **14**, 3559 (1976).
21. L. F. Makarenko, Dokl. Akad. Nauk Belarusi **40** (4), 59 (1996).
22. N. A. Vitovskiĭ, T. V. Mashovets, and S. M. Ryvkin, Fiz. Tverd. Tela (Leningrad) **4**, 2845 (1962) [Sov. Phys. Solid State **4**, 2085 (1963)].
23. G. D. Watkins, J. W. Corbett, and R. M. Walker, J. Appl. Phys. **30**, 1198 (1959).
24. J. M. Trombetta and G. D. Watkins, Appl. Phys. Lett. **51**, 1103 (1987).
25. L. I. Murin, Phys. Status Solidi A **101**, K107 (1987).
26. A. M. Frens, M. T. Bennebroek, A. Zakrzewski, *et al.*, Phys. Rev. Lett. **72**, 2939 (1994).

Translated by A. Spitsyn

Semiconductors, Vol. 34, No. 10, 2000, pp. 1116–1119. Translated from Fizika i Tekhnika Poluprovodnikov, Vol. 34, No. 10, 2000, pp. 1166–1169.

ELECTRONIC AND OPTICAL PROPERTIES OF SEMICONDUCTORS

Space-Charge-Limited Currents in a Synthetic Semiconducting Diamond

Yu. A. Detchuev*, V. A. Kryachkov*, É. G. Pel', and N. G. Sanzharlinskiĭ***

** All-Russia Research Institute for Synthesis of Mineral Raw Materials, Aleksandrov, 601600 Russia*

*** Vereshchagin Institute of High-Pressure Physics, Russian Academy of Sciences, Troitsk, Moscow oblast, 142090 Russia*

Submitted February 21, 2000; accepted for publication March 30, 2000

Abstract—The electrical properties of single crystals of synthetic semiconducting diamonds of *p*- and *n*-types with B and As impurities were studied. The method of space-charge-limited currents revealed As-related monoenergetic carrier traps and traps with exponential distribution of the density of states. The possibility of using the crystals of a synthetic semiconducting diamond in alpha-particle detectors and temperature-sensitive elements is demonstrated. © *2000 MAIK "Nauka/Interperiodica".*

Possessing a set of unique properties, a synthetic semiconductor diamond (SSD) is a promising material for electronics [1]. However, further investigations and applications are restricted by the complexity of its doping. Here, we report results obtained by studying the electrical properties of SSD single crystals grown under varied doping conditions and consider examples of their possible use in sensors.

The single crystals under study were grown by spontaneous crystallization [2], with TiC being introduced into the starting charge as a nitrogen getter, and B and As, as acceptor and donor impurities. By varying the composition and concentration of these additives, several sets of *p*-type SSD crystals were obtained with resistance in the range $R = 10–10^5\ \Omega$, as well as *n*-type crystals with $R > 10^6\ \Omega$.

The single crystals had the shape of a cube or a cubic octahedron 0.4–0.8 mm in size. Contacts with the areas of 5×10^{-4}–1×10^{-5} cm^2 were formed on their opposite (111) faces by a laser technique employing a multicomponent formulation with carbide-forming additives. Silver or gold wires were laser-welded to the contacts.

The conduction type of relatively low-resistivity crystals was determined from thermoelectric power measurements. The impurities responsible for the conduction were identified by the temperature dependence of resistance (Fig. 1). For example, for samples synthesized in the presence of a TiC getter and a minor addition of boron (the content of additives in the charge is given in Fig. 1 captions), the impurity activation energy $E_a = 0.35$ eV (Fig. 1, curves *3*, *4*) is close to that known for boron-related acceptor centers. For a higher boron content (curves *1*, *2*), $E_a \approx 0.20$ eV. A decrease in E_a in crystals of this kind is related, as shown previously [3], to the increasing concentration of boron.

For high-resistivity crystals obtained in the absence of a TiC getter in the charge (curve *6*), the activation energy ($E_d = 1.6$ eV) is characteristic of a deep nitrogen-related donor center. On addition of arsenic to the charge (curve *5*), an activation energy appears ($E_d = 0.7$ eV), corresponding to an As-related level in the band gap of SSD [4].

The specific features of $R(T)$ curves in the low-temperature region are typical of the case of hopping conduction [5].

Figure 2 shows current–voltage (I–V) characteristics for a number of crystals obtained under varied synthesis conditions. Let us consider in more detail the properties of SSD crystals of batch 5 (curve *5* in Fig. 1) with electrically active As centers. The specific features of the I–V characteristics of these crystals can be explained in terms of the model of space-charge-limited currents (SCLC) with the monopolar injection of electrons into an SSD containing electron traps [6].

I–V characteristics 5_1 and 5_2 are typical of the case of two kinds of monoenergetic traps with energy levels E_1 and E_2 and concentrations N_1 and N_2. When the Fermi level (E_F) in SSD crystals satisfies the condition $E_F < E_1 < E_2$, the sharp rise in the current is preceded at low voltages by a quadratic portion in the I–V characteristic (curve 5_2). For $E_1 < E_F < E_2$, an ohmic portion is observed at low voltages (curve 5_1). Each of the I–V characteristics contains two portions of a nearly vertical rise in the current at voltages corresponding to the complete occupation of traps first with energy E_1 and then E_2.

The "trap-controlled" quadratic portions of the I–V characteristics are described by the expression [6]

$$I = (\varepsilon\mu_n\theta U^2)/L^3, \qquad (1)$$

where $\theta = (N_c/gN_t)\exp(E_t - E_c)/kT$, L is the contact spacing, and the remaining symbols have conventional meaning.

1063-7826/00/3410-1116$20.00

For high voltages, the *I–V* characteristics exhibit a "trap-filled" quadratic portion

$$I = (\varepsilon\mu_n U^2)/L^3. \quad (2)$$

The expressions for the characteristic portions and points of the *I–V* characteristics make it possible to determine the parameters of free charge carriers and impurity states. For example, expression (2) was used to evaluate the electron mobility μ_n. The parameters of the donor level governing the equilibrium carrier concentration was determined from the ohmic portion of the *I–V* characteristics. The slope of the $\log I = f(1/T)$ dependence at a fixed voltage in the temperature range T = 300–800 K yields the donor activation energy E_d = 0.7 eV. The donor concentration N_0 was determined from the intersection of this straight line with the ordinate axis at $1/T \longrightarrow 0$. As shown by calculations, the N_0 values in SSD samples with different resistances fall within the range of 10^{16}–10^{19} cm^{-3}.

Using equation (1) and the expression for the voltage corresponding to the complete trap occupation [6], we evaluated the trap parameters. The scatter of the E_1 and E_2 values (0.5 and 0.58 eV, respectively, for sample 5_1) did not exceed 0.05 eV, and that of N_1 and N_2 (2×10^{11} and 5×10^{11} cm^{-3}, respectively) was no larger than an order of magnitude.

Application of the SCLC method to calculations of this kind was also justified by the existence of a linear dependence of I on $1/L^3$ in the quadratic portions of the *I–V* characteristics, obtained in measurements for different samples.

I–V characteristics with stronger-than-linear $I(U)$ dependences (Fig. 2, curves 5_3, 5_4) demonstrate the presence of traps with an exponential energy distribution of density [6] in the SSD single crystals. In this case,

$$I = N_c\mu e^{1-l}\left[\frac{\varepsilon l}{(l+1)h}\right]^l\left(\frac{2l+1}{l+1}\right)^{l+1}\frac{U^{l+1}}{L^{2l+1}}, \quad (3)$$

where $l = T/T_d$, and T_d is a characteristic distribution constant, with $T_d > T$.

When such a distribution begins at the conduction band bottom, it can be described by

$$h(E) = (H/kT_d)\exp(-E/kT_d), \quad (4)$$

where $h(E)$ is the trap-level concentration in a unit energy interval.

The parameters T_d and H calculated from the temperature dependences of *I–V* characteristics for such samples (Fig. 3) exhibit a linear dependence of $\log H$ on $1/kT_d$. As shown in [7] using the method employed in this study, this dependence is well described by a model that takes into account the presence of a monoenergetic trap level with energy E_t in the band gap

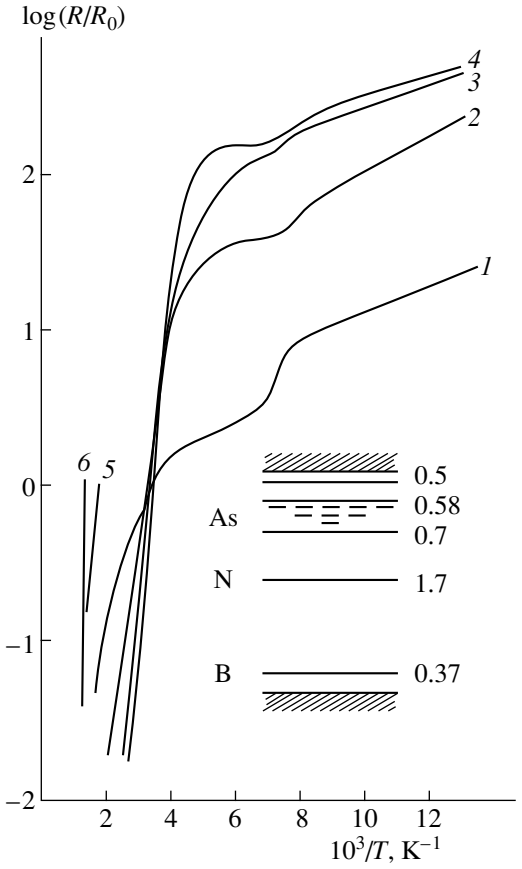

Fig. 1. Temperature dependences of the resistance of SSD samples obtained by synthesis from a charge containing, respectively, B, As, and TiC: (*1*) 0.1, 0, and 6; (*2*) 0.1, 2, and 6; (*3*) 0.003, 0, and 6; (*4*) 0.003, 2, and 6; (*5*) 0.003, 2, and 0; and (*6*) 0.1, 0, and 0 wt %. The insert shows the energy levels of B, As, and N in diamond (in eV with respect to the conduction-band bottom or the valence-band top).

and traps with the density of states exponentially decreasing from this level down into the band gap

$$h = (H'/kT_d)\exp(-E/kT_d)\exp(E_t/kT_d). \quad (5)$$

Here, E is the energy of traps in the exponential distribution, still reckoned from the conduction band bottom; H' is the total density of traps in the distribution below E_t; and $H = H'\exp(E_t/kT_d)$. These traps are shown schematically in the insert in Fig. 1.

The slope of the straight line $\log H = f(1/kT_d)$ yields a value of E_t, and the intersection of this straight line with the ordinate axis at $1/kT_d \longrightarrow 0$, a value of H'. For the SSD samples studied, the values of E_t were within 0.57–0.61 eV, and H', in the range of 10^9–10^{12} cm^{-3}.

At temperatures higher than 520 K and low voltages, an ohmic portion with parameters governed by the 0.7-eV level appears in the *I–V* characteristics.

The calculated energies of local levels are close to the previously obtained values [4, 8]. The fact that the

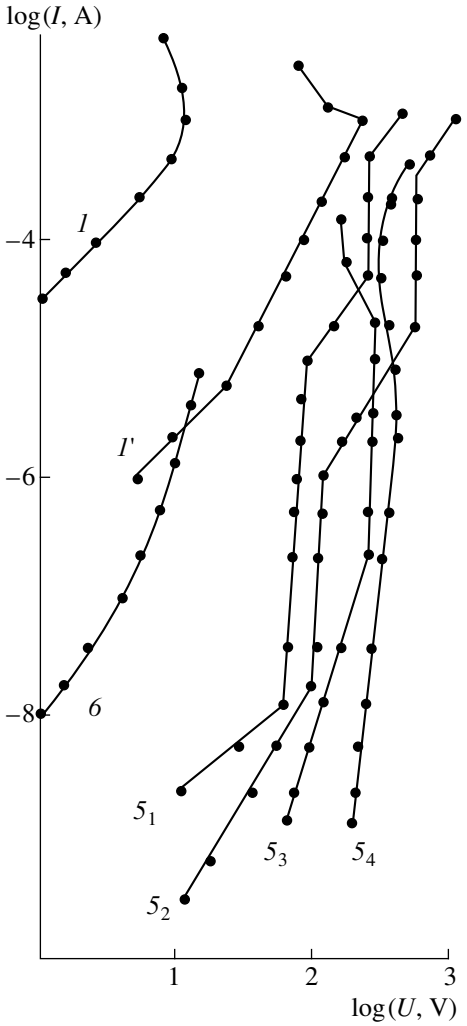

Fig. 2. The *I–V* characteristics of SSD crystals 1, 5, and 6 (see Fig. 1) at 300 K (*1*; 5_1–5_4; *6*) and 77 K (*1*'). SSD crystals 5_1–5_4 were obtained under identical synthesis conditions.

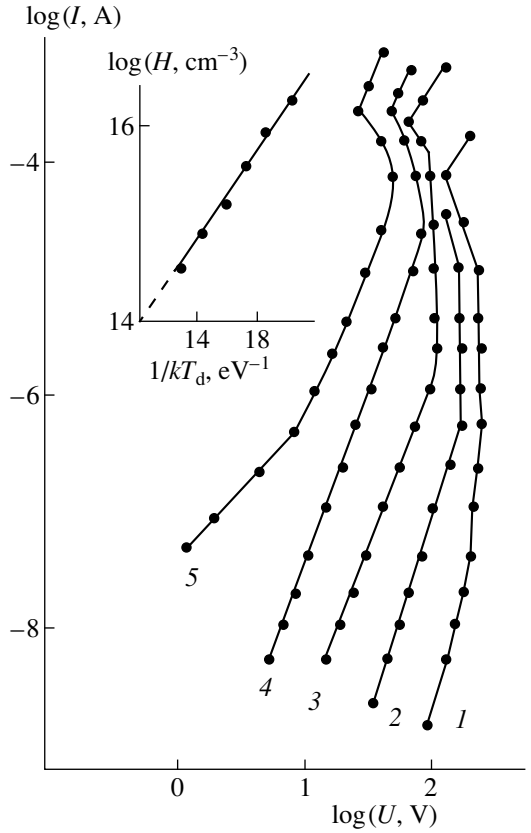

Fig. 3. *I–V* characteristics of sample 5 (see Fig. 1) with exponential trap density distribution. T = (*1*) 300, (*2*) 370, (*3*) 410, (*4*) 520, and (*5*) 500 K. Insert: a $\log H = f(1/kT_d)$ plot.

concentration N_0 exceeds by many orders of magnitude the values of N_1 and N_2 gives no means of explaining the nature of the discovered centers in terms of the multicharged donor model [8]. These centers are probably related to different types of arsenic incorporation into the diamond lattice. The existence of an exponential distribution of trap density below $E_t = E_1$ may be attributed to a strong structural lattice disordering near this trapping center.

The SSD samples studied exhibit sensitivity to alpha particles. This fact is of interest, alpha particle detectors being commonly based on natural diamond.

The highest sensitivity was observed for structures with monoenergetic traps in the second quadratic portion of the *I–V* characteristic. The detection was impaired and eliminated when traps with the exponential energy distribution of trap density appeared in crystals and their concentration increased. This behavior becomes understandable if we take into account the conditions for efficient detection: high carrier drift velocities and the absence of carrier trapping. The trapping can be diminished by using pure samples or by employing conditions in which traps are already filled before irradiation. It is conditions of this kind that are realized in crystals with monoenergetic traps: the deeper trap level is occupied completely, and the second to a large extent.

Let us briefly consider some properties of *p*-type SSD single crystals.

The *I–V* characteristics of low-resistivity crystals at 300 K follow Ohm's law up to currents of ~1 mA. At 77 K, they show (as do high-resistivity crystals at 300 K) power-law $I(U)$ dependences characteristic of the SCLC mode (Fig. 2, curves *1*, *1*').

The strong temperature dependence of the resistance and the constant slope of the $\log R = f(1/T)$ dependence in a wide temperature range (Fig. 1) suggest that *p*-type SSD crystals can be used as efficient temperature sensors. The highest stability was observed for low-resistance (10–10^3 Ω) crystals obtained in the presence of TiC and large amounts of boron.

The SSDs with contacts deposited as described above can be used as chip sensors. Also, SSD samples were fabricated with a working crystal overgrown with an encapsulating insulating diamond layer. These samples, used as thermal vacuum gages at gas pressures in the range from 5×10^{-2} atm to atmospheric pressure, exhibited better sensitivity than such vacuum gages as, e.g., PMT-2.

REFERENCES

1. V. K. Bazhenov, M. M. Vikulin, and A. G. Gontar', Fiz. Tekh. Poluprovodn. (Leningrad) **19**, 1345 (1985) [Sov. Phys. Semicond. **19**, 829 (1985)].
2. V. E. Khadzhi, L. M. Shterenlikht, and M. I. Samoĭlovich, in *Synthesis of Minerals* (Nedra, Moscow, 1989), Vol. 1, p. 481.
3. N. V. Novikov and A.G. Gontar', in *Diamonds in Electronic Engineering* (Énergoatomizdat, Moscow, 1990), p. 57.
4. V. A. Laptev, V. A. Kryachkov, and S. A. Martynov, Élektron. Tekh., Ser. 5, No. 3, 18 (1989).
5. B. I. Shklovskiĭ and A. L. Éfros, *Electronic Properties of Doped Semiconductors* (Nauka, Moscow, 1979; Springer-Verlag, New York, 1984).
6. M. A. Lampert and P. Mark, *Current Injection in Solids* (Academic Press, New York, 1970; Mir, Moscow, 1973).
7. P. I. Reucroft and F. D. Mullins, J. Phys. Chem. Solids **35**, 347 (1974).
8. S. M. Rotner, Yu. M. Rotner, G. V. Krishchuk, *et al.*, Fiz. Tekh. Poluprovodn. (Leningrad) **17**, 198 (1983) [Sov. Phys. Semicond. **17**, 128 (1983)].

Translated by M. Tagirdzhanov

Semiconductors, Vol. 34, No. 10, 2000, pp. 1120–1123. Translated from Fizika i Tekhnika Poluprovodnikov, Vol. 34, No. 10, 2000, pp. 1170–1173.

ELECTRONIC AND OPTICAL PROPERTIES OF SEMICONDUCTORS

Optical Properties of $Ca_4Ga_2S_7:Eu^{2+}$

B. G. Tagiev, U. F. Kasumov, N. N. Musaeva, R. B. Dzhabbarov, and A. S. Abushov

Institute of Physics, Academy of Sciences of Azerbaijan, pr. Dzhavida 33, Baku, 370143 Azerbaijan

Submitted February 22, 2000; accepted for publication March 30, 2000

Abstract—The features of optical transitions in the photon-energy range of 1.85–3.00 eV in single-crystal $Ca_4Ga_2S_7:Eu^{2+}$ were determined from optical measurements in the temperature range of 77–300 K. It was ascertained that indirect and direct optical transitions with band gaps of E_{gi} = 1.889 eV and E_{gd} = 2.455 eV, respectively, occur at 300 K in the photon-energy ranges of 2.2–2.6 and 2.6–3.0 eV. The temperature coefficients of E_{gi} and E_{gd} are equal to -5.15×10^{-4} and -14.86×10^{-4} eV/K, respectively. © *2000 MAIK "Nauka/Interperiodica".*

1. INTRODUCTION

$Ca_4Ga_2S_7:Eu^{2+}$ belongs to the group of highly efficient luminophors with the common formula $Ca_mGa_2S_n$:REE (REE stands for rare-earth element), where n = 4, 5, 6, …, and $m = n - 3$ [1]. As far as we know, there is no available data on the band structure of compounds of the $Ca_4Ga_2S_7$ type. Studying the optical properties of semiconductors makes it possible to reliably determine the most important characteristic parameters, including the band gap, effective masses and mobilities of electrons and holes, and acoustic and optical phonon energies. In this paper, we report the results of studies of the optical-absorption coefficient α in $Ca_4Ga_2S_7:Eu^{2+}$ single crystals.

2. GROWTH OF $Ca_4Ga_2S_7:Eu^{2+}$ SINGLE CRYSTALS

Polycrystalline $Ca_4Ga_2S_7$ samples were obtained by fusing the CaS and Ga_2S_3 components mixed in stoichiometric proportions at a temperature of 1400 K. The samples were synthesized either in evacuated quartz ampules (10^{-5} Torr) or in a quartz crucible under a layer of activated carbon. In order to obtain data on the symmetry and structure of the samples, we performed X-ray diffraction analysis. Four diffraction peaks positioned at $2\theta = 27°40'$, $31°32'$, $42°06'$, and $56°00'$ can be distinguished in the diffraction pattern (Fig. 1) (a DRON 3M diffractometer, CuK_α radiation, and an angle range of $10° < 2\theta < 60°$). The interplanar spacings (d) determined from the corresponding reflections are 3.221, 2.834, 2.082, and 1.642 Å. The synthesized crystals have an fcc structure with lattice constant a = 5.67 Å. The indices of the reflections are (111), (200), (220), and (222). An analysis of the experimental data suggests that, as a result of the interaction of the 4CaS and Ga_2S_3 components, a cubic structure of the sphalerite type is formed.

The fact that the ionic radii of REEs (0.80–1.04 Å) and Ca (0.99 Å) are almost the same is conducive to isomorphous incorporation of an activator into the matrix, which causes high-intensity luminescence with sharply defined spectral lines [2, 3].

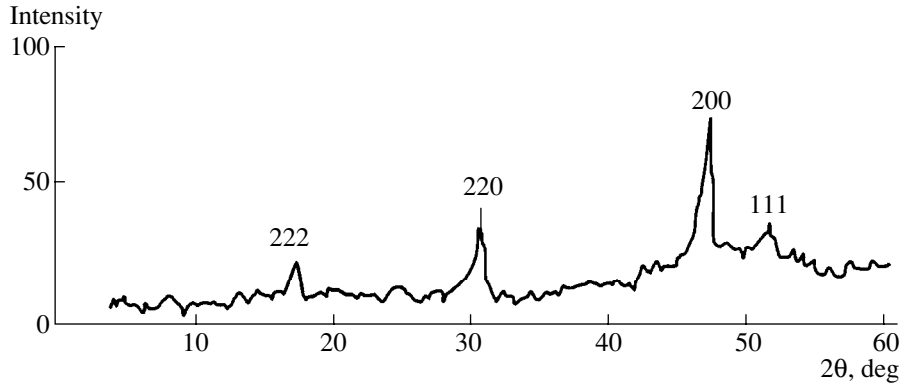

Fig. 1. Diffraction pattern of $Ca_4Ga_2S_7$.

1063-7826/00/3410-1120$20.00 © 2000 MAIK "Nauka/Interperiodica"

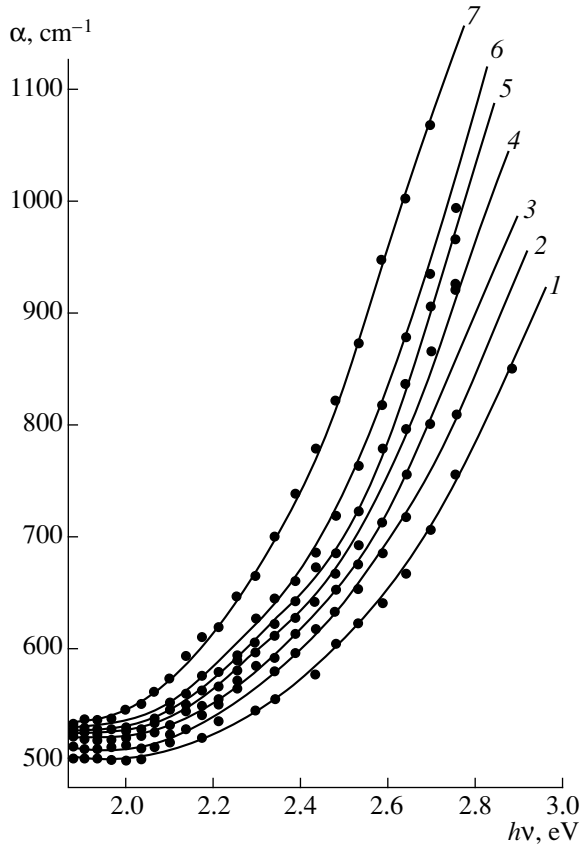

Fig. 2. Spectral dependences of the optical-absorption coefficient of $Ca_4Ga_2S_7:Eu^{2+}$ at temperatures T = (*1*) 115, (*2*) 173, (*3*) 212, (*4*) 233, (*5*) 251, (*6*) 273, and (*7*) 300 K.

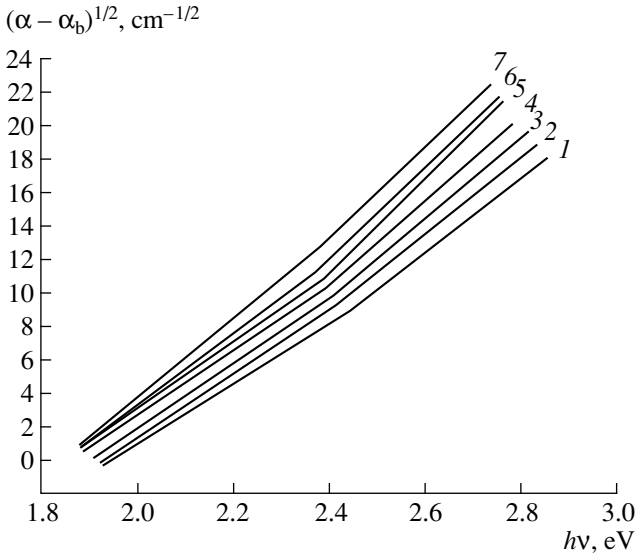

Fig. 3. Spectral dependence of $(\alpha - \alpha_b)^{1/2}$ for $Ca_4Ga_2S_7:Eu^{2+}$ at temperatures T = (*1*) 115, (*2*) 173, (*3*) 212, (*4*) 233, (*5*) 251, (*6*) 273, and (*7*) 300 K.

$Ca_4Ga_2S_7:Eu^{2+}$ single crystals in the shape of cylindrical ingots 8–10 mm in diameter and 15–17 mm long were obtained by the Bridgman–Stockbarger method. The $Ca_4Ga_2S_7:Eu^{2+}$ samples were produced by grinding single-crystal ingots. As the thickness of the samples increases, their color changes from light orange to red.

3. METHOD OF MEASUREMENTS

A setup based on an MDR-12 monochromator was used to study the spectral dependence of the absorption coefficient $\alpha(h\nu)$ for the $Ca_4Ga_2S_7:Eu^{2+}$ single-crystal samples in the temperature range of T = 77–300 K and the photon-energy range of $h\nu$ = 1.85–3.00 eV. An incandescent lamp was used as an excitation source.

4. RESULTS AND DISCUSSION

Figure 2 shows the experimental dependences $\alpha(h\nu)$ for a sample 70 μm thick at various temperatures. Three portions can be distinguished in the curves: α is virtually independent of $h\nu$ in the range of $h\nu$ = 1.85–2.03 eV, α increases rapidly with $h\nu$ in the range of $h\nu$ = 2.03–2.50 eV, and α increases even more rapidly with $h\nu$ in the range of $h\nu$ = 2.50–3.00 eV. In addition, the dependence $\alpha(h\nu)$ shifts to longer wavelengths with increasing temperature and the value of α ranges from 500 to 1040 cm^{-1}.

The results were analyzed in accordance with the theory of direct and indirect transitions [4–7]. It is well

The $Ca_4Ga_2S_7:Eu^{2+}$ parameters determined from optical spectra

T, K	E_{gi}, eV	K_e, $cm^{-1/2}$ eV^{-1}	K_a, $cm^{-1/2}$ eV^{-1}	Θ, K	E_p, eV
115	1.997	22.4	17.7	53.9	0.0445
173	1.975	23.2	19.5	61.31	0.04
212	1.954	24.8	19.2	109.28	0.051
233	1.929	25.2	19.1	128.68	0.0675
251	1.933	29.1	19.5	202.27	0.0785
273	1.922	28.7	23.5	109.12	0.055
300	1.889	28.1	23.7	101.42	0.0415

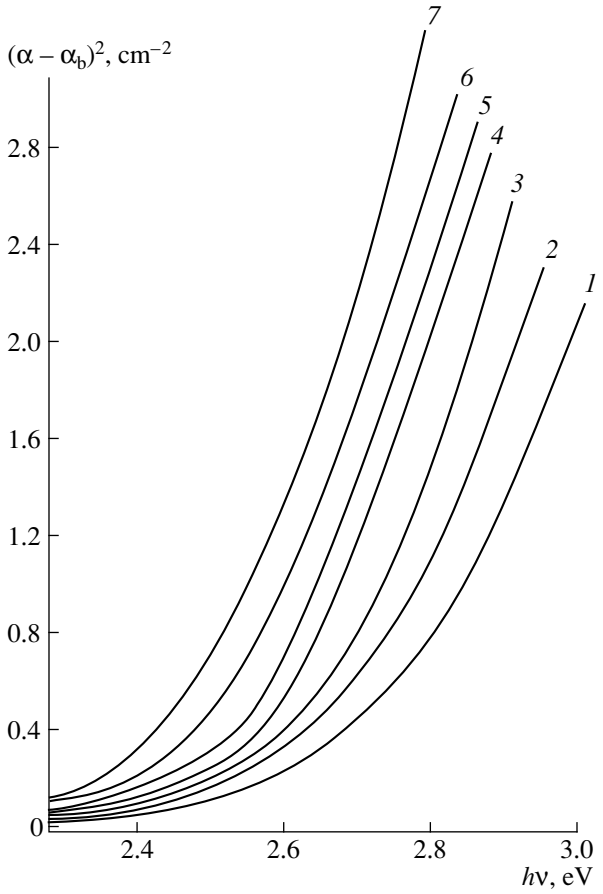

Fig. 4. Spectral dependence of $(\alpha - \alpha_b)^2$ for $Ca_4Ga_2S_7:Eu^{2+}$ at temperatures T = (*1*) 115, (*2*) 173, (*3*) 212, (*4*) 233, (*5*) 251, (*6*) 273, and (*7*) 300 K.

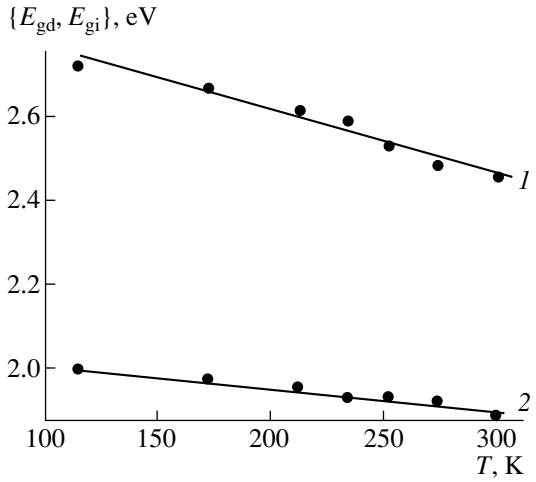

Fig. 5. Temperature dependence of the band gap for (*1*) direct and (*2*) indirect transitions (E_{gd} and E_{gi}, respectively).

known that, in general, the quantity $\alpha(h\nu)$ may be represented as the sum of the following three components:

$$\alpha = \alpha_i + \alpha_d + \alpha_b. \quad (1)$$

Here, α_i and α_d are the optical-absorption coefficients for indirect and direct transitions, respectively; α_b is the optical-absorption coefficient for background absorption and is virtually independent of the photon energy.

Figure 3 shows the experimental dependences of $(\alpha - \alpha_b)^{1/2}$ on $h\nu$. Two rectilinear portions with differing slopes that increase with increasing temperature can be recognized in the curves. According to the theory of indirect transitions, these portions are related to the absorption and emission of phonons; in this case, the optical-absorption coefficient is defined as [8]

$$\alpha(h\nu) = A\left[\frac{(h\nu - E_{gi} + E_p)^2}{e^{\Theta/T} - 1} - \frac{(h\nu - E_{gi} - E_p)^2}{1 - e^{-\Theta/T}}\right], \quad (2)$$

where E_{gi} is the band gap for indirect transitions, E_p is the phonon energy, Θ is the characteristic temperature, T is the absolute temperature, and A is a quantity that depends only slightly on $h\nu$ and T. In formula (2), the first term is related to the absorption of phonons (α_a), whereas the second term accounts for phonon emission (α_e); therefore, the slopes of the straight lines $\alpha_a^{1/2} = f_1(h\nu)$ and $\alpha_e^{1/2} = f_2(h\nu)$ can be determined from the following expressions:

$$K_a = \left(\frac{A}{e^{\Theta/T} - 1}\right)^{1/2}, \quad K_e = \left(\frac{A}{1 - e^{-\Theta/T}}\right)^{1/2}. \quad (3)$$

Thus, we have

$$K_e^2/K_a^2 = e^{\Theta/T}. \quad (4)$$

We used the experimental data and formulas (2)–(4) to determine the values of E_{gi}, E_p, and Θ, which are listed in the table.

As can be seen from Fig. 2, a sharp increase in the absorption coefficient is observed in the photon-energy region of $h\nu \geq 2.5$ eV. In order to clarify the nature of optical transitions in this energy region, we plotted experimental data on $(\alpha - \alpha_b)^2$ against $h\nu$ (Fig. 4) [9]. It can be seen that, for energies $h\nu \geq 2.5$ eV, the values of the optical-absorption coefficient fall nicely on a straight line. Such a dependence indicates that the fundamental-absorption edge in $Ca_4Ga_2S_7:Eu^{2+}$ is due to direct allowed optical transitions. In order to determine the band gap for direct allowed transitions, we extrapolated the straight lines $(\alpha - \alpha_b)^2 = f(h\nu)$ to the value of $\alpha - \alpha_b = 0$.

Figure 5 shows the temperature dependences of E_{gi} and E_{gd} (E_{gd} is the band gap for direct transitions); temperature coefficients of the above band gaps were determined from these dependences and were found to be -5.15×10^{-4} and -14.86×10^{-4} eV/K, respectively.

REFERENCES

1. B. G. Tagiev, A. N. Georgobiani, R. B. Dzhabbarov, *et al.*, Nov. Tekhnol.—21 Vek, No. 2, 58 (1999).
2. B. G. Tagiev, O. B. Tagiev, R. B. Dzhabbarov, *et al.*, Neorg. Mater. **36**, 3 (2000).
3. Seishi Iida, Tamao Matsumoto, N. T. Mamedov, *et al.*, Jpn. J. Appl. Phys. **36** (2), L857 (1997).
4. C. Julien, M. Eddrief, K. Kambas, and M. Balkanski, Thin Solid Films **137**, 27 (1986).
5. E. Guerrero, M. Quinterro, and J. C. Woolley, J. Phys.: Condens. Matter **2**, 6119 (1990).
6. A. M. Elkorashy, Phys. Status Solidi B **135**, 707 (1986).
7. S. Saha, U. Pal, A. K. Chaudhuri, *et al.*, Phys. Status Solidi A **114**, 721 (1989).
8. T. Arant, H. Shimizu, and K. Kudo, in *Proceedings of the IX International Conference on Physics of Semiconductors, Moscow, 1968* (Nauka, Leningrad, 1969), p. 172.
9. J. E. Pankove, *Optical Processes in Semiconductors* (Prentice-Hall, Englewood Cliffs, 1971; Mir, Moscow, 1973).

Translated by A. Spitsyn

Semiconductors, Vol. 34, No. 10, 2000, pp. 1124–1127. Translated from Fizika i Tekhnika Poluprovodnikov, Vol. 34, No. 10, 2000, pp. 1174–1177.

ELECTRONIC AND OPTICAL PROPERTIES OF SEMICONDUCTORS

Dielectric Properties of $Cd_{1-x}Fe_xSe$ Compounds

P. V. Žukowski*, J. Partyka*, P. Wągierek*, Yu. Shostak, Yu. Sidorenko**, and A. Rodzik****

** Lublin Technological University, Lublin, Poland*

*** Belarussian State University, Leningradskaya ul. 14, Minsk, 220080 Belarus*

Submitted February 29, 2000; accepted for publication March 30, 2000

Abstract—The results of studying the temperature and frequency dependences of the permittivity of $Cd_{1-x}Fe_xSe$ ($x = 0.05$, 0.105, and 0.14) semimagnetic semiconductors are reported. In the frequency region of $f < 10$ MHz and at temperatures of $T < 400$ K, a thermally activated increase in the permittivity due to the hopping mechanism of the charge exchange is observed. In the temperature region of $T > 400$ K, transport over the bands becomes prevalent, which brings about a decrease in the permittivity and the disappearance of the frequency dependence of electrical conductivity. *© 2000 MAIK "Nauka/Interperiodica".*

1. INTRODUCTION

Dielectric properties and the electrical conductivity of $Cd_{1-x}Mn_xTe$ [1] and $Cd_{1-x}Fe_xTe$ [2] semimagnetic semiconductors have been studied previously. A model based on the hopping exchange of charges between deep-level amphoteric defects was suggested in [1]; this model accounts for the observed phenomena of a thermally activated increase in the permittivity for frequencies up to 10 MHz. It follows from the available experimental data that the arrangement of manganese atoms in the CdTe lattice is nearly random. In contrast with Mn atoms, Fe atoms tend to be correlatively arranged, and, even for $x \geq 0.02$, the overwhelming majority of these atoms form pairs.

In this paper, we report the results of studying the dielectric properties of $Cd_{1-x}Fe_xSe$ compounds (permittivity ε, the dielectric-loss tangent $\tan\delta$, and the resistance R) in the range of frequencies f from 0.1 kHz to 30 MHz. In order to determine the band gap ΔE_g as a function of the composition of the samples, we studied the cathodoluminescence at liquid-nitrogen temperature (the experimental technique has been described elsewhere [3]).

The $Cd_{1-x}Fe_xSe$ compounds are of potential interest, because these semiconductors, in contrast with the previously studied $Cd_{1-x}Mn_xTe$ and $Cd_{1-x}Fe_xTe$ compounds that have a sphalerite structure, crystallize in the wurtzite structure [4]. The $Cd_{1-x}Fe_xSe$ compounds are single-phase for $x < 0.15$.

2. CATHODOLUMINESCENCE

Figure 1 shows the cathodoluminescence spectra of $Cd_{1-x}Fe_xSe$ compounds ($x = 0.00$, 0.05, 0.105, and 0.14); the spectra were measured at liquid-nitrogen temperature. Two bands are observed in the CdSe spectrum. A band peaked at a wavelength of $\lambda = 670$ nm is related to band-to-band transitions [3]. A band at lower energies ($\lambda = 715$ nm) is most likely a superposition of several known lines of impurity edge emission [5].

The introduction of Fe with a concentration corresponding to $x = 0.05$ results in the complete disappearance of the impurity band, a decrease in the main-band intensity by a factor of about 2, and an insignificant change in its energy position. A further increase in the Fe concentration causes the peak's position to change nonlinearly. The energy positions of the main-band peak, which specify the band gap (ΔE_g) as a function of the Fe content in the compound, are listed in the table.

3. DIELECTRIC PROPERTIES

Temperature dependences of the capacitance, from which the permittivity ε, the dielectric-loss tangent $\tan\delta$ and the resistance R were determined, were measured using an E7-14 immitance meter ($f = 0.1$, 1, and 10 kHz). Before the measurements, platelets ~0.45 mm thick were prepared from the $Cd_{1-x}Fe_xSe$ samples, and layers of silver paste were deposited on the platelet's surfaces. The resulting capacitors were installed in a cryostat with a temperature T varied in the range of 80–450 K. The accuracy of measuring the temperature was ±0.5 K. The frequency dependences of ε, R, and $\tan\delta$ were measured using a VM-507 impedance meter (0.05–500 kHz) and a VM-560 quality-factor meter (0.05–35 MHz) at fixed temperatures of $T = 77$ and 300 K.

Figure 2 shows the temperature dependences of permittivity for $Cd_{1-x}Fe_xSe$ compounds ($x = 0.05$, 0.105, and 0.14) at a frequency of $f = 10$ kHz. It can be seen that a thermally activated increase in permittivity is observed in the compounds under study. The corre-

sponding activation energies ΔE_ε determined from the slope of the curves are listed in the table. Studies of the temperature dependence of the capacitance for a CdSe sample showed that, in the entire temperature range (T = 80–500 K), the permittivity remains high (>100), and a portion of an increase in permittivity is not observed. This means that, as is the case for CdTe [1], the permittivity of CdSe is activated at temperatures lower than 80 K. Most likely, the activation energy for this sample is lower than for a compound with $x = 0.05$. As can be seen from the table, an increase in the energy of thermal activation of permittivity for $Cd_{1-x}Fe_xSe$ compounds occurs virtually simultaneously with an increase in the band gap. This apparently means that, in the $Cd_{1-x}Fe_xSe$ compound, the Fe atoms reside almost randomly in the matrix and do not tend to form pairs or more intricate complexes as is characteristic of $Cd_{1-x}Fe_xTe$ [2]. Such sharp distinctions between the arrangement of Fe atoms in the above compounds may be explained, in our opinion, by a difference in the crystal structures of the starting compounds: CdTe has the zinc blende structure, whereas CdSe has the wurtzite structure.

In $Cd_{1-x}Fe_xSe$ compounds, an interesting phenomenon is observed; this phenomenon is not characteristic of $Cd_{1-x}Mn_xTe$ and $Cd_{1-x}Fe_xTe$ compounds and consists in the fact that the permittivity first increases with temperature, reaches a maximum, and then decreases to a value corresponding approximately to that in the low-temperature region. In order to gain insight into the origin of this phenomenon, we compare the temperature dependences of the permittivity ε and resistance R for the sample with $x = 0.105$ (see Figs. 3 and 4, respectively).

In the range of temperatures lower than that corresponding to the peak of ε, a strong frequency dependence of the sample's resistance is observed, which is characteristic of hopping conduction. This means that, in this temperature region, there exists hopping transport of the charge between defects whose ground state is neutral. As a result of a hop, there appears a dipole that brings about additional polarization; furthermore, during the hop, an electron is involved in hopping conduction [1]. As the temperature is elevated further, the dependences $R(T)$ obtained at different frequencies indicate that the frequency dependence of resistance first becomes much weaker and then ceases to exist at all. In our opinion, this is related to the fact that the levels corresponding to the ground states of defects responsible for the hopping exchange of charges are relatively shallow, as a result of which the rate of charge-carrier excitation to the conduction band increases with increasing temperature. As a consequence, the contribution of hopping processes to the total conductivity decreases (see Fig. 4), and positively charged defects come into existence, which lowers the probability of hops occurring between neutral defects and giving rise to additional polarization. As the temperature deviates further, the dominant conduction mechanism becomes that related to conduction in the band.

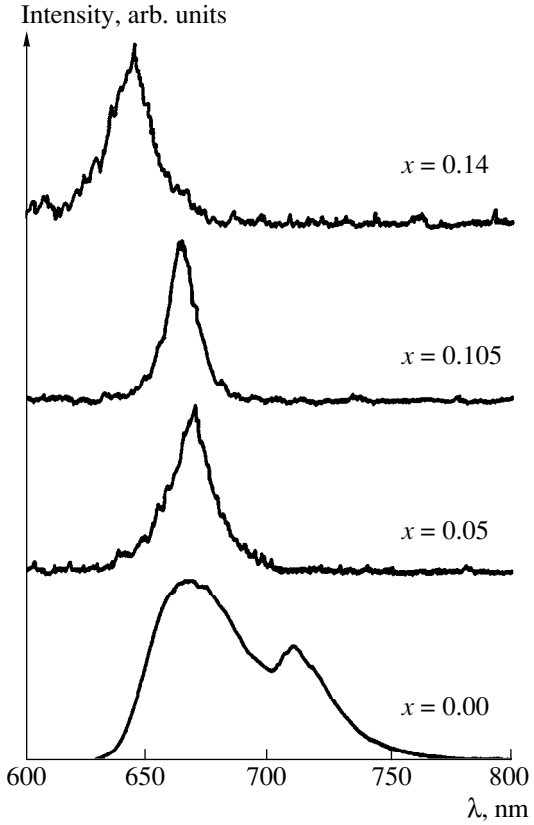

Fig. 1. Cathodoluminescence spectra of $Cd_{1-x}Fe_xSe$ compounds. The spectra were measured at T = 77 K.

4. FREQUENCY DEPENDENCE OF ADDITIONAL POLARIZATION

Previously [1], we obtained the following expression that describes the dielectric susceptibility of semiconductors in which hopping charge exchange between neutral defects occurs:

$$\chi_p = \frac{NP(T)\tau\sinh(e\mathcal{R}E/kT)}{[2P(T)\tau\sinh(e\mathcal{R}E/kT)+1]}\frac{E\mathcal{R}}{\varepsilon_0 E}. \qquad (1)$$

Here, $P(T) = c(\alpha\mathcal{R})^2(\Delta E/kT)\exp[-2\alpha\mathcal{R} - (\Delta E/kT)]$ is the probability of a hop [6], ΔE is the activation energy, N is the defect concentration, $\mathcal{R} \approx N^{-1/3}$, and τ is the time of existence of the defect in a charge state different from neutral.

Formula (1) is valid for a constant electric field with strength E and for the frequency region $f < 2/\tau$. In the case of low-strength fields, formula (1) may be written as

$$\chi_p = \frac{NP(T)\tau e^2\mathcal{R}^2}{\varepsilon_0 kT}. \qquad (2)$$

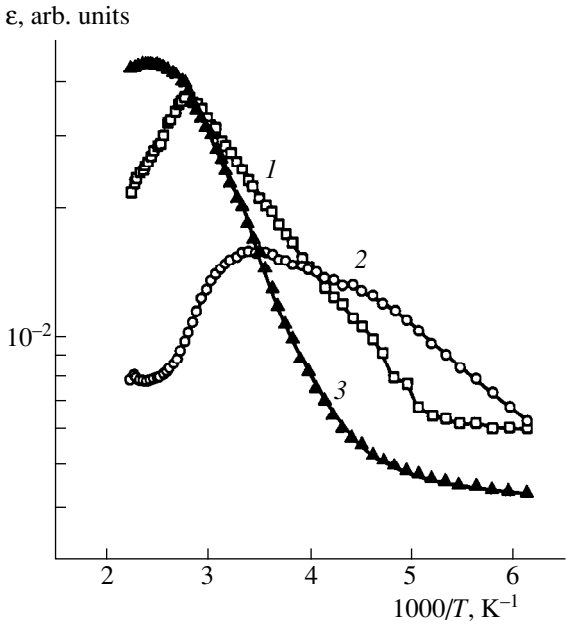

Fig. 2. Temperature dependences of permittivity for $Cd_{1-x}Fe_xSe$ compounds at a frequency of 10 kHz for x = (*1*) 0.05, (*2*) 0.105, and (*3*) 0.14.

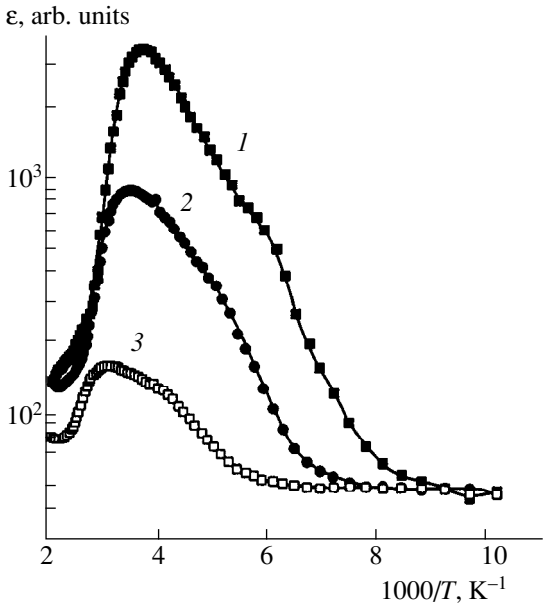

Fig. 3. Temperature dependences of permittivity of $Cd_{0.895}Fe_{0.105}Se$ at the frequencies f = (*1*) 0.1, (*2*) 1.0, and (*3*) 10 kHz.

In actual semiconductors with high concentrations of defects, the quantity τ ceases to be constant. This is related to the fact that neighboring defects interact and their properties become dependent on the interdefect separation (see, for example, [7]). If the defects are distributed randomly, as is the case for the $Cd_{1-x}Mn_xTe$ and $Cd_{1-x}Fe_xSe$ compounds, it should be assumed that the distances r between the components of the defect pairs are also distributed randomly; i.e., we have

$$n(r) \propto \exp\left[-\frac{(\mathcal{R}-r)^2}{2\Delta\mathcal{R}^2}\right], \tag{3}$$

where $\Delta\mathcal{R}$ is the variance.

The magnitude of interaction is defined by the degree of overlap of wave functions for neighboring defects and, thus, depends on the distance between these defects. This, in turn, in the case of high concentrations of defects, would give rise to the distance dependence of the defects' properties that are defined by the electron wave function; in our opinion, these properties also include the time of existence of the defect in the charge state τ that appears in formula (1). It is impossible to ascertain the relation between $n(r)$ and $\tau(r)$ for deep-level centers. Assuming the existence of such a relation, we may write

$$n(\tau) = \varphi(\tau), \tag{4}$$

so that

$$N = \int_{\tau=0}^{\infty} n(\tau)d\tau. \tag{5}$$

Thus, in the case of $f \neq 0$, the quantity $N\tau$ in formula (2) should be replaced by

$$\int_{\tau=0}^{t/2} n(\tau)\tau d\tau, \tag{6}$$

where $t = 1/f$. Thus, we have

$$\chi_p = \frac{P(T)e^2\mathcal{R}^2}{\varepsilon_0 kT}\int_0^{t/2} n(\tau)\tau d\tau. \tag{7}$$

It follows from formula (7) that, in semiconductors with a high concentration of deep-level centers, a dispersion of permittivity should be observed.

Figure 5 shows the frequency dependences of permittivity for the $Cd_{1-x}Fe_xSe$ compound (x = 0.105) at T = 77 and 300 K. It can be seen that there are two por-

Energy-related parameters of the $Cd_{1-x}Fe_xSe$ samples

x	ΔE_ε, eV	ΔE_g, eV
0.00	<0.12	1.85 ± 0.02
0.05	0.12 ± 0.03	1.85 ± 0.02
0.105	0.14 ± 0.03	1.87 ± 0.02
0.14	0.16 ± 0.03	1.92 ± 0.02

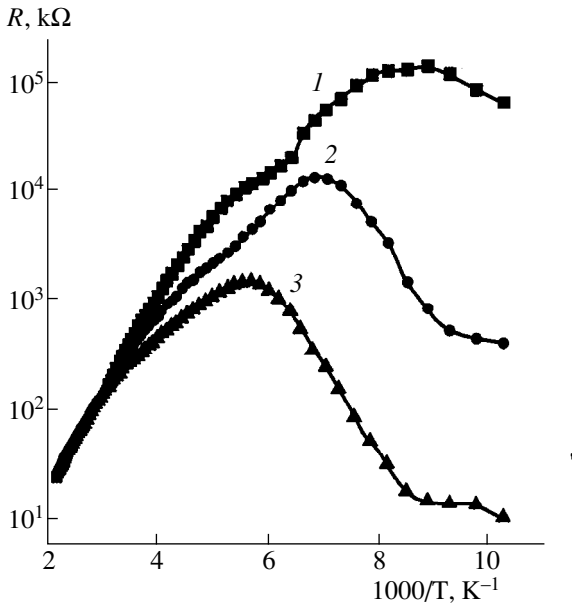

Fig. 4. Temperature dependences of resistance of the $Cd_{0.895}Fe_{0.105}Se$ sample at the frequencies f = (*1*) 0.1, (*2*) 1.0, and (*3*) 10 kHz.

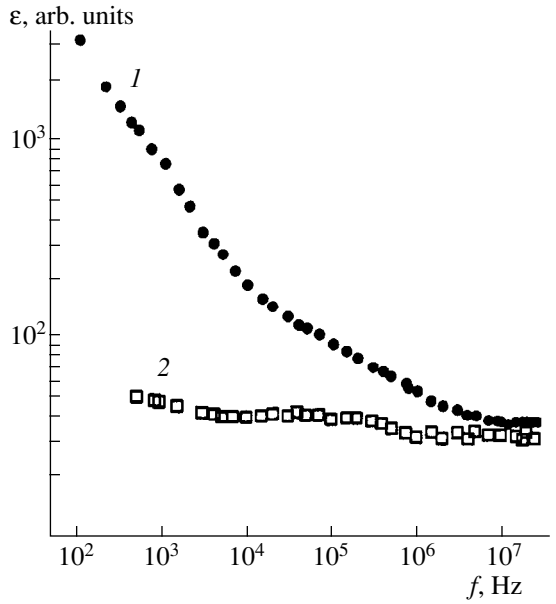

Fig. 5. Frequency dependences of permittivity for the $Cd_{0.895}Fe_{0.105}Se$ compound at the temperatures T = (*1*) 300 and (*2*) 77 K.

tions (10^2–10^4 and 10^4–5×10^6 Hz) where the dependence $\chi_p(f)$ may be represented as

$$\chi_p \approx \tau^{\gamma}. \tag{8}$$

For these portions, we may assume that

$$n(\tau) = A\tau^{\alpha}. \tag{9}$$

Substituting (9) into (7), we obtain

$$\chi_p \propto \int_{\tau_0}^{\tau} A\tau^{\alpha+1}d\tau = \frac{A}{\alpha+2}(\tau^{\alpha+2} - \tau_0^{\alpha+2}), \tag{10}$$

or

$$\chi_p(f) \propto f^{-(\alpha+2)}. \tag{11}$$

We can determine the values of $(\alpha + 2) = -\gamma$ from experimental dependences $\chi_p(f)$. Then, for the linear (on the $\log\chi_p - \log f$ scale) portion of $\chi_p(f)$, the distribution of defects in their times of existence is given by

$$n(\tau) \propto \tau^{-(\gamma+2)}. \tag{12}$$

It follows from formula (11) that, for $\alpha = -2$, there is no dispersion, whereas, for $\alpha > -2$, a normal dispersion takes place, which is observed in our experiments (see Fig. 5 and [2]). In this case, in the range of 10^2–10^4 Hz (Fig. 5), we have $\alpha = -1.4$ (i.e., $n(\tau) \propto \tau^{-1.4}$), whereas, in the range of 10^4–5×10^6 Hz, $\alpha = -1.77$, i.e., $n(\tau) \propto \tau^{-1.77}$. For $\alpha < -2$, an abnormal dispersion should be observed.

REFERENCES

1. P. V. Žukowski, A. Rodzik, and Yu. A. Shostak, Fiz. Tekh. Poluprovodn. (St. Petersburg) **31**, 714 (1997) [Semiconductors **31**, 610 (1997)].
2. P. V. Žukowski, J. Partyka, P. Wągierek, *et al.*, Fiz. Tekh. Poluprovodn. (St. Petersburg) **33**, 270 (1999) [Semiconductors **33**, 276 (1999)].
3. A. Holda, A. Rodzik, A. A. Mielnikow, and P. V. Žukowski, Phys. Status Solidi B **189**, 543 (1995).
4. *Semiconductors and Semimetals*, Vol. 25: *Diluted Magnetic Semiconductors*, Ed. by J. Furdyna and J. Kossut (Academic, New York, 1988; Mir, Moscow, 1992).
5. V. I. Gavrilenko, A. M. Grekhov, D. V. Korbutyak, and V. T. Litovchenko, *Optical Properties of Semiconductors* (Naukova Dumka, Kiev, 1987).
6. S. S. Kirkpatrick, in *Proceedings of the 5th International Conference on Amorphous and Liquid Semiconductors, Garmish–Partenkirchen, 1973*, p. 183.
7. I. M. Lifshits, Zh. Éksp. Teor. Fiz. **53**, 743 (1967) [Sov. Phys. JETP **26**, 462 (1968)].

Translated by A. Spitsyn

Semiconductors, Vol. 34, No. 10, 2000, pp. 1128–1132. Translated from Fizika i Tekhnika Poluprovodnikov, Vol. 34, No. 10, 2000, pp. 1178–1182.

ELECTRONIC AND OPTICAL PROPERTIES OF SEMICONDUCTORS

Luminescent ZnS:Cu Films Prepared by Chemical Methods

S. V. Svechnikov*, L. V. Zav'yalova*, N. N. Roshchina*, V. E. Rodionov*, V. S. Khomchenko*, L. I. Berezhinskiĭ*, I. V. Prokopenko*, P. M. Litvin*, O. S. Litvin*, Yu. V. Kolomzarov, and Yu. A. Tsyrkunov****

**Institute of Semiconductor Physics, National Academy of Sciences of Ukraine, Kiev, 252650 Ukraine*
e-mail: Zavyalov@i.com.ua
***Special Technological and Design Office, Institute of Semiconductor Physics, National Academy of Sciences of Ukraine, Kiev, 252650 Ukraine*
Submitted March 21, 2000; accepted for publication March 30, 2000

Abstract—For the first time, ZnS:Cu films with an intense photoluminescence were prepared by a chemical nonvacuum method. They were produced by means of the combined pyrolytic deposition of zinc and copper dithiocarbamates onto glass and ceramic substrates heated up to 260–300°C. A close packing of practically identical grains is characteristic of these films, with grain sizes depending on the substrate type. The photoluminescence and electroluminescence spectra include the blue, green, and yellow bands typical of copper. The band-intensity ratio depends on the film-preparation conditions, as well as on their excitation, which makes it possible to change the emission color of radiators in a wide range (from blue to white). © *2000 MAIK "Nauka/Interperiodica".*

1. INTRODUCTION

As radiation sources of green and blue emission, thin ZnS:Cu films are of significant interest for producing various types of optoelectronic devices. The operating efficiency of such radiators is governed by the film properties that depend on the film preparation method. ZnS:Cu films obtained by known vacuum methods have still not found a practical application due to the fast degradation of thin-film electroluminescent structures compared with ZnS:Mn-based films.

Recently [1, 2], it was shown that thin-film electroluminescent structures based on ferroelectric ceramics with a ZnS:Cu layer fabricated by electron-beam evaporation in vacuum (EBE method) with subsequent annealing are characterized by slower (by more then 1–2 orders of magnitude) degradation of an electroluminescent layer compared with conventional degradation for ZnS:Cu. This allows us to consider these structures to be promising for practical applications.

At present, chemical methods, first of all, chemical decomposition of metal–organic compounds (MOCVD), are also widely used in the preparation of thin-film electroluminescent structures based on ZnS:Mn films [3]. One of these methods, the simplest, and quite promising, consists in the preparation of films of various semiconductor materials from chelate metal–organic compounds (MOC) [4–6]. Electroluminescent radiators based on ZnS:Mn films with high brightness and light output are fabricated from these precursors, among other thin-film elements and structures [4, 5]. The films were produced at temperatures of 240–300°C as a result of combined pyrolysis of zinc and manganese dithiocarbamates taken in the specified ratios.

The aim of this work was to study the possibility of obtaining electroluminescent ZnS:Cu films by a similar nonvacuum chemical method from chelate MOC of zinc and copper, and to investigate their crystalline structure and emission spectra.

2. THE OBJECTS OF THE STUDY AND EXPERIMENTAL METHODS

The chelate metal–organic compounds of zinc and copper [7] used in this study belong to a class of metal–organic compounds, for which the presence of complex anions—ligands—is typical. The anions, i.e., ligands, join the metal (a complexing agent) simultaneously by their two constituents and form a chelate ring via the chemical elements that produce an inner sphere of a complexing agent. Atoms of sulfur, selenium, tellurium, and oxygen can enter the composition of the inner sphere directly surrounding a metal. We have used dithiocarbamates [8] sulfur-containing compounds, which were used by us previously [4], and later on by the authors of [9] to prepare CdS and CdZnS films.

When depositing ZnS:Cu films doped directly in the growth process (similar to [5] for ZnS:Mn), we used the similar compounds ZnL_2 and CuL, where L is a sulfur-containing dithiocarbamate ligand. When obtaining ZnS films, a single original substance was used, and, for ZnS:Cu films, two substances were used; a pyridine was used as a solvent.

Thermal analysis of ZnL_2 and CuL compounds showed that they have the same stages of substance

transformation due to the effect of temperature. However, all the critical temperatures (melting, decomposition, and crystallization of the decomposition products) have lower values for CuL (by 30–60°C) than for ZnL_2.

The deposition of ZnS:Cu films was accomplished in air in a flow-type nonhermetic reactor. The substrates were mounted on a flat, horizontally placed heater. Sputtering was performed with a sputterer placed above the substrate and with the use of compressed air at a pressure of $(0.6–1.2) \times 10^5$ Pa. The deposition time for a film 0.5–1.0 μm thick is 5–20 min, depending on the sputtering rate and on the temperature of the substrate. The concentration of the main initial species, zinc dithiocarbamate $[(C_2H_5)_2NCS_2]_2Zn$, is 4 wt %, which corresponds to a ~0.1 M solution; the sputtering rate is 1–2 ml/min; and the substrate temperature is 220–300°C.

The study of the dependence of the film growth rate on the substrate temperature showed that, in the range of 220–300°C, the growth rate changes from 5 up to 20 Å/s for ZnS films and from 3 up to 15 Å/s for Cu_2S films.

Due to this difference in the growth rates, the Cu content in the initial solution (C_s) is chosen to be substantially different from the Cu content in the film (C_f); similar to [6],

$$C_s = (V_1/V_2)C_f,$$

where V_1 and V_2 are the growth rates of ZnS and Cu_2S films, respectively, for constant values of the substrate temperature and flux intensity of the source substance. The values of V_1/V_2 obtained experimentally allow us to calculate with sufficient accuracy the ratios of the source substances, which provide a given concentration of copper in the ZnS films.

Electroluminescence studies were carried out on two types of structures, a conventional MISIM (metal–insulator–semiconductor–insulator–metal) structure on a glass substrate, where the radiation left through the substrate, and an inverse MISIM structure on a ceramic substrate, where the radiation left through the transparent upper electrode (similar to [2]). In the conventional type of structure, In_2O_3 and Al were usually used as the electrodes; SiO_2 and Al_2O_3 films 80 and 100 nm thick served as insulators. The electroluminescent layer was ~0.5 μm thick in both types of structures. All the operating layers, except for the electroluminescent one, were deposited by electron-beam or thermal evaporation in vacuum.

In the inversion-type structure, a thick layer of ferroelectric $BaTiO_3$ ceramics served as an insulator (~40 μm), which was deposited by a special technique [2] onto the metallic electrodes deposited on the ceramic substrates.

A nitrogen laser (radiation wavelength $\lambda = 337$ nm) was used for photoluminescence (PL) excitation, and electroluminescence (EL) was excited by a sinusoidal voltage with a frequency of 2 kHz. The morphology studies of the film surfaces were performed using a Nanoscope D3000 (Digital Instruments) scanning probe microscope.

3. RESULTS AND DISCUSSION

The ZnS:Cu films prepared by the technology described above were studied with the aim of assessing their suitability for applications as electroluminescent emitters, and their structural parameters were compared with those of the films obtained by electron-beam evaporation in vacuum [2]. The morphology of the film surface was investigated in connection with the fact that homogeneity of the film crystal structure is a prerequisite for obtaining a uniform steady emission.

The study of the morphology of the ZnS:Cu film surface produced on various substrates showed that the MOCVD-films on polycrystalline ceramic substrates (with a grain size of 7–9 μm) consisted of joined crystallites that had an identical elongated shape with sizes of 0.07×0.15 μm, a quasi-parallel orientation with respect to each other, and poorly pronounced facets (Fig. 1a). The surface of films deposited on the glass substrate consists of microcrystalline grains differing greatly from each other in size, which range from 0.10 up to 0.30 μm (Fig. 1b), and without any predominant shape or orientation.

When depositing ZnS:Cu films on ceramic substrates by EBE, the films are produced in the form of a microcrystalline aggregate with nonuniform joined individual microcrystalline species without inherent facets, i.e., the films consist of a xenomorphic microcrystalline grains (Fig. 1c). In addition, various types of excrescences are observed at the boundaries of individual grains. It is noteworthy that the nonuniformity of the crystallite distribution is not eliminated even after high-temperature annealing (at ~800°C for 1 h in an atmosphere of sulfur vapors) of the films deposited by the EBE method, although the crystallite size increases significantly. The distribution of the crystallite sizes at the surface of a film is rather nonuniform, which is illustrated by Fig. 2 where the distribution of the grain number f_1 over its area s for all three cases of film deposition under consideration is shown.

The degree of microrelief development is shown in Fig. 3 in the form of the height (h) distribution of the number of points (pixels) f_2 on the images of the film surface which are shown in Fig. 1. The curves are obtained by statistically processing the results of measurements carried out in the scanning probe microscope. The height in Fig. 3 corresponds to the distance from the surface point being studied up to the point which occupies the lowest position. The number of points is expressed as a percentage relationship of the calculated points to the total number of points (pixels) of the entire image; the latter number is equal to 256×256, i.e., to 65 536 points. It follows from Figs. 1–3 that the

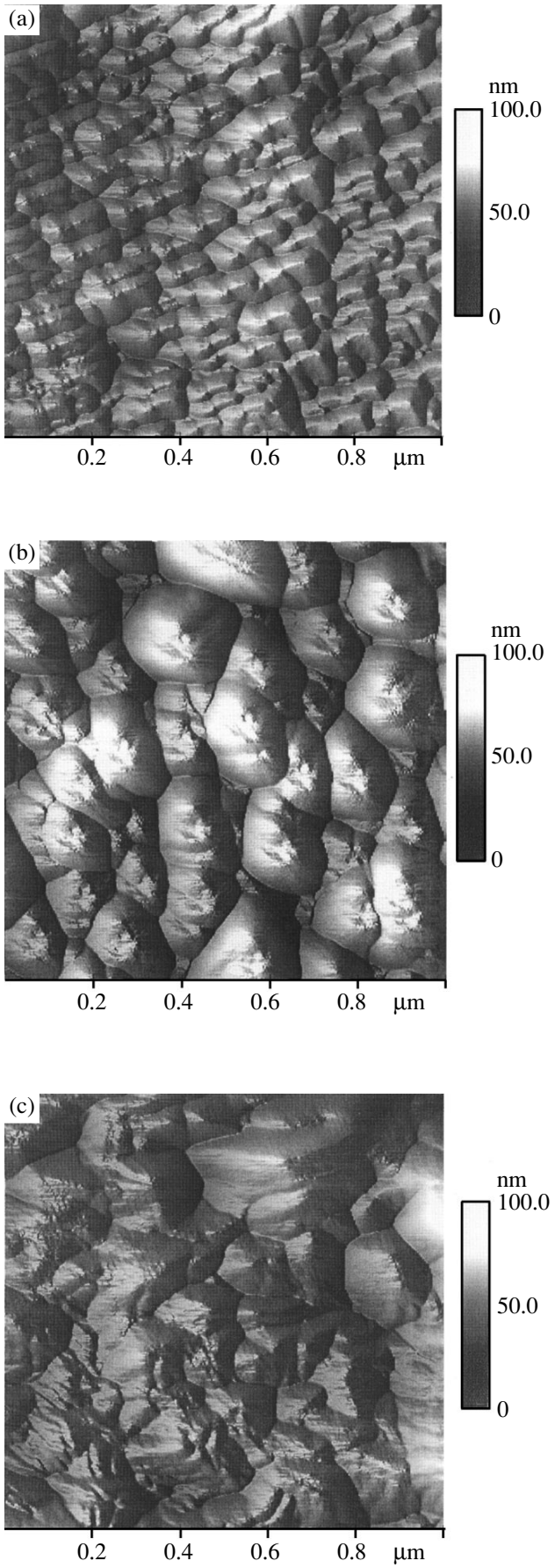

MOCVD films on ceramics have the smallest grain sizes and the most uniform distribution both over the area and by the height of the relief. This can be explained by the fact that the chemical method used corresponds to thermodynamic equilibrium than the EBE method, and, in the case of deposition on the polycrystalline ceramic substrates, initially a significantly larger number of crystallization centers are observed on their surface than on the glass substrate.

It is found that the radiative properties of the films depend most strongly on the copper concentration and the conditions of film formation (the temperature and substrate structure). We found that, at substrate temperatures in the range of 220–300°C, the dependence of the luminescence intensity of ZnS:Cu films on the substrate temperature is profoundly nonmonotonic. A change of temperature in the range of 220–260°C has virtually no influence on a weak luminescence intensity, whereas a temperature increase from 260 to 300°C results in an increase of 2–3 orders of magnitude in the radiation intensity (depending on the copper concentration). The copper concentration in the solution (C_s) was varied from 0.05 up to 1.60 wt %. As a result, it was found that the PL intensity of the films in this range of concentrations increases continuously; as for EL, the intensity increase is limited by the concentration of 0.20 wt %. For higher values of activator concentration (from 0.30 up to 1.60 wt % of Cu) the EL intensity is actually reduced to zero.

It has been established that the radiation spectrum depends on the film preparation conditions and on the excitation of radiation in these films. The green-blue color of PL characteristic of copper is most distinctly revealed at a substrate temperature of ~300°C and a copper concentration of ≥0.2 wt %. The PL spectrum consists of a broad asymmetric band with peaks at λ_{max} = 420 and 525 nm (Fig. 4, curve *1*). The ratio of the band intensities is governed by the substrate temperature and the copper concentration in the films and can change in a wide range, causing blue or green radiation. The EL spectra are in the same range of wavelengths as the PL spectra for ZnS:Cu films prepared for a similar activator concentration and at the same deposition temperature, but differ significantly in the ratio of the band intensities and in their number. They represent the PL spectra resolved in the bands with a half-width of ~30 nm (Fig. 4, curves *2*, *3*). These curves also illustrate the influence of the substrate type—amorphous (glass) or polycrystalline (ceramics)—on the EL spectra. Thus, in the emission spectrum of ZnS:Cu films deposited on a ceramic substrate, a yellow band (λ_{max} = 570 nm) is dominant, whereas a green (λ_{max} = 520 nm)

Fig. 1. Image of the ZnS:Cu film surface obtained using scanning probe microscopy: (a, b) the films were deposited by the MOCVD method on ceramic and glass substrates, respectively; (c) the films were deposited by the EBE method on ceramic substrates.

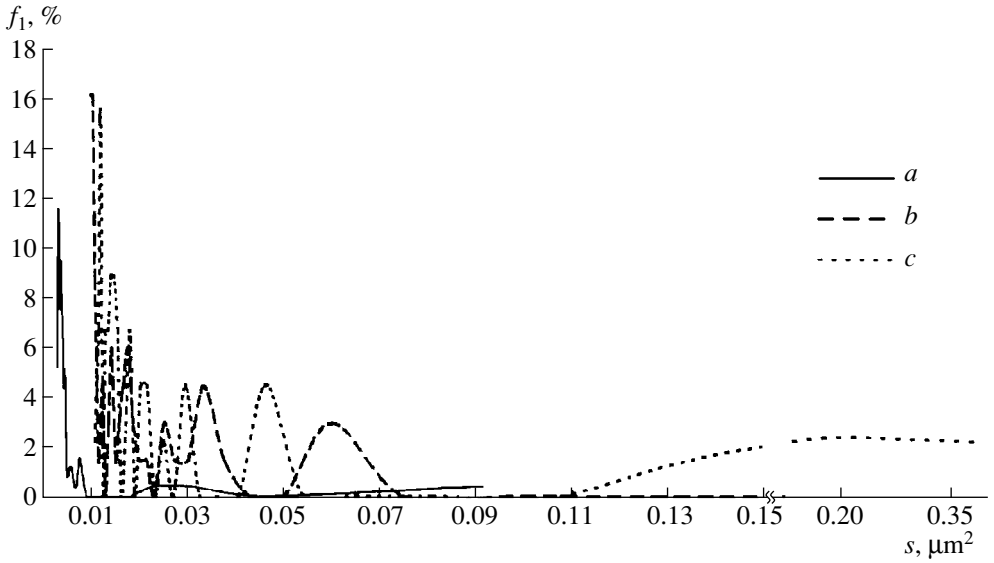

Fig. 2. Distribution of the number of grains by their area; (*a*, *b*) the films were deposited by the MOCVD method on ceramic and glass substrates, respectively; (*c*) the films were deposited by the EBE method on ceramic substrates.

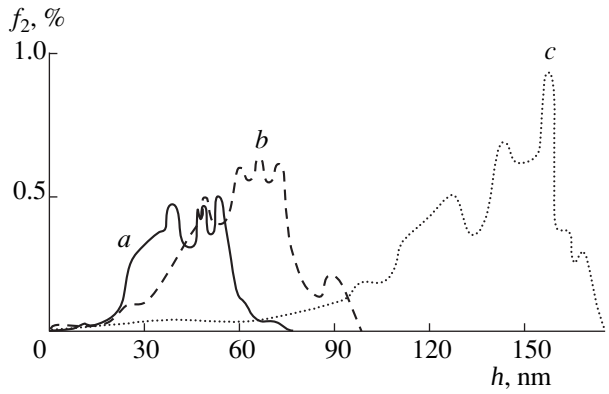

Fig. 3. Distribution of the number of points by their height on the ZnS:Cu film surface obtained by statistical processing of the scanning-probe microscopy data: (*a*, *b*) the films were deposited by the MOCVD method on ceramic and glass substrates, respectively; (*c*) the films were deposited by the EBE method on ceramic substrates.

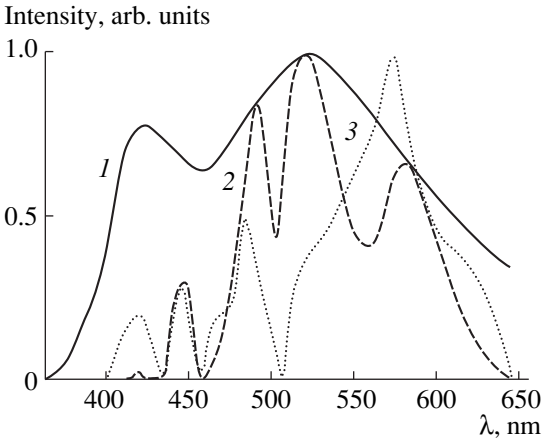

Fig. 4. Photoluminescence (*1*) and electroluminescence (*2*, *3*) spectra of ZnS:Cu films on the (*1*, *2*) glass and (*3*) ceramics.

band prevails in the spectrum of the same films deposited on a glass substrate. In this case, the presence of blue, green, and yellow bands determines a nearly white emission color of electroluminescent structures on the glass substrate and a yellow-green color of the structure on the ceramic one.

The emission spectrum of the ZnS:Cu films being studied is presented in the table as a function of excitation type and substrate material. The wavelengths (λ_{max}), relative intensities (I) of the bands in the emission spectra of ZnS:Cu films, and the identification of emission centers in accordance with published data are given in the table.

The data listed in the table allow us to conclude that the emission bands at 420, 445, and 520 nm are caused by the centers related to copper, whereas the formation of a yellow band (570 nm) possibly involves both the copper centers and the self-activated emission centers. Such a spectral band was observed in both self-activated [15] and copper-doped films of zinc sulfide [1, 13, 14]. As for the radiation band with λ_{max} = 485 nm, we may conclude with a certain confidence that it is not related to the emission of copper centers. According to the available data, this band can be attributed to self-activated ZnS emission or, possibly, to the emission of unknown impurity centers. The presence of blue, green, and yellow emission bands indicates that various emission centers related to copper exist in

Radiation spectrum of ZnS:Cu films

Photoluminescence		Electroluminescence				Type of center	Source
glass substrate		glass substrate		ceramic substrate			
λ_{max}, nm	*I*, arb. units	λ_{max}, nm	*I*, arb. units	λ_{max}, nm	*I*, arb. units		
420	0.78	420	0.02	420	0.2	Cu	[10], [11]
		445	0.30	445	0.3	Cu	[12]
		490	0.85	485	0.5	Self-activated or impurity	–
525	1.00	520	1.00	520	0.3	Cu	[12]
		575	0.67	570	1.0	Cu	[1], 13], [14]
						and self-activated	[15]

ZnS:Cu films; in these centers, compensation of the charge of Cu^+ is accomplished by the various defects of the ZnS structure. The appearance of such centers is caused by the absence of a coactivator, which, as a rule, is introduced to compensate the copper charge in connection with the nonisovalent character of its incorporation into ZnS.

The differences we found in the ratio of band intensities in the emission spectra of structures on glass and ceramic substrates, can apparently be caused by the difference in the crystalline structure (grain sizes) and, thus, in the structural defects in these films (Figs. 1a, 1b). Such a dependence was also recently observed for ZnS:Cu films prepared by the EBE method [11].

The features of radiation spectra observed in the cases of photoexcitation and electroexcitation can be caused by differences in spatial localization of the excitation energy over the film volume in the presence of nonuniformly distributed emission centers of dissimilar types and also by the various ways of excitation energy transfer by the emission centers for different excitation types.

Thus, for the first time we managed to obtain electroluminescent ZnS:Cu films by a chemical nonvacuum MOCVD method from chelate metal–organic compounds—zinc and copper dithiocarbamates—by means of their combined pyrolysis at temperatures of 260–300°C. It is established that these films have a more ordered structure and a less pronounced surface relief compared to films produced by electron-beam evaporation in vacuum. The structure of films deposited on a smooth surface of amorphous glass substrates is characterized by larger crystallites than in the case of deposition on the rough surface of polycrystalline ceramics. A strong dependence of the emission intensity on the substrate temperature and copper concentration is observed. A temperature of 300°C is favorable for film production. The concentration dependences of PL and EL are different. The copper content $C_s \approx$ 0.2 wt % is favorable for EL. As a result of our studies, it is established that the films contain centers of blue, green, and yellow emission characteristic of copper.

REFERENCES

1. V. S. Khomchenko, V. E. Rodionov, and Yu. A. Tzyrkunov, in *Proceedings of the 7th International Symposium SID, Minsk, 1998*, p. 218.
2. L. J. Berezhinsky, V. S. Khomchenko, V. E. Rodionov, and Yu. A. Tzyrkunov, in *Abstracts of the 5th International Conference on Science and Technology of Display Phosphors, San Diego, 1999.*
3. Y. A. Ono, *Electroluminescent Displays* (World Scientific, London, 1995), p. 170.
4. L. F. Zharovsky, L. V. Zavyalova, and G. S. Svechnikov, Thin Solid Films **128** (3/4), 241 (1985).
5. L. V. Zavyalova, A. I. Beletski, and G. S. Svechnikov, Semicond. Sci. Technol. **14**, 446 (1999).
6. L. V. Zavyalova and G. S. Svechnikov, Displays **18**, 73 (1997).
7. J. Staryĭ, *The Solvent Extraction of Metal Chelates* (Pergamon, Oxford, 1964; Mir, Moscow, 1966).
8. V. M. Byr'ko, *Dithiocarbamates* (Nauka, Moscow, 1984), p. 342.
9. D. M. Frigo, O. Khan, and P. O. Brien, J. Cryst. Growth **96**, 989 (1989).
10. Jinman Huang, Yi Yang, *et al.*, Appl. Phys. Lett. **70**, 18 (1997).
11. V. Khomchenko, V. Rodionov, P. M. Lytvyn, *et al.*, in *Proceedings of the 8th International Symposium SID, Novy Svet, Ukraine, 1999.*
12. G. A. Zholkevich and V. D. Dudnik, Opt. Spektrosk. **20**, 687 (1966).
13. A. M. Gurvich, *Introduction to the Physics of Phosphorescent Crystals* (Nauka, Moscow, 1971).
14. Dong-II Kim, Sung-Ho Choi, and Chong-Ook Park, J. Mater. Sci.: Mater. Electron. **9**, 31 (1998).
15. R. Mach, G. U. Reinsperger, *et al.*, J. Cryst. Growth **117**, 1002 (1992).

Translated by T. Galkina

Semiconductors, Vol. 34, No. 10, 2000, pp. 1133–1136. Translated from Fizika i Tekhnika Poluprovodnikov, Vol. 34, No. 10, 2000, pp. 1183–1186.

ELECTRONIC AND OPTICAL PROPERTIES OF SEMICONDUCTORS

Structural Defects and Deep-Level Centers in 4*H*-SiC Epilayers Grown by Sublimational Epitaxy in Vacuum

A. A. Lebedev*, D. V. Davydov*, N. S. Savkina*, A. S. Tregubova*, M. P. Shcheglov*, R. Yakimova, M. Syväjärvi**, and E. Janzén****

** Ioffe Physicotechnical Institute, Russian Academy of Sciences, Politekhnicheskaya ul. 26, St. Petersburg, 194021 Russia*

*** Linköping University, S-58183 Linköping, Sweden*

Submitted March 31, 2000; accepted for publication April 3, 2000

Abstract—The parameters of deep-level centers in lightly doped 4*H*-SiC epilayers grown by sublimational epitaxy and CVD were investigated. Two deep-level centers with activation energies $E_c - 0.18$ eV and $E_c - 0.65$ eV (Z1 center) were observed and tentatively identified with structural defects of the SiC crystal lattice. The Z1 center concentration is shown to fall with decreasing uncompensated donor concentration $N_d - N_a$ in the layers. For the same $N_d - N_a$, the Z1 center concentration is lower in layers with a higher dislocation density. *© 2000 MAIK "Nauka/Interperiodica".*

1. INTRODUCTION

Deep-level centers are known to affect semiconductor device parameters, such as the minority carrier lifetime, leakage currents, breakdown voltages of *p–n*-structures and the temperature coefficients of these voltages. It is also known that, along with impurities, intrinsic defects of the semiconductor crystal lattice may contribute to the deep-level center formation. Accordingly, the device parameter optimization requires that the influence of structural defects on the deep-level center spectrum in the band gap be studied. Investigations of this kind are especially important for silicon carbide in which practically all of the known deep-level centers [1] include, or comprise, intrinsic defects.

We report here the results of a comparative study of the deep-level center spectra in 4*H*-SiC epilayers fabricated by sublimational epitaxy on SiC substrates of varied degrees of structural perfection.

2. SAMPLES

SiC substrates were produced by the Lely [2] and modified Lely methods (ML substrates) [3]. For ML substrates we used crystals commercially manufactured by CREE Co. [4] and those produced at St. Petersburg State Electrotechnical University (SPbSEU). The Lely substrates were fabricated at the Podolsk Chemical-Metallurgical plant (PCMP) [5]. Epitaxial layers were grown by sublimational epitaxy (SE) at the Ioffe Physicotechnical Institute (PTI) [6] and Linköping University, Sweden, (LiU) [7], and also by chemical vapor deposition (CVD) at CREE [4]. The *n*-layer thickness was 5–7 or ~30 μm (for the layers grown at LiU); the substrate thickness was about 400 μm. Schottky diodes 400–800 μm in diameter were fabricated on the epilayer surface by the magnetron sputtering of Ni. Ohmic contacts to the back of the substrate were formed by firing in at ~1000°C a Ni layer deposited by vacuum evaporation.

3. EXPERIMENT

3.1. X-ray Data

The dislocation density in commercial SiC ML substrates is commonly about 10^4–10^6 cm^{-2}; in addition, extended micropipes are present. The "classical" Lely method allows the fabrication of micropipe-free SiC substrates with a dislocation density of 10–10^4 cm^{-2} [8]. However, the Lely substrates have a small area (less than 1.5 cm^2), and fabrication by this method of 4*H* polytype crystals, the most promising for semiconductor devices, is rarely successful, making such substrates commercially unpromising. Previously [9, 10], X-ray studies of 6*H*- and 4*H*-SiC ML substrates before and after SE layer formation showed that the layer perfection may be higher than that of the substrate used. Scanning electron-microscope studies have revealed a total overgrowth of small defects and the partial "healing" of large substrate defects (macropipes). At the same time, no substantial decrease in the dislocation density was observed in CVD-grown epitaxial SiC layers.

In this study, the structural perfection of the substrates with already deposited epitaxial layers was evaluated by X-ray diffractometry in the asymmetric $(10\bar{1}.7)$ Cu$K\alpha$ reflection in the Θ-scan mode. The depth (~5 μm) of the layer responsible for the diffraction peak in this reflection does not exceed the epitaxial layer thickness. The obtained results are listed in the table.

1063-7826/00/3410-1133$20.00

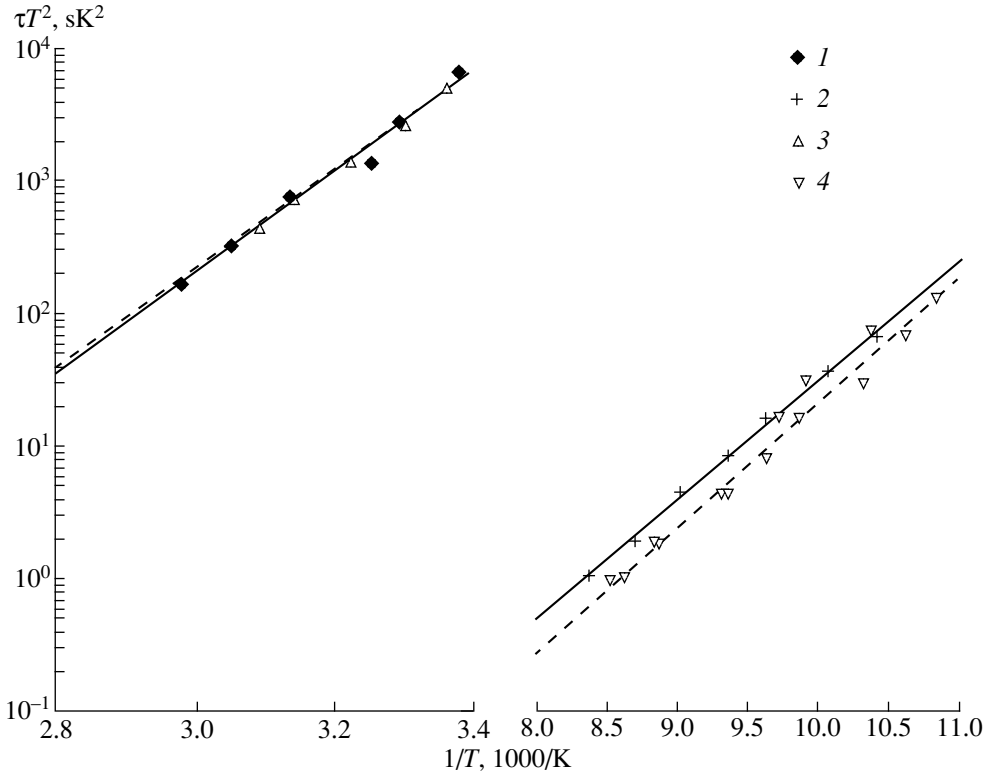

Fig. 1. Arrhenius plots for the observed deep-level centers: (*1*, *3*) Z1 and (*2*, *4*) E_c – 0.18 eV; in samples (see table): (*1*, *2*) CS219, (*3*) S-187, and (*4*) S-187 after irradiation with 8 MeV protons.

As can be seen from the table, the half-widths of the rocking curves (ω_Θ) for the SE layers of samples CS189, CS220, and CS219 do not differ substantially from that for the S-002 sample with a layer grown on a Lely substrate and having the best characteristics of all the epitaxial layers. The high quality of the epitaxial layers on the Lely substrates is ensured by the structural perfection of the substrates. Thus, we can conclude that the structure of the CS series substrates is disturbed only slightly. A large scatter of half-widths is observed for sample S-187, indicating a highly nonuniform distribution of the substrate defects. For the V0017-4 sample with a CVD epitaxial layer, the half-width is noticeably larger.

3.2. Capacitance–Voltage (C–V) Characteristics and DLTS Measurements

The *C–V* characteristics were measured on a standard setup with a parallel equivalent circuit at a frequency of 10 kHz. The concentrations of uncompensated donors ($N_d - N_a$), found from the *C–V* data, and those of deep-level centers, determined from the DLTS-

Parameters of the epitaxial structures studied

Sample	Method (place) of fabrication		$N_d - N_a$, cm^{-3}	ω_Θ, in the $(10\bar{1}.7)$ reflection	N_{dc}, cm^{-3}	
	of the substrate	of the layer			Z1 (E_c – 0.7 eV), $\sigma_n = 10^{-14}$ cm^{-2}	(E_c – 0.18 eV), $\sigma_n = 4 \times 10^{-15}$ cm^{-2}
S-187	ML (SPbSEU)	SE (PTI)	4.5×10^{16}	20–250	1.5×10^{14}	$<10^{13}$
S-002	Lely (PCMF)	SE (PTI)	3.1×10^{16}	8–9	6×10^{14}	$<10^{13}$
V0017-4	ML (CREE)	CUD (CREE)	1.5×10^{16}	50–60	$<10^{13}$	$<10^{13}$
CS189	ML (CREE)	SE (LiU)	1.05×10^{16}	12–30	2.5×10^{14}	$<10^{13}$
CS220	ML (CREE)	SE (LiU)	3.4×10^{15}	8–15	3.5×10^{13}	3.2×10^{14}
CS219	ML (CREE)	SE (LiU)	2×10^{15}	12–30	3.5×10^{13}	6×10^{14}

Note: ML stands for the modified Lely method; SE, for sublimational epitaxy; CVD, for chemical-vapor deposition; N_{dc}, for the concentration of observed deep-level centers.

signal amplitudes for different types of samples, are listed in the table.

A study of deep-level centers revealed two types of traps in the upper half of the band gap, with energy levels E_c – (0.16–0.18) eV and E_c – 0.65 eV. The latter is known in the literature as the Z1 center [11]. Figure 1 shows Arrhenius plots for the observed deep-level centers. It can be seen that the recharging times of the Z1 center are the same for the PTI and LiU layers. The identity of the center parameters for layers grown on different installations, with different impurity compositions of the vapor phase, confirms its purely defect-related nature. The shallower center was not found in the S-002 and S-187 samples, but a center with very close parameters appeared in sample S-187 upon irradiation with protons [12].

Figure 2 shows the Z1 center concentration N_{Z1} as a function of $N_d - N_a$ for the samples studied in this work. It can be seen that the Z1-center concentration typically grows with increasing $N_d - N_a$ in most structures. Samples V0017-4 (where no such center was found) and S-187 (where the Z1 concentration appeared to be much lower than would be expected from the $N_d - N_a$ value) fall outside of the general dependence. We note that in the first case the epitaxial layer was CVD-grown and its ω_Θ value was larger than that of the substrate used; in the second case, a substrate with a low degree of structural perfection was used for SE growth.

It can also be noted that, by contrast, the concentration of the E_c – (0.16–0.18) eV center increases with decreasing $N_d - N_a$ in the layer, but data on this center (including those published) are insufficient for establishing a clear-cut correlation.

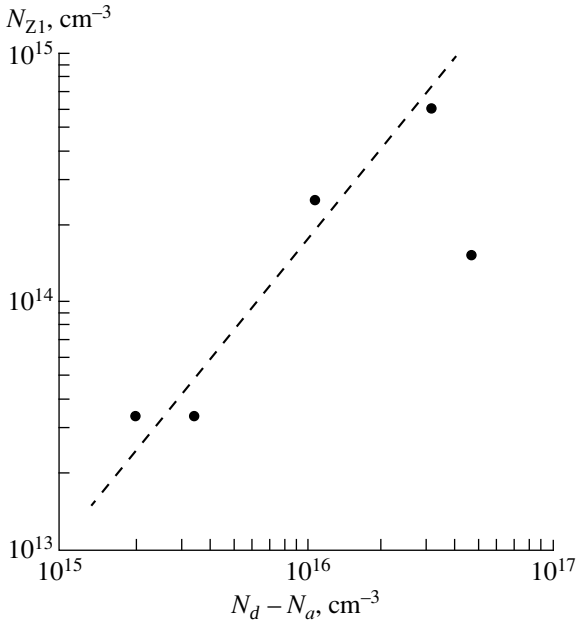

Fig. 2. Concentration of the Z1 center vs. $N_d - N_a$ for the samples studied.

4. DISCUSSION

As follows from the obtained X-ray data, the structural perfection of the 4*H*-SiC SE layers compares well with that of the ML substrates used for their growth. New dislocations are not formed during the sublimation growth. Thus, a conclusion can be made regarding the structural properties of the SE 4*H*-SiC epitaxial layers, similar to that for SE 6*H*-SiC layers.

According to ESR data [10, 11], both kinds of deep centers found in 4*H*-SiC layers are associated with structural defects in the lattice. The shallower center is an elementary defect, i.e., an isolated vacancy in the silicon sublattice or an interstitial atom, and the Z1 center is a vacancy in the carbon sublattice.

As shown previously for 6*H*-SiC [13], the deep-center concentration for SE layers is 2–3 orders of magnitude higher than that for CVD layers with the same $N_d - N_a$, the half-width ω_Θ being larger for the CVD layer. It has been suggested [13] that, since SiC layers grow in CVD epitaxy at substantially lower temperatures, as compared with the SE process, (~1500 and 2000°C, respectively), conditions for strain relaxation via the formation of deep-level centers associated with structural defects do not yet exist in the CVD layers. In the case under consideration, such relaxation may occur, for example, via the formation of a great number of dislocations. In other words, the dislocations formed during CVD layer growth serve as sinks for elementary lattice defects. No sinks of this kind exist in the SE epitaxial layers, and the given defects form electrically active deep-level centers. This assumption explains the observed lower concentration of deep levels and the higher dislocation density in the CVD 4*H*-SiC layers as compared with the layers grown by sublimational epitaxy.

5. CONCLUSION

This study confirms that the correlation between the dislocation density, the concentration of uncompensated donors, and the deep-center concentration, previously established for 6*H*-SiC layers, holds in the case of epitaxial 4*H*-SiC layers. According to the obtained data, the concentration of the characteristic background center Z1 in 4*H*-SiC falls with decreasing $N_d - N_a$. For the same $N_d - N_a$, it is lower in layers with a high dislocation density.

REFERENCES

1. A. A. Lebedev, Fiz. Tekh. Poluprovodn. (St. Petersburg) **33**, 129 (1999) [Semiconductors **33**, 107 (1999)].
2. J. A. Lely, Ber. Dtsch. Keram. Ges. **55**, 229 (1955).
3. Yu. M. Tairov and V. F. Tsvetkov, J. Cryst. Growth **43**, 209 (1978).

4. J. W. Palmour, J. A. Edmond, H. S. Kong, and C. H. Carter, Jr., Physica B (Amsterdam) **185**, 461 (1993).
5. A. A. Glagovskiĭ, E. V. Granovskiĭ, A. K. Drozdov, *et al.*, in *Proceedings of the 2nd All-Union Conference on Physics of Wide-Gap Semiconductors, Leningrad, 1980*, p. 226.
6. N. S. Savkina, A. A. Lebedev, D. V. Davydov, *et al.*, Mater. Sci. Eng., B **61/62**, 165 (1999).
7. M. Syväjärvi, R. Yakimova, M. Tuominen, *et al.*, J. Cryst. Growth **197**, 155 (1999).
8. A. A. Lebedev, A. S. Tregubova, V. E. Chelnokov, *et al.*, Mater. Sci. Eng., B **46**, 291 (1997).
9. N. S. Savkina, A. A. Lebedev, A. S. Tregubova, and M. P. Scheglov, in *Abstracts International Conference on Silicon Carbide and Rel. Mater., 1999*, Research Tringle Park, NC, USA, No. 368.
10. M. Tuominen, R. Yakimova, M. Syväjärvi, and E. Janzén, Mater. Sci. Eng., B **61/62**, 167 (1999).
11. T. Dalibor, G. Pensl, H. Matsunami, *et al.*, Phys. Status Solidi A **162**, 199 (1997).
12. A. A. Lebedev, A. I. Véinger, D. V. Davydov, *et al.*, Fiz. Tekh. Poluprovodn. (St. Petersburg) **34** (2), 897 (2000) [Semiconductors **34**, 861 (2000)].
13. A. A. Lebedev and D. V. Davydov, Fiz. Tekh. Poluprovodn. (St. Petersburg) **31**, 1049 (1997) [Semiconductors **31**, 896 (1997)].

Translated by D. Mashovets

Semiconductors, Vol. 34, No. 10, 2000, pp. 1137–1143. Translated from Fizika i Tekhnika Poluprovodnikov, Vol. 34, No. 10, 2000, pp. 1187–1193.

ELECTRONIC AND OPTICAL PROPERTIES OF SEMICONDUCTORS

Special Features of Photoelectric Properties of *p*-$Cd_xHg_{1-x}Te$ Crystals at Low Temperatures: The Effects of the Freezing-Out of Holes and Elastic Stress

S. G. Gasan-Zade, S. V. Staryĭ, M. V. Strikha, and G. A. Shepel'skiĭ

Institute of Semiconductor Physics, National Academy of Sciences of Ukraine, Kiev, 252028 Ukraine

Submitted March 3, 2000; accepted for publication April 6, 2000

Abstract—The temperature and pressure dependences of photoconductivity, the photoelectromagnetic effect, dark electrical conductivity, and the Hall coefficient in *p*-$Cd_xHg_{1-x}Te$ samples with $x \approx 0.20$–0.22 were measured at low temperatures. It is shown that recombination transitions in the temperature region of $T < 30$–40 K may be interpreted in the context of the two-level Shockley–Read model with allowance made for the freezing-out of majority charge carriers (holes). Furthermore, the second recombination center, which manifests itself only in the aforementioned temperature region, is an acceptor of a non-Coulomb type with an ionization energy of about 10–15 meV. *© 2000 MAIK "Nauka/Interperiodica".*

INTRODUCTION

The photoelectric properties of $Cd_xHg_{1-x}Te$ (CMT) single crystals and epilayers, which is one of the basic materials of infrared (IR) photoelectronics, still attract considerable interest. The *n*-type material has now been reasonably well studied owing to advances in technology. Its kinetic coefficients have been determined with a high accuracy, and the recombination mechanisms in the temperature range of 4.2–300 K are considered as known (see, for example, review [1]). The results of experiments are reproducible. The situation with *p*-type material is much more intricate. Publications devoted to *n*-CMT far outnumber those concerned with *p*-CMT. This is also true for photoelectric studies, especially in the low-temperature range. Meanwhile, in recent years, a wide use of single crystals and epilayers with hole conduction in the IR photodiodes has been evident. As is known, such photodiodes operate at low temperatures. The photodiode characteristics depend appreciably on the parameters of nonequilibrium charge carriers in the *p*-layer.

The recombination processes for the charge carriers in *p*-CMT were studied and reported in a number of publications [2–7]. It was found that, in contrast with *n*-CMT, there was a large spread in the experimental data related to *p*-type material. This is true for both the values of the main parameters of nonequilibrium charge carriers (the lifetime τ, the diffusion length L, the surface-recombination rate s, and so on) and the determination of the predominant recombination mechanism itself in different temperature ranges. The aforementioned spread in the data was primarily attributed to the low structural quality of *p*-type crystals; large differences in the conditions of their growth, annealing, and treatment; and the different state of the surface of samples. The main result of these studies amounts to the fact that, in *p*-CMT with $x = 0.20$–0.30, the Shockley–Read mechanism is predominant, as a rule, in the recombination processes at temperatures of $T < 150$–200 K. On this basis, a large spread in the lifetimes $\tau = 10^{-9}$–10^{-6} s is attributed to different concentrations of defects and impurities in the crystals. In addition, it follows from various publications that at least three types of recombination levels are present in the *p*-CMT band gap, with the depth depending on the composition (for $x = 0.2$, we have the energy separations of 10–15, 40–45, and 60–70 meV, respectively, from the valence-band top); these levels also feature a large spread in the capture cross sections for the majority and minority charge carriers.

In *n*-CMT, the recombination centers are certainly defects of the acceptor type [1]. As for *p*-CMT, the inferences in different publications have been contradictory; and, thus, the type of recombination center has remained uncertain to a large extent. Since attempts to explain the temperature dependences of τ in *p*-CMT in the context of the single-level Shockley–Read model have not met with actual success, several scientists [5, 7] made use of the two-level model. However, the types of recombination centers remained unidentified. On the other hand, it was attempted to interpret the dependences $\tau(T)$ in a wide temperature range on the basis of band-to-band recombination mechanisms alone [4]. Thus, the low-temperature behavior of recombination mechanisms in *p*-CMT calls for further investigation.

It should be taken into account that kinetic coefficients in *p*-CMT feature a number of anomalies in the region of low temperatures ($T < 77$ K) (see the review [8]). These anomalies affect the photoelectric properties of *p*-CMT [9]. The low-temperature anomalies are largely based on two mechanisms: on a drastic decrease

1063-7826/00/3410-1137$20.00

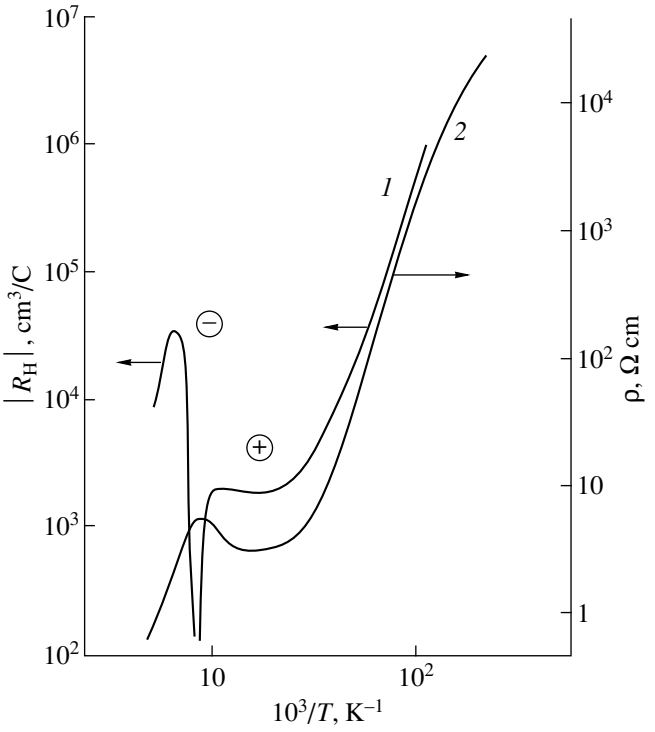

Fig. 1. Temperature dependences of the Hall coefficient R_H and resistivity ρ for a p-$Cd_xHg_{1-x}Te$ crystal with the parameters $x = 0.201$, $p = 3.3 \times 10^{15}$ cm^{-3}, and $\mu = 1.2 \times 10^3$ cm^2/(V s) at $T = 77$ K.

in the concentration of equilibrium holes due to their freezing-out at acceptor states at lowered temperatures and on large difference between the mobilities of electrons and heavy holes in CMT. Therefore, competing channels of *n*-conduction may manifest themselves in the bulk or at the surface of the *p*-type crystal.

In this paper, it is demonstrated that recombination transitions occurring at low temperatures in *p*-CMT crystals with the composition corresponding to $x = 0.20$ may be interpreted in terms of the two-level Shockley–Read model with allowance made for the freezing out of the majority charge carriers (holes). In this case, the second recombination level, which manifests itself only at $T < 30$–40 K, is an acceptor with an ionization energy of about 10–15 meV.

EXPERIMENT AND DISCUSSION OF THE RESULTS

This study has two distinct features that include the simultaneous measurement of the steady-state photoconductivity and the magnitude of the photoelectromagnetic (PEM) effect and also the use of uniaxial elastic stress. The photoconductivity and PEM measurements make it possible to determine the lifetime τ of both majority and minority charge carriers (as is known, the lifetime τ_{phc} determined from the photoconductivity measurements is close to the lifetime τ_h of the majority charge carriers, whereas the value of τ (τ_{phm}) determined from the PEM analysis corresponds to τ_e, i.e., the lifetime of minority charge carriers). The use of uniaxial stress *P* relies on its selective effect: in narrow-gap semiconductors, the stress *P* radically transforms the energy states of the valence band and acceptors without significantly affecting the conduction band and the donor levels related to this band. This may appreciably facilitate the determination of the type of recombination center.

We studied the p-$Cd_xHg_{1-x}Te$ samples with the composition parameter $x = 0.20$–0.22 and the concentration of uncompensated impurities in the range of $N_a - N_d = 3 \times 10^{15}$–$2 \times 10^{16}$ cm^{-3}. The samples were cut from CMT single crystals grown by planar crystallization and annealed at $T = 400$°C in an atmosphere saturated by mercury vapors. The concentration of active impurities was determined from the Hall coefficient R_H at a temperature of $T = 78$ K that corresponded to the depletion of the impurities. In order to eliminate the contribution of light holes to the Hall coefficient, we determined the concentration of free holes from measurements of R_H under reasonably high magnetic fields $H > 3$–5 kOe. Special attention was given to the surface treatment of the samples. The samples were preliminarily subjected to chemical–mechanical polishing and then, immediately before measurements, were etched in a 5% solution of bromine in methanol with subsequent rinsing in isobutyl alcohol. Electrical contacts were formed by alloying aluminum. The dimensions of the samples were $(0.4–0.6) \times (1.5–2) \times (6–8)$ mm^3.

We measured the photoconductivity and the magnitude of the PEM effect using conventional methods with modulation of the excitation radiation. The radiation sources were a globar in the wavelength range of 1–14 μm and an LG-126 laser ($\lambda = 3.39$ μm). For the samples under study, the condition for the low-level excitation $\Delta p \ll p$ (Δp is the concentration of nonequilibrium holes) was satisfied for the globar radiation in the entire temperature range of $T = 4.2$–150 K, whereas, for the unattenuated LG-126 radiation with a power of 5 mW, this condition was met for $T > 20$–30 K. A device for applying uniaxial pressure to produce an elastic strain was installed directly in a liquid-helium cryostat.

Figures 1 and 2 show the temperature dependences of R_H, ρ, τ_{phc}, and τ_{phm} in the temperature range of 4.2–200 K; these dependences are characteristic of the CMT samples studied. Drastic changes in R_H and ρ in the region of $T < 30$–40 K are of concentration-based origin and are related to the freezing-out of free holes at the acceptor level. The depth of this level depends on the concentration N_a and is equal to 6–8 meV in the samples studied. In view of a very high resistance of the sample at $T < 10$ K (the region of hopping conduction), we cannot measure the value of R_H reliably. In the low-temperature region of $T < 30$–40 K, we also observe an

increase in the hole lifetime τ_h simultaneously with a decrease in the electron lifetime τ_e with a drop in temperature. In addition, as in the case of R_H, for $T < 10$ K, the photomagnetic current decreases to such an extent that τ_e becomes virtually unmeasurable. The difference between the values of τ_h and τ_e reaches several orders of magnitude at $T = 10$ K. This makes it possible to make a choice in favor of the Shockley–Read mechanism and abandon the interpretation of the dependences $\tau(T)$ on the basis of the band-to-band recombination mechanisms in the aforementioned temperature region. We are reminded that, in the case of interband recombination, the condition $\tau_h = \tau_e$ should be valid.

Taking into account the effect of the freezing-out of holes, we can easily explain an increase in τ_h with decreasing *T*. In fact, as the temperature is decreased, the Fermi level in the *p*-type samples shifts downward and approaches the valence-band top. The excess electrons are rapidly captured by unoccupied states of the recombination center, so that the recombination rate becomes limited by a slower process, i.e., by the capture of holes by the center:

$$V = r_v p \Delta n_t.$$

Here, r_v is the recombination coefficient for the capture process of a hole, and p and Δn_t are the concentrations of free holes and electrons that are already trapped by the recombination center. The lifetime of the majority of charge carriers may then be written as

$$\tau_h = \frac{\Delta p}{V} = \frac{\Delta p}{r_v p \Delta n_t}, \quad (1)$$

where Δp is the concentration of photogenerated holes.

The freezing-out of holes results in an increase in τ_h, because $\tau_h \propto p^{-1}$. In such a simple model, the lifetime τ_e of the majority charge carriers should not vary, since the freezing-out of holes does not in the least affect the rate of trapping of electrons by the recombination center:

$$\tau_e = (r_c N_t)^{-1}.$$

Here, r_c is the corresponding recombination coefficient and N_t is the recombination-center concentration. However, as can be seen from Fig. 2, the experimental data contradict this inference: in the freezing-out region, an appreciable decrease in τ_e is observed. A decrease in τ_e in the *p*-CMT crystal has also been reported previously [7, 10].

Thus, the simple single-level Shockley–Read model cannot account even qualitatively for the experimentally observed dependences $\tau(T)$. Obviously, in addition to the reliably ascertained deep-level recombination center (its depth is within $E = 40$–45 meV for $x = 0.20$), another recombination center becomes involved in the recombination processes in *p*-CMT at low temperatures. This center comes into force as the temperature is decreased and the Fermi level lowers, in which case the trapping states are depopulated of electrons. As will be shown below, the second recombination center is located near the valence band and is an acceptor whose level lies deeper than that of a Coulomb type center.

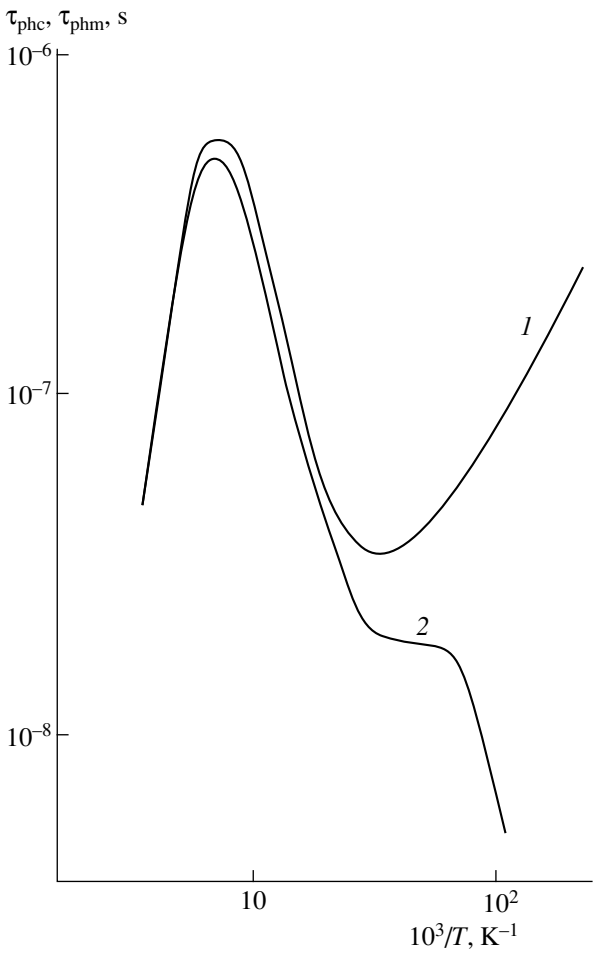

Fig. 2. Temperature dependences of the lifetimes (*1*) τ_{phc} and (*2*) τ_{phm}. The parameters of the sample are the same as in Fig. 1.

It was mentioned above that the impact of uniaxial elastic stress on the energy spectrum of semiconductors with a cubic crystallographic structure was found to be selective. In fact, the uniaxial stress almost does not affect the conduction band (except for the introduction of a slight anisotropy) and the donor states related to the conduction band. We have a completely different situation for the valence band that, in the absence of strain, is doubly degenerate at the point $k = 0$ and consists of subbands of light and heavy holes. By lowering the symmetry, the uniaxial stress removes the valence-band degeneracy. As a result, the energy gap ε_0 proportional to the pressure P emerges at the point $k = 0$, and the states of heavy and light holes become mixed. It is more convenient to characterize the new states by the sub-

bands V_+ and V_- with anisotropic effective masses of holes [11].

The fourfold degenerate (considering the spin) acceptor level is also split into two doubly degenerate states. The magnitude of splitting E_a for small strains (when the relation $\varepsilon_0 < E_a$ is valid) is found to be of the same order of magnitude as that for valence-band splitting [12]. Contrastingly, for large strains where the inverse relation $\varepsilon_0 > E_a$ is valid, the acceptor forms a series of localized states (the ground state and excited states) related to the subband V_+ and the resonance states related to the subband V_- [13].

In conventional semiconductors (for example, Ge and Si), the ratio between the effective masses of heavy and light holes m_h/m_l is small; as a result, the first of the above-described limiting cases is realized up to fairly large strains (corresponding to $P \approx 3$ kbar for Ge). On this basis, we may treat the influence of strain on the states of the valence band and acceptor states as insignificant.

For $Cd_xHg_{1-x}Te$ ($x = 0.20$), we have $m_h/m_l \approx 50$. Therefore, the splitting of subbands, a change in the effective masses of holes in the bands and the depth of the location of the acceptor level are found to be much more pronounced for the same values of strain [14]. In fact, even for $P = 1$ kbar, the magnitude of the band splitting ε_0 amounts to 12 meV for the [100] direction of stress, which exceeds the depth of shallow-level acceptors in the initial material. In this case, the second of the above-described situations is realized. It is clear that, at low temperatures, holes occupy only the upper split-off valence subbands and the ground state of the acceptor is formed from energy states of the top of this subband.

To a first approximation, the acceptor energy may be sought as the energy of a Coulomb center in a simple anisotropic band with the effective masses given by

$$m_\parallel = m_0/(\gamma_1 + 2\bar{\gamma}) \quad \text{and} \quad m_\perp = m_0/(\gamma_1 - \bar{\gamma}).$$

Here, $\bar{\gamma}$ and γ_1 are the Luttinger parameters. In the initial crystal, the mass of heavy holes is equal to $m_h = m_0/(\gamma_1 - 2\bar{\gamma})$. Since the averaged effective mass in the upper part of the split-off bands is found to be much smaller than m_h in the initial crystal, this results in an increase in the Bohr radius a_0 of the acceptor center and a decrease in its ionization energy E_a. In the absence of strain [14], we have

$$a_0 = \hbar/(2m_hE_a)^{-1/2}, \quad E_a(0) = (4/9)m_he^4/2\hbar^2\kappa^2.$$

At the limit of infinitely large strain,

$$E_a[\text{eV}] = \frac{13.52Z^2}{\kappa^2}\sqrt{\frac{2m_\perp^2 m_\parallel}{m_h}}. \qquad (2)$$

Here, Z is the charge of the center and κ is the permittivity of the crystal.

We note that formula (2) is found to be a fairly good approximation for estimating the binding energy of the state 1*s* of the split acceptor level related to the band V_+ at the limit of large strains. Thus, for an acceptor in a severely deformed Ge, formula (2) yields $E_a = 2.8$ meV, whereas the more exact variational calculation [13] results in a somewhat larger value of $E_a = 3.8$ meV. We emphasize that, when reaching the limit of large strains, the value of E_a becomes independent of *P*.

At the limit of a large strain, an estimation of the binding energy of the shallow-level acceptor yields $E_a = 0.6$ meV for CMT. This value is much smaller than that obtained for Ge; this is caused by the smaller effective mass m_l. Therefore, for large strains, the states of an electrically active acceptor are found to be ionized at temperatures $T > 10$ K, and the concentration of free holes p approaches the value of $N_a - N_d$. The latter should result in a drastic decrease in the resistivity of *p*-CMT crystal with increasing pressure. However, if the acceptor concentration in $Cd_xHg_{1-x}Te$ is sufficiently high ($N_a \approx 10^{15}$ cm^{-3}), the uniaxial compression may give rise to the merging of the acceptor states with the valence-band top (the Mott transition) if the doping parameter (the product of the concentration by the Bohr volume $N_a a^3$) exceeds 0.02 [14]. In this case, the energy of the acceptor's ground state vanishes. Thus, the impact of *P* on shallow-level acceptor centers in CMT is found to be profound.

An appreciable decrease in the capture cross section occurs if a charge carrier is trapped by a Coulomb center at the limit of the large strain. In fact, as was shown previously [15], capture by a charged center constitutes a continuous descent in energy, in contrast with the earlier Lax model [16]. In this case, a transition over the zero energy level is not distinguished at all, and the cross section for trapping by a charged center is described by the generalized Thompson formula; i.e.,

$$\sigma = \frac{4}{3}\pi l_0^2\left(\frac{e^2Z}{\kappa kT}\right)^3, \qquad (3)$$

where kT is the thermal energy. The length l_0 is independent of either the energy of the trapped charge carrier or the temperature and is related to the mean free path by the formula

$$l_0 = l\frac{kT}{2ms^2}. \qquad (4)$$

Here, m is the effective mass of a charge carrier and s is the velocity of sound. To a first approximation and in the limit of large strains, the influence of uniaxial stress on the cascade trapping of a hole by an acceptor may be taken into account by introducing the anisotropic effective mass $m^* = (m_\perp^2 m_\parallel)^{1/3}$ into expression (4). For the above-discussed reasons, this will result in an appreciable decrease in the capture cross section and, correspondingly, in an increase in the lifetime of the holes.

A simple estimation of the cross section for trapping by the acceptor level in CMT in the limit of large strain yields $\sigma_\infty/\sigma_0 = 0.04$. A more accurate estimate can be obtained using the data reported previously [17], which yields a qualitatively similar result.

If the recombination center is a deep-level acceptor that is described in terms of a model of the zero-radius potential, the corresponding state is also found to be split by the uniaxial strain into two doubly degenerate states. In this case, as was shown elsewhere [18], the energy separation between the split-off acceptor sublevels is $E_{12} \approx 0.1\varepsilon_0$ as a result of a small ratio m_e/m_h.

Thus, in contrast to the above-considered case of a shallow-level Coulomb acceptor, the binding energy of the lower split-off state with respect to the band V_+ is given by

$$E_a(P) \approx E_a(0) - 0.45\varepsilon_0. \quad (5)$$

For a CMT crystal with the aforementioned composition, we have $\varepsilon_0 = \alpha P$, where $\alpha = 12$ meV/kbar.

We can use the above relationships to approximately estimate the value of strain that converts the lower split-off level to a resonance level. The estimation shows that the level with $E_a(0) \approx 10$ meV remains localized up to at least the value of $P = 2$ kbar. However, for such a level, the process of trapping a hole can be no longer described in the context of the cascade Lax model, because the binding energy significantly exceeds the acoustic-phonon energy. In this case, the simplest analysis of the multiphonon trapping by the center in terms of the Huang–Rhys model yields the following expression for the capture cross section:

$$\sigma = \frac{1}{16\pi^2}\frac{\hbar\omega}{kT}\frac{\hbar^2}{mkT}\exp\left(-\frac{E}{kT}\right). \quad (6)$$

Here, ω is the vibration frequency of the atomic nucleus, E is the activation energy defined by the thermal ionization energy and the constant of the electron–phonon coupling, and m is the density-of-state mass in the band to which the level is related [15].

In the strict sense, in the case of a strained crystal, the use of the anisotropic effective mass m^* is improper in the vicinity of the top of the band V_+. However, this effective mass may be used in qualitative estimations for the values of P for which $E_a(P) \ll E$, where E are all the other energy spacings in a system that consists of the split acceptor level and the split valence-band top. Consequently, the cross section of multiphonon trapping by the deep-level acceptor increases owing to a decrease in the effective mass. The second cause of an increase in σ may be a decrease in the activation energy E in the exponential function in (6). Thus, a uniaxial pressure can unambiguously discriminate between the cases of trapping by a shallow-level Coulomb center and those related to a deep-level center described by the model of the zero-radius potential.

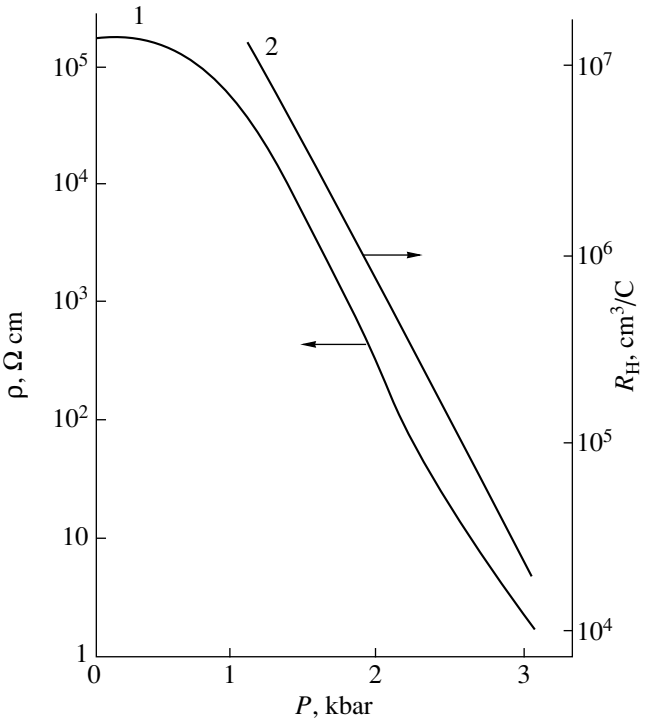

Fig. 3. Dependences of the Hall coefficient R_H and the resistivity ρ on the pressure P at $T = 4.2$ K. The parameters of the sample are the same as in Fig. 1.

Figures 3 and 4 show the pressure dependences of R_H, ρ, τ_{phc}, and τ_{phm} measured at $T = 4.2$ K. In the pressure range of $P = 1$–3 kbar, all the aforementioned parameters change drastically (by several orders of magnitude). We emphasize that qualitatively similar dependences were observed for virtually all studied *p*-CMT samples with the hole concentration in the range of 3×10^{15}–2×10^{16} cm^{-3}. It follows from the dependences $R_H(P)$ and $\rho(P)$ that, due to a decrease in the effective mass, the hole mobility μ_{V_+} in the upper split-off band increases from 3.9×10^2 cm^2/(V s) (the hole mobility μ_h in unstrained crystals) to 4×10^3 cm^2/(V s). Simultaneously, the free-hole concentration increases appreciably owing to the strain-induced depopulation of the acceptor states; this is the effect opposite to the freezing-out of holes. It may be referred to as the "strain-induced boiling-out." For $P = 3$ kbar, the hole concentration in the upper valence subband is as high as $p = 7.2 \times 10^{14}$ cm^{-3}; i.e., it approaches (by an order of magnitude) the value of p in the temperature region that corresponds to the depletion of electrically active acceptors ($T > 60$–70 K).

It can be also seen from Fig. 4 that the pressure dependences of the lifetimes of electrons and holes are radically different: the quantity τ_{phm} rapidly increases with increasing P, whereas τ_{phc} decreases substantially.

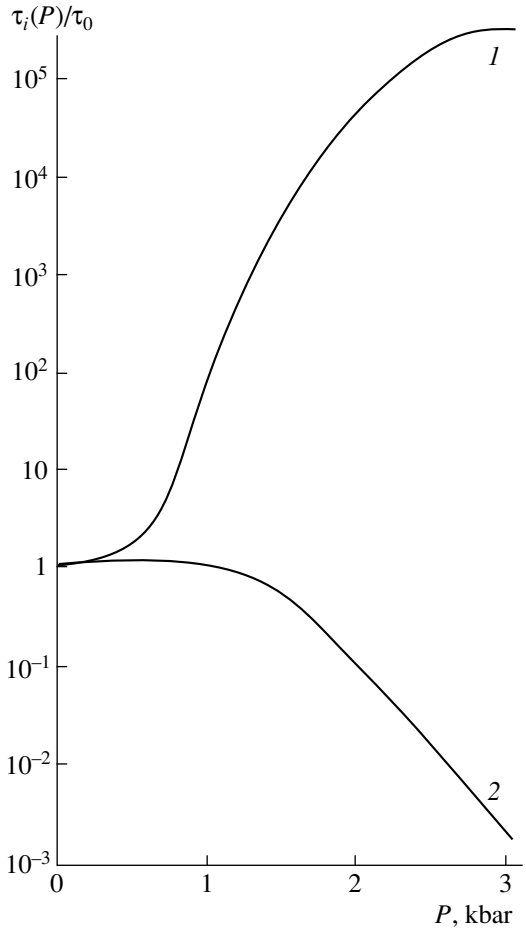

Fig. 4. Dependences of lifetimes (*2*) τ_{phc} and (*1*) τ_{phm} on the pressure P at T = 4.2 K. The parameters of the sample are the same as in Fig. 1.

On the basis of the above dependences, we may infer that the effect of elastic stress on the recombination rate is opposite to that of a decrease in temperature. Obviously, the cause of this consists in the fact that, as the pressure P increases and the acceptor states are depopulated, the Fermi level rises and moves away from the valence-band top. As a result, the free-hole concentration increases substantially, which causes τ_h to decrease [see expression (1)]. On the other hand, the recombination level involved in transitions at low temperatures becomes populated with electrons, and the rate of the further process of trapping of minority charge carriers (electrons) decreases appreciably. This causes the electron lifetime τ_e to increase.

On the basis of the above estimates, we attempt to infer the form of the potential of the recombination center located in the vicinity of the valence-band top. To this end, we take into account the strain-induced variation in the capture cross section. It follows from formulas (1) and (5) for a shallow acceptor level that the lifetime of the majority of charge carriers (holes) is affected by two opposing factors: an increase in the hole concentration p with increasing pressure and a decrease in the capture cross section σ. Their effects compensate for each other to a large extent, so that the ratio τ_h/τ_0 for P = 3 kbar is no larger than 10 according to estimations. This is at least by two orders of magnitude smaller than the experimental value. Thus, we may conclude that the recombination center is not a Coulomb acceptor for which the Lax model is valid; rather, its level is located somewhat deeper in the band gap. The model of the zero-radius potential is better fitted to such a center. The cross section for trapping by such an acceptor is bound to increase with increasing pressure, and, thus, the hole lifetime is bound to decrease. Another cause of the strain-related decrease in the hole lifetime is, as was mentioned above, the increase in the Fermi level. Estimation of the strain-induced shift of the Fermi level using formulas (1) and (5) shows that the depth of the acceptor level should not exceed 10–15 meV from the valence-band top.

CONCLUSION

Thus, the suggested two-level model with allowance made for the freezing-out of holes can be used to describe the special features of the recombination processes in *p*-CMT at low temperatures. Experimental data can be interpreted by considering, in addition to the well-known recombination level located at $E \approx$ 40 meV, another acceptor with E_a = 10–15 meV. It is only in terms of the suggested model that a decrease in the lifetime of the minority charge carriers (electrons) in the low-temperature range, as well as the opposite dependences of the hole and electron lifetimes on elastic stress, can be interpreted.

REFERENCES

1. N. S. Baryshev, B. L. Gel'mont, and M. I. Ibragimov, Fiz. Tekh. Poluprovodn. (Leningrad) **24**, 209 (1990) [Sov. Phys. Semicond. **24**, 127 (1990)].
2. A. V. Voĭtsekhovskiĭ and Yu. V. Lilenko, Fiz. Tekh. Poluprovodn. (Leningrad) **15**, 1457 (1981) [Sov. Phys. Semicond. **15**, 845 (1981)].
3. D. I. Polla and C. E. Jones, J. Appl. Phys. **52**, 5118 (1981).
4. N. L. Bazhenov, V. I. Ivanov-Omskiĭ, N. I. Konstantinova, and V. K. Ogorodnikov, Fiz. Tekh. Poluprovodn. (Leningrad) **16**, 2102 (1982) [Sov. Phys. Semicond. **16**, 1424 (1982)].
5. S. T. Schechman and E. Finkman, J. Appl. Phys. **57**, 2001 (1985).
6. R. Fastow and Y. Nemirowsky, J. Vac. Sci. Technol. A **8**, 1245 (1990).
7. R. Fastow, D. Goren, and Y. Nemirowsky, J. Appl. Phys. **68**, 3405 (1990).
8. V. I. Ivanov-Omskiĭ, N. N. Berchenko, and A. I. Elizarov, Phys. Status Solidi A **103**, 11 (1987).
9. S. G. Gasan-Zade, M. V. Strikha, and G. A. Shepel'skiĭ, Fiz. Tekh. Poluprovodn. (St. Petersburg) **33**, 574 (1999) [Semiconductors **33**, 536 (1999)].

10. S. E. Jones and V. Nair, Appl. Phys. Lett. **39** (3), 248 (1981).
11. G. L. Bir and G. E. Pikus, *Symmetry and Stain-Induced Effects in Semiconductors* (Nauka, Moscow, 1972; Wiley, New York, 1975).
12. R. Buczko, Nuovo Cimento D **9**, 669 (1987).
13. M. A. Odnolyubov and V. M. Chistyakov, Fiz. Tekh. Poluprovodn. (St. Petersburg) **32**, 799 (1998) [Semiconductors **32**, 711 (1998)].
14. A. V. Germanenko, G. M. Min'kov, and O. É. Rut, Fiz. Tekh. Poluprovodn. (Leningrad) **21**, 2006 (1987) [Sov. Phys. Semicond. **21**, 1216 (1987)].
15. V. N. Abakumov, V. I. Perel', and I. N. Yassievich, *Nonradiative Recombination in Semiconductors* (Inst. Yad. Fiz., St. Petersburg, 1997).
16. M. Lax, Phys. Rev. **119**, 1502 (1960).
17. V. V. Akulinichev, Fiz. Tekh. Poluprovodn. (Leningrad) **16**, 254 (1982) [Sov. Phys. Semicond. **16**, 159 (1982)].
18. F. T. Vasko and M. V. Strikha, Phys. Status Solidi B **181**, 447 (1994).

Translated by A. Spitsyn

Semiconductors, Vol. 34, No. 10, 2000, pp. 1144–1146. Translated from Fizika i Tekhnika Poluprovodnikov, Vol. 34, No. 10, 2000, pp. 1194–1196.

ELECTRONIC AND OPTICAL PROPERTIES OF SEMICONDUCTORS

Instability of *DX*-like Impurity Centers in PbTe:Ga at Annealing

D. E. Dolzhenko*, V. N. Demin, I. I. Ivanchik*, and D. R. Khokhlov***

** Physics Department, Moscow State University, Vorob'evy gory, Moscow, 119899 Russia*

e-mail: khokhlov@mig.phys.msu.su

*** Chemistry Department, Moscow State University, Vorob'evy gory, Moscow, 119899 Russia*

Submitted March 21, 2000; accepted for publication April 6, 2000

Abstract—The kinetics of variation in the resistance of PbTe:Ga single crystals, with their Fermi level pinned within the band gap, during annealing at temperatures of up to 400°C was studied for the first time. It is shown that annealing the crystals for only several minutes at 200–250°C leads to the transformation of the material, which is semi-insulating at low temperatures, into a strongly degenerate semiconductor with a free electron concentration of about 10^{-18} cm^{-3}. In other words, annealing results in the decomposition of *DX*-like impurity centers, which account for Fermi level pinning within the PbTe:Ga band gap. The corresponding activation energy is determined. It is found that high-temperature annealing at about 400°C promotes the tendency to a partial recovery of semi-insulating properties. © *2000 MAIK "Nauka/Interperiodica".*

Doping of lead telluride with certain elements of Group III entails Fermi level pinning and persistent photoconductivity, among the other long-term relaxation processes, when the equilibrium is disturbed at low temperatures [1]. Under certain conditions, the Fermi level in PbTe:Ga can be pinned within the band gap, ~70 meV below the conduction-band bottom, and persistent photoconductivity is observed at temperature $T < 80$ K [2]. This effect of doping with gallium is attributed to the formation of *DX*-like impurity centers [3]. When the Fermi level is not pinned, gallium is known to act as a donor with an unstable doping effect, which strongly depends on external conditions, i.e., pressure, temperature, etc. [4]. In this paper, we discuss the stability of *DX*-like centers in PbTe:Ga with the Fermi level unaffected by high-temperature annealing.

Before annealing, we observed the pinned Fermi level and also persistent photoconductivity in crystals that were studied at $T < 80$ K. Annealing was performed by heating the crystals to $T \le 400$°C in a helium atmosphere, and the crystal resistance was measured *in situ* by the four-contact technique. For this purpose, the graphite contacts were pressed to the samples by a spring made of beryllium bronze. The sample temperature was measured with a copper–constantan thermocouple.

Heating PbTe:Ga to a temperature of about 250°C for several minutes leads to a complete loss of semi-insulating properties. Figure 1 shows the temperature dependence of sample resistance during the following cycle: heating from room temperature to 250°C and subsequent cooling. It can be seen that, during heating, the temperature dependence of the resistance is typical of semiconductors, whereas, during cooling, it exhibits "metallic" behavior, with *n*-type conduction. The temperature dependence of the resistance during cooling from 250°C indicates that the free-electron concentration in the annealed sample is no lower than 10^{18} cm^{-3}.

Annealing the samples at a constant temperature between 200 and 280°C results in the approximate exponential decay of the resistance:

$$\rho = \rho_0 - \Delta\rho[1 - \exp(-t/\tau)].$$

Here, τ depends exponentially on the annealing temperature (see Fig. 2):

$$\tau = \tau_0 \exp(E_a/kT).$$

Estimation of E_a from the dependence $\tau(T)$ yields $E_a \approx 1.8$ eV.

The resistance of a sample heated above 380°C rapidly increases, and subsequent cooling gives rise to an activation portion that extends down to ~100°C. The closest approach to the initial (before annealing) resistance of a sample at room temperature was achieved by quenching it by rapid cooling from ~400 to 25°C within tens of seconds. Nevertheless, we failed to completely recover the semi-insulating properties and to achieve persistent photoconductivity at low temperatures.

Fermi level pinning in PbTe:Ga substantially differs from a similar effect observed in PbTe doped with other Group III elements, namely, indium and thallium. This difference can be primarily attributed to the fact that, in PbTe:Ga, Fermi level pinning occurs only in a narrow range of concentrations of the introduced Ga, whereas beyond this range, up to the solubility limit, gallium acts as a donor [5]. In contrast, in PbTe:Tl and PbTe:In, Fermi level pinning occurs for any dopant concentra-

tion exceeding the concentrations of other electrically active impurities and defects [6].

Another important point is the following. It would appear reasonable to assume that, in PbTe doped with various elements of Group III, the position of the impurity level that accounts for Fermi level pinning would depend monotonically on the atomic number of the element. Evidently, gallium breaks this pattern: in PbTe doped with thallium, which is the heaviest Group III element, the Fermi level is pinned deep in the valence band; in PbTe:In, it is pinned at 70 meV above the bottom of the conduction band; and in PbTe doped with gallium, which is lighter than indium, the Fermi level is pinned within the band gap. The described "inconsistency" may be explained by assuming that Fermi level pinning within the band gap in PbTe:Ga does not result from the effect of individual gallium atoms but is governed by complexes of gallium with surrounding defects. A number of experimental results support this conjecture.

Optical excitation to a quasi-local level high in the conduction band was observed in the pioneering studies of optical absorption in PbTe:Ga [7]. However, the relatively low solubility of gallium in lead telluride prevents the Fermi level from reaching this quasi-local level by means of doping. It is possible that this quasi-local level corresponds to a plausible position of the Fermi level pinned by individual gallium atoms.

Furthermore, the fact that the Fermi level pinning within the band gap occurs in a narrow range of Ga concentrations indicates that the density of states at the corresponding level is much smaller than the total quantity of Ga in the crystal. Therefore, such pinning can take place only if gallium atoms, which are not included in complexes, compensate the doping produced by other impurities and defects. Any noticeable disbalance of this compensation results in the Fermi-level shift in either direction.

The results obtained in this study also point to the fact that Fermi level pinning within the band gap in PbTe:Ga is related to a complex consisting of an impurity and a defect. Most likely, this complex is metastable at temperatures below 400°C. As was pointed out above, heating a sample to a mere 200–250°C leads to a complete loss of its semi-insulating properties. Even if all the gallium atoms included in these complexes are transformed into a state in which they do not contribute to Fermi level pinning, the concentration of the complexes should be on the order of 10^{18} cm^{-3}, which is considerably lower than the total amount of gallium in the crystal ~10^{20} cm^{-3}. The height of the barrier between the metastable *DX*-like state of a complex and the ground state, which does not contribute to Fermi level pinning, is about 2 eV. In all probability, at temperatures above 380°C, the *DX*-like state of the complex becomes the ground state, thus implying a rapid increase in resistance and a tendency to recovery of the

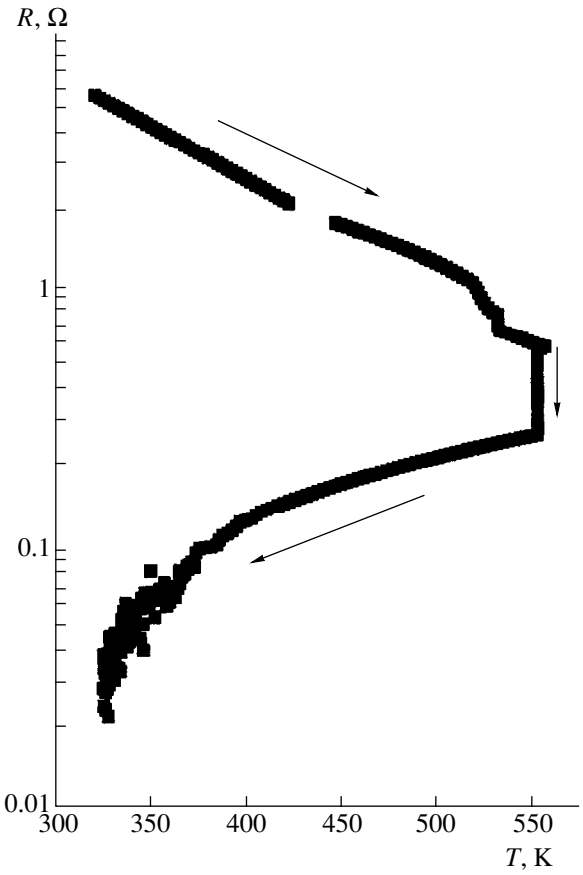

Fig. 1. The temperature dependence of PbTe:Ga resistance during heating to $T \simeq 250$°C and subsequent cooling. The annealing at 250°C lasted for a few minutes.

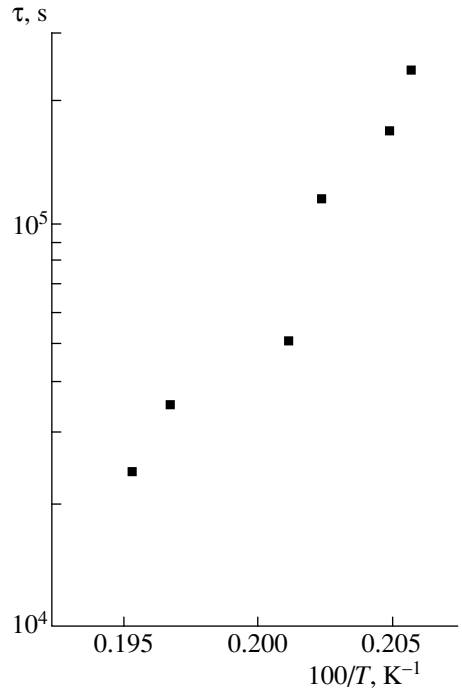

Fig. 2. The characteristic decay time of resistance versus the annealing temperature.

semi-insulating properties during subsequent quenching.

ACKNOWLEDGMENTS

We are grateful to Prof. L.I. Ryabova for her valuable participation in discussions.

The research described in this publication was supported in part by the Russian Foundation for Basic Research (project nos. 98-02-17317 and 96-02-18853) and INTAS–RFBR grant no. 95-1136.

REFERENCES

1. B. A. Akimov, A. V. Dmitriev, D. R. Khokhlov, and L. I. Ryabova, Phys. Status Solidi A **137**, 9 (1993).
2. B. A. Akimov, N. B. Brandt, A. M. Gas'kov, *et al.*, Fiz. Tekh. Poluprovodn. (Leningrad) **17**, 87 (1983) [Sov. Phys. Semicond. **17**, 53 (1983)].
3. A. I. Belogorokhov, I. I. Ivanchik, S. V. Ponomarev, *et al.*, Pis'ma Zh. Éksp. Teor. Fiz. **63**, 342 (1996) [JETP Lett. **63**, 353 (1996)].
4. B. A. Akimov, N. B. Brandt, L. I. Ryabova, *et al.*, Pis'ma Zh. Éksp. Teor. Fiz. **31**, 304 (1980) [JETP Lett. **31**, 279 (1980)].
5. G. S. Bushmarina, B. F. Gruzinov, I. A. Drabkin, *et al.*, Fiz. Tekh. Poluprovodn. (Leningrad) **11**, 1874 (1977) [Sov. Phys. Semicond. **11**, 1098 (1977)].
6. V. I. Kaĭdanov and Yu. I. Ravich, Usp. Fiz. Nauk **145**, 51 (1985) [Sov. Phys. Usp. **28**, 31 (1985)].
7. A. N. Veĭs, V. I. Kaĭdanov, N. A. Kostyleva, *et al.*, Fiz. Tekh. Poluprovodn. (Leningrad) **7**, 928 (1973) [Sov. Phys. Semicond. **7**, 630 (1973)].

Translated by A. Sidorova-Biruykova

Semiconductors, Vol. 34, No. 10, 2000, pp. 1147–1150. Translated from Fizika i Tekhnika Poluprovodnikov, Vol. 34, No. 10, 2000, pp. 1197–1200.

ELECTRONIC AND OPTICAL PROPERTIES OF SEMICONDUCTORS

Effect of Doping with Gadolinium on the Physical Properties of $Hg_3In_2Te_6$

O. G. Grushka, P. M. Gorleĭ, A. V. Bestsennyĭ, and Z. M. Grushka

Chernovtsy State University, Chernovtsy, 58012 Ukraine

Submitted April 4, 2000; accepted for publication April 17, 2000

Abstract—Special features of gadolinium solubility during the $Hg_3In_2Te_6$:Gd crystal growth are considered. The highest attainable gadolinium concentration in the solid phase is equal to 2.3×10^{19} cm^{-3}. It is shown that, as the doping level increases, strains and stresses in the crystal lattice occur and correlate with the dopant concentration. Doping has virtually no effect on the transport properties and the Fermi level located near the middle of the energy gap. The optical absorption observed at photon energies lower than the energy gap is accounted for by the tails of the density of states in the band gap. Absorption-spectra features are explained using the theory of the interaction of light with disordered, heavily compensated semiconductors. Additional structureless absorption in the optical transparency region is caused by the small-angle scattering of light by inclusions formed by the charged impurities. © *2000 MAIK "Nauka/Interperiodica"*.

The most complete knowledge about semiconductors doped with the rare-earth elements (REE) with unfilled 4*f* shell relates to Si, Ge, and III–V and II–VI compounds. As shown in review [1], the behavior of REE impurities in semiconductors is characterized by some special features, for example, by low solubility and the ability to purify material; the latter feature makes it possible to lower the concentration of the residual impurities considerably and to increase electron mobility. Gadolinium and ytterbium impurities are most effective in this respect. Therefore, studies of these impurities in different types of semiconductors, in particular, compounds with stoichiometric vacancies which are characterized by rather high solubility of the impurities, are of great interest.

In this paper, we report the results of a study of gadolinium-doped $Hg_3In_2Te_6$ crystals. The semiconductor $Hg_3In_2Te_6$ is a chemical compound in an In_2Te_3–HgTe system with a congruent type of melting. This compound crystallizes in an imperfect sphalerite structure with a high concentration (~10^{21} cm^{-3}) of the electrically neutral stoichiometric vacancies which define the properties that are useful for practical applications [2]: high stability of the physical parameters against ionizing radiation, electrical neutrality of impurities, and a wide spectral range of photosensitivity (0.74–3.5 eV) and transparency (2–25 μm). Preliminary studies showed an interesting property of gadolinium: it can uniformly reduce the transmission coefficient, proportionally to its content in $Hg_3In_2Te_6$ crystals, in the entire transparency range from the value T = 55–60% corresponding to the undoped material. In this case, the structureless character of the transmission spectra remains unchanged.

We studied ingots of $Hg_3In_2Te_6$ with different concentrations of gadolinium impurity (10^{19}–10^{20} cm^{-3}) grown by planar crystallization from the melt by the Bridgman–Stockbarger method. The ingots were cut into disks, from which the samples were prepared. The impurity concentration of N_{Gd} in the samples was determined from the measurements of static magnetic susceptibility. Taking into account the well-known fact that REE atoms in semiconductors are in the Re^{3+} state [1] (except for Eu^{2+}), we assumed that gadolinium in $Hg_3In_2Te_6$ crystals is also in the Gd^{3+} state.

X-ray diffraction analysis showed that doping with Gd to the solubility limit did not affect either the structure or the lattice constant (6.289 ± 0.001 Å), which remained almost the same as in the undoped material. However, using monochromatic CuK_α radiation, we found that the height and width of the diffraction peaks varied appreciably. For $N_{Gd} < 10^{18}$ cm^{-3}, reflections at large angles are sharp and intense and had split doublets. As the doping level increases, the peaks become lower and wider; splitting of the doublets becomes less noticeable and disappears completely for $N_{Gd} \gtrsim 10^{19}$ cm^{-3}. The transformation of the X-ray diffraction patterns indicates that the introduction of an impurity produces the strained state of the matrix lattice.

Since the lowest impurity concentration was in samples cut from the starting part of the ingots, we came to the conclusion that the distribution coefficient of Gd impurity in $Hg_3In_2Te_6$ samples was $k < 1$. However, due to the fact that the concentration-profile curves were nonmonotonic, we were unable to describe the impurity distribution along the ingots by the Pfann equation for planar crystallization. The higher the impurity concentration introduced into the charge, the larger the

periodical nonuniformity of the gadolinium distribution. One of the possible causes of this effect is impurity accumulation near the crystallization front in accordance with the distribution coefficient $k < 1$. This may lead to a decrease in the crystallization equilibrium temperature. Temperature fluctuations at the phase interface result in unstable crystal growth, with the formation of growth layers with varying impurity concentrations. As a result, impurity inhomogeneities occur along the ingot. The highest concentration of N_{Gd} in the single-crystal samples was 2.3×10^{19} cm^{-3}, which is 1–2 orders of magnitude lower than the solubility limit of other (not REE) impurities in $Hg_3In_2Te_6$ but an order of magnitude higher than in semiconductors that do not contain stoichiometric vacancies. Rare-earth ions with a screened *f* shell are hardly subjected at all to the influence of the crystal field of the matrix, and, as a result, their low solubility is basically defined by a dimensional factor. Due to relatively large size of Gd^{3+} ions ($r = 0.97$ Å), during the growth process, the impurity does not easily enter into the crystal from the melt and accumulates in the end part of the ingot. The part of a crystal that is supersaturated with an impurity has an increased tendency to crack; and, as the ingot is removed from the container, it easily shatters into small pieces that are useless for investigation. Low solubility and substantial deviation of the REE impurity distribution from the statistical one are typical of different classes of semiconductors. This phenomenon is explained [1] by the tendency of REE to form complicated complexes and associations (especially with elements of group VI), the formation of which causes strains in the crystal lattice, which is consistent with the X-ray diffraction pattern.

Studies of $Hg_3In_2Te_6$:Gd transport properties (electrical conductivity, Hall coefficient, and thermoelectric power) showed that the charge-carrier concentration (~10^{13} cm^{-3} at 300 K) is 4–6 orders of magnitude lower than the impurity concentration in the samples. The Hall mobility for an impurity concentration lower than 10^{19} cm^{-3} is virtually the same as the mobility in undoped material (300–320 cm^2/(V s) at 300 K). For higher impurity concentrations, mobility decreases slightly to 270 cm^2/(V s) for $N_{Gd} = 2.3 \times 10^{19}$ cm^{-3}. Thus, purification of the material and improvement of its parameters do not occur. This is probably related to the fact that the concentration of native defects is higher than the impurity concentration. The main native defects in $Hg_3In_2Te_6$ are stoichiometric vacancies (SV) with a concentration (2.7×10^{21} cm^{-3}) which has the same order of magnitude even when all the Gd impurity corresponding to the solubility limit (2.3×10^{19} cm^{-3}) occupies the stoichiometric vacancies. Thus, the SVs define imperfection and disordering of a structure. In the temperature range of 150–400 K impurity conduction does not occur, and $Hg_3In_2Te_6$:Gd crystals are similar to an intrinsic semiconductor. Like many other metal impurities [3], gadolinium has no influence at all on the Fermi level which is located near the middle of the energy gap. This explains the electrical inactivity of Gd^{3+} ions in $Hg_3In_2Te_6$. Pinning of the Fermi level approximately near the middle of the energy gap may be caused by either high temperatures or precise compensation. Realization of both of these cases in $Hg_3In_2Te_6$ is possible at temperatures between 400 and 150 K. According to the theory [4], the Fermi level descends deep into the energy gap in disordered systems due to both large-scale fluctuations of the electrostatic potential in the case of heavy doping ($Na_{e(h)}^3 \gg 1$, where a_e and a_h are the Bohr radii of an electron and a hole) and the approximate equality of donor and acceptor concentrations *N* randomly distributed in the crystal. Large-scale potential fluctuations may be caused by strains and stresses in the lattice of the doped material. However, in $Hg_3In_2Te_6$, this occurs not because of the introduction of high and equal concentrations of donor and acceptor impurities into the matrix but as a result of the self-compensation effect. This effect is characteristic of semiconductors with stoichiometric vacancies, is defined by the nature of the material [5], is not yet convincingly explained and needs further study.

It is well known that optical absorption is sensitive to the degree of material perfection. Because of this, the optical absorption spectra were studied at energies $h\nu$ less than the energy gap E_g. When the difference between the energies $\Delta = E_g - h\nu$ is small, the absorption coefficient α is described well by the Uhrbach rule:

$$\ln[\alpha(h\nu)] \propto -\Delta/\Delta_0,$$

where Δ_0 is a specific energy that is independent of frequency. The linear parts of the curves, which obey the Uhrbach rule (Fig. 1), and correspond to samples with different impurity concentrations, converge to a common point after extrapolation. This is evidence that doping does not change E_g. Both the absorption coefficient and the specific energy Δ_0 (Fig. 1, the insert) are proportional to the doping level. Among the models involving the Uhrbach rule that were suggested previously [4, 6–8], model [4] is most acceptable in our case. In this model, the optical absorption with an energy deficit is explained by the potential fluctuations which form the states in the band gap. Theory [4], developed for a direct-gap semiconductor with randomly distributed impurities, with a hole mass larger than the electron mass, and a Fermi level located deep in the energy gap, may be quite acceptable for a semiconductor such as $Hg_3In_2Te_6$.

According to [4], for small values of energy ε measured from the bottom of the conduction band in the direction of the valence band, the density of states $\rho(\varepsilon)$ decreases according to the relation

$$\ln[\rho(\varepsilon)/\rho(0)] = -\varepsilon^2/\gamma^2, \quad \gamma = e^2(Nr_0^3)^{1/2}/(\kappa r_0), \quad (1)$$

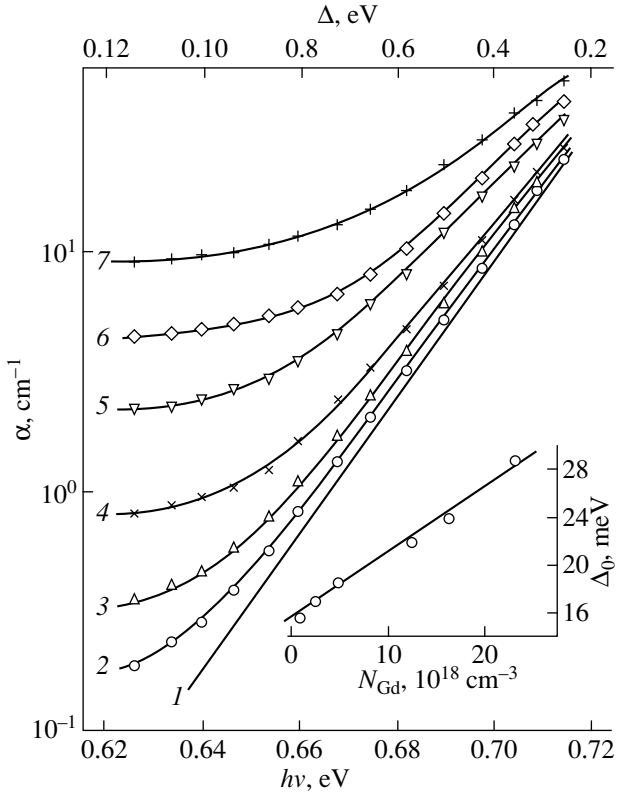

Fig. 1. Absorption-coefficient spectra of $Hg_3In_2Te_6$ samples: (*1*) undoped and (*2–7*) doped with gadolinium for $N_{Gd}(\times 10^{18}, cm^{-3})$ = (*2*) 0.55, (*3*) 2.8, (*4*) 5.0, (*5*) 12.6, (*6*) 15.8, and (*7*) 23.0; the dependence of the specific energy Δ_0 on the gadolinium concentration N_{Gd} is shown in the insert.

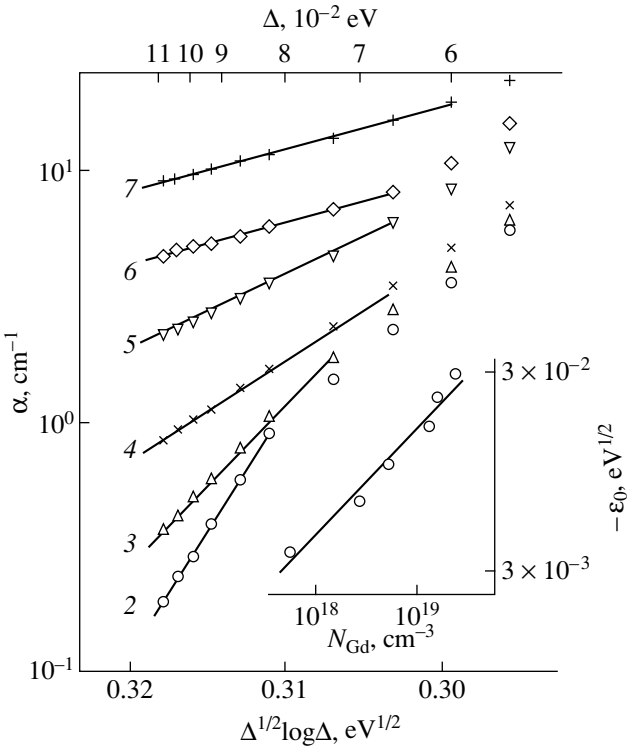

Fig. 2. Dependence of the absorption coefficient α on $\Delta^{1/2}\log\Delta$ for the same samples as in Fig. 1. Dependence of $\varepsilon_0 = -d(\Delta^{1/2}\ln\Delta)d\ln\alpha$ on the gadolinium concentration N_{Gd} is shown in the insert. The labels of curves *2–7* are the same as in Fig. 1.

where e is the elementary charge, r_0 is the screening radius, κ is the permittivity, and N is the impurity concentration.

It follows from Eq. (1) that large-scale fluctuations, which form a smoothly varying potential, influence the density of states. It is shown in [4] that the absorption coefficient in the region where the Uhrbach rule is fulfilled is not proportional to the density of states (Eq. 1) but decreases in accordance with the law

$$\ln[\alpha(\Delta)/\alpha(0)] = -\beta(\Delta/E_B)^{5/4}/(Na^3)^{1/2}, \qquad (2)$$

where β is a numerical factor, E_B is the ionization energy of an isolated impurity, and a is the effective Bohr radius. Equation (2) is similar to the experimentally obtained Uhrbach rule:

$$\alpha(\Delta) \propto \exp(-\Delta/\Delta_0),$$

because the $\Delta^{5/4}$ dependence in a narrow range of frequencies does not differ from the linear. Actually, the dependences $\alpha(\Delta)$ (Fig. 1), plotted in coordinates $\ln\alpha$ versus $\Delta^{5/4}$ in the region of the Uhrbach law, are linear in accordance with formula (2).

It can be seen from Fig. 1 that, for the large values Δ = 0.06–0.11 eV and in the region of comparatively small α, the dependences $\ln\alpha = f(h\nu)$ are less steep and do not follow the Uhrbach rule. As we go deeper into the band gap, the small-scale fluctuations (small in comparison with r_0) become important, because fluctuation size decreases as ε increases, and a major contribution to the density of states is made by the impurity aggregates of the atomic type [4]. In this case, the density of states in the energy gap decreases with increasing energy and follows the law

$$\ln\rho(\varepsilon) \propto -\varepsilon^{1/2}\ln\varepsilon.$$

The absorption coefficient in the deep tail of the dependence $\rho(\varepsilon)$ is proportional to the density of states and is described by the formula

$$\ln[\alpha(\Delta)/\alpha(0)] = -(\Delta/E_B)^{1/2}\ln[(\Delta/E_B)^2/(Na^3)]. \quad (3)$$

The nonlinear portions of $\ln\alpha = f(h\nu)$ dependence in the range Δ = (0.06–0.11) eV (Fig. 1) become linear if we plot them in the coordinates $\ln\alpha$ versus $\Delta^{1/2}\ln\Delta$ as shown in Fig. 2. The slopes of these linear segments

$\varepsilon_0 = -d(\Delta^{1/2}\ln\Delta)/d\ln\alpha$ (see insert in Fig. 2), increase with the gadolinium concentration in the samples. It should be noted that the concentration of N_{Gd} is not identical to the quantity N in formulas (2) and (3), in which N is the total concentration of donors and acceptors. The latter concentration in $Hg_3In_2Te_6$:Gd should depend on N_{Gd} in the case of self-compensation, but may appreciably exceed the gadolinium concentration in the samples. It is impossible to determine N in a multicomponent semiconductor with a high concentration of SVs. Nevertheless, experimental data do not contradict formulas (2) and (3).

In the region of transparency ($0.62 \gtrsim h\nu > 0.05$ eV), the absorption coefficient increases as the dopant concentration increases and, at the same time, remains independent of the wavelength λ. In this case, absorption of light by the free carriers does not appear in the spectra $\alpha(\lambda) = \text{const}$. We succeeded in explaining the transparency decrease defined by the additional absorption, by assuming the occurrence of the well-known small-angle light scattering by inhomogeneities formed by charged impurity aggregates [9]. Such microdefects may be surrounded by elastic stress regions and by regions of the screening space charge. If there are inclusions with electron concentrations different from that of the matrix, the scattering intensity is independent of the wavelength and is proportional to the product $C(\Delta\kappa)^2$ (C is the inclusion concentration, $\Delta\kappa$ is the difference between the permittivities of inclusions and matrix). In the case of $Hg_3In_2Te_6$, the concentration of these inclusions is directly related to the gadolinium content in the samples. Scattering of light by inclusions causes a decrease in the transmission coefficient.

Thus, as the doping level increases, interaction of the gadolinium impurity with the native defects of $Hg_3In_2Te_6$ crystals leads to an increase in the potential fluctuation and, as a result, to an increase in the tail width of the density of states in the energy gap. Pinning of the Fermi level near the middle of the energy gap is defined by the symmetric corrugation of the conduction and valence band edges.

REFERENCES

1. V. F. Masterov and L. F. Zakharenkov, Fiz. Tekh. Poluprovodn. (Leningrad) **24**, 610 (1990) [Sov. Phys. Semicond. **24**, 383 (1990)].
2. G. G. Grushka, A. P. Bakhtinov, and Z. M. Grushka, J. Adv. Mater. **4** (1), 36 (1997).
3. O. G. Grushka, Z. M. Grushka, V. M. Frasunyak, and V. S. Gerasimenko, Fiz. Tekh. Poluprovodn. (St. Petersburg) **33**, 1416 (1999) [Semiconductors **33**, 1272 (1999)].
4. B. I. Shklovskiĭ and A. L. Éfros, *Electronic Properties of Doped Semiconductors* (Nauka, Moscow, 1979; Springer-Verlag, New York, 1984).
5. I. A. Drapkin and B. Ya. Moĭzhes, Fiz. Tekh. Poluprovodn. (Leningrad) **15**, 625 (1981) [Sov. Phys. Semicond. **15**, 357 (1981)].
6. B. L. Gel'mont, V. I. Perel', and I. N. Yassievich, Fiz. Tverd. Tela (Leningrad) **25**, 727 (1983) [Sov. Phys. Solid State **25**, 415 (1983)].
7. É. Z. Imamov and B. R. Mamatkulov, Fiz. Tekh. Poluprovodn. (Leningrad) **15**, 1800 (1981) [Sov. Phys. Semicond. **15**, 1044 (1981)].
8. Yu. A. Astrov and L. M. Portsel', Fiz. Tekh. Poluprovodn. (Leningrad) **17**, 1342 (1983) [Sov. Phys. Semicond. **17**, 851 (1983)].
9. V. V. Voronkov, G. I. Voronkova, and B. V. Zubkov, Fiz. Tverd. Tela (Leningrad) **23**, 117 (1981) [Sov. Phys. Solid State **23**, 65 (1981)].

Translated by I. Kucherenko

Semiconductors, Vol. 34, No. 10, 2000, pp. 1151–1156. Translated from Fizika i Tekhnika Poluprovodnikov, Vol. 34, No. 10, 2000, pp. 1201–1207.

ELECTRONIC AND OPTICAL PROPERTIES OF SEMICONDUCTORS

Comparison of the Polarizations of the 1.2-eV Photoluminescence Band in *n*-GaAs:Te under Uniaxial Pressure and Resonance Polarized Excitation

A. A. Gutkin, M. A. Reshchikov, and V. E. Sedov

Ioffe Physicotechnical Institute, Russian Academy of Sciences, Politekhnicheskaya ul. 26, St. Petersburg, 194021 Russia

Submitted April 17, 2000; accepted for publication April 17, 2000

Abstract—It is shown that the photoluminescence (PL) band at 1.2 eV in *n*-GaAs:Te, which is associated with emission from $V_{Ga}Te_{As}$ complexes with reorienting Jahn–Teller distortions, also includes a contribution from nonreorienting defects. The optical dipole parameters are almost the same for both types of defects. Expressions relating the polarization of the PL band at 1.2 eV under uniaxial pressure and polarized resonant excitation to dipole parameters and to relative contributions to emission from reorienting and nonreorienting defects are derived. A procedure is developed for evaluating these characteristics by analyzing experimental data, and the contributions from each kind of defects to the PL band at 1.2 eV were found to be comparable, even though they vary from sample to sample. The obtained angles characterizing the position of the axes of optical dipoles associated with the defects in light-absorbing and light-emitting states indicate that, in the former state, the effects of donors and the Jahn–Teller distortion on the vacancy orbitals of the $V_{Ga}Te_{As}$ complex are comparable, while in the latter, the effect of distortion is dominant. © *2000 MAIK "Nauka/Interperiodica".*

1. INTRODUCTION

As is known, a broad photoluminescence (PL) band peaked at a photon energy of 1.2 eV in Czochralski-grown *n*-GaAs:Te is related to complexes consisting of a gallium vacancy (V_{Ga}) and a tellurium atom in place of arsenic (Te_{As}) at neighboring lattice sites [1–5]. It is believed that this band is due to radiative recombination of a hole captured by the complex and an electron from the conduction band or a shallow level (excited state) near the conduction band bottom. This interpretation of the 1.2-eV PL band was first proposed by Williams [1, 2] on the basis of similar behavior of this band and the PL related to complexes composed of a cation vacancy and a shallow donor in ZnS.

Investigations of the piezospectroscopic properties of the 1.2-eV emission band and its polarization under resonant polarized excitation [6–9] revealed distortions in the complex associated with this band which lower its initially trigonal symmetry to monoclinic. These distortions have several equivalent orientations for each defect, and their alignment occurs under the action of uniaxial pressure at low temperatures. Phenomena of this kind, caused by the Jahn–Teller effect and previously observed by magnetic resonance for complexes composed of a vacancy and a shallow-level donor in silicon [10, 11], qualitatively confirm the above interpretation of the origin of the 1.2-eV PL band in *n*-GaAs:Te.

At the same time, as reported recently in [12], the contribution to the band in question comes from defects in which no distortion alignment occurs under uniaxial pressure. However, it may be assumed that the optical characteristics of these defects are close to those of complexes with aligning distortions. This makes it possible to use the two-dipole approximation to quantitatively compare the data obtained in experimental studies of the 1.2-eV PL band by piezospectroscopy and polarized PL. The comparison makes it possible to evaluate the contributions of the above kinds of defects to luminescence and to determine the parameters of the optical dipoles describing the emitting and absorbing states of the defects and furnishing information about the relative roles of various intracenter interactions.

The aim of this study was to develop a procedure for obtaining this kind of information and evaluating the characteristics of the emitting and absorbing states of complexes responsible for the 1.2-eV PL band in *n*-GaAs:Te.

2. EXPERIMENTAL RESULTS AND THEIR QUALITATIVE COMPARISON

As established in [6, 8], a uniaxial pressure P applied along crystallographic directions [111] or [110] at temperatures T = 2–4.2 K aligns distortions of the complexes responsible for the 1.2-eV PL band in *n*-GaAs:Te. This alignment results in a steplike increase in the linear polarization of the luminescence from the complex when the pressure is raised. This increase sets in at $P = 0$ and is complete when the splitting of the energy levels corresponding to different complex configurations (equivalent at $P = 0$) starts to substantially exceed both the kT value and similar split-

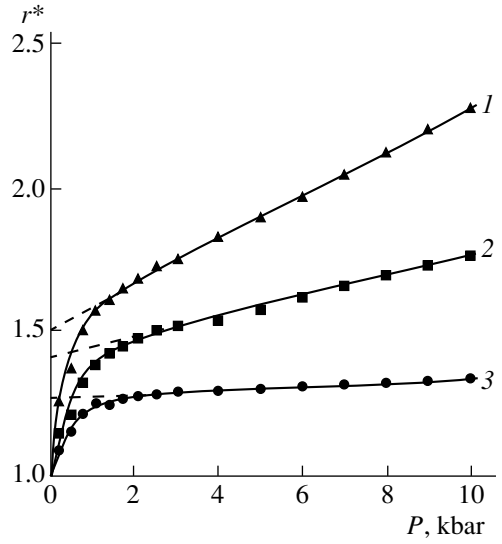

Fig. 1. Integral polarization ratio r^* for the 1.2-eV PL band in *n*-GaAs:Te vs. uniaxial pressure P along the [111] axis; $T = 2$ K. Electron concentration $n = (1, 3)\ 10 \times 10^{17}$ and $(2)\ 5 \times 10^{17}$ cm^{-3}. Sample numbers correspond to those of the curves.

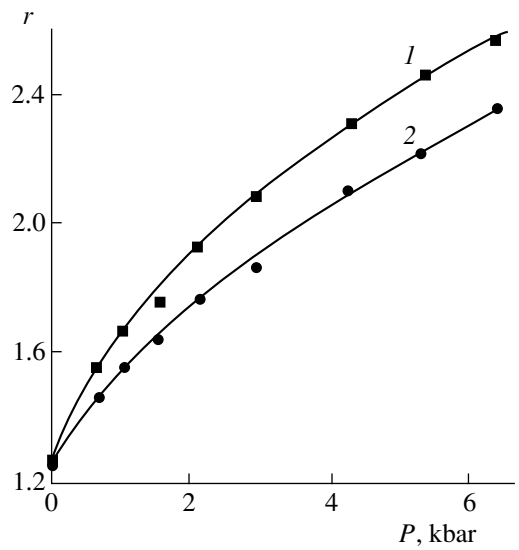

Fig. 2. Polarization ratio r vs. uniaxial pressure P along the [110] axis under polarized resonance excitation of the 1.2-eV PL band in *n*-GaAs:Te. Sample numbers: (*1*) 4 and (*2*) 5; $\hbar\omega_{PL} = 1.2$ eV, $\hbar\omega_{ex} = 1.43$ eV. Excitation direction, [001]; PL observation direction, $[1\bar{1}0]$.

ting in the random electric and deformation fields in the crystal. Dependences of this kind are shown in Fig. 1 for the integral polarization ratio r^* for the 1.2-eV PL band (ratio of total emission intensities with electric vectors parallel and perpendicular to the pressure axis) for several samples cut from various Czochralski-grown *n*-GaAs:Te crystals. The PL was excited with light corresponding to the fundamental absorption band of GaAs, and the experimental procedure was similar to that used previously [6]. The gradual increase in r^* with increasing pressure, observed together with the steplike behavior in the $r^*(P)$ dependences (Fig. 1), may be due to pressure-induced changes in the electronic states of the defects [13]. For this reason, the integral emission polarization r^*, which is associated solely with the maximum alignment of complex distortions possible at a given pressure direction (r_m), can be obtained by extrapolating the $r^*(P)$ dependence at high pressures to $P = 0$, as shown in Fig. 1.

According to the data reported in earlier publications [6, 7], the extrapolated integral polarization ratio r_1 determined by the alignment of distortions at $P \parallel [111]$ is approximately 1.5 in the case of interband excitation of PL. For $P \parallel [110]$ and a direction of PL observation coinciding with the $[1\bar{1}0]$ or [001] axis, the respective polarization ratios (r_2 or r_3) were approximately 1.37 and 1.95. These values may vary substantially from crystal to crystal, as do the $r^*(P)$ values (Fig. 1). A similar difference was also observed in the case of 1.2-eV PL excitation in *n*-GaAs:Te, with electron transitions from the defects to the conduction band (the resonance excitation) being studied (Fig. 2).

At the same time, the emission polarizations under resonance polarized excitation, measured [9, 14] in an orthogonal experimental configuration for $P = 0$, were practically the same for all samples within experimental accuracy. This can be seen (Fig. 3) from the results obtained in the measurements of the degree of 1.2-eV PL polarization for *n*-GaAs:Te samples with different electron concentrations under resonance excitation with linearly polarized light. The degrees of PL polarization ρ_1 and ρ_2 with respect to the axis perpendicular to the propagation directions of the exciting radiation and observed emission correspond to the experimental configurations $[1\bar{1}0]$–[001] and [100]–[010] (first the direction of the exciting light flux and then the direction of the PL observation is given) and exciting-light polarizations along the [110] and [001] axes, respectively. A similar equality of emission polarizations under resonance polarized excitation and $P = 0$ can be seen for two samples in Fig. 2.

The degree of emission polarization in a given experimental configuration under polarized resonance excitation and $P = 0$ is determined only by the parameters of light-emitting and light-absorbing dipoles (namely, by their direction in a local coordinate system that is linked to a defect and depends on its orientation in the lattice, and by the relative contributions of the rotator and the linear oscillator to the emission and absorption of light by a separate dipole [15, 16]). For this reason, the data in Figs.1–3 suggest that the PL band at 1.2 eV in *n*-GaAs:Te is related to two kinds of defects described by optical dipoles with similar parameters. The emission and absorption spectra of

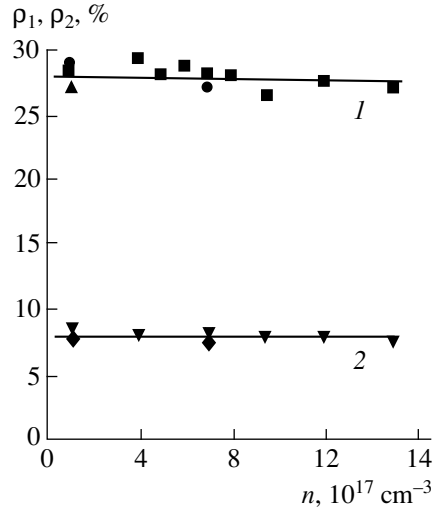

Fig. 3. Degree of polarization of the 1.2-eV PL band in various *n*-GaAs:Te samples under resonance excitation with linearly polarized light; T = 77 K, $\hbar\omega_{ex}$ = 1.43 eV; (*1*) corresponds to ρ_1 and (*2*) to ρ_2.

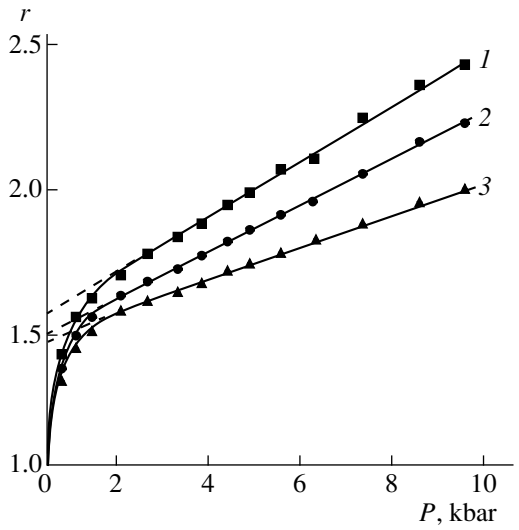

Fig. 4. PL polarization ratio r for different photon energies in the PL band of *n*-GaAs:Te as a function of pressure P. Sample 1, T = 2 K, $\hbar\omega_{PL}$ = (*1*) 1.15, (*2*) 1.175, and (*3*) 1.20 eV.

these defects are also similar. However, defects of the first type possess distortions that can change their orientation at low temperatures and align under the action of relatively low pressures along the directions [111] and [110], whereas no such alignment occurs in defects of the second type. Thus, the difference in the $r^*(P)$ polarization of the 1.2-eV PL band between different samples is due to the unequal relative concentrations of these types of defects.

It should also be noted that extrapolating the pressure dependence of the luminescence polarization ratio to $P = 0$ for a certain photon energy $\hbar\omega$ from the 1.2 eV band, $r(\hbar\omega, P)$, yields a value $r_i(\hbar\omega, 0)$ which decreases somewhat with increasing $\hbar\omega$ (Fig. 4). This indicates that the emission band associated with defects characterized by aligning distortions is shifted to lower photon energies with respect to the emission band related to nonreorienting defects.

3. MODEL FOR QUANTITATIVE ANALYSIS OF THE 1.2-eV PL BAND

It seems reasonable to assume, on the basis of [1, 2, 10, 11] and the results of an analysis qualitatively explaining the piezospectral and polarization properties of the 1.2-eV PL band, that the defects with reorienting distortions are isolated $V_{Ga}Te_{As}$ complexes containing Te in the first coordination sphere of V_{Ga}. According to [6, 17–19], this initially trigonal defect is distorted in the emitting and absorbing states by the Jahn–Teller effect and has a monoclinic symmetry. The symmetry plane of the complex is a plane of the {110} type containing V_{Ga}, Te_{As}, and one of three As atoms nearest to V_{Ga} (Fig. 5). For any complex there exist three such planes and, consequently, three possible orientations of the Jahn–Teller distortion. The optical dipole axis of such a complex lies in its symmetry plane, and the position of the axis is defined by an angle φ measured from the [110] direction also lying in the symmetry plane of the complex (Fig. 5). Where the complex's distortion is reoriented, its symmetry plane changes and, correspondingly, the direction of the dipole axis also changes, however, the angle φ remains the same. All four possible positions of the Te_{As} donor with respect to V_{Ga} are equiprobable; and, at $P = 0$, all three distortion orientations are equiprobable also. Therefore, for $P = 0$, the entire set of reorienting $V_{Ga}Te_{As}$ complexes will be described by a set of 12 dipoles with axes lying in planes of the {110} kind, as shown in Fig. 5. These dipoles may be different in the light-absorbing and light-emitting states of the defect. Taking this into account in calculating the optical properties of this kind of system, we use a two-dipole approximation; i.e., we assume that, in the case of light absorption, the optical dipole is described by angle φ_1 and by the relative rotator contribution μ_1, and in the emission, by φ_2 and μ_2, respectively [15, 16].

According to the preceding section, the same set of absorbing and emitting dipoles can be used for an approximate description of a system of nonreorienting defects. Then, for $P = 0$, the reorienting and nonreorienting defects are indistinguishable and constitute a uniform set of defects. On considering this system, we can readily find that the degrees of PL polarization under resonance excitation with an electric vector perpendicular to the plane containing the PL excitation and observation directions in the experimental configura-

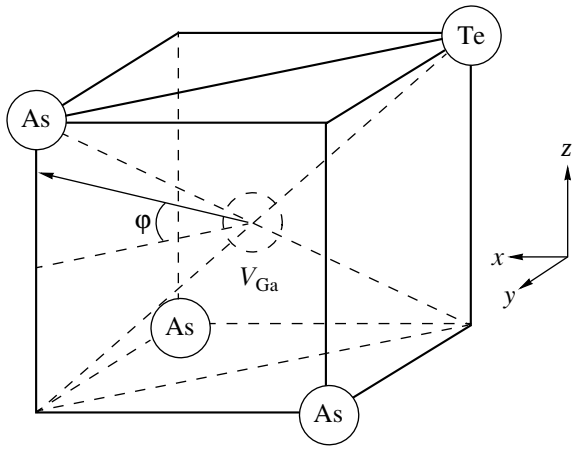

Fig. 5. Optical-dipole axis direction for a $V_{Ga}Te_{As}$ complex in one of its possible symmetry planes.

tions $[1\bar{1}0]$–[001] and [100]–[010] are given, respectively, by

$$\rho_1 = [2\cos\varphi_1\cos\varphi_2(\cos\varphi_1\cos\varphi_2 + 4\sin\varphi_1\sin\varphi_2) \times (1-2\mu_1)(1-2\mu_2)]/R, \quad (1)$$

$$\rho_2 = [(3\cos^2\varphi_1 - 2)(3\cos^2\varphi_2 - 2) \times (1-2\mu_1)(1-2\mu_2)]/R, \quad (2)$$

where the denominator

$$R = [2-(1-2\mu_1)\cos^2\varphi_1][2-(1-2\mu_2)\cos^2\varphi_2] + 2[2\mu_1 + (1-2\mu_1)\cos^2\varphi_1][2\mu_2 + (1-2\mu_2)\cos^2\varphi_2].$$

When the electric vector of the exciting light is aligned with the observation direction, the emission is unpolarized.

We now consider emission polarization for a uniaxial pressure. Let A be the relative number of reorienting defects capturing holes in PL excitation via interband transitions, in the total number of defects contributing to the 1.2-eV PL band. Analysis of the 1.2-eV PL band in *n*-GaAs:Te under polarized resonance excitation in the single-dipole approximation [17] shows that the contribution of the linear oscillator to the optical properties exceeds that of the rotator, and that the optical dipole axis of the defects responsible for the emission is not significantly tilted with respect to the ⟨111⟩ direction that does not coincide with the initial axis of the V_{Ga}–Te_{As} defects. In addition, as demonstrated by experiments at liquid-helium temperatures, applying a uniaxial pressure along the direction [111] or [110] causes a drastic increase in PL polarization with respect to the pressure axis (see, e.g., Fig. 1 and [6, 7]). These facts suggest that the configurations of reorienting defects in which the optical-dipole axis makes the smallest angle with the pressure axis start to be dominant as a result of alignment, since their energy becomes lower than the energies of other configurations.

Then, on considering sets of AN reorienting and $(1-A)N$ nonreorienting defects with monoclinic symmetry, we find that, for interband excitation, the integral PL polarization ratio r_1 associated with the distortion alignment at $P \parallel [111]$ is given by

$$r_1 = \frac{2(1+\mu_2) + 2A(\sqrt{2}\sin\varphi_2 + \cos\varphi_2)(1-2\mu_2)\cos\varphi_2}{2(1+\mu_2) - A(\sqrt{2}\sin\varphi_2 + \cos\varphi_2)(1-2\mu_2)\cos\varphi_2}. \quad (3)$$

For $P \parallel [110]$ and PL observed along the $[1\bar{1}0]$ or [001] axis, the analogous polarization ratios r_2 and r_3 are

$$r_2 = Q/[8(1+\mu_2) + 2A(3\sin^2\varphi_2 - 1)(1-2\mu_2)], \quad (4)$$

$$r_3 = Q/[8(1+\mu_2) - A(5\cos^2\varphi_2 + 6\sqrt{2}\sin\varphi_2\cos\varphi_2 + 2\sin^2\varphi_2)(1-2\mu_2)], \quad (5)$$

with the numerator

$$Q = 8(1+\mu_2) + A(7\cos^2\varphi_2 + 6\sqrt{2}\sin\varphi_2\cos\varphi_2 - 2\sin^2\varphi_2)(1-2\mu_2).$$

4. EVALUATION OF OPTICAL-DIPOLE PARAMETERS

By transforming each of the Eqs. (3)–(5), we readily obtain

$$A\frac{1-2\mu_2}{1+\mu_2} = \frac{r_1-1}{r_1+2}\frac{2}{(\sqrt{2}\sin\varphi_2 + \cos\varphi_2)\cos\varphi_2}, \quad (6)$$

$$A\frac{1-2\mu_2}{1+\mu_2} = \frac{8(r_2-1)}{B - 2r_2(3\sin^2\varphi_2 - 1)}, \quad (7)$$

$$A\frac{1-2\mu_2}{1+\mu_2} = \frac{8(r_3-1)}{B + r_3(5\cos^2\varphi_2 + 6\sqrt{2}\sin\varphi_2\cos\varphi_2 + 2\sin^2\varphi_2)}, \quad (8)$$

where

$$B = 7\cos^2\varphi_2 + 6\sqrt{2}\sin\varphi_2\cos\varphi_2 - 2\sin^2\varphi_2.$$

When measuring the r_2 and r_3 values, we used a single sample in the form of a rectangular parallelepiped whose faces corresponded to the (110), $(1\bar{1}0)$, and (001) planes [6, 7]. Therefore, the relative contributions of reorienting defects are the same for these measurements. Then, equating the right-hand parts of equalities (7) and (8), we obtain an equation for determining φ_2 corresponding to the measured values of r_2 and r_3. Substitution of $r_2 \simeq 1.37$ and $r_3 \simeq 1.95$ [6, 7] into this equa-

tion yields the solution $\varphi_2 \simeq 28°40'$. The other solution, $\varphi_2 \simeq 145°$, cannot satisfy equality (6) for the experimental values r_1 = 1.3–1.5 (Fig. 1 and [6, 7]), since $0 \le A \le 1$ and $0 \le \mu_2 \le 1$ by definition. The physical significance of this result consists in the following. For $\varphi_2 \simeq 145°$, the optical dipole axis in any configuration is close to the initial trigonal axis of the reorienting V_{Ga}–Te_{As} complex, and the pressure-induced transition of these complexes to a configuration with lower energy (distortion alignment) has only a slight effect on the overall polarization of the emission from the entire system; i.e., r_1 must remain close to unity (less than 1.3) even for $A = 1$ and $\mu_2 = 0$.

On the other hand, by solving the system of equalities (1) and (2) for φ_1 and μ_1, we obtain

$$\tan\varphi_1 = \frac{\tan\varphi_2 \pm \sqrt{\tan^2\varphi_2 + \frac{\rho_1}{\rho_2}(2\tan^2\varphi_2 - 1)\left[1 + \frac{\rho_1}{\rho_2}(2\tan^2\varphi_2 - 1)\right]}}{\frac{\rho_1}{\rho_2}(2\tan^2\varphi_2 - 1)}, \quad (9)$$

$$\mu_1 = \frac{1}{2} - \frac{3(1+\mu_2)}{2(1+\mu_2) + C(1-2\mu_2)}, \quad (10)$$

where

$$C = \left[3 - \frac{\rho_2}{\rho_1}\cos\varphi_1\cos\varphi_2(\cos\varphi_1\cos\varphi_2 + 4\sin\varphi_1\sin\varphi_2)\right].$$

Substitution of $\rho_1 \simeq 0.28$ and $\rho_2 \simeq 0.08$ (Fig. 3) and the value $\varphi_2 \simeq 28°40'$ obtained above into (9) yields two values of φ_1: 8°55′ and 137°. The use of these two values in expression (10) shows that the condition $0 \le \mu_1 \le 1$ at $0 \le \mu_2 \le 1$ is satisfied by the value $\varphi_1 = 8°55'$. It follows from (10) that

$$\mu_1 = \frac{0.91 - 3.5\mu_2}{3.5 - 5.32\mu_2}. \quad (11)$$

In view of the restrictions imposed on μ_1 and μ_2 by definition, it follows from this formula that μ_1 falls within the range 0–0.26 and μ_2, correspondingly, falls within 0.26–0. Thus, the dipoles describing the polarization properties of the 1.2-eV emission band in *n*-GaAs:Te are characterized by the following parameters:

$$\varphi_1 \simeq 9°, \quad \mu_1 = 0\text{–}0.26, \quad \varphi_2 \simeq 29°, \quad \mu_2 = 0.26\text{–}0.$$

The fraction of reorienting defects A can be evaluated for each of the samples using (6), (7), or (8); experimental values of r_1, r_2, or r_3; and estimates of μ_2 and φ_2. For the sample for which r_2 and r_3 were measured in [6, 7], this yields A = 0.83–0.32. For samples 1–3 in Fig. 1, the A values fall within 0.55–0.21, 0.44–0.17, and 0.31–0.11, respectively.

5. DISCUSSION AND CONCLUSION

We note in the first place that the above analysis of PL polarization made it possible to uniquely determine the positions of optical dipole axes in the emitting and absorbing states of the defects being studied, despite the fact that the equations used for this purpose have several real solutions.

The results indicate that the axes of the dipoles describing the absorption and emission of light are markedly different and in both cases are tilted appreciably with respect to the direction of the initial trigonal axis of the $V_{Ga}Te_{As}$ complex. Such behavior is associated with the static Jahn–Teller effect. Indeed, if this effect and the resulting three equivalent monoclinic configurations are lacking, the optical dipole axis must coincide with the trigonal axis of the V_{Ga}–Te_{As} complex. Otherwise, if the donor influence in the complex is negligible compared with the Jahn–Teller interaction, the behavior of the complex becomes similar to that of an isolated V_{Ga} vacancy which is distorted trigonally by the Jahn–Teller effect [20]. Hence, it follows that in this case the direction of the optical dipole axis in each of the three equivalent configurations must tend to one of the ⟨111⟩ axes of the crystal not coinciding with the V_{Ga}–Te_{As} axis. Thus, the optical dipole direction furnishes qualitative information about the relative roles of the donor and the Jahn–Teller effect in determining the electronic structure of the complex.

The value $\varphi_1 \simeq 9°$ determined in the preceding section indicates that the effects of the donor and the Jahn–Teller distortion are comparable, even though the former somewhat exceeds the latter [the optical dipole axis is tilted at considerable angles with respect to both the V_{Ga}–Te_{As} axis and another trigonal axis lying in the symmetry plane (Fig. 5), although it is somewhat closer to the latter]. This conclusion agrees with the results of [19], where the relative contributions from the donor and Jahn–Teller effect were evaluated from the energy splitting of Jahn–Teller configurations under uniaxial pressures.

In contrast to the absorbing state, the emitting state, which is characterized by a dipole with an axis close to that of the trigonal Jahn–Teller distortion of an isolated vacancy ($\varphi_1 \simeq 29°$), is influenced to a much greater extent by the Jahn–Teller effect. This distinction is consistent with the general concepts of the magnitude of the Jahn–Teller effect and the possible number of holes localized at the vacancy orbitals of the $V_{Ga}Te_{As}$ complex in the light-emitting and light-absorbing states [19] and is confirmed by the existence of low-temperature reorientations of the complex distortions in the absorbing state only [18].

The nature of nonreorienting complexes is unknown. The similarity of their characteristics to those of the reorienting complexes suggests that these defects also contain V_{Ga} and a donor and also bind a hole at the vacancy state. These conditions are satisfied by a defect in which the donor (Te_{As}) is not at the anion-sublattice site nearest to V_{Ga}, but at the next nearest site. It is also possible that there is one more donor or another defect at close range (at the same kind of site).[1]

The low initial symmetry of defects of this kind and a rather strong influence of donors located at small distances from V_{Ga} may lead to a strong energy splitting of the previously equivalent Jahn–Teller configurations and to the absence of reorientations even under uniaxial pressure. Since the effect of the donor is not dominant, the emission and absorption spectra of such a defect are presumably close to the spectra of the initially trigonal $V_{Ga}Te_{As}$ complex. Indeed, as follows from [8, 22], the emission and absorption spectra of the $V_{Ga}Sn_{Ga}$, $V_{Ga}Si_{Ga}$, and $V_{Ga}Te_{As}$ complexes almost coincide, although in the first two defects the donor occupies the cation-sublattice site and is therefore more remote from V_{Ga}. Identical emission spectra have also been observed in ZnSe for the Frenkel pairs V_{Zn}–Zn_i, in which Zn_i was in different (but close to V_{Zn}) interstitial sites [23]. However, the possibility of the existence of these defects in rather high concentrations in *n*-GaAs:Te crystals being studied is unclear and requires further investigation.

ACKNOWLEDGMENTS

The study was supported by the Russian Foundation for Basic Research, project no. 98-02-18327.

REFERENCES

1. E. W. Williams, Phys. Rev. **168**, 922 (1968).
2. E. W. Williams and H. B. Bebb, Semicond. Semimet. **8**, 321 (1972).
3. F. M. Vorobkalo, K. D. Glinchuk, and A. V. Prokhorovich, Fiz. Tekh. Poluprovodn. (Leningrad) **7**, 896 (1973) [Sov. Phys. Semicond. **7**, 610 (1973)].
4. H. G. Guislain, L. De Wolf, and P. Clauws, J. Electron. Mater. **7**, 83 (1978).
5. I. Ya. Buyanova, S. S. Ostapenko, and M. K. Sheĭnkman, Fiz. Tverd. Tela (Leningrad) **27**, 748 (1985) [Sov. Phys. Solid State **27**, 461 (1985)].
6. N. S. Averkiev, A. A. Gutkin, E. B. Osipov, *et al.*, Fiz. Tekh. Poluprovodn. (St. Petersburg) **26**, 1269 (1992) [Sov. Phys. Semicond. **26**, 708 (1992)].
7. A. Gutkin, M. Reshchikov, V. Sedov, and V. Sosnovski, Proc. Est. Acad. Sci. Phys. Math. **44**, 212 (1995).
8. A. A. Gutkin, N. S. Averkiev, M. A. Reshchikov, and V. E. Sedov, in *Proceedings of the 18th International Conference on Defects in Semiconductors, Sendai, Japan, July 23–28, 1995*, Ed. by M. Suezawa, H. Katayama-Yoshida; Mater. Sci. Forum **196**–**201** (1), 231 (1995).
9. N. S. Averkiev, A. A. Gutkin, E. B. Osipov, *et al.*, in *Proceedings of the 1st National Conference on Defects in Semiconductors, St. Petersburg, April 26–30, 1992*, Ed. by N. T. Bagraev; Defect Diffus. Forum **103**–**106**, 31 (1993).
10. G. D. Watkins and J. W. Corbett, Phys. Rev. A **134**, 1359 (1964).
11. E. L. Elkin and G. D. Watkins, Phys. Rev. **174**, 881 (1968).
12. A. A. Gutkin, M. A. Reshchikov, and V. E. Sedov, in *Proceedings of the International Conference "Physical Processes in Unordered Semiconductor Structures"* (Ul'yanovsk. Gos. Univ., Ul'yanovsk, 1999), p. 12.
13. N. S. Averkiev, A. A. Gutkin, E. B. Osipov, *et al.*, Fiz. Tekh. Poluprovodn. (Leningrad) **25**, 58 (1991) [Sov. Phys. Semicond. **25**, 33 (1991)].
14. N. S. Averkiev, A. A. Gutkin, E. B. Osipov, *et al.*, Fiz. Tekh. Poluprovodn. (Leningrad) **25**, 50 (1991) [Sov. Phys. Semicond. **25**, 28 (1991)].
15. P. P. Feofilov, *The Physical Basis of Polarized Emission: Polarized Luminescence of Atoms, Molecules, and Crystals* (Fizmatgiz, Moscow, 1959; Consultants Bureau, New York, 1961).
16. E. E. Bukke, N. N. Grigor'ev, and M. V. Fok, Tr. Fiz. Inst. Akad. Nauk SSSR **79**, 108 (1974).
17. A. A. Gutkin, M. A. Reshchikov, and V. E. Sedov, Fiz. Tekh. Poluprovodn. (St. Petersburg) **31**, 1062 (1997) [Semiconductors **31**, 908 (1997)].
18. A. A. Gutkin, M. A. Reshchikov, and V. E. Sedov, Z. Phys. Chem. (Munich) **200**, 217 (1997).
19. N. S. Averkiev, A. A. Gutkin, and M. A. Reshchikov, Fiz. Tekh. Poluprovodn. (St. Petersburg) **33**, 1323 (1999) [Semiconductors **33**, 1196 (1999)].
20. Y. Q. Jia, H. J. von Bardeleben, D. Stievenard, and C. Delerue, Phys. Rev. B **45**, 1645 (1992).
21. V. I. Vovnenko, K. D. Glinchuk, and A. V. Prokhorovich, Fiz. Tekh. Poluprovodn. (Leningrad) **10**, 1097 (1976) [Sov. Phys. Semicond. **10**, 652 (1976)].
22. N. S. Averkiev, A. A. Gutkin, M. A. Reshchikov, and V. E. Sedov, Fiz. Tekh. Poluprovodn. (St. Petersburg) **30**, 1123 (1996) [Semiconductors **30**, 595 (1996)].
23. F. C. Rong, W. A. Barry, J. F. Donegan, and G. D. Watkins, Phys. Rev. B **54**, 7779 (1996).

Translated by M. Tagirdzhanov

[1] We note that minor variations of the parameters of the 1.2-eV PL band from sample to sample were explained by assuming that this band is due to various modifications of associations of the $V_{Ga}Te_{As}$ complex with other defects [21].

Semiconductors, Vol. 34, No. 10, 2000, pp. 1157–1160. Translated from Fizika i Tekhnika Poluprovodnikov, Vol. 34, No. 10, 2000, pp. 1208–1211.

ELECTRONIC AND OPTICAL PROPERTIES OF SEMICONDUCTORS

Evolution of the Density of States during Phase Transitions in Films of Cadmium Sulfotellurides Synthesized under Profoundly Nonequilibrium Conditions

A. P. Belyaev, V. P. Rubets, and M. Yu. Nuzhdin

St. Petersburg Institute of Technology, Zagorodnyĭ pr. 49, St. Petersburg, 198013 Russia

Submitted April 11, 2000; accepted for publication April 19, 2000

Abstract—The results of structural, electrical, and photoelectric investigations of phase transitions in layers of cadmium-sulfide and cadmium-telluride solid solutions synthesized under profoundly nonequilibrium conditions are reported. As a model process, the thermally activated decomposition of a CdS_xTe_{1-x} single-phase solution containing the α_1 (x_1 = 0.4–0.6) phase was chosen. Increasing the temperature was shown to result in the formation a heterophase system with two phases α_2 (x_2 = 0.1–0.2) and α_3 (x_3 = 0.78–0.99). The electron diffraction patterns, the photoelectric-current spectrum, and the temperature dependences of the dark electrical conductivity in the course of and after phase transitions are reported. The results of electrical and photoelectric investigations are compared with the results of structural investigations. Changes in the dark conductivity in the course of phase transitions are shown to simultaneously account for the evolution of the density of states near the Fermi level. © *2000 MAIK "Nauka/Interperiodica"*.

1. INTRODUCTION

Electrical properties are known to be extremely sensitive to changes in structure. Therefore, it seems promising to use investigations of these properties to analyze phase-transition processes. Consequently, we report below the results of investigations of the electrical and photoelectric properties during the thermally activated decomposition of films of a cadmium-sulfotelluride solid solution and analyze the possibilities of using them in investigating phase-transition processes.

2. INVESTIGATED SAMPLES AND EXPERIMENTAL PROCEDURE

We investigated the layers of CdS_xTe_{1-x} ($0.4 < x < 0.6$) solid solutions prepared by thermal evaporation and condensation under profoundly nonequilibrium conditions [1]. The choice of the method was dictated by the purpose of the investigation that implies a model object prone to phase transitions. As substrates, we used the laminas of potash mica. The film thickness for all the investigated samples did not exceed a few tenths of μm. The layers were of polycrystalline structure with crystallites of cubic modification both before and after the thermal treatment.

Prior to the electrical measurements, the samples were cut into several parts, and silver contacts were deposited on some of them. The ohmic behavior of the contacts was checked against initial portions of the current–voltage characteristics.

Structural investigations were carried out using an ÉMR-100 electron diffractometer and a PZM-100 electron microscope. Electrical measurements were carried out under the current operating conditions in vacuum (a residual gas pressure of 10^{-3} Pa) using a B7-30 electrometer and a special heat controller making it possible either to maintain a constant temperature (with an accuracy of 0.1 K) or to vary it linearly. The rate of heating and cooling was varied within 0.05–0.2 K/s.

The possibility of measuring the electric field influencing phase transitions was checked by comparing the properties of the samples that experienced phase transitions under the effect of an electric field with properties of the samples subjected to these transitions without a field.

The influence of temperature on the properties of the contacts was tested by comparing electrical properties of samples with the contacts deposited before annealing with the similar properties of samples whose contacts were deposited following thermal treatment.

3. EXPERIMENTAL RESULTS

We investigated the influence of temperature on the structure, the phase composition, and the electrical and photoelectric properties of the solid-solution layers of cadmium sulfotelluride in relation to the temperature-field characteristics.

The main results of the experiment are shown in Figs. 1 and 2.

In Fig. 1, we display the typical electron-diffraction patterns from an as-prepared solid-solution film and a thermally treated film. In Fig. 1, curve *1* is indicative of the presence of only the α_1 phase corresponding to the composition of the solid-solution with x_1 = 0.5 in the

1063-7826/00/3410-1157$20.00

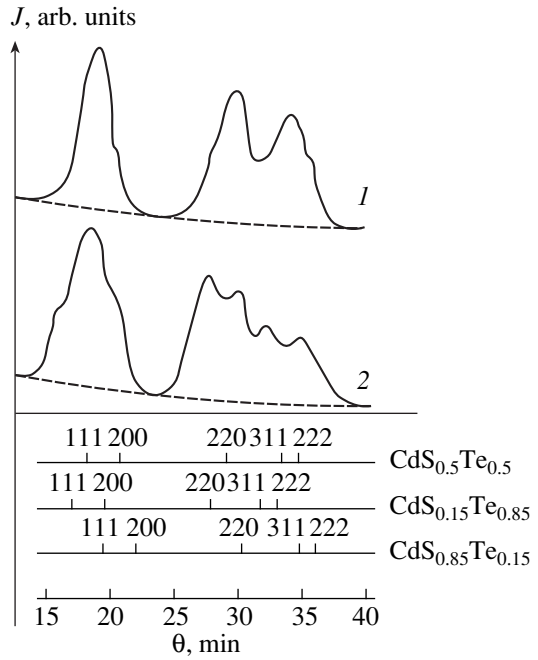

Fig. 1. Electron diffraction patterns of the films of a CdS–CdTe system: curve *1* was recorded before annealing, and curve *2*, after annealing.

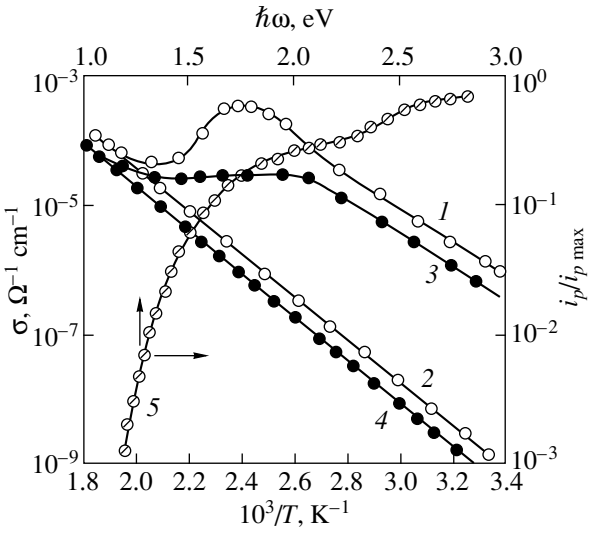

Fig. 2. Variations in the conductivity σ during the phase transitions in the $CdS_{0.5}Te_{0.5}$ layer: curves *1* and *3* correspond to heating with a rate v, curves *2* and *4* show the temperature dependences of the conductivity of the layer after the phase transitions. Curves *1* and *2* correspond to v = 0.05 K/s; curves *3* and *4* correspond to v = 0.2 K/s (the conductivity scale is on the left, and the temperature scale is at the bottom); curve *5* is the typical photoelectric-current spectrum for the $CdS_{0.5}Te_{0.5}$ layer (the current scale is on the right, and the photon-energy scale is at the top).

as-prepared film. Curve *2* obtained for an annealed sample implies the appearance of two phases α_2 and α_3 in the bulk: the CdS_xTe_{1-x} solid solutions with compositions of $x_2 = 0.15$ and $x_3 = 0.85$, respectively.

The phase inhomogeneity in the samples after annealing was also detected from the optical transmission spectrum [2]. The character of the electron-diffraction patterns was independent of the sample-annealing methods used in this study.

In Fig. 2, we show the typical behavior of the electrical conductivity σ of the films in the course of annealing in relation to the heating rate of the samples. Curve *1* shows the dark conductivity for an as-prepared sample heated with a rate of 0.05 K/s. A constant activation energy of about 0.5 eV corresponds to its initial section. At the temperature $T \approx 360$ K, the conductivity-increase rate first grew somewhat with temperature and then decreased rapidly. After that, the temperature dependence of the conductivity was described by a simple exponential curve with an activation energy of 0.72 eV. The indicated exponential temperature dependence was retained further within the entire temperature range under investigation under the subsequent heating and cooling (curve *2*). A simple exponential temperature dependence with the same activation energy for the given sample was also successfully reproduced after subjecting the sample to atmospheric air.

Curves *3* and *4* in Fig. 2 represent the changes in the electrical conductivity of another area of the same CdS_xTe_{1-x} layer, but heated with a rate of 0.2 K/s. Exposing the samples to the highest temperature of heating for several hours leaves their conductivity unchanged at this temperature.

A cumulative result of the thermal treatment was a multifold decrease in the conductivity of layers (for the samples, the results of the investigation of which are displayed in Figs. 1 and 2, this decrease amounts to three orders of magnitude). Samples with similar properties could be produced from the as-prepared layers by "shock" heating using an electron beam.

The influence of the heating rate on the properties of the samples was determined by investigating the photoconductivity. The lower the heating rate, the larger the photoconductivity increase which could be obtained for a sample. For example, part of the sample annealed at a heating rate of 0.5 K/s (Fig. 2, curves *1*, *2*) showed a photoconductivity increase by three orders of magnitude after annealing at room temperature, while a "shock"-heated part was virtually photoinsensitive (undergoing irradiation with a 90-W incandescent lamp). In the as-prepared samples, the increase in photoconductivity is only severalfold.

A typical photoconductivity spectrum of the samples is shown in Fig. 2, curve *5*. Annealing almost did not affect the shape of the photoconductivity spectrum or the absorption spectrum of the samples. The temperature dependences of the photoelectric current had a form characteristic of the monomolecular mode of recombination, and their qualitative shape was invariant under the thermal treatment. The current–illuminance characteristics were linear for all the investigated samples.

4. DISCUSSION OF THE RESULTS

As can be seen from Fig. 1, the as-prepared films represent homogeneous solid solutions containing only the α_1 phase. For the sample whose electron diffraction pattern is shown in Fig. 1, the α_1 phase is the $CdS_{0.5}Te_{0.5}$ solid solution. For other investigated samples, this can be a solid solution with a composition in the range of $x_1 = 0.4$–0.6. According to the equilibrium phase diagram [3], such a composition corresponds to the domain of a limited mutual solubility. Moreover, it corresponds to the part of the domain, where, as might be expected, the absolute loss of solid-solution stability should occur. Consequently, the as-prepared samples represent the metastable systems maintained in the nonequilibrium state by internal potential barriers. The annealing of such systems is found to induce the decomposition of the original solid solution and the formation of a heterogeneous thin-film structure composed of two solid solutions: CdTe-based (α_2) and CdS-based (α_3). Their composition must correspond to the mutual-solubility domains of their components in the equilibrium phase diagram of the system.

The results obtained by us for the CdS–CdTe system are completely consistent with the aforesaid. A mixture of the $\alpha_2 + \alpha_3$ phases was detected in the annealed samples by the electron-diffraction and optical methods. The composition of the α_2 and α_3 phases corresponds to the mutual-solubility domains ($x_2 = 0.1$–0.2; $x_3 = 0.78$–0.99). The subsequent thermal treatments influence neither the electron-diffraction pattern nor the electrical and photoelectric properties. Thus, we can state that, in this study, we actually investigated the process of phase transition of the system (a homogeneous solid solution) from a metastable state to an equilibrium state (a two-phase mixture of solid solutions).

As a rule, the system passes from a metastable state to an equilibrium state due to fluctuations, i.e., by means of the formation and growth of new-phase nuclei. This process takes a certain amount of time. It is reasonable to assume that the conditions taking place during this time must influence both the phase-transition kinetics and the properties of the newly formed phases. This explains the cause of the distinction between the electrical and photoelectric properties of the solid-solution samples annealed at various heating rates. This is related to distinctions in the structure, which cannot be detected by electron diffraction. Consequently, we attempt to analyze the kinetics of the thermally activated decomposition of a homogeneous metastable solid solution on the basis of the electrical properties of this compound.

The condensed solid-solution layers belong to disordered systems [4]. The charge transport proceeds in such systems at high temperatures over the mobility-gap edge and is described by the expression [5]

$$\sigma = \sigma_{min}\exp[-(E_c - E_F)/kT], \quad (1)$$

which is qualitatively consistent with our experimental data. Here, σ_{min} is the minimum metallic conductivity, E_c is the mobility-edge, E_F is the Fermi level, k is the Boltzmann constant, and T is the temperature. The fact that the charge transport takes place over the mobility-gap edge is also confirmed by the results of calculations. According to Mott and Davis [5], a specific test for conduction over the mobility-gap edge is the representation of the experimental conductivity in the form of

$$\sigma = C\exp(-E/kT)$$

with the subsequent calculation of the parameter C. For the samples investigated both before and after annealing, the value of the factor C was on the order of $10^3\ \Omega^{-1}\ cm^{-1}$, which agrees closely with the results obtained by Mott and Davis and with a minimum metallic conductivity σ_{min} in expression (1). Thus, we can state that the charge transport over the mobility-gap edge takes place both during and after the phase transition.

An appreciable change in the dark conductivity during the charge transport over the mobility-gap edge similar to that taking place on annealing the investigated samples is possible only owing to a change in the Fermi-level position. There are two reasons for this fact. The first is a change in the value of the mobility gap; the second is a change in the density of states. No experimental facts supporting the former reason have been revealed. Moreover, investigations of photoconductivity indicate the opposite: neither the photoconductivity spectrum nor absorption spectrum vary on annealing. At the same time, a number of experimental results testify in favor of the latter reason. These include the shape of the photoconductivity spectrum (Fig. 2, curve *5*), the linear current–illuminance characteristic, the dependence of the photoelectric current on annealing conditions, and the stability of the temperature dependence of the photoelectric current with respect to thermal treatments.

Actually, the first two facts imply that the photoelectric current in the investigated samples was monomolecular [5]; i.e.,

$$i_p = eF\mu_D G\tau, \quad (2)$$

where e is the elementary charge, F is the electric-field strength, μ_D is the drift mobility, G is the rate of generation of nonequilibrium charge carriers, and τ is the lifetime of these carriers. In the experiment under discussion, a substantial variation of μ_D is improbable, because the value of μ_D typically specifies the form of the photoelectric-current temperature dependence, which was stable here with respect to the thermal treatment. It only remains for us to consider the lifetime τ. This lifetime is very sensitive to the defect-level concentration near the Fermi level. Consequently, various photoelectric properties of cadmium sulfotellurides are

governed precisely by the density of states near the Fermi level.

Thus, we can state that the photosensitive properties acquired by the samples of cadmium-sulfotelluride solid solutions in the course of their phase transitions are caused by a change in the density of states near the Fermi-level position. In turn, the density of states controls the Fermi-level position. As was shown above, the Fermi-level position specifies the dark conductivity. Therefore, a change in the dark conductivity occurring in cadmium sulfotelluride on annealing (Fig. 2, curves *1*, *3*) also accounts simultaneously for the evolution of the density of states near the Fermi level and the character of variations in the Fermi-level position in the course of phase transitions.

In conclusion, we will make a remark concerning the peak in the temperature dependence of the dark conductivity (Fig. 2, curve *1*). As can be seen from Fig. 2, no peak is observed at high heating rates. We relate this fact to the inertial behavior of our detecting instrumentation. For high heating rates, the rate of formation of new-phase islands turns out to be very high, and is exponentially related to the temperature, which rises fast at high heating rates. As to the time constant of our detecting instrumentation, it amounts to seconds.

5. CONCLUSION

From the results of the investigation carried out, we can conclude the following.

(i) The phase transitions in metastable solid solutions of cadmium sulfotellurides are accompanied by a drastic changes in the density of states near the Fermi level and its subsequent monotone relaxation to the equilibrium concentration.

(ii) The microstructure and the photosensitive properties of the phases formed as a result of the thermally activated phase transition of a metastable solid solution are specified by the temperature-rise rate.

(iii) Variations in the dark conductivity during the thermally activated decomposition of metastable solid solutions simultaneously reflect the features of variations in the Fermi-level position and the features of variations in the density of states during the indicated phase transitions.

ACKNOWLEDGMENTS

This work was supported by the Russian Foundation for Basic Research, project no. 99-03-32676.

REFERENCES

1. A. P. Belyaev, V. P. Rubets, and I. P. Kalinkin, Fiz. Tverd. Tela (St. Petersburg) **39**, 382 (1997) [Phys. Solid State **39**, 333 (1997)].
2. A. P. Belyaev, V. P. Rubets, and I. P. Kalinkin, Fiz. Tekh. Poluprovodn. (St. Petersburg) **31**, 635 (1997) [Semiconductors **31**, 540 (1997)].
3. J. Saraie, H. Kato, N. Yamada, *et al.*, Phys. Status Solidi A **39**, 331 (1977).
4. A. P. Belyaev, V. P. Rubets, and I. P. Kalinkin, Fiz. Tekh. Poluprovodn. (St. Petersburg) **31**, 966 (1997) [Semiconductors **31**, 823 (1997)].
5. N. F. Mott and E. A. Davis, *Electronic Processes in Non-Crystalline Materials* (Clarendon, Oxford, 1979; Mir, Moscow, 1982).

Translated by V. Bukhanov

Semiconductors, Vol. 34, No. 10, 2000, pp. 1161–1162. Translated from Fizika i Tekhnika Poluprovodnikov, Vol. 34, No. 10, 2000, pp. 1212–1213.

ELECTRONIC AND OPTICAL PROPERTIES OF SEMICONDUCTORS

Band Gap Estimation for a Triaminotrinitrobenzene Molecular Crystal by the Density-Functional Method

K. F. Grebenkin* and A. L. Kutepov

All-Russia Research Institute of Technical Physics, Russian Federal Nuclear Center, Snezhinsk, Chelyabinsk oblast, 454070 Russia

** e-mail: greb@nine.ch70.chel.su*

Submitted February 22, 2000; accepted for publication March 7, 2000

Abstract—Numerical estimations showed the crystalline triaminotrinitrobenzene explosive to be a wide-gap semiconductor with a band gap of 2–4 eV under normal conditions and 1.5–2.0 eV under pressures of 10–20 GPa, which is typical of shock-wave-initiated detonation. *© 2000 MAIK "Nauka/Interperiodica".*

Recently, a physical model was proposed for the shock-wave-initiated detonation of pressed fine-crystalline triaminotrinitrobenzene (TATB) explosive [1]. The model is based on the assumption that TATB is a semiconductor with a 2-eV band gap under pressures of 10–20 GPa typical of shock-wave initiation.

An experimental value of the TATB band gap is unknown. Based on the electron structure of the TATB molecular crystal, calculated in the Hartree–Fock approximation, it was concluded in [2] that this material is an insulator with a band gap of about 10 eV. However, the Hartree–Fock calculations as a rule grossly overestimate the band gap (see table). Thus, the problem of the TATB crystal band gap remains unsolved. Furthermore, molecular crystals of some nitro compounds (TATB belongs to this class) are indeed known to be semiconductors [3].

This study is aimed at finding a refined numerical estimate of the band gap of the TATB molecular crystal by the density-functional technique with a local approximation for the exchange–correlation energy (local density approximation, LDA). The fact that the density-functional method yields more accurate band gaps compared to the Hartree–Fock method is illustrated in the table where experimental band gaps of some materials are compared to those calculated by the Hartree–Fock and LDA methods.

The electron structure was calculated for a TATB crystal structure taken from crystallographic data [8]. We note that TATB crystallizes in the triclinic Bravais lattice and the crystal unit cell contains two molecules composed of 48 atoms. We use the electron-density functional method [9] with a local approximation for the exchange–correlation energy (LDA) [10]. To solve the Kohn–Sham single-particle equations, we employ the nonlinear method of augmented plane waves. The calculation is based on the warped-muffin-tin approximation where the electron density and the effective potential between nonoverlapping muffin-tin (MT) spheres and inside these are described by Fourier series and assumed to be spherically symmetric [11], respectively. The basic calculation error is caused by truncating the Fourier series to represent the density and potential in the region between MT spheres and by a limited number of augmented plane waves to represent the wave functions. The number of plane waves for the density and potential is 4261, the largest number of augmented plane waves is 332. Integration over the Brillouin zone was carried out using eight special points [12].

To estimate the error related to incomplete convergence of expansions outside the MT spheres, two calculations were carried out with a different choice of sphere radii. In the first case, all sphere radii were taken to be identical. In the second case, hydrogen atom radii were halved whilst the radii of heavier atoms were retained. Under the condition of complete convergence, such a radius variation should not affect the result. Under the condition of incomplete convergence, the difference in results yields a computational-error estimate.

In these cases, the band gap was found to be 1.71 and 1.88 eV, respectively. This means that the computational error is reasonably small. Thus, the obtained

Calculated band gaps found by the Hartree–Fock (HF) and LDA methods in comparison to the experiment

Material	Calculation		Experiment
	LDA	HF	
Diamond	4.0 [4]	12.4 [4]	5.5 [4]
Si	0.5 [4]	6.3 [4]	1.2 [4]
MgO	4.64 [7]	25.3 [5]	7.833 [6]
CaO	4.30 [7]	15.8 [5]	7.09 [6]

Note: The band gaps are given in electronvolts.

1063-7826/00/3410-1161$20.00

data allow the conclusion that the TATB molecular crystal is a semiconductor with the band gap of about 1.8 eV or about 40 kcal/mole.

The density-functional technique used yields more accurate, though systematically underestimated, values of the band gap than the Hartree–Fock method. Judging from the data listed in the table, the true band gap of TATB may exceed 1.5–2 times that found by the LDA calculations. Hence, the expected value of the band gap can be estimated at 2–4 eV for TATB under standard conditions. According to estimations, at pressures of 10–20 GPa typical of the TATB shock-wave initiation, the band gap can probably decrease to the value of 1.5–2 eV found by the explosion experiments [1].

Thus, the measured TATB band gap and its dependence on pressure are of great interest for verifying computations of the band structure of complex molecular crystals and for understanding the physics of detonation in crystalline explosives.

Preliminary estimates show that other explosives based on nitro compounds (for example, hexogen) can have an analogous electron structure and their band gap can be on the order of 2–5 eV under standard conditions.

ACKNOWLEDGMENTS

We are grateful to S.Yu. Savrasov for the FPLMTO code [13] used for testing the technique and to G.V. Sin'ko for his valuable participation in discussions.

REFERENCES

1. K. F. Grebenkin, Pis'ma Zh. Tekh. Fiz. **24** (20), 1 (1998) [Tech. Phys. Lett. **24**, 789 (1998)].
2. A. B. Kunz, Phys. Rev. B **53** (15), 9733 (1996).
3. J. Simon and J.-J. Andre, *Molecular Semiconductors* (Springer-Verlag, Berlin, 1985; Mir, Moscow, 1988).
4. S. Massidda, M. Posternak, and A. Baldereschi, Phys. Rev. B **48**, 5058 (1993).
5. R. P. Pandey, J. E. Jaffe, and A. B. Kunz, Phys. Rev. B **43**, 9228 (1991).
6. R. C. Whited, C. J. Flaten, and W. C. Walker, Solid State Commun. **13**, 1903 (1973).
7. Kotani Takao, Phys. Rev. B **50**, 14816 (1994).
8. R. Jackson, L. Green, R. Barlett, *et al.*, in *Proceedings of the 6th International Symposium on Detonation, Coronado, 1976.*
9. W. Kohn and L. J. Sham, Phys. Rev. A **140**, 1133 (1965).
10. J. P. Perdew and Y. Wang, Phys. Rev. B **45** (23), 13244 (1992).
11. N. Elyashar and D. Koelling, Phys. Rev. B **13**, 5362 (1976).
12. H. J. Monkhorst and J. D. Pack, Phys. Rev. B **13** (12), 5188 (1976).
13. S. Yu. Savrasov and D. Yu. Savrasov, Phys. Rev. B **46** (19), 12181 (1992).

Translated by A. Kazantsev

Semiconductors, Vol. 34, No. 10, 2000, pp. 1163–1171. Translated from Fizika i Tekhnika Poluprovodnikov, Vol. 34, No. 10, 2000, pp. 1214–1222.

SEMICONDUCTOR STRUCTURES, INTERFACES, AND SURFACES

Static and High-Frequency Transverse Electrical Conductivity of Isotypical Silicon Structures Obtained by Direct Bonding

V. A. Stuchinskiĭ* and G. N. Kamaev**

Institute of Semiconductor Physics, Siberian Division, Russian Academy of Sciences, pr. Akademika Lavrent'eva 13, Novosibirsk, 630090 Russia

**e-mail: stuchin@isp.nsc.ru*

***e-mail: kamaev@isp.nsc.ru*

Submitted September 6, 1999; accepted for publication March 30, 2000

Abstract—The possibility of using the results of measuring the quasi-static current–voltage characteristics and high-frequency impedance of symmetrically doped bicrystal structures obtained by direct bonding to simultaneously determine the electrical parameters of the bonding interface [differential density of the surface states $\nu(E)$] and the near-boundary layers (the dopant-concentration distribution in the vicinity of the boundary) is discussed. Attention is given to the fact that the ratio of static current to high-frequency conductivity is extremely sensitive to the presence of "punch-throughs" (regions with enhanced electrical conductivity) in the potential barrier of the bonding interface. It is shown experimentally that the electrical conductivity of actual bicrystal structures obtained by direct bonding of silicon is governed to a large extent by the presence of such "punch-throughs," which should be taken into account, in addition to the possible doping of interfacial layers in the course of bonding, when determining the dependence $\nu(E)$. *© 2000 MAIK "Nauka/Interperiodica".*

1. INTRODUCTION

The use of the technology of direct bonding of silicon in the production of electronic devices makes the electrical characterization of the structures thus formed a topical problem. In particular, this concerns the methods for determining the differential density of surface states $\nu(F)$ at the bonding interface. Thus far, the form of the dependence $\nu(E)$ has been considered as the main factor that defines the electrical (including the varistor) properties of directly bonded silicon structures [1].

The previously suggested methods for determining the dependence $\nu(E)$ from electrical measurements are based on an *a priori* assumption that the transverse distribution of the dopant concentration $N(x)$ is uniform in the vicinity of the bonding interface and that the structures are laterally homogeneous [1–3]. However, there are reports that, in a number of cases, the effect of parasitic *p*-doping of the bicrystal near-interface region is observed; this effect is caused by diffusion of residual boron and (or) aluminum from the cleaned wafer surface [4–8]. It is noteworthy that the use of destructive methods for testing the structures (using thinning of wafers subjected to bonding with subsequent measurement of the parameters of the near-surface regions) in order to determine the distribution $N(x)$ in the vicinity of the interface leads to problems caused by difficulties with ensuring the "plane-parallel" approach to this interface. On the other hand, measurement of the parameters of the near-surface layers in the regions of the wafers that were not bonded for technological reasons (for example, at the periphery of the structures or in the region of bonding defects of the "bubble" type) also introduces an ambiguity. This is caused by the fact that residual impurities can penetrate into the gap between the wafers and then into the environment [7], in contrast with the case where these impurities remain confined in the structure and may diffuse only in the silicon bulk. The stress-defined conditions for the formation of structural defects are evidently also different in the above two cases, so that the impurity and defect composition of the near-surface region of nonbonded zones and near-interface layers in monolithic structures may, in general, be different.

The presence of large structural defects in the bonding-boundary region [9] also calls for an analysis of what error in determining $\nu(E)$ is introduced by the assumption that the directly bonded silicon structures are laterally electrically homogeneous. This issue has not been elaborated thus far, notwithstanding the available evidence that the transverse conductivity of directly bonded silicon structures may fluctuate appreciably over the interface, which gives rise to pronounced punch-throughs (highly conducting regions) in the corresponding potential barrier (see, for example, [10]).

In this paper, we consider two methods for determining the quantity $\nu(E)$ at the bicrystal interface from the results of measurements of high-frequency (HF) capacitance and the static and HF conductances of directly bonded silicon structures. These methods are not based on special assumptions about the distribution $N(x)$ in the vicinity of the interface but rely on lateral homogeneity of the structures. It is demonstrated that the internal parameter of one of the considered algo-

1063-7826/00/3410-1163$20.00

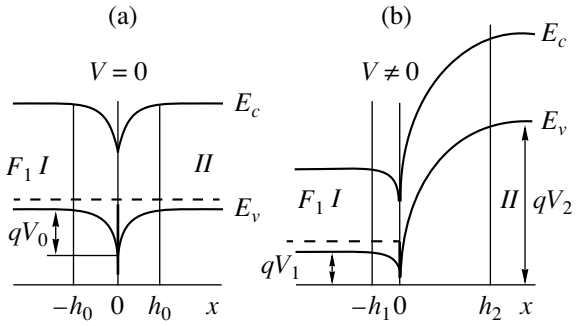

Fig. 1. The energy-band diagram of a symmetric, directly bonded *p*-Si/*p*-Si structure under (a) zero and (b) nonzero external biases.

rithms (the ratio of the static current to the HF conductance of directly bonded silicon structures) is a quantity which is extremely sensitive to the presence of punch-throughs, which makes it possible to use this parameter to check the lateral homogeneity of the conductance in the structure being studied.

2. A MODEL OF A DIRECTLY BONDED SILICON STRUCTURE AND A METHOD FOR ITS CHARACTERIZATION

The energy diagram of the bicrystal boundary ($x = 0$) in a *p*-Si–*p*-Si symmetrically doped, directly bonded silicon structure for both zero and nonzero external biases is shown in Fig. 1. As in [1–3], it is assumed that the oxide layer present (possibly) at the boundary is transparent to tunneling for the charge carriers. Here, h is the width of the space-charge region (SCR) considered in the approximation of the Shockley layer ($h \gg l_D$, where l_D is the Debye screening length), h_1 and h_2 are the widths of the forward- and reverse-biased parts of the SCR ($h = h_1 + h_2$), and V_1 and V_2 are the barrier heights for the forward and reverse currents.

The static above-barrier current j^- is controlled by the barrier height V_1; i.e.,

$$j^- = j_0 e^{-qV_1/kT}(1 - e^{-qV/kT}), \quad (1a)$$

where $j_0 = A^*T^2(p_0/N_v)$ and $q\mu_h p_0[E_1E_2/(E_1 + E_2)]$ correspond to the current in the diode and diffusion models, respectively (A^* is the Richardson constant for holes, p_0 and μ_h are their concentration and mobility, N_v is the effective density of states in the valence band, and E_1 and E_2 are the field strengths to the right and left of the boundary) [3, 11, 12], so that, for the bias voltage $V \gg kT/q$, we have

$$j^- \approx j_0 e^{-qV/kT}. \quad (1b)$$

The general procedure for determining $\nu(E)$ is based on the fact that the difference between the variations in the SCR charge at its left- and right-hand boundaries dQ_2 and dQ_1 resulting from a change in the external bias dV is related to a change in the surface-state charge dQ_s caused by variation of the Fermi-level position at the boundary (F_s) by the expression

$$\begin{aligned} dQ_s &= dQ_2 - dQ_1 = q(N_2 dh_2 - N_1 dh_1) \\ &= q\nu(E)dF_s \approx -q\nu(E)dV_1, \end{aligned} \quad (2)$$

in this case,

$$dV = dV_2 - dV_1 = \frac{q}{\varepsilon_a}(N_2 h_2 dh_2 - N_1 h_1 dh_1). \quad (3)$$

Here, all the quantities dQ_i and dh_i are considered to be positive, and N_1 and N_2 are the concentrations of acceptors at the left- and right-hand SCR boundaries that are assumed to be unknown.

The total SCR thickness h is determined from the measured capacitance C ($h = \varepsilon_a S/C$, where S is the structure area), whereas, in order to determine the ratio between the SCR widths in wafers I and II, the HF conductivity ($G^\sim$) of the structure has to be additionally measured. In fact, if an HF component $V^\sim$ is added to the constant bias V^- ($V = V^- + V^\sim$), the total current is given by

$$j = j^- + j^\sim \approx j^-\left[1 - \frac{qV_1^\sim}{kT} + \frac{qV^\sim}{kT}(e^{qV/kT} - 1)^{-1}\right].$$

Since the surface-state charge Q_s has no time to change at a high frequency ($dQ_s = 0$), the alternating field $E^\sim$ at any point in time is spatially uniform in a region with thickness h ($E^\sim = -V^\sim/h$); therefore, $V_1^\sim = -V^\sim(h_1/h)$ and $G^\sim = j^\sim/V^\sim = (q/kT)j^-\{(h_1/h) + [\exp(qV/kT) - 1]^{-1}\}$. Thus, we have

$$\frac{h}{h_1} = \left[\frac{kT}{q}\frac{G^\sim}{j^-} - (e^{qV/kT} - 1)^{-1}\right]^{-1}, \quad (4a)$$

or, for $V \gg kT/q$,

$$\frac{h}{h_1} = \frac{q}{kT}\frac{j^-}{G^\sim}. \quad (4b)$$

After the quantities h and h/h_1 (and thus h_1 and h_2 separately) have been determined, the concentrations N_1 and N_2 can be found from conventional formulas for C–V profiling with allowance made for the barrier heights V_1 and $V_2 = V + V_1$ [11] determined from the measured current j^-; i.e.,

$$N_i = \frac{2\varepsilon_a}{q}\frac{dV_i}{d(h_i^2)}, \quad i = 1, 2. \quad (5)$$

Using formulas (1b), (2), and (3) and ignoring the dependence $j_0(V)$ in (1b) that is weaker than the one

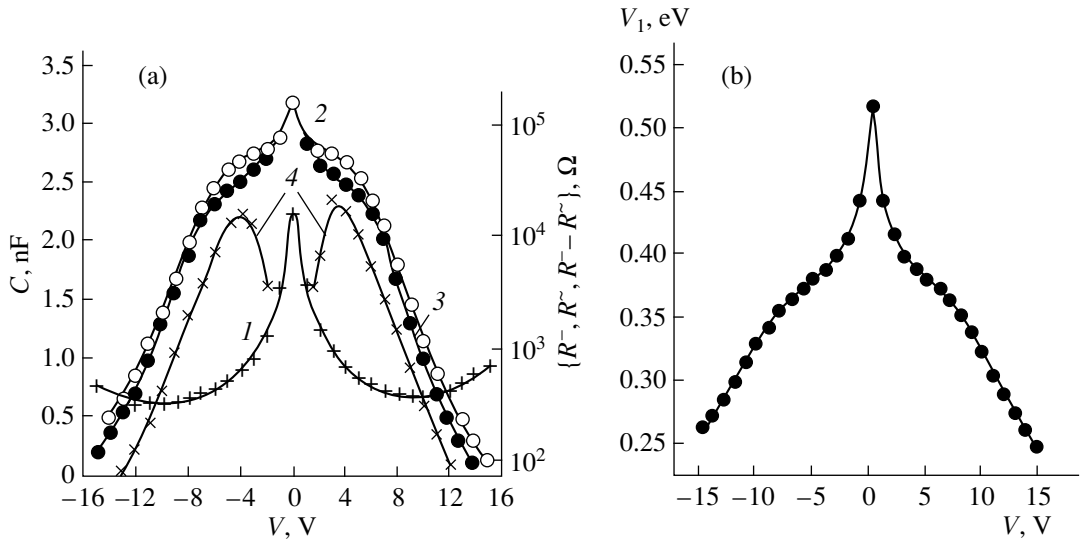

Fig. 2. (a) The dependences of (*1*) the barrier capacitance C, the resistances (*2*) R^- and (*3*) $R^{\sim}$, and (*4*) the difference $R^- - R^{\sim}$ on the bias V; (b) the bias dependence of the barrier height V_1 for a symmetric, directly bonded *p*-Si/*p*-Si structure.

introduced by the exponential law $\exp(-qV_1/kT)$, we obtain

$$\nu = \frac{\varepsilon_a j^-(R^- - R^{\sim})}{kTh_2}, \qquad (6)$$

where $(R^-)^{-1} = dj^-/dV = G^-$ is the differential conductance of the static current–voltage (I–V) characteristic and $R^{\sim} = (G^{\sim})^{-1}$. Formula (6) clearly demonstrates that, as might be expected, the difference between $G^{\sim}$ and G^- is defined by the presence of a nonvanishing differential surface-state density ν. Thus, the considered approach to determining the dependence $\nu(E)$ from the measured quantities j^-, R^-, and $R^{\sim}$ and the determined value of h_2, as outlined above, is in fact based on the known method of frequency discrimination for the contribution of deep states to the current response to the voltage applied to the structure.

3. EXPERIMENT

In the experiment, we used symmetric structures obtained by bonding KDB-20 Si (*p*-Si:B, $\rho = 20\ \Omega$ cm) wafers with boron concentration $N_B = (6–7) \times 10^{14}$ cm^{-3} and (100) orientation. Prior to bonding, the wafers were subjected to the conventional RCA treatment with subsequent hydrophilization of the surface in an ammonium–peroxide solution, rinsing in distilled water, and dehydration in a centrifuge. The wafers were bonded in atmospheric air at room temperature under an applied external pressure. The final bonding was accomplished in a dry nitrogen atmosphere at a temperature of 1050°C for 2 h without using any additional load. After bonding, one of the wafers was thinned by mechanical polishing to a thickness of ~100 μm. A diamond disc was then used to form grooves about 80 μm deep at the surface of this wafer; these grooves were subsequently expanded by etching in an aqueous solution of KOH in order to remove the damaged layer down to the intersection of the groove bottom with the bonding interface. The samples were 0.3 × 0.3 and 0.3 × 0.6 cm in size. Ohmic contacts to the samples were formed by applying In + Ga paste to the surface.

The quasi-static I–V characteristics and the HF impedance (at a frequency of $f = 1$ MHz) of the structures were measured in the dark at temperatures of T_m = 78–300 K. A VM-508 impedance meter was used. It was assumed that the equivalent circuit of the structures at high frequency includes a barrier capacitance C connected in parallel to the resistance $R^{\sim}$ that defines the above-barrier current; C and $R^{\sim}$ are connected in series to the resistance r of the quasi-neutral bulk of the wafers. The inequalities $R^{\sim} \gg (\omega C)^{-1} \gg r$ are typical; the first of these changes to $R > (\omega C)^{-1}$ with increasing external bias, and, for V = 10–15 V, the values of $R^{\sim}$ and $(\omega C)^{-1}$ become comparable. The parameters of the equivalent circuit were determined from measurements of the frequency dependence of the samples' impedance in the range of ω = 0.5–5 MHz. To this end, we first calculated the parameters of the electric circuit composed of the parallel-connected capacitance C' and resistance R', which were related to $R^{\sim}$, C, and r by the expressions $C' \approx C$ and $R'^{-1} \approx R^{-1} + \omega^2 C^2 r^{-1} \approx R^{-1} + \omega^2 C'^2 r^{-1}$; the latter of these expressions was used to determine r from the dependence $R'^{-1}(\omega^2)$ and then the conductance $G^{\sim} = (R^{\sim})^{-1}$.

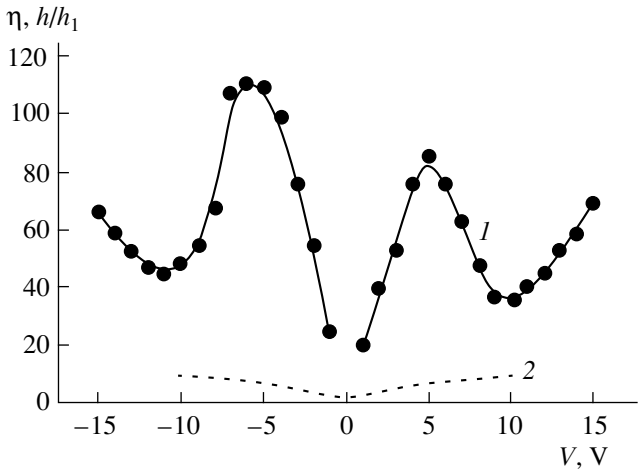

Fig. 3. Dependences of (*1*) the parameter $\eta = (q/kT)(j^-/G^\sim)$ and (*2*) the ratio h/h_1 determined using the iteration procedure on the bias *V*.

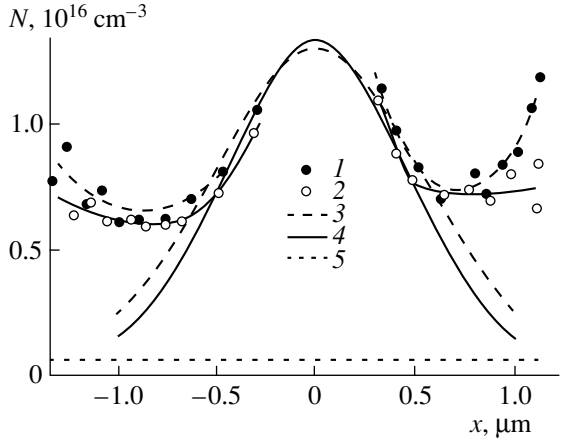

Fig. 4. The dependences $N(x)$ calculated using an iteration procedure: (*1*) the first approximation under the assumption that $h_1 = (h_0)[V_1(V)/V_0]^{1/2}$; (*2*) the resulting distribution after several iterations; (*3* and *4*) approximating distributions of the diffusion-related type for *1* and *2*, respectively; and (*5*) the doping level of the initial wafers.

4. RESULTS AND DISCUSSION

The dependences of C, $R^\sim$, R^-, and the difference $R^- - R^\sim$ on the bias V applied to the structure are shown in Fig. 2a. It can be seen that $G^- < G^\sim$, in accordance with the fact that recharging of the deep levels has time to occur at a low frequency of a quasi-steady scan of V and thus hinders variation of the barrier height V_1 by the external bias. We note that the SCR width h for $V = 0$ calculated from the capacitance C ($2h_0 \approx 0.3$ μm) is found to be much smaller than that expected from the bulk doping level of the wafers (~2 μm). An increase in C with increasing bias magnitude above 10 V can result from errors in calculating the barrier capacitance C from the results of measurements of the structure's impedance; these errors are caused by the fact that the equivalent circuit for $V > 7$–10 V (in which case the role of punch-throughs becomes more important) is more intricate than expected and (or) by the contribution of the surface-state capacitance to the total structure capacitance measured for these biases in the regions with a lowered barrier. The barrier heights V_1 calculated with the formula

$$V_1 = (kT/q)\ln\{(j_0/j^-)[1 - \exp(-qV/kT)]\}$$

(here, $j_0 = A^*T^2(p_{ch}/N_v)$, where $A^* = 79.2$ A cm^{-2} K^{-2} [11] and $p_{ch} \approx 1 \times 10^{16}$ cm^{-3} is the characteristic hole concentration defined as $p_{ch} = (2\varepsilon_a/q)[dV/d(h - h_0)^2]$) is shown in Fig. 2b for various values of the bias V. Using these results and the formulas reported in [12], we can verify that, under the experimental conditions used here, the conductance caused by the minority charge carriers (electrons) for both alternating and constant current is negligible compared to the hole-induced conductance. The bias (V) dependence of the parameter $\eta = (q/kT)j^-R^\sim$ associated (in accordance with the above) with the ratio h/h_1 in a laterally homogeneous, directly bonded silicon structure is shown in Fig. 3. It can be seen that the parameter η first increases to a value on the order of 100 for $V = -(5–6)$ V; then decreases to 40–50 with increasing V; and, after that, increases again. Such values of h/h_1, even for low V, (several volts) would seem to be unrealistically large.

In fact, for symmetric, directly bonded silicon structures, another method for calculating the thicknesses h_1 and h_2 and all other sought-for parameters is also possible. This method is based on the current-related measurements only to the extent needed for determining the variation of the barrier height V_1 caused by the bias V (i.e., the quasi-static I–V characteristics $j^-(V)$, rather than the structures' admittance, are measured). In the latter procedure, we use the fact that, for a significant surface-state density, the SCR-boundary position in the forward-biased part of the structure changes much more slowly with variations in the bias V than does the opposite boundary of SCR [1–3]. In view of this and also making allowance for nominal symmetry of the structure, we may then assume to a first approximation that, for zero bias, the width h_1 is equal to the half-width of the SCR and either remains unchanged with further variations in V [$h_1(V) \approx h_1(V = 0) = h_0$, which corresponds to $V_1 \approx \text{const}(V) = V_0$], or varies according to the dependence $h_1 = h_0[V_1(V)/V_0]^{1/2}$ that is characteristic of the situation with a constant doping level $N(x) = \text{const}$. Thereby, the dependence $h_2(V) = h(V) - h_1(V)$ is determined, and the possibility arises of finding a first approximation to the profile $N(x)$ for $x > h_0$ using formula (5). To a first approximation, the profile $N(x)$ is shown by the dashed line in Fig. 4 (the second of the above two dependences for $h_1(V)$ was used). It can be

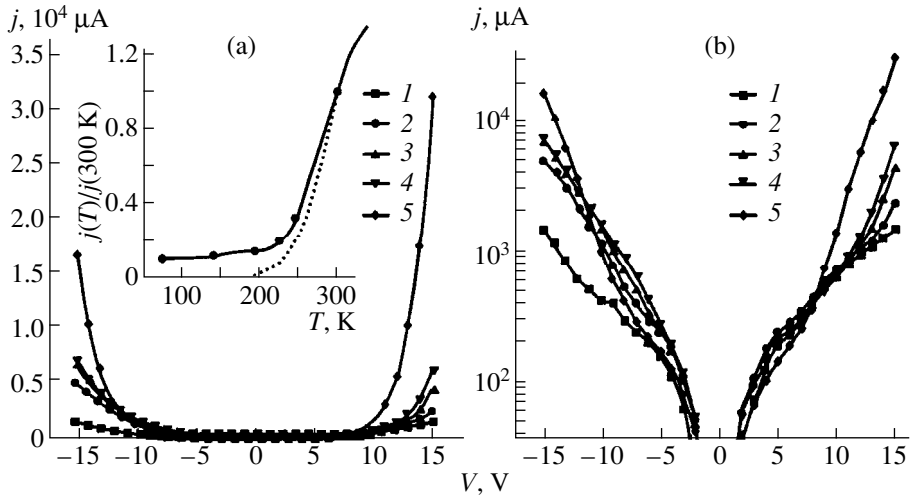

Fig. 5. The static *I–V* characteristic of a symmetric *p*-Si/*p*-Si directly bonded structure on the (a) linear and (b) logarithmic scales. T = (*1*) 78, (*2*) 142, (*3*) 197, (*4*) 230, and (*5*) 300 K. In the insert, the experimental curve (solid line) and the curve calculated on the assumption that $j_0(T)$ = const and $V_1(T)$ = const (dashed line) represent the temperature dependences of current for V = 13 V.

seen that the acceptor concentration increases as the boundary is approached, in accordance with the aforementioned smallness of $2h_0$ and the numerous published data on *p*-doping of interfacial layers in directly bonded silicon structures.

As the second step, we can take into account in more detail the variation in $h_1(V)$ with allowance made for the available experimental data on the dependence $V_1(V)$. To this end, we should approximate the dependence $N(x)$ in the region $x \geq h_0$ with a certain physically meaningful function $N^{\text{appr}}(x)$ (for example, with a function of the type of $N(x) = N_0^* \exp(-x^2/x_d^2) + N_B$, which describes the result of impurity diffusion from an exhaustible surface source into a wafer with a doping level of N_B [13]). The function $N^{\text{appr}}(x)$ is chosen such that the experimental value of V_0 can be obtained using the expression $V_0 = (q/\varepsilon_a)\int_0^{h_0} N^{\text{appr}}(x)x dx$. We then calculate the differential variations of $h_1(dh_{1j})$ under small variations in $V_1(dV_{1j})$ using the formula $dh_{1j} = dV_{1j}/[(q/\varepsilon_a)N^{\text{appr}}(h_1)h_{1j}]$, where h_{1j} is the current value of h_1 determined with allowance made for all accumulated variations dh_{1j} as V increases from the zero value to the current value (the subscript j enumerates the points according to the voltage); i.e., we have

$$h_1(V) = h_0 - \sum_j dh_{1j}(V_{1j}).$$

Thus, the dependences $h_1(V)$ and $h_2(V) = h(V) - h_1(V)$ are determined; the latter dependence is necessary to refine the profile $N(x)$ for $x \geq h_0$ using formula (5).

Further on, the procedure is repeated iteratively until a sufficiently small variation in the distributions $N(x)$ is attained at the next step. The resulting distribution $N(x)$ for the case under consideration is shown in Fig. 4 by the solid line (in the range of x = 0.3–0.5 μm, the approximating function is given by $N^{\text{appr}}(x)[\text{cm}^{-3}] = (1.27 \times 10^{16})\exp(-x^2/0.4) + 6 \times 10^{14}$, where x is expressed in micrometers). Thus, the calculation yields $N(x = 0) = 1.33 \times 10^{16}$ cm^{-3} and the value of the coefficient in the exponent corresponds to the diffusion coefficient for a surface diffusant $D \approx 9 \times 10^{-14}$ cm^2/s, which is close to the diffusion coefficient for boron ($D_B \approx 10^{-13}$ cm^2/s at T = 1050°C [13, 14]). The discrepancy between the approximating curve and the profile $N(x)$ calculated from experimental data for $x \geq 0.5$ μm may be caused by both the presence of a more rapidly diffusing entity (for example, aluminum for which the diffusion coefficient is $D_{Al} = (6–8) \times 10^{-13}$ cm^2/s at T = 1050°C [13, 14]) and by the reasons given above for the appearance of the portion in the dependence where C increases with increasing bias. The inference that the effect of parasitic *p*-doping of the interfacial region in directly bonded silicon structures may be due to the diffusion of boron and aluminum impurities is consistent with the previously published data [4, 5] and with the results of mass spectrometry studies of the impurity composition of interfacial layers in directly bonded silicon structures [6–8]. It is significant that the calculated values of h/h_1 (Fig. 3, the dotted line) do not exceed ~10 up to V = 10 V.

The causes of the observed differences in the parameter η and the ratios h/h_1 determined by the iteration procedure become clear if we consider the experimental data on the temperature dependence of the *I–V* characteristics of the structures (Fig. 5) and on the transient current in the case where a reverse-voltage step is applied to the structures (Fig. 6). It can be seen from Fig. 5b that, for V = 2–7 V (i.e., in the exact region

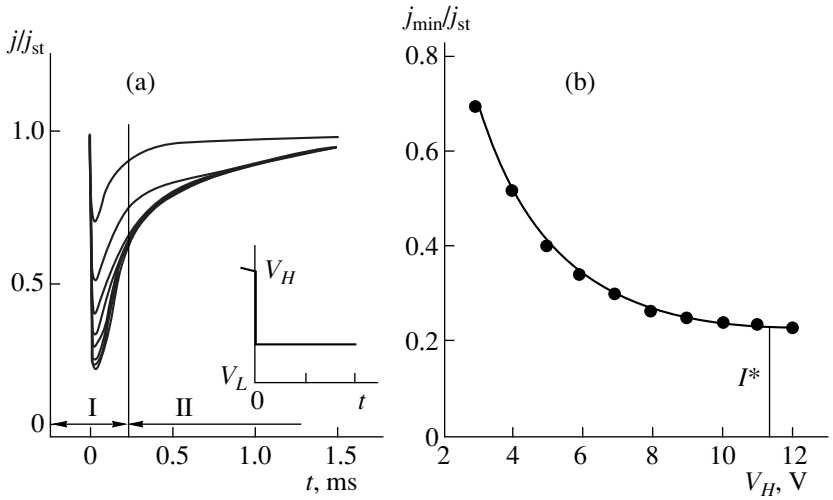

Fig. 6. (a) The current relaxation in a directly bonded silicon structure after the external bias was abruptly decreased from V_H to V_L = 2 V at time t = 0 and (b) the dependence of the nonblocked fraction of the current j_{min} on V_H. In Fig. 6a (for the curves from top to bottom): V_H = 3, 4, 5, 6, 7, 8, 10, and 12 V.

where the increased values of η are characteristic), an increase in j^- with decreasing temperature is observed; this dependence is opposite to that for thermally activated above-barrier charge transport. For higher voltages, in which case the current decreases with decreasing temperature, the current decreases more slowly than might be expected on the basis of the experimentally obtained barrier height V_1. Actually, as the temperature is lowered, the surface-state charge Q_s (and, simultaneously, the barrier height V_1) should increase, or at least remain unchanged, owing to the fact the Fermi level shifts to the valence-band top in the bulk and (possibly, to a lesser extent) at the boundary; this should ensure the steep falloff of the current shown in the insert in Fig. 5a by the dotted line or even steeper than that. The presence of a slowly decreasing current component clearly indicates that punch-throughs (regions with a lowered barrier or even without a barrier at all) exist for the transverse current. It may be inferred that, for $V < 7$ V, the major part of the current j^- passes through such punch-throughs where the local current density is governed by the temperature dependence of the corresponding spreading resistance; this dependence is controlled by the temperature dependence of the hole mobility ($\mu_h \sim T^{-2.3}$ [15]). An increase in electrical conductivity with decreasing temperature in the relevant temperature range has been observed previously for zero-biased *p*-Si/*p*-Si bicrystal structures with grain boundaries [16] and for $V < 5$ V in directly bonded *n*-Si/*n*-Si structures [10].

The presence of punch-throughs in the potential barrier of the boundary also manifests itself in observations of the current relaxation when a steplike voltage is applied to the structure (Fig. 6). The general form of the corresponding dependences that coincides qualitatively with those we observed experimentally was described previously for monoenergetic surface states [17]. At the stage when a high-density current $j(t)$ flows (for $V = V_H$; see the insert in Fig. 6a), the surface charge Q_s is found to be increased compared to the values observed at lower steady-state external voltages; if the external voltage is abruptly decreased to V_L, the surface charge has no time to significantly change initially, which results in a high nonequilibrium barrier height V_1^* immediately after switching and in small values of the current at stage I. In addition, as long as the difference between V_1^* and the equilibrium value V_1 for $V = V_L$ remains much larger than kT, the current through the laterally homogeneous structure is bound to be negligible compared to the corresponding steady-state j_{st} for $V = V_L$. At stage II, as a result of hole emission from the surface states at the boundary, the barrier height approaches its equilibrium value for $V = V_L$ by the value of $\sim kT/q$ and the nonequilibrium current is found to be comparable to j_{st}. It is important here that the experimentally observed current patterns are indicative of a fairly large fraction (of the steady-state value of j^- at a bias of $V = V_L$) of the current at stage I; in addition, there is a clear tendency towards leveling off, depending on the filling-pulse amplitude (Fig. 6b). This current component I^*, which is not blocked by the surface charge, may be interpreted as being due to punch-throughs.

Large values of the parameter η may be related to the presence of punch-throughs in the barrier only if these punch-throughs are rather clearly pronounced (i.e., if the local conductance in the corresponding areas differs greatly from the conductance in the remaining area, so that, in spite of the small relative total area of

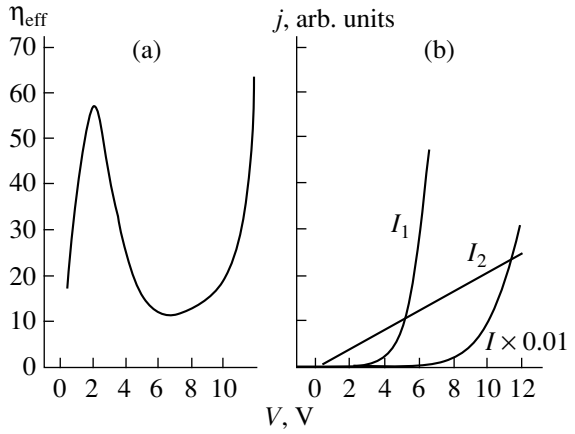

Fig. 7. (a) The effective parameter η_{eff} as a function of the bias V for a sample that contains a barrier region and nonrectifying punch-throughs (see the text for the parameters), and (b) the I–V characteristics of a region with a barrier $I_1(V)$ and a nonrectifying region $I_2(V)$ ($I = I_1 + I_2$ is the total current).

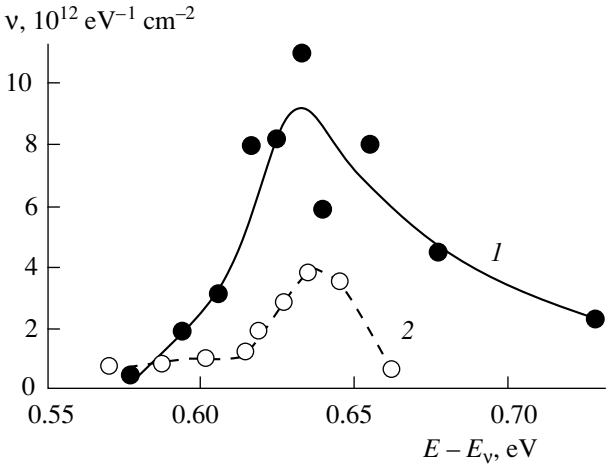

Fig. 8. Distributions of differential density of the surface states at the bicrystal boundary in the directly bonded Si structures. The distributions were calculated using (*1*) an iteration procedure and (*2*) formula (6).

punch-throughs, the predominant fraction of the total current passes through these punch-throughs). It follows, first, from the fact that the introduction of additional leakage results in an increase in both j^- and $G^{\sim}$; the appearance of these quantities in the numerator and denominator, respectively, in the expression for η partly compensates these variations. Second, considering the simplest case of lateral inhomogeneity for a sample composed of two homogeneous regions that have the parameters $\eta = \eta_1$ and $\eta = \eta_2$ ($\eta_2 \gg \eta_1$ and $S_1 \gg S_2$), with an arbitrary ratio between the currents I_1 and I_2, we may readily conclude that the measured effective parameter $\eta_{eff} = (I_1 + I_2)\eta_1\eta_2/(I_2\eta_1 + I_1\eta_2)$ would approach η_2 only for $I_2 \gg I_1(\eta_2/\eta_1)$. For an ohmically conducting region, the parameter $\eta = qV/kT$ is very large (~40 for $V = 1$ V and ~200 for $V = 5$ V), which may indeed lead to the large observed values of η_{eff}.

The dependence $\eta_{eff}(V)$ obtained for actual *p*-Si/*p*-Si structures can be qualitatively described in the following way. For $V < 5$ V, the major fraction of the total current flowing through the structure passes through the "quasi-ohmic" regions that occupy a small fraction of the total area of the structure and have a low barrier, which is responsible for the large values of η_{eff} in the initial quasi-ohmic portion of the I–V characteristic (see Fig. 5a). At a later stage, the current through the main area with a comparatively high barrier V_1 increases, which causes the quantity η_{eff} to decrease ($5 < V < 10$ V). A further increase in η_{eff} is caused by an increase in the local values of η for this low-conductance area and (or) by an increase in the area of relatively highly conducting punch-throughs due to lowering of the barrier in the poorly pronounced punch-throughs (with intermediate barrier heights). It is also significant that the role of progressively smaller (micro-scale) inhomogeneities becomes more and more important as the local SCR width h_1 approaches the local Debye length; in the latter case, there arise additional special features related to violation of the Schottky-layer approximation in considering the SCR. It is noteworthy that, in the context of the above concepts, the "soft" breakdown characteristics of bicrystal structures may be interpreted [1, 12]. As an illustration, Fig. 7 shows the dependences $\eta_{eff}(V)$ that demonstrate the effect of adding an ohmic conducting region with a spreading resistance of $R = 50\ \Omega$ to the homogeneous boundary (with an area of $S = 9 \times 10^{-2}$ cm^2, initial barrier height of $V_0 = 0.4$ eV, and differential surface-state density equal to $\nu = 5 \times 10^{11}$ eV^{-1} cm^{-1} and constant within the range of the Fermi-level variations) on the effective parameter η_{eff} of the total sample in a structure with the spatially uniform acceptor concentration $N_B = 6 \times 10^{14}$ cm^{-3}.

The cause of the origination of lateral inhomogeneity in the bicrystal interface is difficult to determine precisely. The punch-throughs can be caused by nonuniform distribution of charged surface states over the boundary area [this nonuniformity may be correlated with dislocation-type structural defects [9] or be related to the statistical scatter of their areas (for small $h_1 \sim l_D$), see above]; by statistically nonuniform spatial distributions of the doping and compensating impurities in the near-boundary SCR; by conducting channels at the periphery of large, electrically active structural defects formed at the boundary (precipitates and the like); by agglomerates of the impurity of the opposite (to the main impurity) type of doping at the boundary; by the presence of "ideally" bonded regions; and so on. Our experiments with samples having different ratios of the area to the perimeter and also measurements of the

fractions of currents flowing through the peripheral and central surface electrodes formed at one of the surfaces of separated pieces of wafers with a continuous second (rear) electrode (a check on the correspondence to the ratio of the electrode areas) indicate that the inhomogeneities discussed here are local and are not related to the corresponding boundaries. Here it should be noted that, for small punch-throughs (on the order of h_1), their I–V characteristics, even with zero barriers, may be nonlinear owing to modulation of their effective areas by the surface-state charge at the adjoining portions of the boundary; as a result, the corresponding electrical conductivity may be frequency-dependent. Because of this, in calculating the ratio h/h_1 with formula (4), it is difficult to readily take into account the presence of such quasi-ohmic punch-throughs by subtracting the current component I^* (Fig. 6b), which is not blocked by the surface-state charge, from the total current j and subtracting the corresponding differential conductance dI^*/dV from the HF conductance.

The following comments can be made concerning the determination of the dependence $\nu(E)$ in directly bonded silicon structures. It is clear that the addition of a small amount (in the sense of the occupied area) of conducting regions with a specific I–V characteristic, which negligibly influence the total structure capacitance but appreciably influence the structure conductance, may dramatically affect the result of determining $\nu(E)$ by any method that involves a combination of capacitance and current measurements and is based on the assumption of lateral homogeneity of the samples. Therefore, the data on $\nu(E)$ obtained in the cases where lateral inhomogeneity is apparent in the experiment (for example, concerning the parameter η) should treated as effective values. Taking this reservation into account, we present two dependences $\nu(E)$ (Fig. 8), one of which was obtained using the above iteration procedure and formula (2) directly (the solid line) and the other (the dashed line) of which was obtained using formula (6), where R^- and $R^\sim$ were measured experimentally, whereas h_2 was taken from a more realistic result of the iteration procedure. In the first case, it can be seen that somewhat larger values of ν are obtained; on the whole, in order of magnitude, the values of ν are consistent with the results obtained previously by other methods (see, for example, [1–3, 18]). It appears probable that numerical experiments simulating the simplest inhomogeneity (for example, for samples including two homogeneous regions with differing electrical parameters) and the methods described above for determining $\nu(E)$ for such objects could help to clarify the question of whether the results of applying the corresponding methods to inhomogeneous structures are reliable.

5. CONCLUSION

In terms of the conventional model of a laterally homogeneous bicrystal boundary, we suggested two new methods for determining the electrical parameters of symmetric, directly bonded silicon structures from the results of measuring their static current–voltage characteristics, high-frequency capacitance–voltage characteristics, and conductance.

The first method is based on data on the voltage dependence of the parameter $\eta = (q/kT)(j^-/G^\sim)$ that coincides, in the high-frequency limit, with the ratio of the total thickness h of the near-boundary SCR to the thickness of its forward-biased part h_1. In combination with the determination of h from the capacitance measurements and of the barrier height from the measured current j^-, this method is actually an extension of the widely known procedure for C–V profiling to the case where the positions of both boundaries of the SCR depend on the bias. The second method is an iteration procedure in which the fact that the structure is symmetric and the results of the capacitance and current measurements are used. These methods exhibit different sensitivities of the results to lateral inhomogeneity of the bonding interface, which makes it possible to use them to assess this inhomogeneity without performing any local measurements.

The measurements carried out on actual directly bonded p-Si/p-Si structures indicate that there are punch-throughs in the bonding-interface potential barriers; to a large extent, these punch-throughs govern the transverse conductance of the structures. We reported additional experimental data that verified the presence of such punch-throughs in the case where the transient current (after a steplike bias was applied to the structures) and the temperature dependences of constant current were measured. It was shown that the acceptor concentration in the vicinity of the interface is higher than the bulk doping level of the wafers; in addition, a pronounced peak with a magnitude of about $\sim 1 \times 10^{13}$ cm^{-2} eV^{-1} for $E \approx E_V + 0.63$ eV was observed in the distribution $\nu(E)$.

On the whole, the experimental data reported here suggest that the electrical characteristics of actual directly bonded silicon structures may depend appreciably on their local spatial inhomogeneity, which, to a great extent, shifts the problem of describing the electrical parameters of the bicrystal interface to the problem of studying the factors inducing this inhomogeneity.

ACKNOWLEDGMENTS

One of us (V.A.S.) thanks the Watchman Tower Corp. for partial support of this study and A.V. Vishnyakov for his fruitful participation in discussions.

REFERENCES

1. C. H. Seager and G. E. Pike, Appl. Phys. Lett. **35** (9), 709 (1979).
2. S. Bengtsson and O. Engstrom, J. Appl. Phys. **66** (3), 1231 (1989).
3. S. Bengtsson and O. Engstrom, Jpn. J. Appl. Phys. **30** (2), 356 (1991).
4. E. V. Astrova, V. B. Voronkov, Yu. N. Daluda, *et al.*, Pis'ma Zh. Tekh. Fiz. **18** (14), 51 (1992) [Sov. Tech. Phys. Lett. **18**, 457 (1992)].
5. K. Nagai, H. Takato, and Y. Hayashi, Jpn. J. Appl. Phys. **31**, L1529 (1992).
6. K. L. Enisherlova, T. F. Rusak, G. G. Shmeleva, and I. G. Ierusalimchik, Mikroélektronika **23** (6), 46 (1994).
7. X. Mitani, M. Katayama, and K. Nakazawa, in *Proceedings of the 3rd International Symposium on Semiconductor Wafer Bonding: Physics and Applications, Pennington, 1995*, p. 96.
8. C. Okada, Y. Kawai, E. Morita, and Y. Saitoh, in *Proceedings of the 3rd International Symposium on Semiconductor Wafer Bonding: Physics and Applications, Pennington, 1995*, p. 363.
9. A. Laporte, G. Sarrabayrose, L. Lescouzeres, *et al.*, in *Proceedings of the 6th International Symposium on Power Semiconductor Devices and ICs, Davos, 1994.*
10. S. Bengtsson, G. I. Andersson, M. O. Andersson, and O. Engstrom, J. Appl. Phys. **72** (1), 124 (1992).
11. S. M. Sze, *Physics of Semiconductor Devices* (Wiley, New York, 1981; Mir, Moscow, 1984), Vol. 1.
12. W. E. Taylor, N. H. Odell, and H. Y. Fan, Phys. Rev. **88** (4), 867 (1952).
13. B. I. Boltaks, *Diffusion in Semiconductors* (Fizmatgiz, Moscow, 1961; Academic, New York, 1963).
14. A. G. Milnes, *Deep Inpurities in Semiconductors* (Wiley, New York, 1973; Mir, Moscow, 1977).
15. V. L. Bonch-Bruevich and S. G. Kalashnikov, *The Physics of Semiconductors* (Nauka, Moscow, 1990).
16. F. G. Stutzler and H. J. Queisser, J. Appl. Phys. **60** (11), 3910 (1986).
17. E. I. Gol'dman and A. G. Zhdan, Fiz. Tekh. Poluprovodn. (Leningrad) **10** (10), 1839 (1976) [Sov. Phys. Semicond. **10**, 1098 (1976)].
18. A. Broniatowski, Phys. Rev. B **36** (11), 5895 (1987).

Translated by A. Spitsyn

Semiconductors, Vol. 34, No. 10, 2000, pp. 1172–1176. Translated from Fizika i Tekhnika Poluprovodnikov, Vol. 34, No. 10, 2000, pp. 1223–1227.

SEMICONDUCTOR STRUCTURES, INTERFACES, AND SURFACES

Influence of an Electric Field on the Strained State of a Heterostructure

R. M. Peleshchak*, B. A. Lukiyanets, and G. G. Zegrya*****

** Drogobych State Pedagogical University, Drogobych, 293720 Ukraine*

*** State University "Lvivska Polytechnika", Lviv, 290005 Ukraine*

**** Ioffe Physicotechnical Institute, Russian Academy of Sciences, Politekhnicheskaya ul. 26, St. Petersburg, 194021 Russia*

Submitted March 21, 2000; accepted for publication March 27, 2000

Abstract—In the framework of an electron–deformation model, a mechanism of electron–deformation dipole formation at a strained heterointerface was considered. For a ZnSe/ZnS heterostructure, an external electric field ~120 kV/cm normal to the heterointerface brought about an additional compression strain of ~4% (~3%) in the ZnSe (ZnS) lattice. For an opposite field direction, a tensile strain of ~5% (~5%) was observed. © *2000 MAIK "Nauka/Interperiodica".*

1. INTRODUCTION

Modern technology, in particular, molecular beam epitaxy [1], enables one to obtain heterostructures with the lattice mismatch of materials brought into contact (for example, ZnS/ZnSe [2]), or, in the general case, with misaligned crystallographic characteristics. Lattice mismatch causes strain in the vicinity of the heterointerface. The strain type and level can be controlled by the thickness of the grown layer [3]. The purpose of this study was to demonstrate that this effect can also be achieved by applying an external electric field. In this case, we used the self-consistent model, which was developed previously [4]. This model takes into account the interaction of strain with the electron subsystem of the crystal. The purposeful control of the strained state of the heterostructure using an external electric field enables one to vary physical characteristics of the heterostructure continuously in a certain range. In some cases, this should lead to radically new results.

In the context of the model [4], we considered the mechanism of electron–deformation-dipole formation at the strained heterointerface and calculated its dipole moment. We analyzed the influence of an external electric field through the electron–deformation dipole on the strained state of the heterointerface and estimated numerically this influence for the ZnS/ZnSe heterostructure.

We note that this problem can be solved by several methods. One of them includes a consideration of the heterostructure in an external electric field *ab initio*. In this case, the Hamiltonian for the problem will contain a term, which takes the form $\sum_{nm} e\,\mathbf{E}\mathbf{r}_{mn}c_m^+ c_n$, where $\mathbf{E}$ is the electric field strength. This term has no effect on the equation describing the condition of mechanical equilibrium (see below). However, the self-consistent determination of the electron correlator $\langle c_{\mathbf{k}}^+ c_{\mathbf{k}'}\rangle$ [4] and eventually the strain parameter are functions of the electric field.

The other method, which is used below, includes a two-stage solution. At the first stage, the electron–deformation effects in the heterostructure, particularly the formation of the dipole moment, are considered in the absence of an external electric field. The field effects are considered at the second stage only.

It is clear that both approaches should lead to identical final results. However, the second method that we used gives clearer insight into the physical mechanism of the problem under consideration.

2. ELECTRON–DEFORMATION DIPOLE OF THE STRAINED HETEROINTERFACE

The nature of the near-boundary dipoles is defined by states in the band gap, which appear due to the band discontinuity for contacting heteroregions [5]. In contrast with this, the electron–deformation dipole appears at the strained heterointerface due to the mismatch of the unit-cell parameters a_β. Here, $\beta = 1, 2$, where subscript "1" corresponds to the region $L_w \le x \le 0$ of the narrow-gap crystal. For the ZnS/ZnSe heterostructure, this is ZnSe with the band gap $\Delta E_{\mathrm{ZnSe}} = 2.822$ eV. Subscript "2" corresponds to the region $0 \le x \le L_w$ for a wide-gap material (for ZnS, $\Delta E_{\mathrm{ZnS}} = 3.840$ eV). Henceforth, we assume that $L_w \longrightarrow \infty$.

The origin of the electron–deformation dipole is the local charge-carrier redistribution at the strained heterointerface due to electron–strain interaction [4]. Specifically, this is the appearance of regions enriched with and depleted of electrons (for ZnSe and ZnS, in the

vicinity of $x = 0^-$ and $x = 0^+$, respectively, Fig. 1). Thus, the electron–deformation dipole is formed at the strained heterointerface (the plane $x = 0$, see Fig. 1). The moment $\mathbf{P}$ of this dipole is normal to the heterointerface plane. Its magnitude equals [6]

$$P = -es\int_{-\infty}^{\infty} x\Delta n(x), \tag{1}$$

where $s = L_yL_z$ is the heterointerface area and $\Delta n(x)$ is the change in the electron density due to the electron–deformation interaction.

The problem under consideration could be described by a Hamiltonian, whose site representation in the framework of the one-band model has the form

$$\hat{H} = \sum_{i\sigma}[W_i + a_{ci}\varepsilon(\mathbf{r}_i)]c_{i\sigma}^+c_{i\sigma} + \sum_{ij\sigma}\lambda_{ij}^0 c_{i\sigma}^+c_{j\sigma} + \frac{1}{2}\sum_i K_i\Omega_0\varepsilon^2(\mathbf{r}_i) + \hat{H}_{\text{Coul}}, \tag{2}$$

where $c_{i\sigma}^+$ and $c_{i\sigma}$ are the Fermi operators (σ is the spin index); W_i is the position of the electron level at the site with the radius vector $\mathbf{R}_i$ and $a_{ci}\varepsilon(\mathbf{r}_i)$ is the level shift caused by the electron–deformation interaction (a_{ci} is the hydrostatic-deformation potential constant, which is equal to $a_1(a_2)$ for sites in regions 1 (2));

$$\varepsilon(\mathbf{r}_i) = \frac{\Omega(\mathbf{r}_i) - \Omega_0}{\Omega_0}$$

is the relative change of the unit-cell volume Ω_0); λ_{ij}^0 is the integral of the electron mixing between the $\mathbf{R}_i$ and $\mathbf{R}_j$ sites regardless of the strain; $\mathbf{K}_i$ is the lattice elastic stiffness; and $\hat{H}_{\text{Coul}}$ is the electron Coulomb interaction.

In order to derive the electron density $\Delta n(x)$, the self-consistent solution of the following set of equations is required [4]:

(i) the time-independent Schrödinger equation for the strained system

$$\left[\nabla^2 - \frac{a_c}{\alpha}\varepsilon(\mathbf{r}) + \frac{e}{\alpha}\varphi(\mathbf{r})\right]\Psi_n(\mathbf{r}) = -\frac{1}{\alpha}[E_n - (W - \Delta_\lambda)]\Psi_n(\mathbf{r}), \tag{3}$$

where Δ_λ is the band gap and $\alpha = \hbar^2/2m^*$;

(ii) the mechanical-equilibrium condition

$$\left\langle \frac{\partial\hat{H}}{\partial\varepsilon(\mathbf{r})} \right\rangle = \sigma_{\text{mech}}V, \tag{4}$$

where V is the crystal volume;

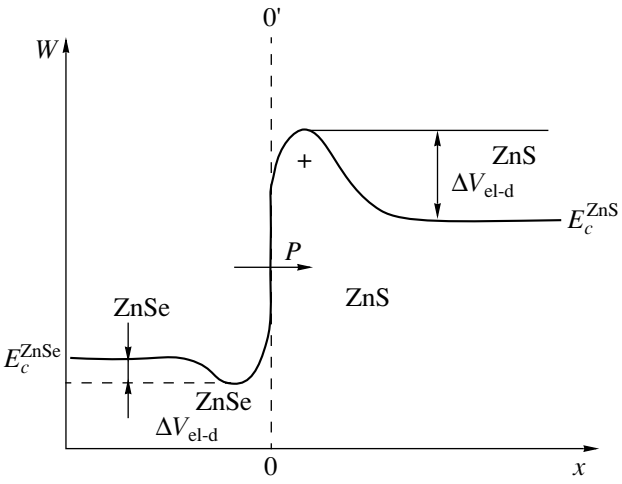

Fig. 1. Energy diagram of the strained heterointerface ZnSe/ZnS with allowance made for the electron–deformation interaction. P is the dipole moment, $\Delta V_{\text{el-d}}(x)$ is the local change in the potential-barrier height or the quantum-well bottom due to the electron–deformation interaction.

(iii) the equation determining the chemical potential position

$$\bar{n} = \frac{\Omega_0}{V}\int n(\mathbf{r})d\mathbf{r}, \quad 0 \le n \le 2; \tag{5}$$

(iv) the equation determining the charge-carrier density $n(r)$,

$$n(\mathbf{r}) = \sum_{\mathbf{k}\mathbf{k}'\sigma}\langle c_{\mathbf{k}\sigma}^+c_{\mathbf{k}'\sigma}\rangle\exp[-i(\mathbf{k} - \mathbf{k}')\mathbf{r}], \tag{6}$$

where $\langle c_{\mathbf{k}\sigma}^+ c_{\mathbf{k}'\sigma}\rangle$ is the Fourier transform of the $\langle c_{i\sigma}^+ c_{j\sigma}\rangle$ correlator; and

(v) the Poisson equation for the electrostatic potential $\varphi(\mathbf{r})$ caused by the redistribution of the electron density $\Delta n(x)$.

As a result,

$$\Delta n(x) = R[e\varphi(x) - V_{\text{mech}}], \tag{7}$$

where

$$R = \left(\frac{3}{8\pi^4}\right)^{1/3}\frac{1}{\alpha}\frac{\bar{n}_0^{1/3}\sqrt{1 + q\bar{n}_0^{1/3}}}{1 - \frac{3}{2}q\bar{n}_0^{1/3}\sqrt{1 + q\bar{n}_0^{1/3}}} \tag{8}$$

with

$$q = \frac{a_c^2}{(3\pi^2)^{2/3}\alpha K}, \tag{9}$$

$\bar{n}_0$ is the average carrier density, and

$$V_{\text{mech}} = a_c\varepsilon_{\text{mech}} \tag{10}$$

is the potential energy of electrons, which is conditioned by the lattice strain. The latter is caused by the mismatch of the unit-cell parameters a_1 and a_2 in the heterointerface plane (for ZnSe/ZnS, $(a_1 - a_2)/a_1 \approx 4\%$ [3]).

Above, in Eqs. (3)–(10), the omitted index $\beta = 1, 2$ should be taken into account, depending on the considered region of the heterostructure. In Eq. (8), $\bar{n}_{0\beta}$ is the average carrier density in the βth material. With regard for the β index, the parameter of strain in the region β, $\varepsilon_{\beta mech}$, is determined by the following equation:

$$\varepsilon_{mech}(\mathbf{E}) = \mathrm{Sp}\hat{\varepsilon}_{mech} = \frac{1}{2}[2a_{\parallel}(\mathbf{E}) + a_{\perp\beta}(\mathbf{E})] - 3, \quad (11)$$

where

$$a_{\parallel}(\mathbf{E}) = \frac{a_1 G_1 + a_2 G_2}{G_1 + G_2} \quad (12)$$

and the unit-cell parameter in the region of the strained heterointerface under the electrical field **E** normal to the heterointerface (G_β is the shear modulus for the β region);

$$a_{\beta\perp}(\mathbf{E}) = a_\beta\left[1 - D_\beta\left(\frac{a_{\parallel}(\mathbf{E})}{a_\beta} - 1\right)\right], \quad (13)$$

where D_β is the coefficient determined by the ratio of the elastic constants and depends on the crystallographic orientation. For the (100) orientation, $D_\beta = 2c_{12}^\beta/c_{11}^\beta$ [3], where c_{11}^β and c_{12}^β are the elastic constants.

It follows from Eq. (1) that the dipole moment P is proportional to the area of contacting regions. This conclusion, which is similar to the conclusion that the dipole moment is proportional to the length of rectilinear dislocation [7], is a manifestation of the fact that the charge redistribution is independent of the contact-plane coordinates. A similar conclusion is implicitly included in the expression for the free energy of the elastic field of the dislocation [8].

The field potential $\varphi_\beta(x)$ appears as a result of local carrier redistribution in the vicinity of the strained heterointerface [4]. This potential can be determined by solving the Poisson equation for the first and second regions of the heterostructure:

$$\frac{d^2\varphi_\beta}{dx^2} - \lambda_\beta^2\varphi_\beta = -\frac{\lambda^2}{e}\Delta V_{\beta mech}. \quad (14)$$

The conduction-band bottom for the first material is chosen as the reference point for the $\varphi_\beta(x)$ potentials. In Eq. (14),

$$\lambda_\beta^2 = \frac{e^2 R_\beta}{\varepsilon_\beta\varepsilon_0},$$

where ε_β is the static permittivity for the βth material (for example, ZnSe), and ε_0 is the permittivity of free space.

Solutions to Eq. (14) in view of the finiteness of the potential $\varphi_\beta(x)$ for $x \longrightarrow \pm\infty$ are given by

$$\varphi_1(x) = A\exp(\lambda_1 x) + \frac{V_{1mech}}{e}, \quad (15)$$

$$\varphi_2(x) = B\exp(-\lambda_2 x) + \frac{V_{2mech}}{e}. \quad (16)$$

Coefficients A and B in these equations are determined from the continuity conditions for the potentials $\varphi_1(x)$ and $\varphi_2(x)$ at the strained heterointerface (i.e., for $x = 0$) and from the normal component of the electric displacement vector $D^{in}(x)$ and $D^{in}(x)$ at $x = 0$:

$$A = -\frac{V_{1mech} - V_{2mech}}{e}\frac{1}{1 + \sqrt{\frac{R_1\varepsilon_1}{R_2\varepsilon_2}}}, \quad (17)$$

$$B = \frac{V_{1mech} - V_{2mech}}{e}\frac{1}{1 + \sqrt{\frac{R_2\varepsilon_2}{R_1\varepsilon_1}}}. \quad (18)$$

Substituting (7) into Eq. (1) and taking into account (15) and (16), we derive the explicit expression for the dipole moment P, which appears at the strained heterointerface due to the electron–deformation interaction:

$$P = \frac{(V_{1mech} - V_{2mech})s\varepsilon_0}{|e|} \times\left(\frac{\varepsilon_1}{1 + \sqrt{\frac{R_1\varepsilon_1}{R_2\varepsilon_2}}} + \frac{\varepsilon_2}{1 + \sqrt{\frac{R_2\varepsilon_2}{R_1\varepsilon_1}}}\right). \quad (19)$$

In the case of the unstrained heterointerface, $V_{\beta mech} = 0$, and, according to (19), the dipole moment P is equal to zero.

3. CHANGE OF THE STRAINED STATE OF THE ZnSe/ZnS HETEROINTERFACE UNDER THE INFLUENCE OF AN EXTERNAL ELECTRIC FIELD

It is reasonable to expect that the presence of the dipole moment P (19) in the heterostructure with the strained heterointerface can be used to change its strained state by an external electric field **E** (see Fig. 1). In this case, the electron–deformation dipole in an external electric field acquires the potential energy

$$\Delta W_p = \mathbf{PE}. \quad (20)$$

In particular, for our problem, the geometry of the electrical field is such that yields $|\cos\alpha| = 1$, where α is the

angle between the vectors **P** and **E**. In Fig. 2, $\alpha = 0$ for curves *1a* and *2a* and $\alpha = \pi$ for curves *1b* and *2b*. This energy is spent on a change in the elastic energies for the first and second materials:

$$|\mathbf{PE}| = \frac{k}{2}[\Delta a_{i\perp}(\mathbf{E}) + \Delta a_{j\perp}(\mathbf{E})]^2, \qquad (21)$$

where $k = k_1k_2/(k_1 + k_2)$ is the coefficient of rigidity of the strained heterostructure ($k_\beta = E_\beta s/a_\perp^\beta(0)$ is the coefficient of rigidity, and E_β is the Young modulus for the βth material); $\Delta a_{\beta\perp}(\mathbf{E})$ is the change in the lattice parameter of the βth material along the normal to the plane of the strained heterointerface, as a result of interaction between an external electric field and the field of the local carrier redistribution in the vicinity of the heterointerface; and $a_{\beta\perp}(0)$ is the lattice parameter of the βth material along the 0*x* axis in the absence of an external electric field.

Equation (19) together with the equation

$$k_1\Delta a_{1\perp}(\mathbf{E}) = k_2\Delta a_{2\perp}(\mathbf{E}), \qquad (22)$$

which describes the mechanical equilibrium at the heterointerface, form a set of equations with the solution

$$\Delta a_{1\perp}(\mathbf{E}) = \pm\sqrt{\frac{2a_{1\perp}(0)|\mathbf{PE}|}{sE_1\left(1 + \dfrac{a_{2\perp}(0)E_1}{a_{1\perp}(0)E_2}\right)}}. \qquad (23)$$

Here, the sign "+" ("–") corresponds to the additional tensile (compressive) strain, which appears due to the influence of electric field $\mathbf{E} = (-E_x, 0, 0)$ ($\mathbf{E} = (E_x, 0, 0)$) applied to the heterostructure (see Fig. 1). In this case, the expression for the strain parameter $\varepsilon_\beta(\mathbf{E})$ as a function of the field **E** in view of Eqs. (11), (13), and (23) has the form

$$\varepsilon_\beta(\mathbf{E}) = 2\left(1 + \frac{1}{D_\beta}\right) + \frac{1}{a_\beta}\left(1 - \frac{2}{D_\beta}\right) \times (a_{\beta\perp}(0) + \Delta a_{\beta\perp}(\mathbf{E})). \qquad (24)$$

Thus, the applied electric field changes the local redistribution of the electron density by the quantity $\delta n(\mathbf{E}) = \Delta n(\mathbf{E}) - \Delta n(0)$. This in turn causes a variation in the electronic strain component $\Delta V_{\beta\text{el-d}}(\mathbf{E}) = -\dfrac{|a_{\beta c}|}{K_\beta}\Delta n(\mathbf{E})$ [4]. Depending on the $\Delta n(\mathbf{E})$ sign, the lattice strain for ZnSe and ZnS can be either tensile ($\Delta n(\mathbf{E}) < 0$) or compressive (for $\Delta n(\mathbf{E}) > 0$).

To illustrate the inferences from the model suggested, let us consider the influence of the external electric field **E** on the type and level of strain for the lattices of ZnSe/ZnS heterostructures with the following parameters:

$E_i = 0.282$ eV/Å^3, $E_j = 0.347$ eV/Å^3;

$a_i = 5.6687$ Å, $a_j = 5.4093$ Å;

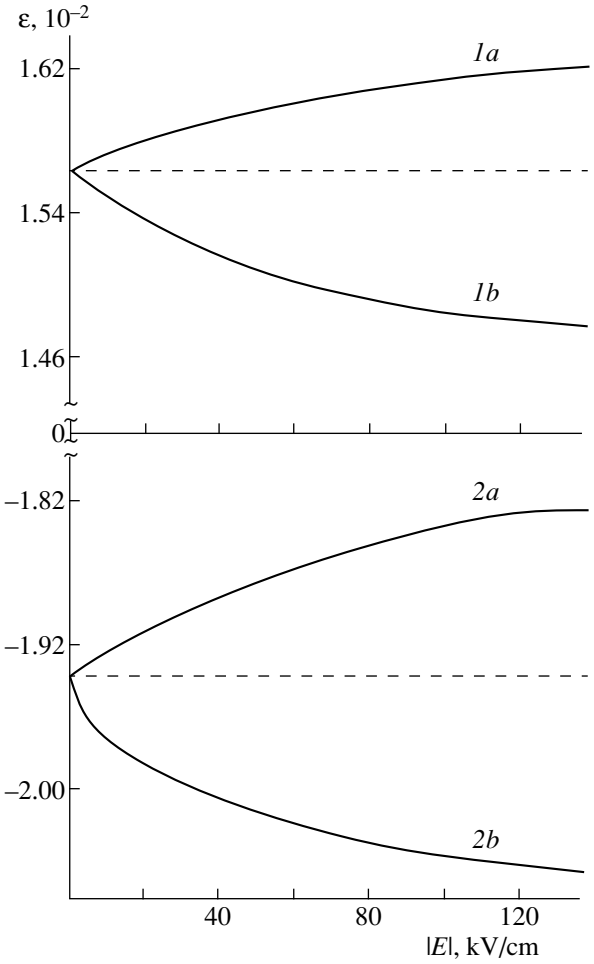

Fig. 2. Strain parameter $\varepsilon_\beta(\mathbf{E})$ as a function of the external electric field **E** for the lattices: curves *1a* and *1b* are for ZnS, and *2a* and *2b* for ZnSe. The dependences *1a* and *2a* correspond to the case of $E \parallel P$ ($\alpha = 0$), and dependences *1b* and *2b* correspond to the antiparallel direction of *E* and *P* ($\alpha = \pi$).

$a_{ic} = -3.65$ eV, $a_{jc} = -2.78$ eV;

$D_{i001} = 1.206$, $D_{j001} = 1.248$;

$G_{i001} = 0.9044$ eV/Å^3, $G_{j001} = 1.1269$ eV/Å^3 [3, 5];

$\bar{n}_{i0} = 10^{18}$ cm^{-3}, $\bar{n}_{j0} = 10^{16}$ cm^{-3};

$m_{ic} = 0.17m_0$, $m_{jc} = 0.25m_0$, $\varepsilon_i = 8.1$, and $\varepsilon_j = 8.3$.

The calculated dependences $\varepsilon_\beta(\mathbf{E})$ for two cases are shown in Fig. 2: curves *a* correspond to the electric field directed along the normal to the heterointerface plane from ZnSe to ZnS, and curves *b* to the electric field directed oppositely.

As follows from Fig. 2, the ZnS and ZnSe lattices undergo either the additional tensile (curves *1a* and *2a*) or compressive strain (curves *1b* and *2b*) with increasing electric field. The strain sign depends on the electric field direction. Particularly, for the electric field $E = 120$ kV/cm, the ZnSe crystal lattice undergoes an addi-

tional tensile strain of ~4% or a compressive strain of ~5%; and the ZnS crystal lattice, ~3 or ~5%, respectively. The obtained curves $\varepsilon_\beta(\mathbf{E})$ demonstrate that the ZnSe lattice is more strain-sensitive than the ZnS lattice. This is explained by the larger compliance of the ZnSe lattice compared to the ZnS lattice.

The effect of increasing (decreasing) the strain state of the ZnSe/ZnS heterostructure with the electric field can apparently be used for the growth of lattice-mismatched heterolayers.

REFERENCES

1. B. A. Jois, in *Molecular Bean Epitaxy and Heterostructures*, Ed. by L. L. Chang and K. Ploog (Martimus Nishoff, Amsterdam, 1985; Mir, Moscow, 1989).
2. M. S. Brodin, V. V. Tishchenko, N. V. Bodnar', *et al.*, Ukr. Fiz. Zh. **37**, 1802 (1992).
3. G. Chris and van de Walle, Phys. Rev. B **39**, 1871 (1989).
4. I. V. Stasyuk and R. M. Peleshchak, Ukr. Fiz. Zh. **36**, 1744 (1991).
5. T. Bechshtedt and R. Enderlein, *Semiconductor Surfaces and Interfaces. Their Atomic and Electronic Structures* (Academie-Verlag, Berlin, 1988; Mir, Moscow, 1990).
6. L. D. Landau and E. M. Lifshitz, *Course of Theoretical Physics*, Vol. 8: *Electrodynamics of Continuous Media* (Nauka, Moscow, 1982; Pergamon, New York, 1984).
7. R. M. Peleshchak and B. A. Lukiyanets, Pis'ma Zh. Tekh. Fiz. **24** (2), 37 (1998) [Tech. Phys. Lett. **24**, 57 (1998)].
8. A. M. Kosevich, *Foundations of Crystal-Lattice Mechanics* (Nauka, Moscow, 1972).

Translated by N. Korovin

Semiconductors, Vol. 34, No. 10, 2000, pp. 1177–1182. Translated from Fizika i Tekhnika Poluprovodnikov, Vol. 34, No. 10, 2000, pp. 1228–1233.

SEMICONDUCTOR STRUCTURES, INTERFACES, AND SURFACES

Effect of Low-Temperature Interphase Charge Transport at the Si/SiO_2 Interface on the Photoresponse of Silicon Barrier Structures

N. I. Bochkareva* and S. A. Khorev

Ioffe Physicotechnical Institute, Russian Academy of Sciences, Politekhnicheskaya ul. 16, St. Petersburg, 194021 Russia

** e-mail: n.bochkareva@pop.ioffe.rssi.ru*

Submitted April 4, 2000; accepted for publication April 4, 2000

Abstract—The effect of low-temperature electron charge redistribution at the Si/SiO_2 interface between the interphase states and the conduction band of an *n*-Si crystal on the temperature behavior of conductance, photovoltage, and photocurrent in Si barrier structures with edge surface electron channels was studied in the temperature range of 77–300 K. The dynamics of the channel-current response to the voltage changes in the dark and under illumination can be explained qualitatively by dispersive hopping transport of holes in SiO_2, which induces electron transfer to, and accumulation at, the Si surface near the barrier contact. The leveling off of the photovoltage at low temperatures and the nonmonotonic temperature dependence of the photocurrent are attributed to the nonmonotonically increasing, localized hole density at the Si/SiO_2 interface and the free electron density at the Si surface with decreasing temperature, which reflects changes in the valence of oxygen complexes. © *2000 MAIK "Nauka/Interperiodica".*

As was shown in [1–3], the nonmonotonic temperature behavior of the surface conductance of Si and Ge crystals in the 77–300 K range exhibits some general trends. Temperature variations of the surface charge were ascribed to changes in the valence of oxygen complexes localized at the crystal–oxide-film interface [3, 4]. The effect of low-temperature interphase redistribution of charges at the semiconductor–oxide interface manifests itself in high-frequency measurements in the form of nonmonotonic temperature dependences of the active and reactive current components in the edge surface channels in barrier structures. In this case, a set of peaks is observed in the conductance relaxation spectra for crystals with surface defects [4]. This can be used to study the nature of the effect and its manifestations at the interface between the crystal and oxide or oxygen precipitates [5] and, in particular, to investigate the contribution of this effect to surface losses in the barrier structures of the device.

The goal of this work was to study how the mechanism of low-temperature interphase charge redistribution at the semiconductor–oxide interface influences the photoresponse of barrier structures. Schottky diodes on *n*-Si, in which the edge surface electron channel was induced by the positive charge in the thermal oxide film formed during oxidation, were chosen as the model.

1. EXPERIMENT

We used *n*-type Si wafers with electron concentration 2×10^{12} cm^{-3} and near-surface oxide stacking faults (OSF) introduced by thermal oxidation to a depth (<1 μm) less than the Debye screening length [3, 4]. The thermal oxide was then removed by chemical etching in a 15-mm^2 window, and a Schottky barrier was fabricated by depositing a 19-mm^2 semitransparent gold layer to form a structure with an extended electrode (Fig. 1b). In control samples, the thermal oxide film was removed from the entire surface prior to depositing the gold layer (Fig. 1c).

Considerable excess reverse currents were observed in the diodes with peripheral thermal oxide; these currents increased nonmonotonically as the temperature was lowered. The reverse current of the control diodes decreased upon cooling. After the samples were kept in air for several months, the reverse currents decreased. Figure 1a shows reverse current–voltage (*I–V*) characteristics of the extended electrode structures in the dark (curves *1'–3'*) and under the illumination with an incandescent lamp (curves *4–6*). The *I–V* characteristics are nonlinear, with a tendency to be superlinear for $U \approx$ 2–4 V and sublinear for $U >$ ~4 V. The reverse *I–V* characteristics of the control samples show similar nonlinearity in the dark, with sublinear *I–V* characteristics observed under illumination (Fig. 1c). We note that similar dark *I–V* characteristics of Schottky diodes on *n*-Si with OSF have been ascribed to the existence of a surface channel [4].

Temperature dependences of the capacitive, ωC (C is the measured capacitance, $\omega = 2\pi f$, and f is the test signal frequency), and active, $\tilde{G}$, components of the high-frequency susceptance and the dependence of the

1063-7826/00/3410-1177$20.00

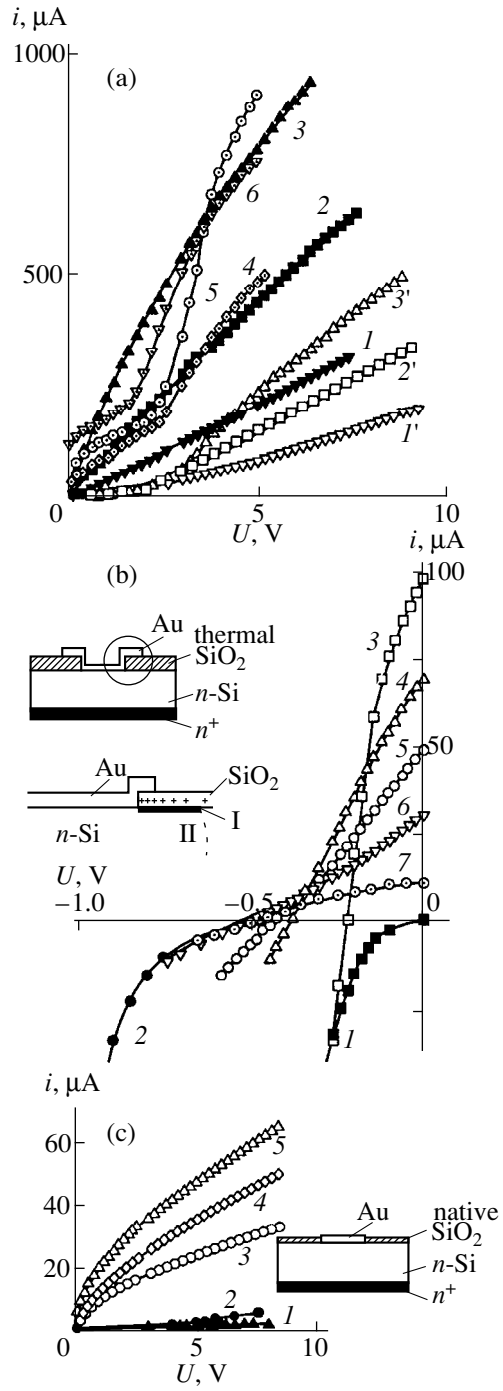

Fig. 1. Reverse (a, c) and forward (b) *i–U* characteristics of Au–*n*-Si (OSF) diodes with (a, b) thermal and (c) natural oxide at the periphery. (a) (*1–3*, *1'–3'*) Without illumination, (*4–6*) under illumination of the entire diode; T = (*1*, *1'*) 300, (*6*) 250, (*2*, *2'*, *5*) 185, (*3*, *3'*, *4*) 77 K; (*1–3*) as-prepared sample, (*1'–3'*, *4–6*) the sample after several months of storage. (b) (*1*, *2*) Without illumination, (*3–6*) illumination of the entire diode, and (*7*) illumination of its central part; T = (*1*, *3*) 300, (*4*) 220, (*5*) 185, and (*2*, *6*, *7*) 77 K. (c) (*1*, *2*) Without illumination, (*3–5*) illumination of the entire diode; T = (*2*, *5*) 300, (*4*) 250, and (*1*, *3*) 77 K. Inserts show the sample configuration. The insert in Fig. 1b illustrates the formation of a surface channel (I) through the depletion region of the Schottky barrier Au-*n*-Si (II) owing to hole accumulation at the barrier contact.

dc conductance G of the structures we studied are nonmonotonic (Fig. 2). The temperature behavior of the dc and ac conductances exhibits similar trends. In the diodes with thermal oxide, the susceptance ωC and conductance $\tilde{G}$ increase with decreasing temperature for $U > \sim 2$ V (curves *6*, *8*) and decrease for lower U, as in the control diodes (curves *3*, *4*); the high-frequency susceptance grows somewhat only at $T < 160$ K (curves *5*, *7*).

Figure 3 shows the susceptance relaxation spectra for the diodes in the form of temperature curves $\omega\Delta C = \omega[C(t_2) - C(t_1)]$, where t_2 and t_1 are fixed instants of time after reverse voltage switching. A set of peaks in the spectra of the control diodes (curve *1*) is similar to that observed earlier in Schottky diodes on *n*-Si with OSF [1, 3]. For structures with thermal oxide, an appreciable monotonic background, which diminishes with sample aging (curves *4–6*), is observed in the spectra. A monotonic background is also present in the spectra measured under illumination (curves *3*, *7*). It can be seen from Fig. 3 that the peaks in the spectra are observed at the same temperatures.

Figure 4 shows temperature dependences of the photovoltage U_{oc} for the diodes we studied (curves *1–4*), the short-circuit photocurrent (i_{sc}) for the structures with thermal oxide (curve *5*), and the photodiode photocurrent (i_{ph}) for the control diodes (curve *6*). It can be seen from the Fig. 4 that, as the temperature is lowered, the photovoltage tends to level off and the photocurrent tends to decrease, with similar nonmonotonic temperature dependences of the photocurrent observed for both types of diodes. Worth noting is the correlation between the photocurrent $i_{sc}(T)$ (curve *5*) and susceptance $\omega C(T)$ temperature dependences (Fig. 2, curve *5*) for the diodes with thermally oxidized surfaces and between $i_{ph}(T)$ (curve *6*) and $\omega C(T)$ (Fig. 2, curve *3*) for the control diodes.

2. DISCUSSION OF THE RESULTS

2.1. Influence of Hopping Transport of Holes in SiO_2 on the Edge Channel Conductance

The common temperature dependences of the electrical and photoelectric characteristics of the diodes we studied indicate their relation to the specific features of the surface channel susceptance. A comparison of the temperature dependences of high-frequency susceptance components and conductance relaxation spectra (Figs. 2, 3) shows that features of the channel current response in the microsecond range are observed in the same temperature ranges as the relaxation spectra peaks corresponding to transient processes with characteristic times of ~1–100 ms. The characteristic times of the slow and fast stages of conductance relaxation can be written as $\tau_f \propto \exp(\Delta E_i/kT)$ and $\tau_s \propto \exp(-\Delta E_i/kT)$, respectively, where ΔE_i is the conductance activation energy at the corresponding peak in the

relaxation spectrum. Therefore, $\tau_s(T) \propto \tau_f^{-1}(T)$, and the faster the initial stage of relaxation, the slower the final stage [2, 3]. These features of the channel dynamics find no explanation in terms of the models of surface conductance in the presence of potential barriers that relate the conductance dynamics to the recharging times of shallow and deep surface states (see, e.g., [6–8]). At the same time, they point to a relation between the channel dynamics and the establishment of the diffusion–drift balance. The surface channel is localized in a potential well bounded by the depletion region of the potential barrier in Si and the wide-gap insulator SiO_2, both of which serve as the channel "gates." When the voltage is switched, the potential distributions in the depletion region and in the SiO_2 film produce transverse fields at the channel boundaries; screening of these fields must change the channel conductance. The influence of the transverse field on the interface between the channel and the space charge region was discussed previously [3]. In this study, we consider the contribution of hopping transport of holes in SiO_2 and their accumulation near the cathode which also induces transport of free electrons over the Si surface to the channel conduction dynamics, taking into account the high hole density in the thermal SiO_2 film. First, we note that the experimentally observed characteristic features of transient processes are typical of the dynamics of disordered systems. In particular, when the field is screened in amorphous insulators, slow "tails" in the polarization current pulses are longer if the initial current falloff is faster [9, 10]. The polarization dynamics of thermal SiO_2 reflects a wide spectrum of characteristic times in the range of 10^{-6}–10^2 s [11]. An additional argument is furnished by the similar temperature dependences of the channel conductance at the Si/SiO_2 interface, observed in this study (Fig. 2, curves *3*, *4*), and the hole mobility $\mu(T)$ in SiO_2 [11]. We also note that the oxygen deficit in the oxides can give rise to a set of dielectric loss $\varepsilon''(T, \omega)$ peaks [12] with temperature positions close to the set of $\Delta\omega C(T)$ peaks observed in this study (and a similar set of $\Delta\tilde{G}(T)$ peaks [1]). In addition, peaks of this kind were also observed at low temperatures in studies of the absorption of sound in Si crystals with surface defects [13] and dislocations [14] in the temperature spectra of internal friction. Similarly to the $\varepsilon''(T, \omega)$ spectra, these spectra reflect the onset of defect mobility [15].

Competitive contributions to the surface channel conductance come from negative ($Q_{ox}^- = Q_{ss}^- + Q_f^-$) and positive ($Q_{ox}^+ = Q_{ss}^+ + Q_f^+$) surface charges. Here, Q_{ss}^- and Q_{ss}^+ are the electron and hole charges localized at the interfacial states at the Si/SiO_2 interface and Q_f^- and Q_f^+ are the negative and positive built-in charges

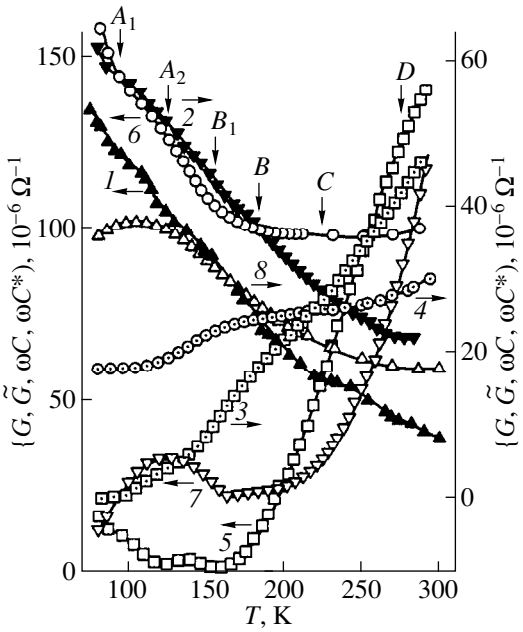

Fig. 2. Temperature dependences of the static conductance G (*1*, *2*), conductive $\tilde{G}$ (*7*, *8*) and capacitive ωC (*4*, *6*) components of the high-frequency susceptance, temperature-dependent part of the capacitive component ωC^* (*3*, *5*) for Schottky diodes after several days (*1*) and several months of storage (*2–8*). (*1*, *2*, *5–8*) Thermal oxide and (*3*, *4*) natural oxide at the periphery. Ordinate axis: (*1*, *5–7*) on the left, (*2–4*, *8*) on the right. U = (*1*, *2*) 7, (*3*, *5*, *7*) 0.6, and (*4*, *6*, *8*) 2.5 V. f = 160 kHz. Arrows indicate the temperature positions of the spectral peaks in curve *1* of Fig. 3.

localized in traps in SiO_2 at the Si surface [16, 17]. The surface current leakage in diodes with thermal oxide at $U \ll kT/e$ (Fig. 1, curves *1–3*) is associated with the formation of positive charge in SiO_2 during oxidation. In this case, $|Q_{ox}^+| > |Q_{ox}^-|$ and the nonmonotonic temperature dependence of the conduction is determined by the variation of Q_{ox}^+ with temperature. The decrease in conductance upon cooling for small U in the samples subjected to aging (Fig.1, curves *1'–3'*) can be attributed to partial recovery of the surface barrier due to Q_{ox}^+ annealing, followed by an increase in the Si dangling-bond density at the surface [17]. However, the increase in voltage compensates for the influence of Q_{ox}^+ annealing, and the temperature behavior of $G(T)$ remains unchanged (Fig. 2, curves *1*, *2*).

This can be explained by the participation of holes in edge-field screening. On switching the reverse voltage, the hole flow to the negative electrode (i.e., the blocking $Au–SiO_2$ contact) induces the corresponding electron flow over the Si surface. The slight rise in current with increasing voltage for small U may be due to the predominance of broadening of the Schottky barrier depletion region with increasing voltage ($w \propto U^{1/2}$) and,

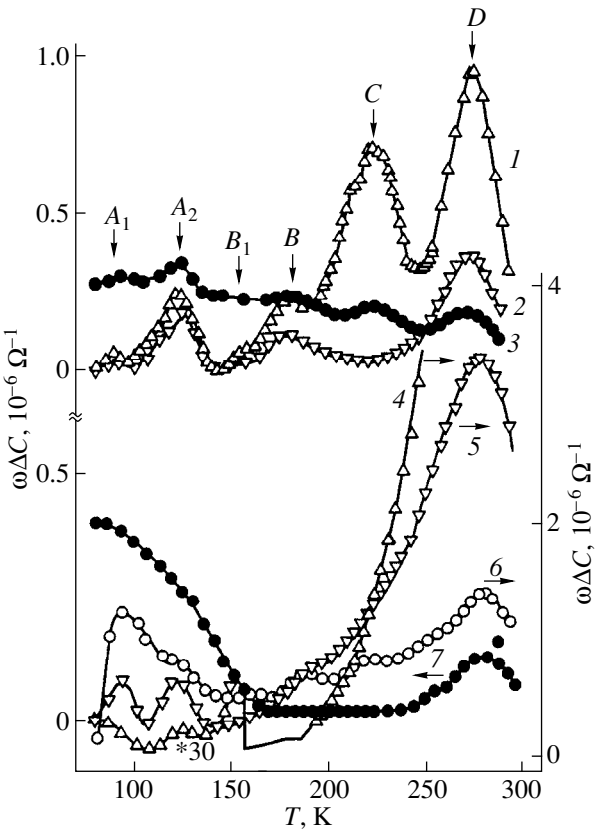

Fig. 3. Relaxation spectra of the capacitive component of the high-frequency susceptance in the surface channel at the interface of Si with (*1–3*) natural and (*4–7*) thermal oxides, measured (*1, 2, 4–6*) in the dark and (*3, 7*) under illumination after sample storage for (*1, 4*) several days and (*2, 3, 5–7*) several months. t_1 = 2 ms, t_2 = 10 ms. f = 160 kHz. Switching ($U_1 \longrightarrow U_2$): (*1, 3*) (0 ⟶ 8), (*2*) (0.2 ⟶ 1), (*4, 5*) (0 ⟶ 4.5), and (*6, 7*) (1 ⟶ 2.5) V.

correspondingly, to channel narrowing with the channel length L becoming larger. The superlinear increase in the channel current at $U > 2$V may be due to the accumulation of holes in SiO_2 at the cathode, which leads to enrichment of the near-cathode surface with electrons and higher conductance of the channel. The sublinear behavior observed with a further increase in U may be associated with saturation of the Q_{ox}^+ charge redistribution and with an increase in $L \propto U^{1/2}$.

In the model discussed here, the dynamics of the channel current response are determined by the dynamics of the hole accumulation in SiO_2 at the cathode. The kinetics of the hole current response to a steplike voltage change in amorphous SiO_2 films are typical of dispersive hopping transport of charge carriers. After the initial current jump, a fast falloff is observed within times $t < t_{tr}$, where t_{tr} is the hole transit time ($i_1 \propto t^{-(1-\beta)}$, β = 0.15–0.3), with subsequent slow decay at $t > t_{tr}$ ($i_2 \propto t^{-(1+\beta)}$), so that the faster the initial falloff, the slower the final decay [11].

The kinetics of the current response in the channel can also be affected by negative feedback [4]. When the voltage is switched, the fast rise in the channel conductance at the cathode induced by hole accumulation must terminate because of a voltage redistribution, where the field is decreased at the cathode and increased at the anode. The decay of the channel conductance must slow down owing to the increase in the channel length and the resulting rise in the number of holes involved in the field screening. Thus, negative feedback in the channel must cause the characteristic time of the fast initial relaxation stage to shorten and the final slow stage to become even slower.

The phase shift between the current and voltage at high frequency $f \sim (2\pi t_{tr})^{-1}$ determines the nature (capacitive or inductive) of the reactive current in the channel and the active current strength and depends on ωt_{tr}. Since $t_{tr} = [L(n_s)]^2/\mu U$ and $n_s \sim Q_{ss}^+$, where n_s is the surface electron density, the $G(T)$ and $\omega C(T)$ dependences are associated with temperature changes in the hole mobility and concentration in SiO_2 and are representative of the $Q_{ss}^+(T)$ dependence. The prevalence of Q_{ox}^+ results in an increase in the conductance on cooling. When Q_{ox}^- is prevalent, the $Q_{ss}^+(T)$ dependence is manifested as a tendency for the above-barrier surface current decay to become nonmonotonically slower on cooling, and the slope of the $\tilde{G}(T)$ and $\omega C(T)$ curves to decrease. The conductance relaxation spectra reflect the decrease in the inductive component (and the corresponding increase in the susceptance ωC) and the rise in conductance $\tilde{G}$, with the through-channel conductance increasing upon a steplike change of the reverse voltage.

2.2. Influence of Hole Trapping by Surface States on the Channel Photoresponse

During excitation by light, which generates electron–hole pairs in Si, photogenerated holes are captured by surface states and the channel conductance increases. Under illumination, the downward band bending at the Si surface adjacent to the SiO_2 film gives rise to a photovoltage U_s with a polarity opposite to that of the Schottky barrier photovoltage, U_{oc}. Thus, the surface channel can be simultaneously a photovoltage source and a nonlinear photoresistor $R_s(U_s)$ (Fig. 4). Without an external bias, the direction of the channel photocurrent $i_s(U_s, R_s)$ is opposite to that of the photocurrent generated in the space-charge region of the Schottky barrier i_{sc}^*. The resulting decrease in the short-circuit photocurrent $i_{sc} = i_{sc}^* - i_s(U_s, R_s)$ becomes more pronounced with increasing downward band bending at the surface. The nonmonotonic $i_{sc}(T)$ depen-

dence in the structures with thermal oxide can be explained by the nonmonotonic increase in downward band bending with decreasing temperature. The channel resistance reduces the photovoltage contribution U_s to i_{sc}, which is observed in the control diodes where i_{sc} is nearly temperature-independent.

As the bias is increased, which causes hole accumulation at the cathode and barrier removal, the photocurrent of the diodes with a thermally oxidized surface increases with cooling in the temperature range of $140 < T < 300$ K (Fig. 1a, curves *5*, *6*). In the control diodes, Q_{ox}^- is dominant, as shown by the increase in the dark resistance on cooling and by the sublinear behavior of the *I–V* characteristics under illumination. Accordingly, the increase in Q_{ss}^+ on cooling only causes the photocurrent decay in the channel to become slower, which accounts for the correlation between the $i_{sc}(T)$ dependences in the diodes with a thermally oxidized surface and $i_{ph}(T)$ in the control diodes.

Under forward bias, the channel resistance $R_s(T)$ decreases with voltage faster than the resistance of a Schottky diode without surface leakage, $R_i(T)$. This leads to a decrease in the photocurrent i_{sc} (Fig. 1b, curve *6*). The rise in photovoltage on cooling (due to widening of the band gap and a temperature shift of the Fermi level toward the conduction-band bottom in the Si bulk) also terminates, because of the great surface leakage. The leveling off of the photovoltage at low temperatures (Fig. 4, curves *1–4*) is more pronounced under local illumination of the photodiode periphery (curve *3*). Under local illumination of the central part of the photodiode, the leveling off of the photovoltage (curve *2*) and reduction in the photocurrent (Fig. 1b, curve *7*) are less pronounced, thus supporting the model.

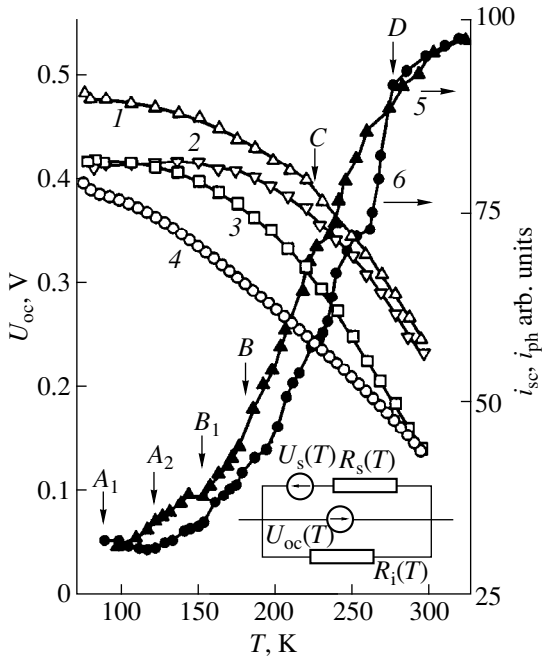

Fig. 4. Temperature dependences of the U_{oc} (*1–4*) photovoltage, (*5*) short-circuit photocurrent i_{sc} and (*6*) photocurrent i_{ph} at $U = 7$ V for Schottky diodes with (*1–3*, *5*) thermal and (*4*, *6*) native oxides at the periphery. (*1*, *4–6*) Illumination of the entire diode, (*2*) local illumination of the periphery, and (*3*) illumination of the central part of the diode. Arrows indicate the temperature positions of the peaks in spectrum *1* of Fig. 3. Insert: approximate equivalent circuit of a sample, illustrating the influence of the surface channel on the photovoltage and photocurrent.

2.3. Temperature Dependences of Conductance, Photovoltage, and Photocurrent

It was suggested previously [3, 4] that the formation of the positive charge Q_{ss}^+ at the Si/SiO_2 interface and its buildup on cooling is due to oxygen complexes with labile chemical bonds, whose valence changes in the temperature region of microscopic phase transitions. In frozen oxygen [18] and hydrogen–oxygen condensates [19], these transformations are governed by the disproportionation reaction

$$2O_2^{2-} \longrightarrow O_2 + 2O^{2-}. \quad (1)$$

As a result, molecular ions of oxygen peroxide O_2^{2-} are transformed on heating from 77 to 300 K into atomic ions O^{2-} and molecular oxygen O_2, whose release increases abruptly at 150 and 220 K. In SiO_2, the covalent bond fraction is rather large and we can only conditionally discuss the oxygen ions by representing reaction (1) as a decrease in the energy of quasi-molecular bonds (O–O) between two oxygen atoms with dangling bonds and holes localized on the nonbonding orbitals (O^-). In the Si/SiO_2 system, oxygen atoms with captured holes (O^-) and their dimers, O_2^{2-} ions, can supply free electrons to the Si surface:

$$2O^- + 2e \rightleftharpoons O_2^{2-} + 2e \rightleftharpoons 2O^{2-}.$$

The nonmonotonic increase in the surface density of O_2^{2-} and O^- and, hence, in that of Q_{ss}^+, also results in an increase in the electron density at the Si surface on cooling.

3. CONCLUSION

In Schottky diodes on Si, the current response of the edge electron channels induced by the positive charge in the oxide film is associated with hopping transport of holes in SiO_2 and their accumulation at the blocking contact, which also causes accumulation of electrons at the barrier contact in *n*-Si. The localized-hole and free-electron densities at the Si/SiO_2 interface vary with temperature owing to changes in the valence of oxygen complexes. The increase in the free-electron density at

the Si surface in the dark and under illumination leads to leveling off of the photovoltage and a nonmonotonic decrease in the diode photocurrent on cooling.

REFERENCES

1. N. I. Bochkareva and A. V. Klochkov, Fiz. Tekh. Poluprovodn. (St. Petersburg) **32**, 82 (1998) [Semiconductors **32**, 71 (1998)].
2. N. I. Bochkareva, Fiz. Tekh. Poluprovodn. (St. Petersburg) **28**, 290 (1994) [Semiconductors **28**, 175 (1994)].
3. N. I. Bochkareva and A. V. Klochkov, Fiz. Tekh. Poluprovodn. (St. Petersburg) **32**, 1432 (1998) [Semiconductors **32**, 1277 (1998)].
4. N. I. Bochkareva and S. A. Khorev, Fiz. Tekh. Poluprovodn. (St. Petersburg) **33**, 1340 (1999) [Semiconductors **33**, 1212 (1999)].
5. V. V. Voronkov, G. I. Voronkova, V. P. Kalinushkin, *et al.*, Fiz. Tekh. Poluprovodn. (Leningrad) **18**, 938 (1984) [Sov. Phys. Semicond. **18**, 584 (1984)].
6. E. H. Nicollian and A. Goetzberger, Bell Syst. Tech. J. **46**, 1055 (1967).
7. E. V. Vlasenko, R. A. Suris, and B. I. Fuks, Fiz. Tekh. Poluprovodn. (Leningrad) **11**, 1112 (1977) [Sov. Phys. Semicond. **11**, 657 (1977)].
8. V. N. Alfeev, A. V. El'tsov, S. T. Ivanchenko, and V. V. Shirokov, Fiz. Tekh. Poluprovodn. (Leningrad) **16**, 692 (1982) [Sov. Phys. Semicond. **16**, 443 (1982)].
9. H. Scher and E. W. Montroll, Phys. Rev. B **12**, 2455 (1975).
10. N. F. Mott and E. A. Davis, *Electronic Processes in Non-Crystalline Materials* (Clarendon, Oxford, 1979; Mir, Moscow, 1982).
11. R. C. Hughes, Phys. Rev. B **15**, 2012 (1977).
12. Z. Yu, C. Ang, and L. E. Cross, Appl. Phys. Lett. **74**, 3044 (1999).
13. B. M. Mecs and A. S. Nowick, Appl. Phys. Lett. **8**, 75 (1966).
14. L. P. Khiznichenko, P. F. Kromer, D. K. Kaipnazarov, *et al.*, Phys. Status Solidi **21**, 805 (1967).
15. A. S. Nowick and B. S. Berry, *Anelastic Relaxation in Crystalline Solids* (Academic, New York, 1972; Atomizdat, Moscow, 1975).
16. R. W. Gurtler, IEEE Trans. Electron Devices **ED-15**, 980 (1968).
17. A. P. Baraban, V. V. Bulavinov, and P. P. Konorov, *Electronics of SiO_2 Layers on Silicon* (Leningradsk. Gos. Univ., Leningrad, 1988).
18. M. Yu. Smirnov and V. V. Gorodetskiĭ, Poverkhnost, No. 7, 21 (1986).
19. T. V. Yagodovskaya and L. I. Nekrasov, Zh. Fiz. Khim. **51**, 2434 (1977).

Translated by D. Mashovets

Semiconductors, Vol. 34, No. 10, 2000, pp. 1183–1185. Translated from Fizika i Tekhnika Poluprovodnikov, Vol. 34, No. 10, 2000, pp. 1234–1236.

SEMICONDUCTOR STRUCTURES, INTERFACES, AND SURFACES

A Study of an Al–Ge_3N_4–Ge Structure by the Method of Photo-Capacitance–Voltage Characteristics

R. B. Dzhanelidze, M. B. Dzhanelidze, and M. R. Katsiashvili

Institute of Cybernetics, Academy of Sciences of Georgia, Tbilisi, 380086 Georgia

Submitted March 21, 2000; accepted for publication April 6, 2000

Abstract—Results are reported of a study of a Ge–Ge_3N_4 interface by the method of capacitance–voltage characteristics, with the structure irradiated with photons of varied energy. The employed technique revealed trap levels in germanium nitride located at 0.75, 0.89, and 3.0 eV below the conduction-band bottom. A study of the current through the Ge–Ge_3N_4 structure yielded two levels in Ge_3N_4 at depths of 0.75 and 0.87 eV. © *2000 MAIK "Nauka/Interperiodica".*

1. INTRODUCTION

Germanium nitride (Ge_3N_4) occupies a prominent place among films of insulating materials used in metal–insulator–semiconductor (MIS) structures. It suffices to say that Ge_3N_4 provides the best solution to the complicated problem of developing a gallium arsenide MIS transistor [1]. A vast body of information has been accumulated concerning methods for obtaining Ge_3N_4 and studying its properties. However, the position of energy levels in the band gap of germanium nitride has only been reported in a single publication [2].

In this communication, we report the results obtained in studying (with the aim of gaining insight into the nature of various defects in Ge_3N_4 and determining the trap levels in this material) the effect exerted by irradiation with photons of varied energy on the charge state of the Ge_3N_4–Ge interface. These data are also compared with the results of a study of current flow through a Ge_3N_4–Ge structure.

2. EXPERIMENTAL

MIS structures of the Al–Ge_3N_4–Ge type were fabricated using germanium substrates with [111] orientation (resistivity $\rho = 4.5\ \Omega$ cm). Thin films of amorphous Ge_3N_4 (0.12–0.15 μm thick) were deposited onto germanium at 350–400°C [3]. Semitransparent aluminum contacts 0.5 mm in diameter were deposited by vacuum evaporation. Capacitance–voltage (*C–V*) characteristics were measured at a frequency of 1 MHz on an IPPM-02 setup and recorded with an N-307 XY-recorder. For a light source, we used a TRU-1100-2350 incandescent lamp. The *C–V* characteristics were measured with a metal probe as a contact to the semitransparent metal electrode.

3. RESULTS AND DISCUSSION

Figure 1 shows a typical *C–V* characteristic of an Al–Ge_3N_4–Ge structure (curve *1*). The flat-band voltage (V_{FB}) calculated for this structure is 0.5 V, with a hysteresis of 0.05–0.1 V. Illumination of a structure of this kind with UV radiation (photon energy $\hbar\omega$ = 4.6 eV) shifts the *C–V* characteristic to more positive voltages, with V_{FB} increasing to 0.8–0.9 V (Fig. 1, curve *2*). This indicates a build-up of positive charge at the germanium surface. Figure 2 shows V_{FB} as a function of the illumination time τ at photon energies $\hbar\omega$ = 0.75, 1.5, and 4 eV. As initial V_{FB} values, we took those

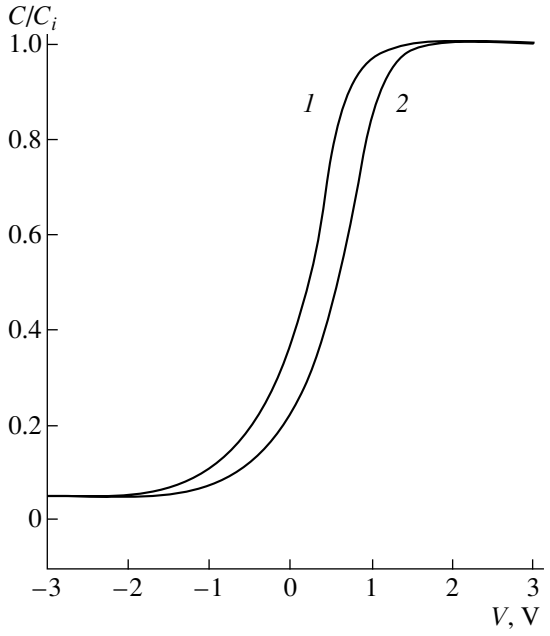

Fig. 1. *C–V* characteristics of an Al–Ge_3N_4–Ge structure: (*1*) in the dark and (*2*) under illumination with UV light. C_i is the calibration capacitance.

1063-7826/00/3410-1183$20.00 © 2000 MAIK "Nauka/Interperiodica"

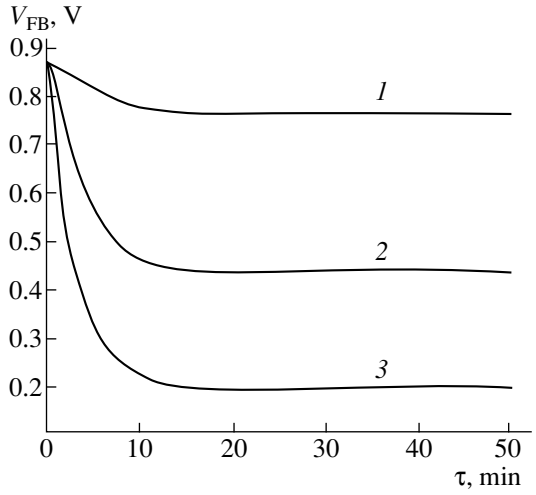

Fig. 2. Flat-band voltage vs. time of irradiation with photons with energies $\hbar\omega$ = (*1*) 0.75, (*2*) 1.5, and (*3*) 4 eV.

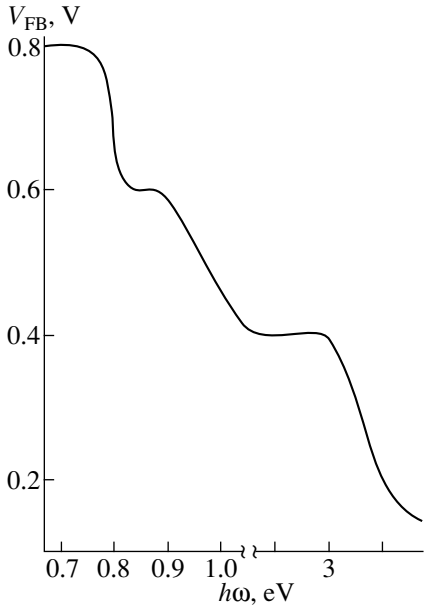

Fig. 3. The leveling-off value of V_{FB} vs. photon energy.

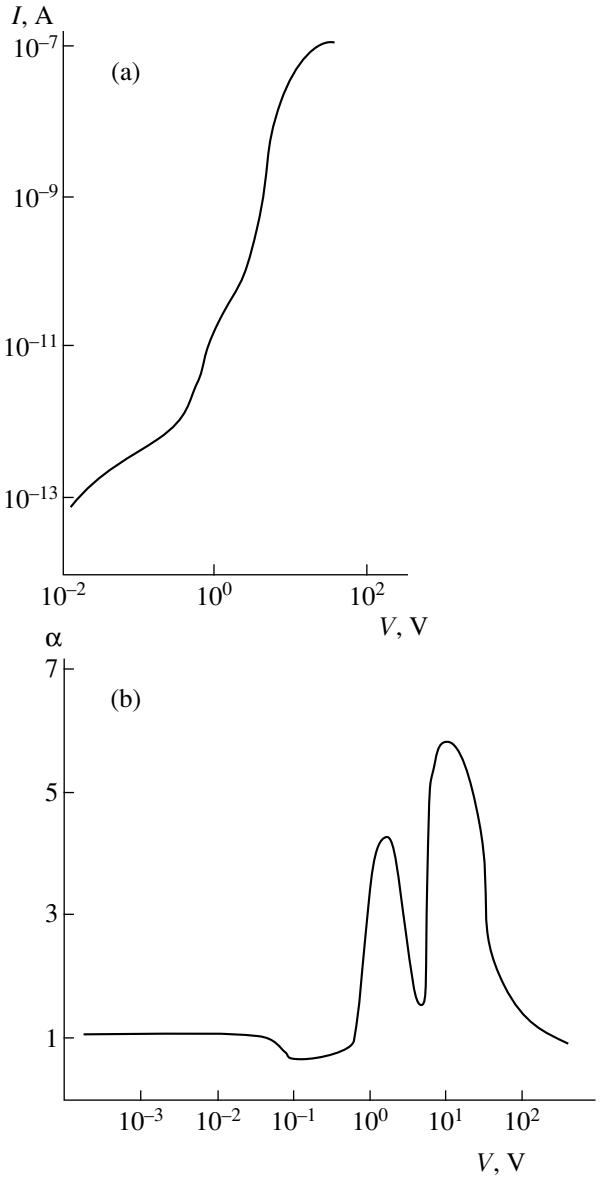

Fig. 4. (a) I–V characteristic of an Al–Ge_3N_4–Ge structure and (b) exponent α in the $I(V)$ dependence vs. voltage.

after irradiation of the Al–Ge_3N_4–Ge structure with UV light. As can be seen from Fig. 2, irradiation with photons with different energies causes V_{FB} to decrease during a certain initial period and then to level off. The time after which leveling-off occurs τ = 10 min. For low light intensity, V_{FB} levels off more slowly but its values remain the same. To determine the trap levels in germanium nitride, the V_{FB} level-off values, obtained in the same way as in Fig. 2, are plotted against photon energy (Fig. 3). It can be seen that V_{FB} starts to decrease at 0.75 eV and then a plateau is observed in the range from 0.80 to 0.89 eV. Further, V_{FB} decreases to 1.5 eV. A second plateau is observed in the energy range of 1.5–3.0 eV. Beginning with 3.0 eV, V_{FB} falls abruptly. The dependence in Fig. 3 can presumably be explained as follows. Since the band gap of Ge_3N_4 equals 4.2 eV, illumination of the MIS structure with UV light depopulates all traps in Ge_3N_4. Simultaneously, free carriers are generated in germanium. In view of the fact that the work function for electrons in Ge (4.4 eV) is smaller than the value determined in this study for Ge_3N_4 (4.9 eV),[1] electrons mainly pass from Ge into Ge_3N_4. This gives rise to a contact field directed from Ge to Ge_3N_4. The electrons that have passed into Ge_3N_4 occupy empty states in the Ge_3N_4 band gap, increase the positive charge in Ge, and, consequently, cause the

[1] The work function for electrons in Ge_3N_4 was determined from the contact-potential difference (the Kelvin method).

V_{FB} to increase. Further illumination of such a structure with photons of varied energy causes electron emission from the traps in Ge_3N_4. These electrons again pass, under the action of the contact field, into Ge, thus reducing the positive charge in Ge and, correspondingly, the V_{FB}. Thus, the surface potential of Ge can be reversibly changed by irradiation with photons with energy in the range of 0.75–3.0 eV. From the obtained results (Fig. 3) it follows that Ge_3N_4 contains shallow- and deep-level traps located at 0.75, 0.89, and 3.0 eV below the Ge_3N_4 conduction-band bottom.

The existence of these levels in Ge_3N_4 was confirmed by measuring the current–voltage (*I–V*) characteristics of the structures under study. The mechanism of current flow has been considered for an Al–Ge_3N_4–Ge structure, and the energy spectrum of localized states in the band gap of Ge_3N_4 was calculated [4]. This was done using a generalized approximate theory of injection-contact phenomena and the method developed on its basis for quantitatively determining the above parameters [5]. Figure 4a shows a typical *I–V* characteristic of the Al–Ge_3N_4–Ge structure, and Fig. 4b shows the voltage dependence of the exponent in the $I(V)$ dependence, $\alpha = d\log I/d\log V$. The concentrations and depths of trap levels in Ge_3N_4 were calculated for the system in question. Two levels were clearly recognized in a germanium nitride film, lying at depths of 0.87 and 0.75 eV, with concentrations of 6.2×10^{16} and 1.6×10^{17} cm^{-3}, respectively. A comparison of the trap level depths found by this method with those determined from photocurrent–voltage characteristics shows that the results are in a reasonably good agreement. As for the level with an energy of 3.0 eV, fields stronger than 10^6 V/cm would be necessary to observe its manifestation in the *I–V* characteristics. However, the existence of this level is indicated by the data elsewhere [2].

4. CONCLUSION

It was shown by the methods of photo-capacitance–voltage and current–voltage characteristics that energy levels located at depths of 0.75, 0.89, and 3.0 eV exist in germanium nitride.

ACKNOWLEDGMENTS

The authors are grateful to N.I. Kurdiani for his interest in this study and helpful participation in discussions.

REFERENCES

1. G. D. Bagratishvili, R. B. Dzhanelidze, N. I. Kurdiani, *et al.*, Thin Solid Films **56**, 209 (1979).
2. Takehisa Yashiro, Jpn. J. Appl. Phys. **10**, 1691 (1971).
3. G. D. Bagratishvili, R. B. Dzhanelidze, N. I. Kurdiani, and O. V. Saksaganskiĭ, Mikroélektronika **2**, 173 (1973).
4. G. D. Bagratishvili, R. B. Dzhanelidze, D. A. Jishiashvili, *et al.*, Phys. Status Solidi A **65**, 701 (1981).
5. A. N. Zyuganov, P. S. Smertenko, and E. P. Shulga, Poluprovodn. Tekh. Mikroélectron. **29**, 48 (1979).

Translated by M. Tagirdzhanov

Semiconductors, Vol. 34, No. 10, 2000, pp. 1186–1192. Translated from Fizika i Tekhnika Poluprovodnikov, Vol. 34, No. 10, 2000, pp. 1237–1243.

SEMICONDUCTOR STRUCTURES, INTERFACES, AND SURFACES

ZnMgSe/ZnCdSe-Based Distributed Bragg Mirrors Grown by Molecular-Beam Epitaxy on ZnSe Substrates

V. I. Kozlovskiĭ*, P. A. Trubenko, Yu. V. Korostelin*, and V. V. Roddatis*****

** Lebedev Institute of Physics, Russian Academy of Sciences, Leninskiĭ pr. 53, Moscow, 117924 Russia*
e-mail: vikoz@x4u.lebedev.ru
*** Fiber Optics Research Center, Institute of General Physics, Russian Academy of Sciences, Moscow, 117756 Russia*
**** Shubnikov Institute of Crystallography, Russian Academy of Sciences, Leninskiĭ pr. 59, Moscow, 117333 Russia*
Submitted April 3, 2000; accepted for publication April 6, 2000

Abstract—Molecular-beam epitaxy was used to grow distributed Bragg mirrors on ZnSe substrates. These mirrors are composed of 10.5 and 20 pairs of alternating quarter-wave ZnMgSe and ZnCdSe layers with reflectance peaks at the wavelengths of 530 and 560 nm, respectively, which fall in the transparency region of the substrate. These structures were studied by low-temperature cathodoluminescence, atomic-force microscopy, and transmission electron microscopy. The maximum of the reflection coefficient was 78% for a 20-pair mirror and 66% for a 10.5-pair mirror. This result is interpreted in terms of a model that takes into account the roughness of the interlayer boundaries. *© 2000 MAIK "Nauka/Interperiodica".*

1. INTRODUCTION

Distributed Bragg mirrors (DBMs) are the key elements in surface-emitting semiconductor lasers and light-emitting diodes with a "vertical" microcavity [1]. A small number of quantum wells acting as an amplifying medium is typical of injection lasers. The total effective amplification length per pass in such a cavity is hundredths of a micrometer. In this case, even for a material gain of 10^4 cm^{-1}, the losses in the cavity mirrors by transmission and scattering of radiation should not exceed about 1%. Such parameters are attained for DBMs formed of oxides of the SiO_2/TiO_2 type that are noted for their large (~1.0) difference in the refractive indices of alternating layers. However, at least one mirror should be conducting in the case of injection pumping. In addition, the use of insulating mirrors requires removal of the substrates on which the structure is grown, which adds to the complexity of the fabrication technology.

For III–V-based lasers emitting in the infrared region of the spectrum, this problem is solved to a large extent owing to the transparency of the GaAs, InP, and GaP substrates that are used, and to the unique properties of the GaAs and AlAs pair. With widely differing refractive indices ($\Delta n \approx 0.7$), this pair exhibits an insignificant mismatch in the crystal-lattice period $\Delta a \approx 0.0016$. This makes it possible to use a large number of pairs without significantly affecting the morphology of interlayer boundaries and the surface. A high surface quality is important not only for diminishing the losses in the cavity by radiation scattering but also for subsequent growth of an efficient active medium for DBMs.

Much less progress has been made in this field for II–VI compounds. The use of gaseous-phase epitaxy from metal-organic compounds to form DBMs on a GaAs substrate was reported elsewhere [2]. These DBMs had a reflection coefficient $R = 0.945$ ($\lambda = 465$ nm) when 10 ZnSe/ZnS pairs were used. The formation of mirrors that had $R = 0.93$ ($\lambda = 510$ nm) were formed of a mere five pairs of ZnSe and ZnMgS layers was also reported [3]. However, due to a large mismatch in the lattice parameters of these layers, the DMB quality is low, which makes the formation of a active size-quantization structure monolithic with the mirror. On the basis of matched ZnMgSe/ZnCdSe pairs, a DBM with $R = 0.98$ at $\lambda = 616$ nm was attained [4] by molecular-beam epitaxy on a GaAs substrate. Such a high reflection coefficient was also attained at $\lambda = 595$ nm using 30 alternating pairs of $Mg_{0.1}(Zn_{0.48}Cd_{0.52})_{0.9}Se$ and $Mg_{0.6}(Zn_{0.48}Cd_{0.52})_{0.4}Se$ layers matched to the InP substrate [5]. Growth problems also presented a serious obstacle to attaining high reflectance. Thus, in a ZnMgSe/ZnSeTe system distinguished by its relatively large difference in refractive indices ($\Delta n \approx 0.35$), a reflection coefficient as small as $R = 0.85$ (at $\lambda = 750$ nm) was obtained [4]. If the ZnSSe/ZnMgSSe pair that is most widely used in injection lasers and is matched to the GaAs substrate, it is also impossible to obtain high reflectance. In order to increase the value of Δn, it is necessary to increase the concentration of S and Mg in the ZnMgSSe layers, which causes the solid-solution crystal structure to deteriorate. The best result corresponds to $R = 0.9$ for $\lambda = 500$ nm [6].

However, all the data on DBMs made of II–VI compounds have been obtained so far in the case of nontransparent GaAs or InP substrates. Therefore, these data cannot be used to construct the output mirror of the cavity without using the complicated technology for

1063-7826/00/3410-1186$20.00

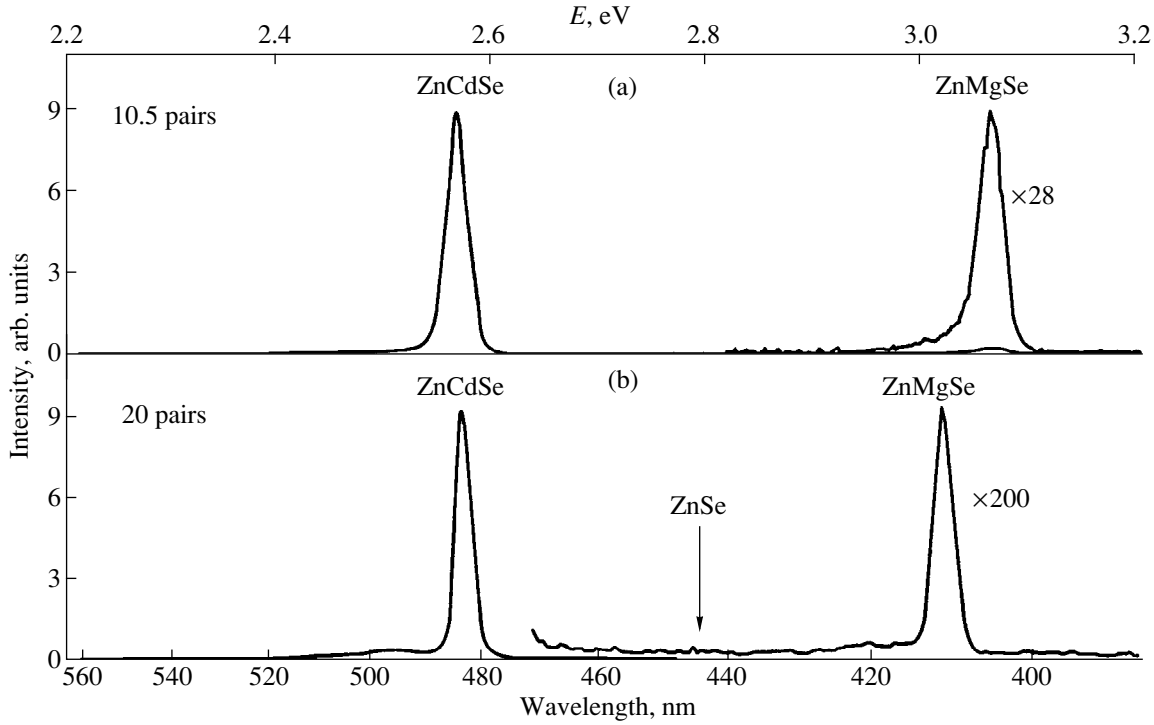

Fig. 1. Cathodoluminescence spectra of the structures with (a) 10.5 and (b) 20 pairs of alternating ZnCdSe and ZnMgSe layers at $T = 14$ K, $j_e = 1$ mA/cm^2, and $E_e = 10$ keV.

removing the substrate. In this study, for the first time, we obtained DBMs using ZnMgSe and ZnCdSe layers on a ZnSe substrate in its transparency region. In future, it is expected that such a mirror will be used in the development of a monolithic active element of a laser electron-beam tube with a low lasing threshold at room temperature [7]. Moderately high reflectivities ($R \approx 0.9$) are required for such applications.

2. EXPERIMENTAL

The wafers for the (100)-oriented substrates were cut from a ZnSe single crystal grown from the vapor phase by the method of free growth by chemical transport in a hydrogen atmosphere [8]. The ZnSe single crystal had an etch-pit density no higher than 5×10^4 cm^{-2} revealed at the (100) surface using a Br solution in methanol. The wafers were first subjected to mechanical grinding and polishing and were then etched in a CrO_3 polishing solution in HCl to remove the damaged layer. Immediately before being installed in the growth chamber, the substrates were kept in a diluted HCl solution in order to remove the oxide layer [9]. A thin Se layer formed as a result of the latter treatment was removed in the growth chamber by heating the substrate to a temperature of 350°C.

Epitaxial structures were grown by molecular-beam epitaxy. The substrate temperature during growth was 300°C. In the course of growth, the substrate was rotated with constant speed in order to ensure a higher uniformity of the epitaxial-structure parameters. The growth rate for the layers with differing composition was determined by transmission electron microscopy for reference samples. The typical growth rate was 0.25 μm/h for ZnSe films.

Several multilayer structures were grown. Here we report the results of measuring the parameters of two of these structures. In the structures, a 380-nm-thick buffer ZnSe layer was grown first and then a set of alternating quarter-wave ZnCdSe and ZnMgSe layers that terminated with a ZnCdSe layer was grown. In structure 134, the first layer following the buffer was a ZnMgSe layer. The total number of layers was 40 (20 pairs). The first layer in the second (142) structure was ZnCdSe, and there were 21 layers (10.5 pairs) in total. The quarter-wave layers corresponded to a wavelength of 520 nm, based on the data on refractive indices reported elsewhere [10].

Cathodoluminescence of the structures was studied at $T = 14$ K for the electron energy $E_e = 10$ keV and the current density $j_e = 1$ mA/cm^2. The samples were studied by transmission electron microscopy (TEM) using a Philips EM-430ST microscope with an accelerating voltage of 200 kV. The samples for TEM were thinned by conventional methods (by mechanical polishing with subsequent ion etching with an argon beam). The optical transmission and reflection spectra were measured using a UV/VIS/NIR Spectrometer Lambda 900

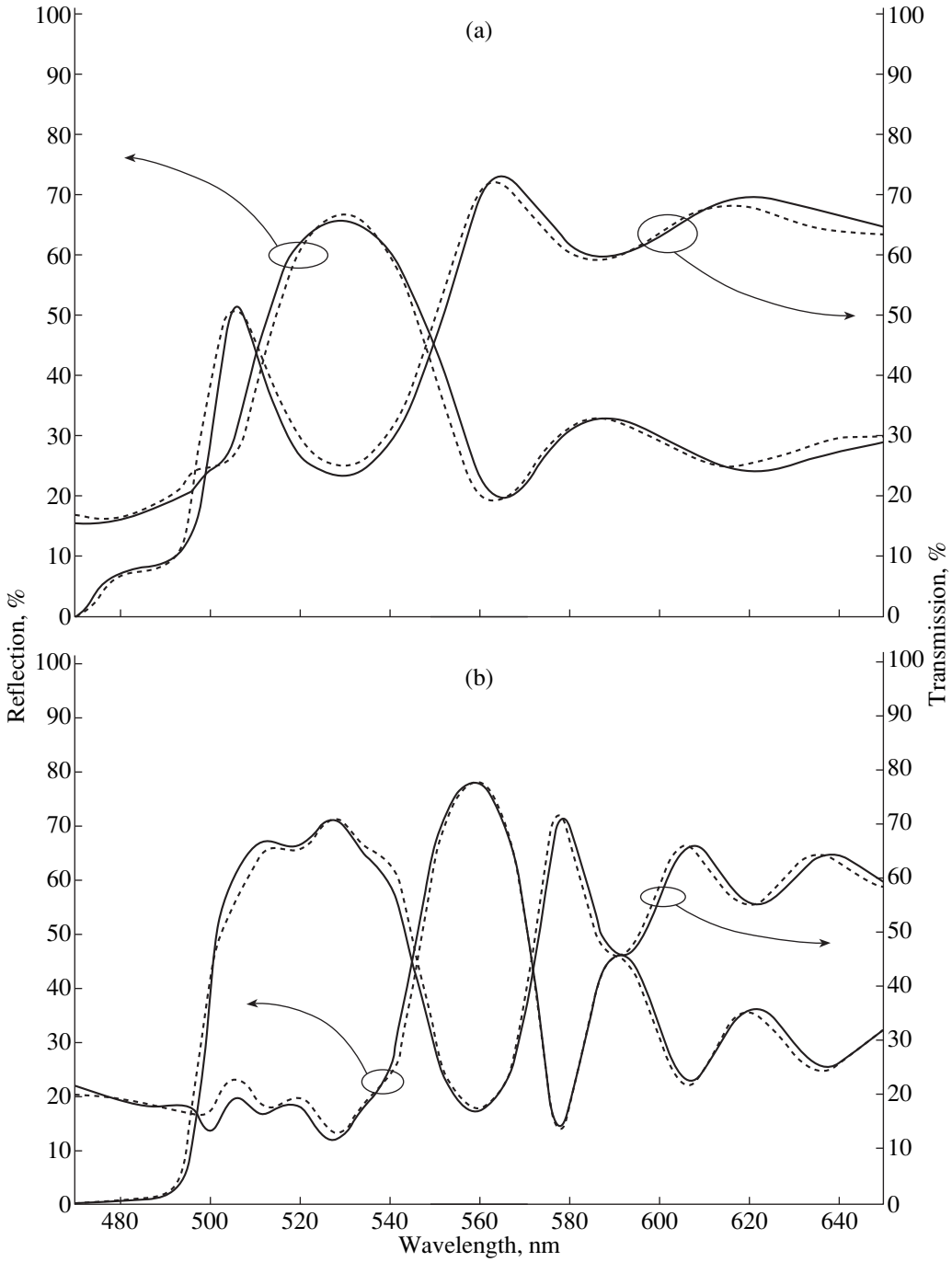

Fig. 2. The optical transmission and reflection spectra of the Bragg mirrors with (a) 10.5 and (b) 20 pairs of ZnCdSe and ZnMgSe layers grown on a ZnSe substrate 1.1 mm thick: the solid lines correspond to the experiment and the dashed lines represent the results of the numerical simulation. The numbers of the samples are (a) 142 and (b) 134.

(Perkin Elmer). The reflection spectrum of the samples was measured from the multilayer-structure side. Absolute values of the reflection coefficient were determined from the reflection coefficient of a freshly deposited Al layer that exhibited $R = 0.89$ in the green region of the spectrum.

3. RESULTS AND DISCUSSION

Figure 1 shows the cathodoluminescence spectra of two structures with DBMs. Emission lines of the structures are fairly narrow (the half-width at half maximum is less than 25 meV), which makes it possible to determine the composition of the layers with high accuracy.

Using the data on the dependence of the band gap on the solid-solution composition for $Zn_{1-x}Cd_xSe$ [11] and $Zn_{1-y}Mg_ySe$ [12], we obtained $x = 0.14$ for both structures and $y = 0.2$ and 0.24 for samples 134 and 142, respectively. Then, on the basis of the x dependence of the solid-solution atomic spacing for $Zn_{1-x}Cd_xSe$ [13] and $Zn_{1-y}Mg_ySe$ [12], we found that the lattice mismatch of the alternating layers was less than 0.04% in sample 134 and about 0.24% in sample 142. For such values of mismatch, the critical scale of coherent growth ($h_c \approx 130$ nm for $\Delta a/a = 0.24\%$ [14]) exceeds the layer thicknesses in the samples studied, which, in the case of growth on a matched substrate, makes it possible to obtain DBMs with a low concentration of structural defects. However, in the structures we studied, the lattice mismatch of the layers with respect to the ZnSe substrate was appreciable, amounting to about 1% ($h_c \approx 20$ nm) in sample 134, and was even larger for the ZnMgSe layer in sample 142. Since the critical scale of coherent growth in this case is smaller than the thickness of a single DBM layer, both structures are bound to have defects of the misfit-dislocation type.

In Fig. 2, the solid lines represent the optical transmission and reflection spectra of the structures studied at room temperature. As can be seen, the peaks of the Bragg reflection ($R = 78\%$ at a wavelength of 560 nm for sample 134 and $R = 66\%$ at a wavelength $\lambda = 530$ nm for sample 142) fall in the transparency region of the ZnSe substrate. The short-wavelength edge of the transmission spectra for the structures is governed by absorption in the ZnCdSe layers that have a narrower band gap. Using the data on the refractive-index dispersion $n(\lambda)$ in ZnCdSe and ZnMgSe [10], we estimated the variation Δn in alternating layers at the peak of the Bragg reflection: $\Delta n = 0.16$ and 0.21 for samples 134 and 142, respectively. In an ideal structure with precisely matched thicknesses of alternating layers, disregarding the losses by absorption and scattering, such changes in Δn should ensure a reflection coefficient of $R = 87\%$ for 20 pairs of layers (see also Fig. 5) and $R = 75\%$ for 10.5 pairs of DBM layers. The difference between these values and experimental data cannot be attributed to errors in determining Δn and is related to the degree of structural perfection of the structures.

Figure 3 shows TEM microphotographs of a cross section of the structures. The buffer ZnSe layers, alternating ZnCdSe layers that exhibit darker contrast, and ZnMgSe layers with lighter contrast can be clearly seen. The structures have extended defects caused by lattice mismatch between the layers and the ZnSe substrate. The roughness of the interfaces over the structure is also distinct. This roughness increases in the region of sample 142 with higher dislocation density. This indicates that, if the lattice constants of the substrate and layers are matched, the quality of the interfaces and the structure in general should improve. However, as the number of layers increases, a zigzag-type of roughness can arise even if the lattices are completely matched, as was observed in DBMs formed of AlGaAs and AlAs layers on GaAs substrates [15]. It was ascertained that it is necessary to use disoriented substrates in this case.

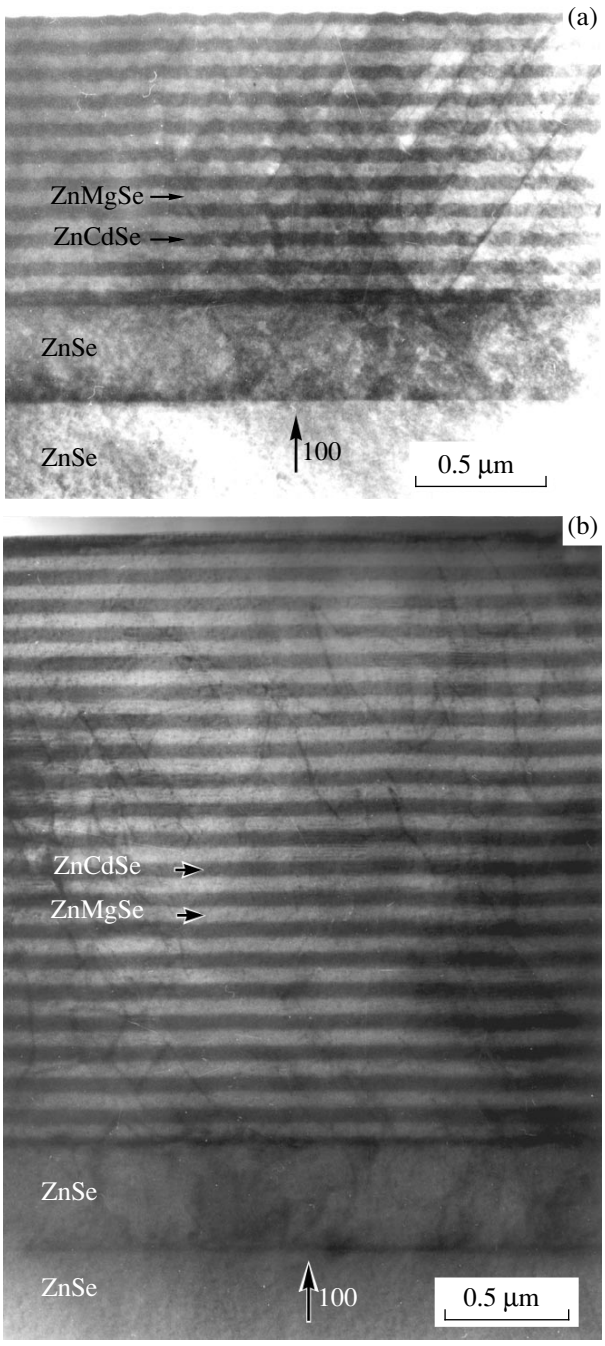

Fig. 3. A microphotograph of the cross section of the Bragg mirror with (a) 10.5 and (b) 20 pairs of layers. The arrows indicate the ZnCdSe and ZnMgSe layers, the ZnSe substrate, and the ZnSe buffer layer.

Topograms of the sample surfaces are shown in Fig. 4. The surface roughness can be described by the rms deviations of the heights σ from the mean value,

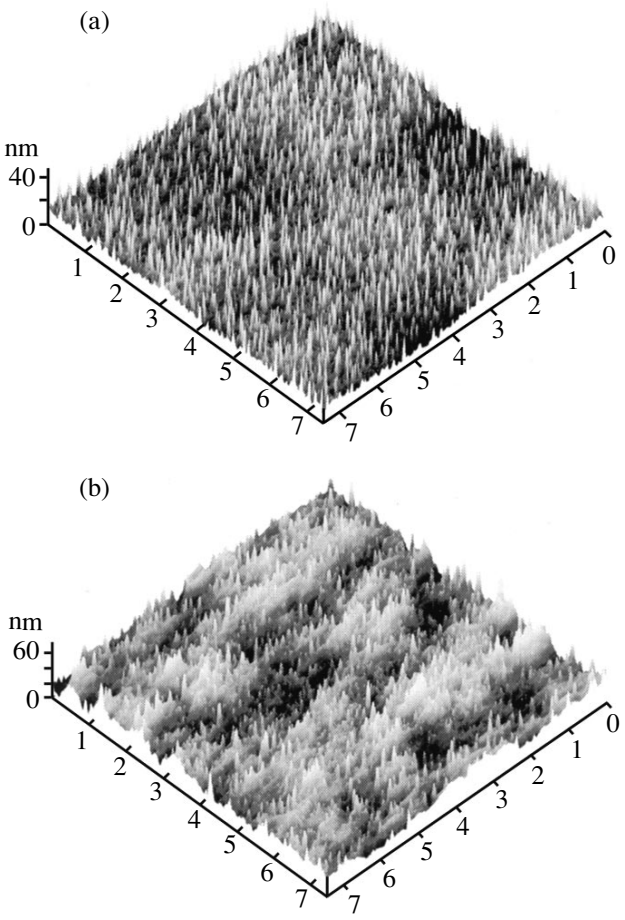

Fig. 4. Topograms of the surface (with an area of 7.5 × 7.5 μm^2) of the Bragg mirrors with (a) 10.5 and (b) 20 pairs of ZnCdSe and ZnMgSe layers; the rms deviation of the roughness heights σ is (a) 4.8 and (b) 8 nm.

which are 8 and 4.8 nm for samples 134 and 142, respectively. It is noteworthy that the characteristic size of small-scale irregularities over the surface is appreciably smaller than the wavelength in the DBM layers ($\lambda_0/n \approx 200$ nm) that corresponds to the reflection-spectrum peak. In sample 134, irregularities that have a large transverse size and act as sort of pedestals for smaller irregularities (nanoirregularities) can also be seen. The deviation of the heights of this pedestal from the mean value is much less than in the case of nanoirregularities. In general, the surface relief pattern is consistent with irregularities observed in the microphotographs shown in Fig. 3.

The interlayer-boundary irregularities with a characteristic size appreciably exceeding the wavelength of light in the layer should cause scattering of light [16–18]. This scattering causes the specular-reflection coefficient R to decrease at each boundary according to formula (1) in [17]:

$$R = R_0 \exp[-(4\pi\sigma n/\lambda_0)^2], \quad (1)$$

where R_0 is the reflectivity from an ideally smooth interlayer boundary, σ is the rms deviation of the points of the irregular-boundary surface from the mean value, n is the refractive index of the layer from which the wave impinges on the boundary, and λ_0 is the wavelength of light in vacuum. Formula (1) also holds for an optical beam of finite aperture if the characteristic size of the irregularities is smaller than the cross-sectional size of the beam. Scattering gives rise to a decrease in both the reflection coefficient and the transmission coefficient. Figure 5 shows the calculated reflection and transmission spectra for an ideal DBM composed of 20 pairs of quarter-wave ZnCdSe and ZnMgSe layers (solid lines, $\sigma = 0$) and for a Bragg mirror with an interlayer-boundary irregularity characterized by a deviation $\sigma = 1.8$ nm (dashed line) that causes the reflectivity to change according to formula (1). Calculations were performed by the matrix method [19]. The losses by scattering at the interlayer boundary were accounted for in terms of equivalent losses by absorption in the layer from which the optical wave impinged on this boundary. Absorbance in a layer was described by the imaginary component of the complex refractive index; i.e.,

$$\begin{aligned} N(\lambda_0) &= n(\lambda_0) + ik(\lambda_0, \sigma), \\ k(\lambda_0, \sigma) &= 4\pi(\sigma n)^2/(\lambda_0 h), \end{aligned} \quad (2)$$

where h is the layer thickness. A similar result is obtained when using a modified method, in which case the matrices describing the pairs of layers are corrected to account for the changes in the boundary conditions if there is scattering [16]. We note that, although the peak of the mirror's reflection coefficient is close to the experimental value for $\sigma = 1.8$ nm, the minimum in the transmission spectrum is significantly less than the measured value. In addition, atomic force and transmission microscopies yield larger values of σ.

In the other limiting case where the characteristic size of irregularities is smaller than the wavelength, scattering is suppressed. In this case, roughness of the interlayer boundary is experienced by an optical wave as a broadened boundary. This also results in a decrease in the reflection-coefficient maximum, which is equivalent to a decrease in the difference between the refractive indices of the layers. Furthermore, the transmission of a Bragg mirror increases at the reflectance peak, which is closer to the experimental data. In Fig. 5, the dash-and-dot lines represent the reflection and transmission spectra calculated in the case where broadening of the interlayer boundaries is simulated by a 20-nm-thick transition layer with the average refractive index. It follows from a comparison of theoretical and experimental spectra (see Fig. 2, solid lines) that this model better describes the influence of roughness on the transmission and reflection spectra at the reflection peak of a Bragg mirror. For a better description of the experimental curves within the entire spectral range, the model used in the calculation took into account a

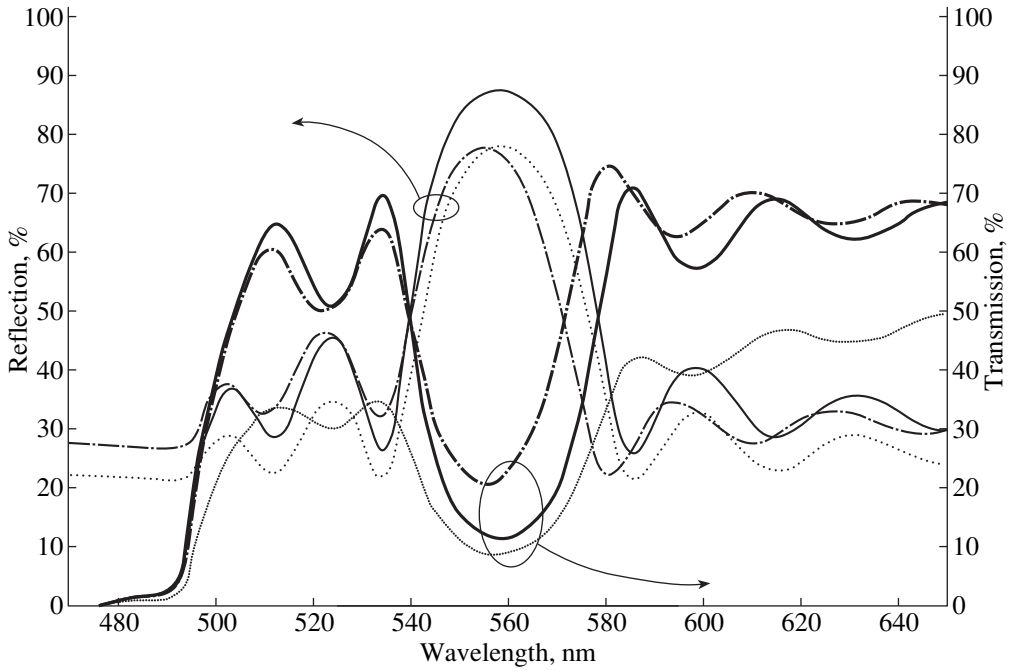

Fig. 5. Calculated spectra of optical transmission and reflection for a structure composed of 20 pairs of $Zn_{0.86}Cd_{0.14}Se$ and $Zn_{0.8}Mg_{0.2}Se$ quarter-wave layers designed for a wavelength of 560 nm for ideally flat interlayer boundaries (solid lines); for irregular boundaries, scattering by which is accounted for by formula (1) with $\sigma = 1.8$ nm (dashed lines); and for flat boundaries ($\sigma = 0$) incorporating a transition layer with a thickness of $\delta = 20$ nm and the refractive index $n = (n_{ZnCdSe} + n_{ZnMgSe})/2$ for $Zn_{0.86}Cd_{0.14}Se$ and $Zn_{0.8}Mg_{0.2}Se$ layers with the thickness decreased by δ (dash-and-dot lines).

slight mismatch in the thickness of quarter-wave layers, in particular, a decrease in the layer thickness with growth of the structure (apparently due to temperature instability of the substrate) and edge absorption in the ZnCdSe layers and the ZnSe substrate according to the Uhrbach rule [20, 21]. The results of the numerical simulation are shown in Fig. 2 by the dotted lines. It is worth noting that there is a good agreement between the calculated and experimental curves for both samples.

4. CONCLUSION

Distributed Bragg mirrors composed of 10.5 and 20 pairs of alternating quarter-wave $Zn_{1-x}Cd_xSe$ and $Zn_{1-y}Mg_ySe$ layers with reflectance peaks at the wavelengths of 530 and 560 nm, respectively, which fall in the transparency region of the substrate, were grown on a ZnSe substrate. The peak reflection coefficients were 78 and 66% for mirrors comprising 20 and 10.5 pairs of layers, respectively. For the compositions corresponding to $x = 0.14$ and $y = 0.20$ and 0.24 determined from the low-temperature cathodoluminescence spectra, the largest calculated reflection coefficient should be equal to 87 and 75% for mirrors composed of 20 and 10.5 pairs of layers, respectively. This inconsistency is explained by roughness of the interfaces, which is confirmed by atomic force and transmission electron microscopy studies. A comparison of theoretical and experimental results showed that the observed roughness of the interlayer boundaries does not result in significant lateral scattering of the light wave. The observed decrease in the reflection coefficient is equivalent to a decrease caused by broadening of the interlayer boundaries. In order to increase the reflection coefficient of the Bragg mirror, it is necessary to improve the flatness of the interlayer boundaries. In particular, this can be done by choosing other compositions for the quarter-wave layers matched to the substrate in the lattice constant and by optimizing the substrate orientation.

ACKNOWLEDGMENTS

This work was supported by the Russian Foundation for Basic Research (project no. 98-02-16890) and Principia Optics Inc., CA.

REFERENCES

1. C. Weisbuch, J. Cryst. Growth **138**, 776 (1994).
2. T. Tawara, M. Arita, K. Uesugi, and I. Suemune, J. Cryst. Growth **184/185**, 777 (1998).
3. T. Tawara, I. Suemune, and S. Tanaka, in *Proceedings of the 9th International Conference on II–VI Compounds, Kyoto, 1999*, J. Cryst. Growth (2000) (in press).

4. F. C. Peiris, S. Lee, U. Bindley, and J. K. Furdyna, J. Appl. Phys. **86**, 719 (1999).
5. T. Morita, H. Shinbo, T. Nagano, *et al.*, J. Appl. Phys. **81**, 7575 (1997).
6. P. Uusimaa, A. Rinta-Moykky, S. Orsila, *et al.*, J. Cryst. Growth **184/185**, 783 (1998).
7. N. G. Basov, E. M. Dianov, V. I. Kozlovsky, *et al.*, Laser Phys. **6**, 608 (1996).
8. Yu. V. Korostelin, V. I. Kozlovsky, A. S. Nasibov, and P. V. Shapkin, J. Cryst. Growth **161**, 51 (1996).
9. A. B. Krysa, V. I. Kozlovskiĭ, Yu. V. Korostelin, *et al.*, Kratk. Soobshch. Fiz., No. 4, 16 (1999).
10. F. C. Peiris, S. Lee, U. Bindley, and J. K. Furdyna, J. Appl. Phys. **86**, 918 (1999).
11. U. Lunz, J. Kuhn, F. Goschenhofer, *et al.*, J. Appl. Phys. **80**, 6861 (1996).
12. B. Jobst, D. Hommel, U. Lunz, *et al.*, Appl. Phys. Lett. **69**, 97 (1996).
13. N. N. Berchenko, V. E. Krevs, and V. G. Sredin, *Semiconductor Solid Solutions and Their Applications, II-VI: Reference Book* (Voenizdat, Moscow, 1982).
14. P. J. Parbrook, B. Henderson, K. P. O'Donnell, *et al.*, J. Cryst. Growth **117**, 492 (1992).
15. Y. H. Wang, K. Tai, Y. F. Hsieh, *et al.*, Appl. Phys. Lett. **57**, 1613 (1990).
16. J. Faist, J.-D. Ganiere, Ph. Buffat, *et al.*, J. Appl. Phys. **66**, 1023 (1989).
17. H.-E. Shin, Y.-G. Ju, H.-W. Song, *et al.*, Appl. Phys. Lett. **72** (18), 2205 (1998).
18. G. Lerondel and R. Romestain, Appl. Phys. Lett. **74**, 2740 (1999).
19. M. Born and E. Wolf, *Principles of Optics* (Pergamon, Oxford, 1969; Nauka, Moscow, 1973).
20. V. P. Gribkovskii, L. G. Zimin, S. V. Gaponenko, *et al.*, Phys. Status Solidi B **158**, 359 (1990).
21. L. Samuel, Y. Brada, A. Burger, and M. Roth, Phys. Rev. B **36**, 1168 (1987).

Translated by A. Spitsyn

Semiconductors, Vol. 34, No. 10, 2000, pp. 1193–1198. Translated from Fizika i Tekhnika Poluprovodnikov, Vol. 34, No. 10, 2000, pp. 1244–1249.

LOW-DIMENSIONAL SYSTEMS

On the Theory of Photoionization of Deep-Level Impurity Centers in a Parabolic Quantum Well

V. D. Krevchik*, R. V. Zaĭtsev, and V. V. Evstifeev***

** Penza State University, Penza, Russia*

*** Penza State Pedagogical University, Penza, Russia*

Submitted January 20, 2000; accepted for publication March 23, 2000

Abstract—The localized state of a deep-level impurity in a quantum well (QW) with a parabolic potential profile is investigated within the context of a zero-range impurity potential model. It is demonstrated that, if the well is sufficiently thin, an effect of positional disorder exists: the binding energy of a deep-level impurity center is a decreasing function of the center transverse coordinate. It is found that the positional disorder effect is enhanced in the parabolic potential well in comparison with the rectangular well of finite depth. The spectral dependence of the photoionization cross section of deep-level impurity centers is examined. It is shown that the spectral dependence of the photoionization cross section is not monotonic, and the position of the impurity-absorption edge depends strongly on the impurity center coordinate and the QW parameters. © *2000 MAIK "Nauka/Interperiodica".*

1. It has been shown in a number of studies that localized impurity states can exist in actual quantum wells (QWs) [1–4]. Therefore, it is of interest to determine the magnitude and spectral dependence of the probabilities of optical transitions involving electrons localized at impurity centers.

In this paper, we use a generalization for the quantum-confinement case of the zero-range potential method [5] to consider the photoionization of deep-level impurity centers in a QW with a parabolic potential profile. A single parabolic QW can be formed, e.g., in p–n^+–p structures, which comprise a heavily doped n^+-GaAs layer clad by lightly doped p-GaAs barrier layers [6]. In the model of parabolic QW considered here, the energies of stationary quantum states are determined by

$$\varepsilon_n = \left(n + \frac{1}{2}\right)\hbar\omega_0 = \left(n + \frac{1}{2}\right)\frac{\hbar}{L}\sqrt{\frac{2V_0}{m^*}}, \quad n = 0, 1, 2, \ldots, \tag{1}$$

where L is the QW width, $\varepsilon_0 = \hbar\omega_0/2$ is the harmonic oscillator zero-point energy, V_0 is the QW potential amplitude, and m^* is the electron effective mass. Note that formula (1) is only an approximation, since it does not account for the finiteness of the QW depth. However, satisfactory agreement with the photoluminescence experimental data can be obtained by a judicious choice of the parameter V_0 [7, 8].

2. In the following consideration, we are mainly interested in the case of fairly narrow QWs, $L \sim a_d$ (where a_d is the effective Bohr radius). In this situation, quantum confinement of the charge carriers in the QW is important. Let the position of the deep-level center be described by $\mathbf{R} = (0, 0, z_0)$, where $-L/2 < z_0 < L/2$. To determine the wave functions $\Psi_\lambda(\boldsymbol{\rho}, z, z_0)$ and the energy spectrum $E_\lambda = -\hbar^2\lambda^2/2m^*$ of the deep-level center in the QW, it is convenient to formulate the problem in the integral form. Let us introduce the Green function

$$G(\boldsymbol{\rho} - \boldsymbol{\rho}_1, z, z_1, E_\lambda) = \sum_{n=0}^{\infty}\int\frac{d\mathbf{k}}{(2\pi)^2}\frac{\exp[i\mathbf{k}(\boldsymbol{\rho} - \boldsymbol{\rho}_1)]}{E_\lambda - E_\mathbf{k} - \varepsilon_n}\varphi_n(z)\varphi_n(z_1), \tag{2}$$

where $\varphi_n(z)$ and ε_n represent the single-particle wave functions and the energy spectrum for a given distribution of the QW potential.

The Lippmann–Schwinger equation for the bound state can be written as[1]

$$\Psi_\lambda(\boldsymbol{\rho}, z, z_0) = \int d\boldsymbol{\rho}_1\int_{-\infty}^{+\infty} dz_1 G(\boldsymbol{\rho} - \boldsymbol{\rho}_1, z, z_1, E_\lambda) \times V_\delta(\boldsymbol{\rho}_1, z_1, z_0)\Psi_\lambda(\boldsymbol{\rho}_1, z_1, z_0). \tag{3}$$

Here, V_δ is the zero-range potential of strength $\gamma = 2\pi/\alpha$:

$$V_\delta(\boldsymbol{\rho}, z, z_0) = \gamma\delta(\boldsymbol{\rho})\delta(z - z_0)\left[1 + \boldsymbol{\rho}\nabla_\boldsymbol{\rho} + (z - z_0)\frac{\partial}{\partial z}\right]. \tag{4}$$

[1] The problem of low-energy electron scattering by a zero-range potential in a uniform magnetic field was considered previously [9].

1063-7826/00/3410-1193$20.00 © 2000 MAIK "Nauka/Interperiodica"

Substituting (4) into (3), we obtain

$$\Psi_\lambda(\boldsymbol{\rho}, z, z_0) = \gamma G(\boldsymbol{\rho}, z, z_0, E_\lambda)(\hat{T}\Psi_\lambda)(0, z_0, z_0), \quad (5)$$

where

$$(\hat{T}f)(0, z_0) \equiv \lim_{\substack{\boldsymbol{\rho}\to 0\\ z\to z_0}}\left[1 + \boldsymbol{\rho}\nabla_{\boldsymbol{\rho}} + (z - z_0)\frac{\partial}{\partial z}\right] f(\boldsymbol{\rho}, z). \quad (6)$$

Applying operator $\hat{T}$ to both sides of relation (5), we arrive at an equation that determines the dependence of the deep-level center bound-state energy E_λ on the strength and the transverse coordinate z_0 of the zero-range well:

$$\alpha L_0 = 2\pi(\hat{T}G)(0, z_0, z_0, E_\lambda). \quad (7)$$

Here, $L_0 = (\hbar/m^*\omega_0)^{1/2}$. Using an integral representation of the Macdonald function $\mathrm{K}_0(x)$

$$\int_0^\infty \frac{t\mathbf{J}_0(t)}{t^2 + x^2}dt = \mathrm{K}_0(x), \quad (8)$$

we obtain the following expression for the Green function in (5):

$$G(\boldsymbol{\rho}, z, z_0, E_\lambda) = -\frac{1}{\pi\sqrt{\pi}L_0^3\varepsilon_0}$$
$$\times\sum_{n=0}^\infty \frac{\mathrm{K}_0\left(\sqrt{|E_\lambda|/\varepsilon_0 + 1 + 2n}\,\frac{\rho}{L_0}\right)}{2^n n!} \quad (9)$$
$$\times \mathrm{H}_n\left(\frac{z}{L_0}\right)\mathrm{H}_n\left(\frac{z_0}{L_0}\right)\exp\left(-\frac{z^2 + z_0^2}{2L_0^2}\right).$$

In Eq. (8), $\mathbf{J}_0(x)$ is the zero-order Bessel function of the first kind. Substituting into (9) the integral representation of the Macdonald function

$$\mathrm{K}_0(x) = \int_0^\infty dt\exp(-x\cosh t), \quad (10)$$

we obtain

$$G(\boldsymbol{\rho}, z, z_0, E_\lambda) = -\frac{1}{2\pi\sqrt{\pi}L_0^3\varepsilon_0}\exp\left(-\frac{z^2 + z_0^2}{2L_0^2}\right)$$
$$\times\int_0^\infty \frac{du}{u}\exp\left[-\frac{1}{u} - \left(\frac{|E_\lambda|}{\varepsilon_0} + 1\right)\frac{\rho^2 u}{2L_0^2}\right] \quad (11)$$
$$\times\sum_{n=0}^\infty\left[\frac{\exp(-u\rho/L_0)}{2}\right]^n\frac{\mathrm{H}_n(z/L_0)\mathrm{H}_n(z_0/L_0)}{n!}.$$

To perform the summation in (11), the following generating function can be used:

$$\sum_{n=0}^\infty\left(\frac{z}{2}\right)^n\frac{\mathrm{H}_n(x)\mathrm{H}_n(y)}{n!}$$
$$= \frac{1}{\sqrt{1 - z^2}}\exp\left[\frac{2xyz - (x^2 + y^2)z^2}{1 - z^2}\right]. \quad (12)$$

Next, isolating the divergent part of (11), we obtain (for $z \longrightarrow z_0$)

$$G(\boldsymbol{\rho}, z_0, z_0, E_\lambda) = -\frac{1}{2\pi L_0^2\varepsilon_0\rho}$$
$$\times\exp\left[-\left(\sqrt{\frac{|E_\lambda|}{\varepsilon_0}} + 1\right)\frac{\rho}{L_0}\right] + \frac{1}{2\pi\sqrt{\pi}L_0^3\varepsilon_0} \quad (13)$$
$$\times\int_0^\infty\frac{du}{u}\exp\left(-\frac{\rho^2}{2L_0^2 u} - \left(\frac{|E_\lambda|}{\varepsilon_0} + 1\right)\frac{u}{2}\right)f(u, z_0),$$

where

$$f(u, z_0) = \frac{1}{\sqrt{2u}} - \frac{1}{\sqrt{1 - \exp(-2u)}}$$
$$\times\exp\left\{-\frac{z_0^2[1 - \exp(-u)]}{L_0^2[1 + \exp(-u)]}\right\}. \quad (14)$$

Substituting (13) into (7), we obtain an equation that determines the bound-state energy[2]

$$\sqrt{\beta\eta^2 + 1} = \eta_i - \sqrt{\frac{2}{\beta\pi}}\int_0^\infty\frac{dt}{t}\exp[-(\beta\eta^2 + 1)t/2]$$
$$\times\left[\frac{1}{\sqrt{2u}} - \frac{1}{\sqrt{1 - \exp(-2t)}}\exp\left\{-2\beta a^2\frac{[1 - \exp(-t)]}{[1 + \exp(-t)]}\right\}\right], \quad (15)$$

where

$$\eta = \sqrt{|E_\lambda|/E_d}, \quad \beta = L^*/\sqrt{V_0^*}, \quad L^* = L/a_d,$$
$$V_0^* = V_0/E_d, \quad a = z_0/L, \quad \eta_0 = \sqrt{|E_i|/E_d};$$

E_i is the binding energy of the deep-level center in the bulk semiconductor,[3] and E_d is the effective Bohr energy. Equation (15) can be analyzed numerically. In Fig. 1, we show the calculated dependences of the localized-level energy η^2 on the coordinate $a = z_0/L$ of a deep-level impurity center for different zero-range potential strengths characterized by the parameter η_i

[2] Localized states can exist between the QW bottom and the first quantum-confinement level as well [10]. Then, for the levels located above the QW bottom, $E_\lambda > 0$, and the parameter λ becomes imaginary.

[3] E_λ and E_i are measured from the bottom of the QW.

and QW potential amplitudes $V_0^* = V_0/E_d$. One can see that, in fairly narrow QWs ($L^* \approx 1$), the positional disorder effect takes place: the binding energy of a deep-level impurity center is a decreasing function of the center coordinate. With increasing QW potential amplitude (represented by the parameter V_0^*), the condition necessary for a bound state below the QW bottom to exist becomes more stringent (cf. curves *1*, *2*). Comparing curves *2* and *3*, one can also conclude that the positional disorder effect becomes less pronounced with the increasing strength of the zero-range potential (parameter η_i). Thus, the positional disorder effect is most significant in fairly deep QWs where $V_0^* \gg \eta_i^2$. For comparison purposes, the results of a numerical calculation of the localization energy dependence on the impurity-center position in a QW with the rectangular potential profile [9] are presented in Fig. 1 by curves *1'*–*3'*. Equation (9) of the referred paper was used [9] to analyze the dependence of the localized level energy on the QW parameters and the defect position. In our notation, this equation is written as

$$\eta = \eta_i + \frac{1}{L^*}\int\limits_{L^*\eta}^{\infty} dt\left[a_1 \exp\left(-\frac{z_0}{L}t\right) + a_2 \exp\left(\frac{z_0}{L}t\right)\right], \quad (16)$$

where

$$a_1 = \frac{(1-\xi)^2 \exp\left[\left(\frac{z_0}{L}-1\right)t\right] - (1-\xi^2)\exp\left(-\frac{z_0}{L}t\right)}{(1+\xi)^2 \exp t - (1-\xi)^2 \exp(-t)},$$

$$a_2 = \frac{(1-\xi)^2 \exp\left[-\left(\frac{z_0}{L}+1\right)t\right] - (1-\xi^2)\exp\left(\frac{z_0}{L}t\right)}{(1+\xi)^2 \exp t - (1-\xi)^2 \exp(-t)},$$

$$\xi = \frac{m^*}{m_b^*}\frac{t}{L^*\sqrt{m_b^*/m^*(V_0^* + t^2/L^{*2})}}.$$

Here, m_b^* is the effective mass in the barrier; to perform numerical calculations, it was assumed that $m^*/m_b^* = 0.75$. Comparing curves *1–3* and *1'–3'* in Fig. 1, one can see that the positional-disorder effect is more pronounced in parabolic QWs than in rectangular ones. If $\eta_i^2 > V_0^*$, this effect can be neglected in QWs with a rectangular potential profile (curve *1'*).

3. Let us consider the photoexcitation of an electron from a localized level of energy E_λ to one of the two-dimensional quantum-confinement subbands. An effective Hamiltonian of interaction with the light-wave field can be written as [5]

$$\hat{H}_{\text{int}} = \frac{\lambda_0 \hbar e}{im^*}\left(\frac{2\pi\hbar\bar{N}}{\varepsilon\omega}\right)^{1/2} \exp(iq_\perp z)(\mathbf{e}_\parallel \nabla_{\boldsymbol{\rho}}), \quad (17)$$

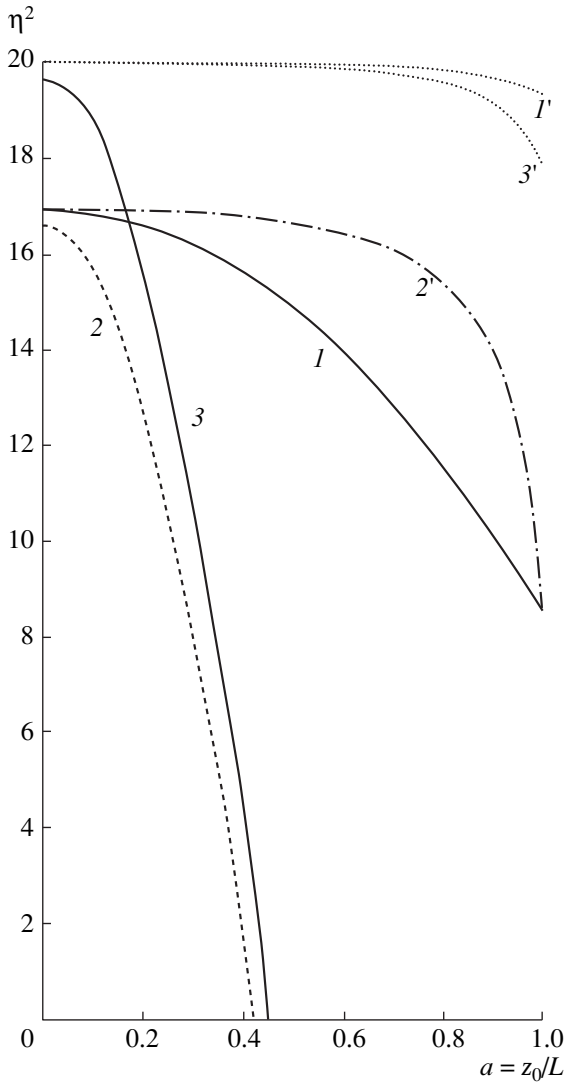

Fig. 1. Dependence of the localized-level position η^2 on the impurity center coordinate $a = z_0/L$, zero-range potential strength η_i, and the amplitude $V_0^* = V_0/E_d$ of the QW potential: (*1*) $V_0^* = 17$ and $\eta_i^2 = 17$; (*1'*) $V_0^* = 17$ and $\eta_i^2 = 20$; (*2*, *2'*) $V_0^* = 200$ and $\eta_i^2 = 17$; and (*3*, *3'*) $V_0^* = 200$ and $\eta_i^2 = 20$. Curves (*1–3*) and (*1'–3'*) are related to the QWs with parabolic and rectangular potential profiles, respectively.

where λ_0 is the local-field factor accounting for the difference between the amplitudes of the local and average (macroscopic) fields; $\bar{N}$ is the number of photons per unit volume; ω, $q_\perp$, and $\mathbf{e}_\parallel$ are the frequency, the wave vector, and the (longitudinal) polarization unit vector of the absorbed light; ε is the static permittivity; and e is the elementary charge.

According to Eq. (5), the wave function of a localized electron occupying the ground state of a deep-level impurity center differs from the Green function only by

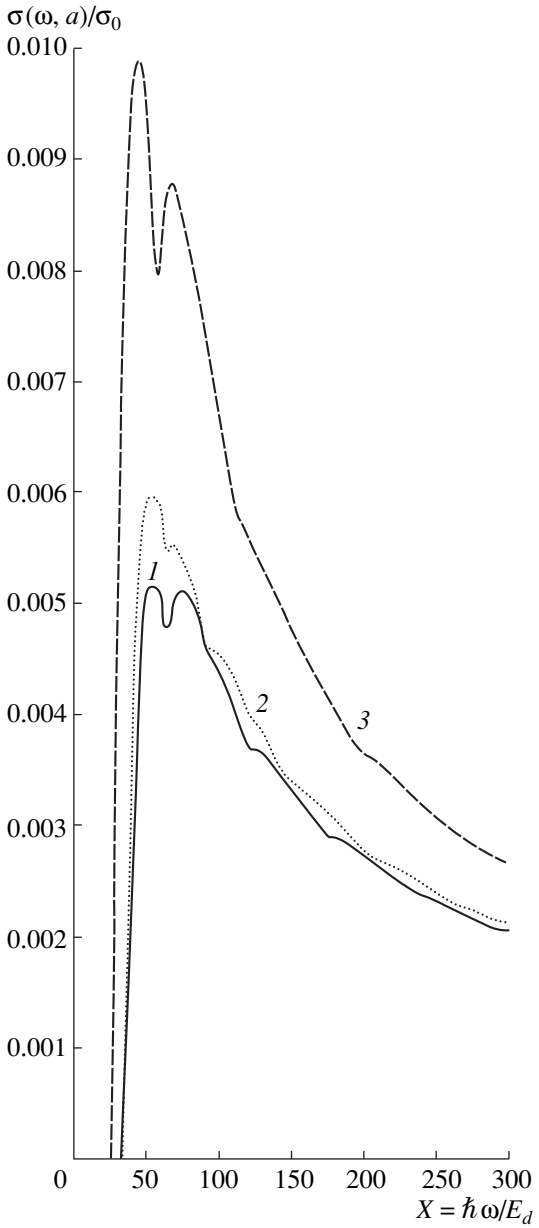

Fig. 2. Spectral dependence of the normalized photoionization cross section $\sigma(\omega, a)/\sigma_0$ of a deep-level impurity center for the center coordinate $a = z_0/L$ equal to (*1*) 0.01, (*2*) 0.1, and (*3*) 0.3; $V_0^* = 200$ and $\eta_i^2 = 20$.

a constant factor:

$$\Psi_\lambda(\boldsymbol{\rho}, z, z_0) = -C\int \frac{d\mathbf{k}}{(2\pi)^2}\exp(i\mathbf{k}\boldsymbol{\rho})g(z, z_0, E_\lambda - E_\mathbf{k}), \quad (18)$$

where $C = [2\pi\varepsilon_0/g(z_0, z_0, E_\lambda)]^{1/2}$ is the normalization factor and $g(z, z_0, E_\lambda - E_\mathbf{k})$ is the Green function of a one-dimensional Schrödinger equation with the oscillator potential given by

$$g(z, z_0, E_\lambda - E_\mathbf{k}) = \sum_{n=0}^{\infty}\frac{\varphi_n(z)\varphi_n(z_0)}{E_\lambda - E_\mathbf{k} - \varepsilon_n} \quad (19)$$

or in the closed form

$$g(z, z_0, E_\lambda - E_\mathbf{k}) = -\frac{\Gamma(-\nu)}{\sqrt{\pi}\varepsilon_0 L_0}D_\nu\left(\frac{\sqrt{2}}{L_0}x_>\right)D_\nu\left(-\frac{\sqrt{2}}{L_0}x_<\right), \quad (20)$$

where

$$x_> = \max\{z, z_0\}, \quad x_< = \min\{z, z_0\},$$

$$\nu = (E_\lambda - E_\mathbf{k} - \varepsilon_0)/\varepsilon_0,$$

$D_\nu(x)$ is the parabolic cylinder function, and $\Gamma(x)$ is the gamma function.

The following form of the final-state wave function is adopted to calculate the photoionization cross section of a deep-level impurity center in a QW:

$$\Psi_f^\pm(\boldsymbol{\rho}, z, z_0) = \frac{1}{\sqrt{S}}\exp(i\mathbf{k}\boldsymbol{\rho})\varphi_n(z) + G(\boldsymbol{\rho}, z, z_0, E \pm i0)(\hat{T}\Psi_f^\pm)(0, z_0, z_0). \quad (21)$$

Here, S is the QW normalization area. Using (17)–(21), the partial cross section of the photoionization can be expressed as

$$\sigma_n(\omega, z_0) = \frac{(2\pi)^2\alpha^*\hbar^2\lambda_0^2}{|g(z, z_0, E_\lambda)|m^*} \times \theta(\hbar\omega - \varepsilon_n - |E_\lambda|)\frac{(\hbar\omega - \varepsilon_n - |E_\lambda|)}{\hbar\omega} \times \left|\int_{-\infty}^{+\infty} dz g(z, z_0, \varepsilon_n - \hbar\omega)\exp(iq_\perp z)\varphi_n(z)\right|^2, \quad (22)$$

where α^* is the effective fine-structure constant (with account taken for the material permittivity), and $\theta(x)$ is the unit Heaviside function. The integral under the modulus sign in (22) can be rather easily split into two integrals of the form

$$I_1 = \int_{-\infty}^{+\infty} dz\exp\left(-\frac{z^2}{L_0^2}\right)\cos(q_\perp z)\mathrm{H}_n\left(\frac{z}{L_0}\right)\mathrm{H}_m\left(\frac{z}{L_0}\right), \quad (23)$$

$$I_2 = i\int_{-\infty}^{+\infty} dz\exp\left(-\frac{z^2}{L_0^2}\right)\sin(q_\perp z)\mathrm{H}_n\left(\frac{z}{L_0}\right)\mathrm{H}_m\left(\frac{z}{L_0}\right). \quad (24)$$

Calculation of I_1 and I_2 involves the following selection rules:

$$I_1 = \begin{cases} 0, & \text{if } m \neq n + 2k, \quad k = 0, 1, 2, \ldots \\ 2^n n! \sqrt{\pi} L_0 (-1)^k (q_\perp L_0)^{2k} \exp\left(-\frac{q_\perp^2 L_0^2}{4}\right) & \\ \times L_n^{2k}\left(\frac{q_\perp^2 L_0^2}{2}\right), & \text{if } m = n + 2k, \end{cases} \quad (25)$$

$$I_2 = \begin{cases} 0, & \text{if } m \neq n + 2k + 1, \quad k = 0, 1, 2, \ldots \\ i 2^n n! \sqrt{2\pi} L_0 (-1)^k (q_\perp L_0)^{2k} \exp\left(-\frac{q_\perp^2 L_0^2}{4}\right) & \\ \times L_n^{2k+1}\left(\frac{q_\perp^2 L_0^2}{2}\right), & \text{if } m = n + 2k + 1. \end{cases} \quad (26)$$

It follows from (25) and (26) that optical transitions from an impurity level to the nth subband take place only in the case where the localized state is formed from the states of neighboring subbands with numbers $m = n + 2k$ and $m = n + 2k + 1$. Under the assumption that $q_\perp L_0 \ll 1$, the total cross section of the photoionization has the following form:

$$\sigma(\omega, z_0) = \sigma_0 X^{-1} \beta^{-2} \exp(-b^2) \times [\Gamma(\mu) D_{-\mu}(\sqrt{2}b) D_{-\mu}(-\sqrt{2}b)]^{-1} \times \sum_{n=0}^{N} \frac{\left[X - \eta^2 - \frac{2}{\beta}(2n+1)\right]}{n! 2^n} \left[\frac{H_n^2(b)}{X^2} + \frac{1}{2}\frac{H_{n+1}^2(b)}{(X + 4\beta^{-1})^2}\right], \quad (27)$$

where

$$\sigma_0 = 2(2\pi)^2 \alpha^* \lambda_0^2 \hbar^2 / (E_d m^*);$$

$$\mu = (\eta^2 \beta + 1)/2; \quad b = \sqrt{2L^* \sqrt{V_0^*}}\, a;$$

$N = [A]$ is the integer part of the number $A = \beta(X - \eta^2 - 2/\beta)/4$; $X = \hbar\omega/E_d$; and $H_n(X)$ are the Hermit polynomials.

Figure 2 shows the spectral dependence of the normalized photoionization cross section $\sigma(\omega, a)/\sigma_0$ for the deep-level impurity centers located in different monoatomic layers of a QW with $L^* = 1$. It can be seen that the spectral dependence of the photoionization cross section is not monotonic, which is related to the quantum-confinement effect. The cross section in the vicinity of the absorption edge increases considerably with the shift of the impurity center to the QW boundary (cf. curves *1*, *3*). This occurs because of an increase in the localized state radius due to the positional-disorder effect.

Dependences of the impurity absorption threshold position $X_{thr} = (\hbar\omega)_{thr}/E_d$ on the impurity center coordinate for different QW potential amplitudes V_0^* and zero-range potential strengths η_i are shown in Fig. 3.

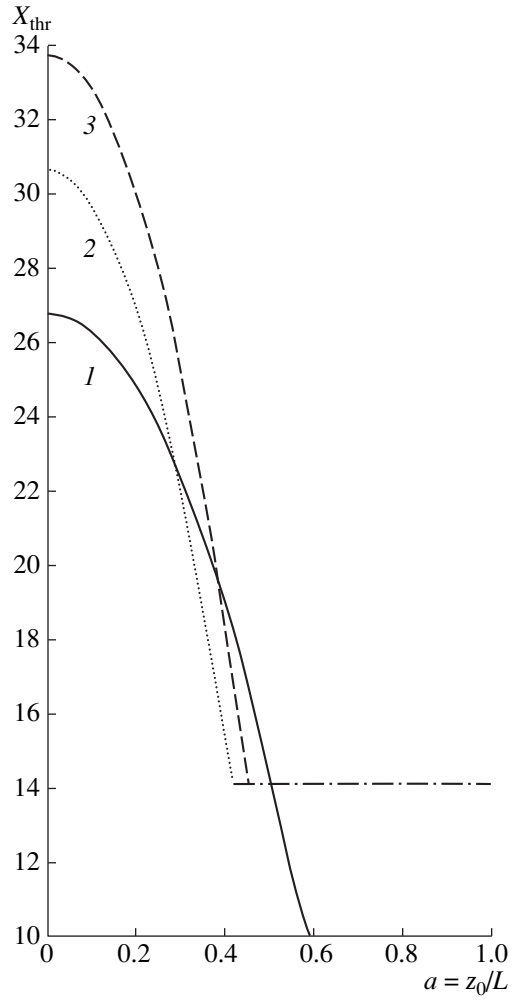

Fig. 3. Dependence of the impurity-absorption threshold (expressed in Bohr energy units) on the deep-level impurity center coordinate for different values of the QW potential amplitude and the zero-range potential strength: (*1*) $V_0^* = 100$ and $\eta_i^2 = 17$; (*2*) $V_0^* = 200$ and $\eta_i^2 = 17$; and (*3*) $V_0^* = 200$ and $\eta_i^2 = 20$.

It should be noted that the impurity absorption of light in a QW is also possible in the case where the strength of the zero-range potential is insufficient for the formation of a bound state in a bulk semiconductor (i.e., the local energy level crosses the QW bottom, $\eta = 0$). In this case, which corresponds to the horizontal portion of curves *2* and *3* in Fig. 3, the photoionization threshold is determined by the QW ground-state energy.

4. Thus, states localized by a short-range potential (simulated by δ-function) in QWs with a parabolic potential profile were considered. In the adopted model of the QW, the amplitude V_0 of the well potential is an

empirical parameter. Using this approximation, we demonstrated that the shape of the QW potential profile has a considerable influence on the impurity-level energy. Qualitative modifications of the spectral dependence of the photoionization cross section take place as well. This can be seen by comparing Fig. 2 with the corresponding curves in Fig. 1 from publication [5], where the photoionization of a deep-level impurity center in a rectangular QW with infinitely high barriers is treated.

REFERENCES

1. P. Voisin, Y. Guldner, J. P. Vieren, *et al.*, J. Phys. Soc. Jpn., Suppl. A **49**, 1005 (1980).
2. R. C. Miller, A. C. Gossard, W. T. Tsang, and O. Munteanu, Phys. Rev. B **25**, 3871 (1982).
3. D. Gammon, R. Merlin, W. T. Masselink, and H. Morkos, Phys. Rev. B **33**, 2919 (1986).
4. G. S. Rune, P. O. Holtz, M. Sundaram, *et al.*, Phys. Rev. B **44**, 4010 (1991).
5. V. D. Krevchik and É. Z. Imamov, Fiz. Tekh. Poluprovodn. (Leningrad) **17**, 1235 (1983) [Sov. Phys. Semicond. **17**, 780 (1983)].
6. G. H. Döhler, Surf. Sci. **73**, 97 (1978).
7. R. C. Miller, A. C. Gossard, D. A. Kleinman, and O. Munteanu, Phys. Rev. B **29**, 3740 (1984).
8. R. C. Miller, D. A. Kleinman, and A. C. Gossard, Phys. Rev. B **29**, 7085 (1984).
9. V. G. Skobov, Zh. Éksp. Teor. Fiz. **37**, 1467 (1959) [Sov. Phys. JETP **10**, 1039 (1960)].
10. A. A. Pakhomov, K. V. Khalipov, and I. N. Yassievich, Fiz. Tekh. Poluprovodn. (St. Petersburg) **30**, 1387 (1996) [Semiconductors **30**, 730 (1996)].

Translated by M. Skorikov

Semiconductors, Vol. 34, No. 10, 2000, pp. 1199–1202. Translated from Fizika i Tekhnika Poluprovodnikov, Vol. 34, No. 10, 2000, pp. 1250–1253.

LOW-DIMENSIONAL SYSTEMS

A Model of Conduction in Carbon Nanopipe Bundles and Films

V. É. Kaminskiĭ

Institute of Radio Engineering and Electronics, Russian Academy of Sciences, ul. Mokhovaya 18, Moscow, 103907 Russia
e-mail: kamin@mail.cplire.ru

Submitted September 16, 1999; accepted for publication March 30, 2000

Abstract—To describe electron transport in nanopipes, a two-band model with a very narrow band gap was proposed. In the effective mass approximation, the Hamiltonian of quasiparticle kinetic energy was found to be isotropic and strongly nonparabolic. Formulas for the rates of momentum relaxation by scattering on acoustic phonons were derived. The model parameters ensuring good agreement with available experimental data were determined at temperatures above 4 K. The proposed model within a unified approach was shown to explain the observed differences in the temperature dependences of nanopipe bundle and film conductivities. © *2000 MAIK "Nauka/Interperiodica"*.

Since the discovery of carbon nanopipes [1], their electrical conductivity has received much attention due to potential applications in nanoelectronic devices and as cold cathodes. Currently, a large number of experiments are being carried out in this line of inquiry (see review [2]). However, conductivity measurements of solitary nanopipes present substantial experimental difficulties. Therefore, most of the studies are conducted using nanopipe films or bundles prepared by various methods.

Most of the measured temperature dependences of the conductivities of solitary nanopipes [3, 4] and films [5–8] show that it increases with temperature. Both longitudinal and transverse (relative to the nanopipe axis) conductivities have approximately identical temperature dependences typical of semiconductors. Hall voltage [5] and thermal emf [7] measurements are indicative of predominantly hole conduction in nanopipes. However, in contrast to known semiconductors, the temperature dependences have no activation property. For example, linear dependences of the conductivity on logarithm of temperature were observed within the ranges of $2 < T < 100$ K [3] and $2 < T < 50$ K [8] (see Fig. 1). In [5], the dependence of the film resistivity $\rho(T)$ was observed and was described well in the range of $4 < T < 300$ K as

$$\rho = \rho_0 + \rho_1 \exp\left(-\frac{T}{T_0}\right), \quad (1)$$

where ρ_0, ρ_1, and T_0 are constants. Dependences $\rho(T)$ similar to (1) were measured in [6, 7]. The experiments [7, 9] with single-layer nanopipe bundles also showed decreased resistivity at low temperatures. At the same time, resistivity growth at temperatures above 180 and 50 K was observed in [7] and [9], respectively.

Notwithstanding the extensive experimental data, clear concepts of the conduction mechanism in carbon nanopipes are so far lacking. Conduction parameters such as the carrier density and effective mass remain unknown. The high negative magnetoresistance was not even qualitatively explained by known models. This is primarily caused by insufficiently developed microscopic transport models. The dependences found in [3, 6] were related to the weak-localization effects. The dependence measured in [5] was qualitatively explained by mesoscopic conduction in nanopipes separated by low (about 10 meV) potential barriers. In [9], a one-dimensional model was proposed, in which the basic resistivity mechanism was scattering by nanopipe torsional vibrations. According to this model, the resistivity should grow linearly with temperature in the range of $50 < T < 300$ K. This qualitatively conforms to experimental data. However, the resistivity increment observed in [9] exceeds the calculated value by more than an order of magnitude. In [10], proceeding from the similarity of the temperature dependences, a model which described nanopipe conductivity by analogy with high-conductivity polymers was proposed.

In this study, a model for describing electron transport in dense nanopipe bundles and films is proposed. Carbon nanopipes are self-organized one-dimensional conducting crystals, whose structure may vary greatly [2]. The electron energy spectrum in the direction transverse to the solitary nanopipe axis consists of size quantization subbands. Their energy differences are large in single-layer nanopipes with diameters no larger than 1–2 nm. Therefore, their electron transport is markedly one-dimensional. A large number of studies (see, for instance, [9, 11–14]) were dedicated to describing it. A simple calculation (analogous to two-dimensional electron systems) shows that the region of

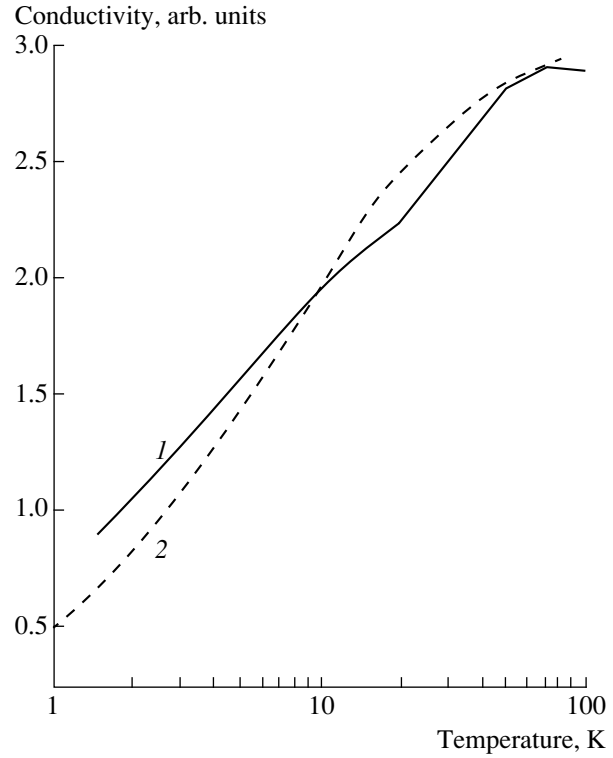

Fig. 1. Experimental (*1*) [8] and calculated (*2*) temperature dependences of the nanopipe film conductivity.

electron wave-function localization in the direction transverse to the axis considerably exceeds the single-layer nanopipe diameter. The distance between nanopipes in bundles is of the order of 1 nm. This causes strong overlap of the wave functions. Therefore, the electron energy spectrum in bundles and films is three-dimensional. This is partially confirmed by measurements reported previously [5]. Nanopipe bundles conserve long- and at least short-range order between atoms along and across the pipe axis, respectively. Films represent a set of spatially ordered nanopipes and (or) bundles. Therefore, there is good reason to consider these objects as a crystalline material to a first approximation. Experimentally observed conductivity features show that these materials are semiconductors with a very narrow band gap. A general method for constructing the Hamiltonian for such semiconductors was described in detail in [15]. As is known, it is strongly nonparabolic. However, available experimental data are insufficient to determine the parameters of this Hamiltonian. In this case, it is reasonable to construct relatively simple models that allow determination of the electron kinetic parameters from the results of measurements. Therefore, we write the conduction band Hamiltonian in the following simple form:

$$H = E_e \ln\left(1 + \frac{H_e}{E_e}\right). \qquad (2)$$

Here, $E_e = kT_e$ is the band parameter and H_e is the parabolic band Hamiltonian in the effective mass m_e approximation. An analogous Hamiltonian can be written for the valence band with the band parameter $E_h = kT_h$. We note that the wave eigenfunctions of the Hamiltonians H and H_e coincide. This model differs from the conventional one by a single additional parameter for either band (T_e and T_h). With infinite growth of these parameters, the model transforms into the conventional one. One can assume that these parameters (as other quantitative parameters of a material) are mainly controlled by the type of nanopipes and their mutual arrangement in the film. In this case, according to measurements carried out on the films, the electron kinetic parameters can be estimated in solitary nanopipes.

For Eq. (2), the electron concentration is given by

$$n = N_c^* \frac{2}{\sqrt{\pi}} \int G(G-1)^{1/2} F(x-\eta)\,dx, \qquad (3)$$

where

$$N_c^* = 2\frac{m_e\sqrt{m_e E_e}kT}{(2\pi\hbar^2)^{3/2}}$$

is the effective density of states in the conduction band, $x = E/kT$, E is the energy,

$$G = \exp\left(\frac{E}{E_e}\right),$$

F is the Fermi–Dirac distribution function, $\eta = E_f/kT$, and E_f is the Fermi energy.

According to [16], the electron conductivity in a homogeneous semiconductor is given by

$$\sigma_e = \frac{2}{(2\pi)^3}\frac{e^2}{m_e}\int \frac{d^3k}{\nu(E)}\frac{\partial F}{\partial E}\left(\mathbf{k}\frac{\partial E}{\partial \mathbf{k}}\right), \qquad (4)$$

where ν is the momentum-relaxation rate. Since the phonon spectrum of nanopipes is inadequately known, we restrict ourselves to consideration of scattering by deformation (DA) and polarization (PA) acoustic phonons. Using relationships from [16] to calculate ν and (2), it is readily shown that dependence $\nu(E)$ for these phonon types at moderately low temperatures is written as

$$\nu_{\mathrm{DA}} = \frac{G}{\tau_{\mathrm{DA}}}(G-1)^{1/2}, \quad \nu_{\mathrm{PA}} = \frac{G}{\tau_{\mathrm{PA}}}(G-1)^{-1/2}, \qquad (5)$$

where

$$\tau_{\mathrm{DA}} = \frac{\sqrt{2}\pi^2\rho_m s^2\hbar^4}{kTE_A^2\sqrt{kT_e}m_e^{3/2}},$$

$$\tau_{\mathrm{PA}} = \frac{2\sqrt{2}\pi^2\hbar^2\kappa}{kTe^2\beta}\left(\frac{kT_e}{m_e}\right)^{1/2}.$$

Here, ρ_m is the material density, s is the velocity of sound, E_A is the deformation potential, κ is the dielectric constant, and β is the coefficient of electromechanical coupling. Analogous relationships also hold for holes. The total film conductivity is $\sigma = \sigma_e + \sigma_h$. We note that as T_e is infinitely increased, formulas (2)–(5) become conventional semiconductor relationships.

Figure 1 displays the experimental temperature dependence of the film conductivity [8] (curve *1*). The following parameters were chosen in calculating the dependences: $g = m_e/m_h = 1$, $T_e = 700$ K, and $T_h = 5000$ K. The ratio $p = \tau_{DA}/\tau_{PA}$ for electrons is taken to be 0.02. Henceforth, the band gap is assumed to be zero. As is evident, the calculated dependence is in good agreement with the experimental data.

Figure 2 shows experimental temperature dependences of resistivity ρ. Curve *1* corresponds to the data obtained [5] for the film. Curves *2* and *3* are constructed in [7] for separate bundles of single-layer sintered and unsintered nanopipes, respectively. The calculated dependences reproduce the experimental ones well if we assume that $p = 0.2$, $T_e = 550$ K (curves *1* and *2*) and $p = 0.035$, $T_e = 1400$ K (curve *3*). The value $g = 1$ and the hole band parameter $T_h = 5000$ K are identical for all curves. The disagreement between experimental and calculated dependences does not exceed 10% for this set of parameters. The model parameters corresponding to these dependences can be determined more accurately, for example, by the method of least squares. The total conductivity is the sum of the band conductivities. Therefore, the same results can be obtained by interchanging the band parameters. The hole-band conductivity is higher for the chosen set of parameters. This conforms to the data of Hall voltage and thermal emf measurements.

Figure 3 displays the experimental temperature dependence (curve *1*) of the resistivity ρ for a separate bundle of single-layer nanopipes [9]. The calculated dependence was found at $g = 1$, $p = 0.0001$, $T_e = 1900$ K, and $T_h = 5000$ K. At $T > 50$ K, the logarithmic derivatives of ρ for the calculated and experimental dependences are 0.0003 and 0.0004 K^{-1}, respectively. This difference may indicate that it is necessary to take into account the scattering by optical phonons.

As is evident, varying only two model parameters can yield good agreement with experiment in a wide temperature range (1–300 K) for various samples. This indicates that the given model takes into account the dominant factors affecting transport in films. Various samples exhibit a rather wide scatter in the model parameters p and T_e. This can be assumed to be partially related to different black-carbon contents and quality of electrical contacts between bundles in films. Furthermore, other scattering mechanisms should be taken into account in the calculations. However, on the basis of good agreement of calculation and experiment, one can assume that the model parameters (T_e, T_h, m_e, m_h, and p) are mainly controlled by nanopipe characteristics (the number of layers and chirality). In this case, the measured dependence $\sigma(T)$ can be used to determine the model parameters and corresponding kinetic character-

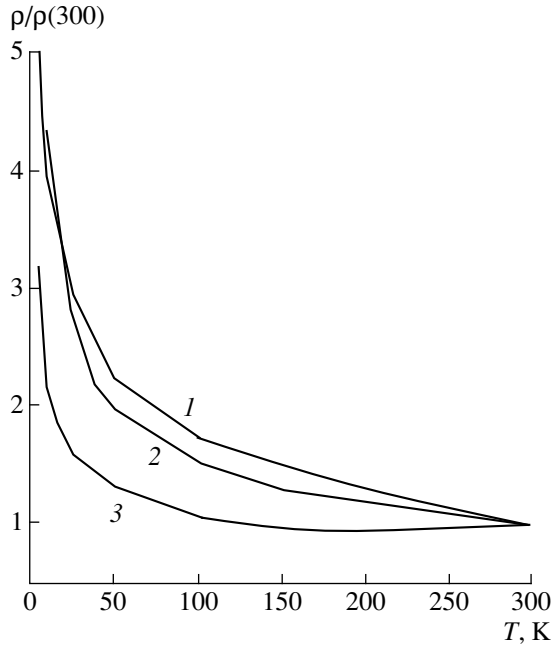

Fig. 2. Temperature dependences of the resistivity of (*1*) the film [5] and (*2*, *3*) separate bundles [7].

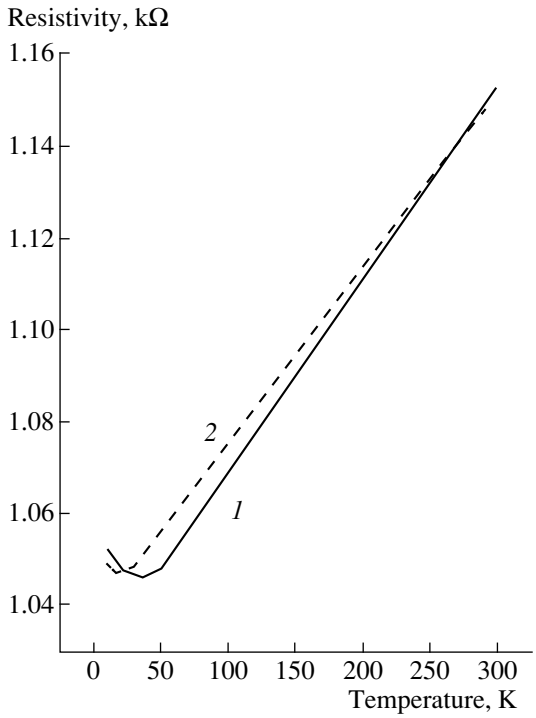

Fig. 3. Dependences of the resistivity of a single-layer nanopipe: (*1*) measured in [9] and (*2*) calculated by us.

istics of charge carriers for films consisting of various nanopipes. In particular, it follows from (2) that the carrier concentration should grow infinitely and, hence, $\rho \longrightarrow 0$ at $T \longrightarrow (2/3)T_m$, where T_m is the lower of the values T_e and T_h. Hence, the lower of the two values T_e or T_h can be determined by measuring $\rho(T)$ at high temperatures. If the measurement yields an absolute value of the resistivity, the value $N_c^* \tau_{DA}/m_e$ can be calculated by (4). Obviously, the kinetic parameters determined for films can be used as estimates for solitary nanopipes.

Thus, a simple model of the band structure of bundles and films of oriented nanopipes was proposed. It allows a sufficiently accurate conductivity calculation and explanation of the observed differences in the temperature dependences of conductivity of these objects within a unified approach.

ACKNOWLEDGMENTS

The author is grateful to Z. Ya. Kosakovskaya for critical comments and her participation in discussions.

This work was supported by the Russian Foundation for Basic Research, project no. 98-02-17130.

REFERENCES

1. S. Iijima, Nature (London) **354**, 56 (1991).
2. A. V. Eletskiĭ, Usp. Fiz. Nauk **167**, 940 (1997) [Phys. Usp. **40**, 899 (1997)].
3. L. Langer, V. Bayot, E. Grivei, *et al*., Phys. Rev. Lett. **76**, 479 (1996).
4. A. Y. Kasumov, I. I. Khodos, P. M. Ajayan, *et al.*, Europhys. Lett. **34**, 429 (1996).
5. G. Baumgartner, M. Carrard, L. Zuppiroli, *et al.*, Phys. Rev. B **55**, 6704 (1997).
6. M. Baxendale, V. Z. Mordkovich, and S. Yoshimura, Phys. Rev. B **56**, 2161 (1997).
7. J. Hone, I. Ellwood, M. Muno, *et al.*, Phys. Rev. Lett. **80**, 1042 (1998).
8. A. V. Bazhenov, V. V. Kveder, A. A. Maksimov, *et al.*, Zh. Éksp. Teor. Fiz. **113**, 1883 (1998) [JETP **86**, 1030 (1998)].
9. C. L. Kane, E. J. Mele, R. S. Lee, *et al.*, Europhys. Lett. **41**, 683 (1998).
10. A. B. Kaiser, G. Düsberg, and S. Roth, Phys. Rev. B **57**, 1418 (1998).
11. O. M. Yevtushenko, G. Ya. Stepyan, S. A. Maksimenko, *et al.*, Phys. Rev. Lett. **79**, 1102 (1997).
12. P. García-Mochales and P. A. Serena, Phys. Rev. Lett. **79**, 2316 (1997).
13. R. Egger and A. O. Gogolin, Phys. Rev. Lett. **79**, 5082 (1997).
14. C. Kane, L. Balents, and M. P. A. Fisher, Phys. Rev. Lett. **79**, 5086 (1997).
15. V. F. Gantmakher and I. B. Levinson, *Scattering of Carriers in Metals and Semiconductors* (Nauka, Moscow, 1984), Chap. 1, p. 28.
16. F. G. Bass and Yu. G. Gurevich, *Hot Electrons and High-Power Electromagnetic Waves in a Plasma in Semiconductors and Gas Discharge* (Nauka, Moscow, 1975), Chap. 1.

Translated by A. Kazantsev

Semiconductors, Vol. 34, No. 10, 2000, pp. 1203–1206. Translated from Fizika i Tekhnika Poluprovodnikov, Vol. 34, No. 10, 2000, pp. 1254–1257.

LOW-DIMENSIONAL SYSTEMS

Recombination of Self-Trapped Excitons in Silicon Nanocrystals Grown in Silicon Oxide

K. S. Zhuravlev* and A. Yu. Kobitsky

Institute of Semiconductor Physics, Siberian Division, Russian Academy of Sciences, pr. Akademika Lavrent'eva 13, Novosibirsk, 630090 Russia

** e-mail: zhur@thermo.isp.nsc.ru*

Submitted March 27, 2000; accepted for publication April 18, 2000

Abstract—The kinetics of photoluminescence (PL) and steady-state PL from silicon nanocrystals formed in the SiO_2 matrix by silicon ion implantation were studied experimentally for the first time in the temperature range from liquid-helium to room temperature. A dramatic increase in the photoluminescence decay time, accompanied by PL intensity quenching, is observed below 70 K. The results obtained indicate that the silicon nanocrystal PL arises from radiative recombination of excitons self-trapped at the silicon nanocrystal–SiO_2 interface. © *2000 MAIK "Nauka/Interperiodica".*

1. INTRODUCTION

The discovery of efficient photoluminescence (PL) from porous silicon in the visible region of the spectrum at room temperature [1] has stimulated extensive investigations of silicon nanostructures fabricated by a variety of methods, because of the possibility of using these structures in light-emitting optoelectronic devices. The nature of the visible PL from silicon nanostructures, not established until now, is the most intriguing puzzle. A great number of models of radiative recombination have been proposed to explain the visible PL [2, 3]. The interpretation of experimental data on PL in silicon nanocrystals fabricated by silicon ion implantation is facilitated by the fact that only the models unrelated to the presence of chemical impurities can be considered. These are the following: recombination of non-equilibrium carriers occupying size-quantization states in silicon nanocrystals [1], recombination of self-trapped excitons formed on Si–Si dimers at the Si nanocrystal–SiO_2 interface [4, 5], or recombination at the interface with a silicon oxide layer [6]. The self-trapped excitons in fairly small nanocrystals have been shown to be stable on the basis of semi-empirical and *ab initio* calculations [4]. Various ways to create such excitons by photoexcitation were studied in [7].

In this paper, we report the results of an experimental study of the temperature dependence of the PL decay time and the steady-state PL intensity in silicon nanocrystals. The nanocrystals were obtained by silicon ion implantation with subsequent thermal annealing. Joint analysis of these dependences suggests that the recombination of self-trapped excitons is the dominant mechanism of radiative recombination in the silicon nanocrystals studied.

2. EXPERIMENTAL

PL analysis was carried out for samples in which the formation of silicon nanocrystals 2–6 nm in size was demonstrated in the preceding study [8]. The samples were fabricated as follows. Silicon ions with energies of 200 and 100 keV were implanted into a 500-nm-thick silicon oxide film grown on a crystalline silicon substrate. The implantation dose was 1×10^{17} cm^{-2}. Then, the sample was annealed for 1 s at 1200°C and 30 min at 400°C. An Ar^+ laser (with a wavelength of 488 nm, and excitation power density of 0.01–1 kW/cm^2) was used for PL excitation. Nonsteady PL was excited by pulsed nitrogen laser radiation (with a wavelength of 337 nm, a pulse duration of 7 ns, and an average excitation power density of 0.04 kW/cm^2). The PL intensity was recorded with a sampling interval of 64 μs. The PL spectrum was analyzed with a spectrometer based on a double diffraction monochromator equipped with a photomultiplier operating in the single-photon-counting mode. The temperature T was varied within 4.2–300 K.

3. RESULTS AND DISCUSSION

A room-temperature PL spectrum of silicon nanocrystals is shown in Fig. 1. It comprises a single broadband (full width at half-maximum ~300 meV) peaked at about 1.5 eV. The decay curve of the integral PL intensity at room temperature is shown in the insert. The shape of this curve is evidently nonexponential. The decay time was determined by approximating the decay curve with a stretched exponential function: $I(t) = I_0 \exp\{-(t/\tau)^\beta\}$, where τ is the decay time and β is

1063-7826/00/3410-1203$20.00

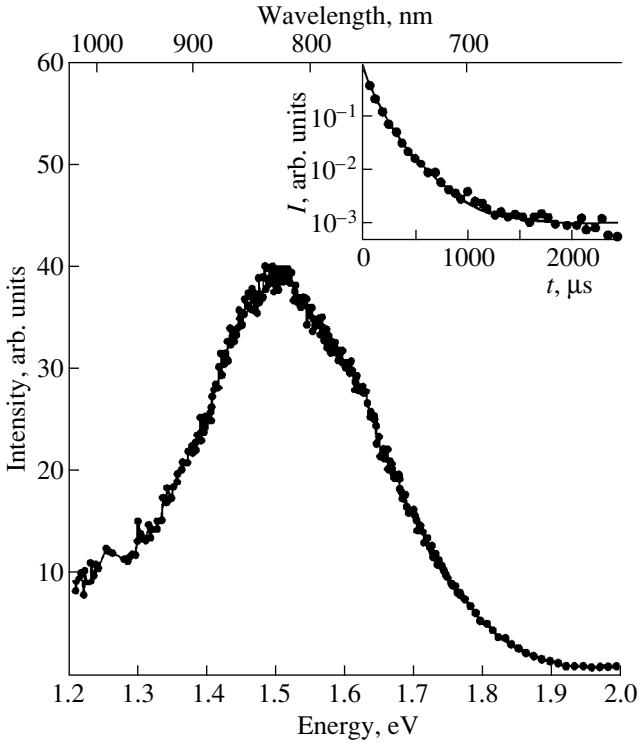

Fig. 1. PL spectrum of silicon nanocrystals. Insert: decay curve of the PL integrated intensity. $T = 300$ K.

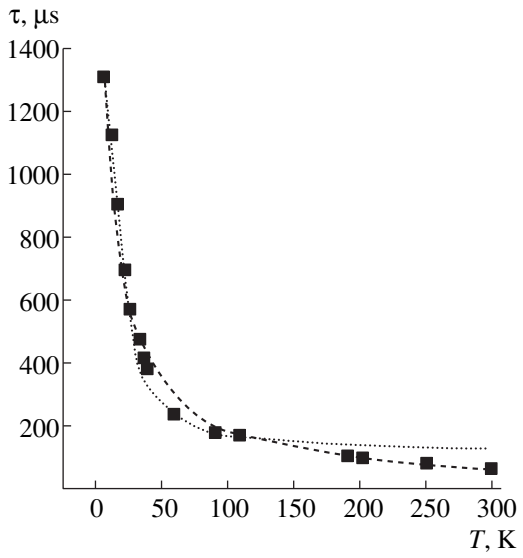

Fig. 2. Temperature dependence of the PL decay time for silicon nanocrystals. Squares represent experimental data; dotted line, results of calculations in terms of Calcott's model; dashed line, calculations based on the STE model.

the dispersion factor of the system. In the approximation, τ and β were considered as independent parameters and their values were determined by the method of least squares.

Figures 2 and 3 show the decay time τ and the integrated PL intensity I in relation to temperature. It can be seen that the decay time first sharply decreases as the temperature increases up to $T = 70$ K, with the PL intensity simultaneously increasing. Then, at $T > 70$ K, the decay time continues to decrease slowly, with the PL intensity following the same trend.

The observed temperature behavior of the decay time is qualitatively similar to that in the porous silicon. In [9], the recombination of an exciton (with a strong splitting of singlet and triplet states, caused by the enhancement of the electron–hole exchange interaction in quantum dots) was considered in terms of the size-quantization model. Approximating the temperature dependence of the decay time in terms of this model yields a good fit at low temperature ($T < 150$ K) with, however, a discrepancy observed at higher temperatures ($T > 150$ K) (see Fig. 2). This model assumes that radiative recombination is a dominant recombination channel over the entire temperature range, with the nonradiative recombination completely ignored. It was shown [10] that the efficiency of room temperature PL from silicon nanocrystals grown by chemical vapor deposition is 1% at most. An estimate of the PL efficiency for our samples yields a value of no more than several percent at room temperature. At the same time, it can be seen from Fig. 3 that the PL intensity increases with decreasing temperature by no more than a factor of 1.5. Thus, over the entire temperature range, the dominant recombination channel in the samples studied is nonradiative recombination.

Let us consider possible channels of nonradiative recombination in Calcott's model [9]. In the first place, this may be the nonradiative recombination of excitons with trapping by nonradiative recombination centers or the thermal destruction of excitons with the subsequent nonradiative recombination of nonequilibrium carriers. The second possible channel is hot-carrier trapping by nonradiative recombination centers, a process more probable than exciton formation. Since these two processes affect the exciton recombination time, their contribution cannot be significant at low temperatures where there is rather good agreement with experimental data even without these processes being taken into account. In order to explain the low PL efficiency, the trapping of hot carriers by nonradiative recombination centers has to be considered. It has been shown [11] that such a process is, indeed, possible and its probability much exceeds that of exciton formation. Thus, the PL efficiency is determined by hot-carrier trapping by nonradiative recombination centers, with the PL decay governed by the slower process of exciton recombination. Consideration of the nonradiative recombination makes it possible to describe the decay time as a function of temperature, but, as evident from Fig. 3, this model fails to explain the temperature dependence of the PL intensity. The strongest discrepancy is observed at low temperatures. Thus, Calcott's model does not account for the temperature dependences of both the

decay time and the PL intensity simultaneously, and the temperature dependence of the decay time cannot be considered as unequivocal evidence in favor of the recombination of a low-dimensional exciton.

Much better agreement of the calculated decay time and PL intensity as functions of temperature with experimental data can be obtained by using a recombination model with the formation of a self-trapped exciton, considered theoretically elsewhere [4, 7]. A schematic configuration diagram of the Si–Si dimer at the nanocrystal boundary is illustrated in Fig. 4. Here, E is the Si–Si bond vibration potential energy summed to the exciton energy and Q is the configurational parameter characterizing the atomic displacement in the Si–Si bond. The ground (G) and excited (E) states are those with a delocalized exciton. Capture of the exciton by the Si–Si bond causes a state with atoms shifted from their equilibrium positions to become more energetically favorable. Such a state is called self-trapped exciton (STE). There is an energy barrier Δ between the excited and STE states, with the height depending on the crystal size [4]. An exciton in the excited state can overcome the barrier and be captured either by a Si–Si bond or by a nonradiative recombination center. In its turn, an STE can recombine either radiatively (E_{PL}) or nonradiatively. A possible mechanism of STE nonradiative recombination involves its tunneling through the barrier E^* into the ground state (Fig. 4). The probability of such a recombination was shown [12] to be proportional to temperature. The total STE recombination time τ_{rec} is given by

$$\tau_{rec}^{-1} = \tau_r^{-1} + \tau_{nr}^{-1}, \quad (1)$$

where τ_r and $\tau_{nr} \propto T^{-1}$ are the radiative and nonradiative recombination times, respectively. If the STE formation time is appreciably shorter than its recombination time, then the PL intensity decay time is only determined by the STE recombination time. It can be seen from Fig. 2 that the temperature dependence of the decay time can be described by (1) with the same accuracy as that furnished by Calcott's model. Approximation of the experimental temperature dependence of the decay time with expression (1) yields 2 ms and 68 μs for the radiative and nonradiative recombination times, respectively (at $T = 300$ K).

At low temperature, the PL efficiency is determined by the probability ratio of exciton capture from an excited state by a nonradiative recombination center and STE formation. Since the STE formation is a thermally activated process with an activation energy equal to the barrier height Δ (Fig. 4), it is suppressed at $T < 70$ K, which explains the PL quenching. Approximation of the PL temperature dependence yields a barrier height of 5 meV. At high temperature, when the probability of STE formation is nearly temperature-independent, the decrease in the PL intensity is due to an increase, with decreasing temperature, in the probability of tunneling through the barrier E^* with the subsequent nonradiative recombination. This yields good agreement with the experimental results (Fig. 3).

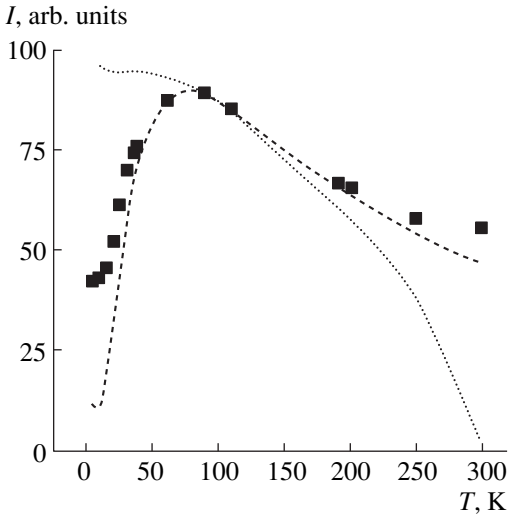

Fig. 3. Temperature dependence of the PL integrated intensity. Squares represent experimental data; dotted line, results of calculations in terms of Calcott's model; dashed line, calculations based on the STE model.

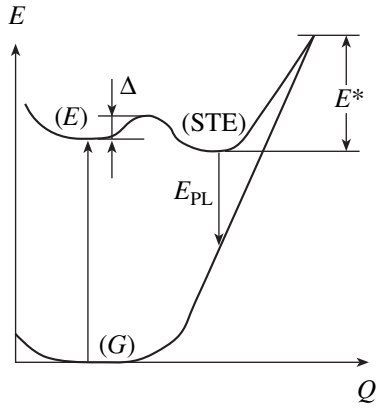

Fig. 4. Schematic configuration diagram for an Si–Si dimer at the interface between a silicon nanocrystal and the amorphous matrix.

4. CONCLUSION

The temperature dependence of the steady-state and transient PL from silicon nanocrystals grown by silicon ion implantation into a silicon oxide matrix with subsequent thermal annealing was studied. The experimental results are analyzed in terms of the models assuming the recombination of low-dimensional excitons localized in silicon nanocrystals and the recombination of STE formed on Si–Si dimers at the Si nanocrystal–SiO_2 interface. Good agreement with the experimental data is provided by calculations based on the model taking into account the STE formation.

ACKNOWLEDGMENTS

This work was supported by the Russian Foundation for Basic Research, project no. 97-02-18409.

REFERENCES

1. L. T. Canham, Appl. Phys. Lett. **57**, 1046 (1990).
2. G. Amato and M. Rosenbauer, *Structural and Optical Properties of Porous Silicon Nanostructures*, Ed. by G. Amato, C. Delerue and H.-J. Bardeleben (Amsterdam, 1997).
3. A. G. Cullis, L. T. Canham, and P. D. J. Calcott, J. Appl. Phys. **82**, 909 (1997).
4. G. Allan, C. Delerue, and M. Lannoo, Phys. Rev. Lett. **76**, 2961 (1996).
5. K. S. Zhuravlev, A. M. Gilinsky, and A. Yu. Kobitsky, Appl. Phys. Lett. **73**, 2962 (1998).
6. Y. Kanemitsu and S. Okamoto, Mater. Sci. Eng., B **48**, 108 (1997).
7. M. H. Nayfeh, N. Rigakis, and Z. Yamani, Phys. Rev. B **56**, 2079 (1997).
8. G. A. Kachurin, K. S. Zhuravlev, N. A. Pazdnikov, *et al.*, Nucl. Instrum. Methods Phys. Res. B **127/128**, 583 (1997).
9. P. D. J. Calcott, K. J. Nash, L. T. Canham, *et al.*, J. Phys.: Condens. Matter **5**, L91 (1993).
10. A. J. Kenyon, P. F. Trwoga, C. W. Pitt, and G. Rehm, Appl. Phys. Lett. **73**, 523 (1998).
11. C. Delerue, G. Allan, and M. Lannoo, Phys. Rev. B **48**, 11024 (1993).
12. S. D. Ganichev, I. N. Yassievich, and W. Prettl, Fiz. Tverd. Tela (St. Petersburg) **39**, 1905 (1997) [Phys. Solid State **39**, 1703 (1997)].

Translated by S. Ktitorov

Semiconductors, Vol. 34, No. 10, 2000, pp. 1207–1213. Translated from Fizika i Tekhnika Poluprovodnikov, Vol. 34, No. 10, 2000, pp. 1258–1264.

PHYSICS OF SEMICONDUCTOR DEVICES

Anomalous Dispersion, Differential Gain, and Dispersion of the α-Factor in InGaAs/AlGaAs/GaAs Strained Quantum-Well Semiconductor Lasers

A. P. Bogatov*, A. E. Boltaseva, A. E. Drakin*, M. A. Belkin**, and V. P. Konyaev*****

** Lebedev Physics Institute, Russian Academy of Sciences, Leninskiĭ pr. 53, Moscow, 117924 Russia*
**e-mail: bogatov@sci.lebedev.ru*
*** Moscow Institute of Physics and Technology, Institutskiĭ per. 9, Dolgoprudnyĭ, Moscow oblast, 141700 Russia*
**** Polyus State Research Institute, Moscow, 117342 Russia*
Submitted March 6, 2000; accepted for publication March 30, 2000

Abstract—A new procedure for the experimental determination of the differential gain and dispersion of the amplitude–phase coupling coefficient in semiconductor injection lasers was proposed and implemented. The α-factor and differential gain for InGaAs/AlGaAs/GaAs single quantum well (QW) semiconductor lasers were determined using this procedure in a wide spectral range (from 957 to 996 nm) at various pumping current densities (from 280 to 850 A/cm^2). The factor which characterizes the dispersion of the group velocity and restricts the minimum duration of the lasing pulse at the level of 10^{-13} s was experimentally determined for InGaAs lasers for the first time. © *2000 MAIK "Nauka/Interperiodica".*

INTRODUCTION

The strong dependence of the refractive index of an active medium on the density of the injected charge carriers plays an important part in semiconductor lasers. This dependence is caused by an anomalous dispersion and is characterized by the so-called amplitude–phase coupling coefficient (or α-factor), which is expressed as the ratio between the rates of the changes in the effective refractive index and modal gain with charge carrier density

$$\alpha = -\frac{4\pi}{\lambda}\frac{dn/dN}{dG/dN}. \quad (1)$$

Here, λ is the wavelength (in vacuum), n is the effective refractive index, G is the mode gain, and N is the density of the injected charge carriers. The amplitude–phase coupling coefficient affects a variety of the most important parameters of the laser radiation, such as the laser linewidth (α is also referred to as the broadening factor of the line) [1–3], lateral (along the layers of the structure) instability of the radiation field [4, 5], and frequency chirping of radiation [6, 7]. Both the theoretical calculations of the α-factor [8–10] and experimental studies of this parameter [11–16] have received much attention in the past decade. The problem of decreasing the α-factor is of great importance for the development of semiconductor lasers with improved dynamic and noise characteristics of the radiation. Thus, studies of the α-factor for new types of laser structures [13–17] are of particular interest at present. In this paper, the results of the experimental determination of the parameter discussed above are reported for InGaAs/GaAs strained QW lasers. These results were obtained in studies of their amplified spontaneous emission in the subthreshold mode using a new procedure. Such studies, which permit the variations in the effective refractive index and the mode gain with the pumping current to be determined simultaneously, provide data on the concentration dependence of the α-factor [18], differential gain, and dispersion of the α-factor in the lasers being studied.

This paper is concerned with a determination of the anomalous dispersion, differential gain, and variance of the α-factor in strained QW lasers based on the InGaAs/AlGaAs/GaAs single-QW heterostructure which emit in the spectral range of 0.94–0.98 μm.

EXPERIMENTAL

The samples we studied were laser diodes with a ridge waveguide (the ridge width was 3.5 μm) fabricated from the same heterostructure but with different cavity lengths (200, 400, and 600 μm). The diode mirrors had no reflecting coatings. The parameters of the structure are listed in the table. The calculated parameter of optical confinement for this structure was $\Gamma \approx 0.017$. The refractive indices of all the layers (except for the active layer) used in the calculations were obtained by extrapolating the data reported elsewhere [19]. The refractive index of the active layer was taken to be 3.63 [20]. The threshold currents of all the diodes were in the range of 13–15 mA, while the external differential efficiency (from both mirrors) was 0.6–0.8 W/A.

1063-7826/00/3410-1207$20.00

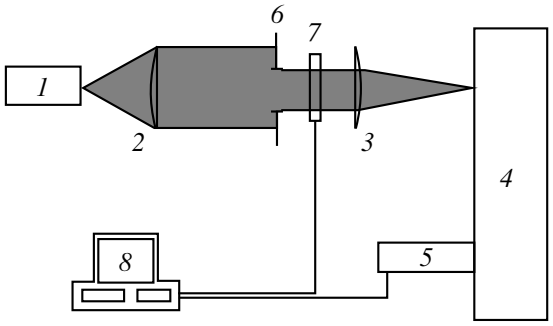

Fig. 1. Schematic diagram of the experimental setup: (*1*) laser diode; (*2*, *3*) focusing microobjectives; (*4*) DFS-24 spectrometer; (*5*) photodiode array; (*6*) slit diaphragm; (*7*) shutter; and (*8*) a PC.

The amplified spontaneous emission spectra were studied using a computer-controlled setup based on an optical multichannel spectrum analyzer (Fig. 1). The diode emission was focused onto the entrance slit of a DFS-24 spectrometer with two microobjectives. The data from the linear photodiode array, which had 1024 elements with a pitch of 25 μm and was placed in the plane of the exit slit of the spectrometer, were transmitted to the PC. A slit diaphragm between the objectives oriented normally to the structure layers served to select the fundamental transverse mode of the emission. A computer-controlled shutter in front of the focusing objective permitted us to check the dark current of the array elements and the background radiation during the measurement of each spectrum. The spectra were measured at a constant temperature of the copper holder of the laser, which was equal to 18°C. The temperature was adjusted by variation of the current through the Peltier cell or heater. The photodiode array was cooled to –25°C to decrease the noise. The dynamic range for the intensity recording was about 1.6×10^3.

The spectra were measured in the continuous pumping mode. Sets of spectra with a current step of 1 mA were measured for each laser diode. The magnitude of the step was chosen such that the mode shift caused by such a variation in the current was much less than the intermode spacing. This allowed us to determine the shift of each mode. The spectral range of ≈200 Å was covered by the linear array in a wavelength region of about 1 μm. The entire spectral range studied was ≈1300 Å. It was broken up into nine overlapping subranges of ≈200 Å each (nine fixed positions of the spectrometer gratings). Matching of the spectra was performed by determining the shift of particular modes when passing from one spectral range to another.

Parameters of the structure under study

Layer		Thickness, μm
Contact layer	p^+-GaAs	0.2
Emitter	P-$Al_{0.33}Ga_{0.67}As$	1.3
Waveguide layer	$Al_{0.23}Ga_{0.77}As$	0.09
Spacer	GaAs	0.006
Active layer	$In_{0.20}Ga_{0.80}As$	0.01
Spacer	GaAs	0.006
Waveguide layer	$Al_{0.23}Ga_{0.77}As$	0.09
Emitter	N-$Al_{0.33}Ga_{0.67}As$	1.6
Substrate	n-GaAs	100

The mode shift with the pumping current resulted not only from the change in the injected carrier density, but also from the variations in temperature caused by variations in the power released at the laser diode. For this reason, several spectra for each diode above the lasing threshold were also measured. This allowed us to evaluate the temperature contribution to the change in the refractive index.

Thus the initial data for mathematical processing were the digitized superluminescence spectra measured at various pumping currents (12–14 spectra in the subthreshold mode and 5–6 spectra above the threshold for each diode). These spectra contained, e.g., up to 480 longitudinal modes for a diode with the resonator length L = 600 μm.

PROCEDURE FOR SPECTRUM PROCESSING

The experimental determination of the differential gain and α-factor variance is based on processing the superluminescence spectra of laser diodes, i.e., optically amplified spontaneous emission of a laser operating in the subthreshold mode. A new procedure for determining the mode gain from the superluminescence spectra was used in this study.

In processing the superluminescence spectra, we used to advantage the fact that, in semiconductor lasers, the intensity of the spontaneous emission in its active region is sufficiently high to be experimentally detectable. This emission can be used as a probe radiation in the laser cavity. The latter can be considered as a Fabry–Perot resonator if the lateral structure of the field is assumed to correspond to a single fundamental mode. The spontaneous emission will be spectrum-modulated by the longitudinal resonances of this resonator. It should be noted that there is a direct analogy between the classical transmission spectrum of a Fabry–Perot resonator and the spectrum emitted inside it and emerging from it [21]. In both cases, we are dealing with the longitudinal resonances in the Fabry–Perot resonator. The waveguide behavior of the propagation of radiation between the resonator mirrors inherent in a semiconductor laser will cause some distinction of this resonator from the classical Fabry–Perot resonator. This distinction consists in the replacement of the refractive index of the homogeneous medium filling the classical resonator by the effective refractive index n for the mode under consideration. The latter is defined

as $n = \beta'/k_0$, where β' is the real part of the complex constant of the waveguide propagation $\beta = \beta' + i\beta''$ and $k_0 = \omega/c$ is the wave number in vacuum (c and ω have the conventional significance). In what follows, we assume that the dependence of the amplitude of electromagnetic wave on the coordinate z along the resonator axis and time t is proportional to $\exp(i\beta z - i\omega t)$. In this case, the coefficient of the amplitude–phase coupling α can be also defined as $\alpha = \left(\frac{\partial\beta'}{\partial N}\right)/\left(\frac{\partial\beta''}{\partial N}\right)$. The parameters of the resonator, in particular the reflectivities of its mirrors or the absorption (gain) inside it, can be determined from the width of the transmission line of the resonator or from the ratio of intensities in the minimum and maximum. This fact serves as a basis for a number of procedures for measuring the pumping current dependence of the gain in a semiconductor laser [22–24].

To determine the change in the refractive index with the pumping current, one has to know the exact positions of the resonator maxima for each spectrum that is measured. The numerical procedure of the least-squares fit of the theoretical model to the experimental spectra was used for this purpose. Each peak was described by the Airy function

$$I_k(\lambda) = \frac{A_k[1]}{A_k[2] - \cos(A_k[3](A_k[4] - \lambda))}, \qquad (2)$$

where λ is the wavelength. The fitting was performed for the coefficients $A_k[i]$, $i = 1,\ldots,4$. In Fig. 2, we show a portion of the superluminescence spectrum of a diode with the resonator length $L = 600$ μm for a pumping current of 10 mA (squares) and the model function (2) with coefficients determined by the fit to the central peak (solid curve). Thus the set of fitting coefficients completely defines the peak position of each longitudinal mode, intermode spacing in the region of the mode, and its shape.

The change in the effective refractive index was determined from the shift of the superluminescence modes with the pumping current. The unified numbering of the peaks for all pumping currents was introduced when processing the joined spectra; i.e., the maxima at the closest wavelengths had the same number for the neighboring values of the current. The condition for the Fabry–Perot resonances was written as

$$\frac{2Ln(\lambda_m(i), i)}{\lambda_m(i)} = M - m. \qquad (3)$$

Here, M is the unknown "absolute" number of the mode with the shortest wavelength in the experimental spectra of each diode; m is the "relative" number of the mode obtained in the through-numbering process (the maxima were numbered in order of increasing wavelength); and $\lambda_m(i)$ is the peak position of the mth mode for the pumping current i, which was determined by fitting the experimental points with formula (2). Next,

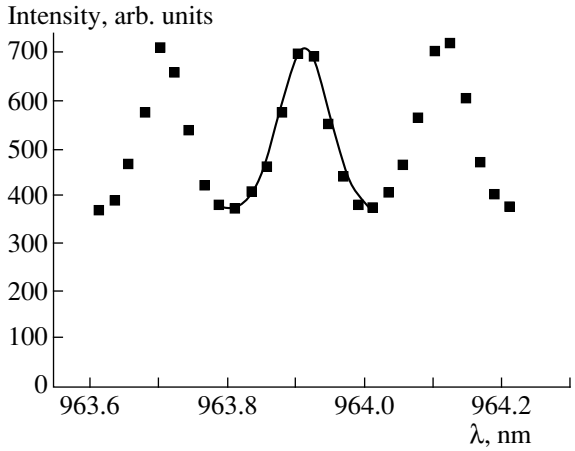

Fig. 2. Portion of the superluminescence spectrum of the diode with the cavity length $L = 600$ μm for a pumping current of 10 mA (squares) and the model function of superluminescence (formula (2) in the text) (solid curve).

some mode m_0 with a peak position λ_0 at the pumping current i_0 was chosen (the currents corresponding to the spectra with the largest number of maxima were chosen as i_0)

$$\frac{2Ln(\lambda_0, i_0)}{\lambda_0} = M - m_0. \qquad (4)$$

The expansion of the difference of expressions (4) and (3) in $\Delta\lambda_m/\lambda_0$ ($\Delta\lambda_m = \lambda_m(i) - \lambda_0$) up to the second-order terms resulted in the following expression for the difference of the relative numbers of the modes:

$$(m - m_0) = a(i) + b(i)\Delta\lambda_m + c(i)\Delta\lambda_m^2. \qquad (5)$$

The following notation was used in (5):

$$\Delta\lambda_m = \lambda_m(i) - \lambda_0, \qquad (6)$$

$$a(i) = -\frac{2L}{\lambda_0}(n(\lambda_0, i) - n(\lambda_0, i_0)), \qquad (7)$$

$$b(i) = \frac{2L}{\lambda_0^2}\left(n - \lambda\frac{\partial n}{\partial\lambda}\right)_{\lambda_{0,i}} = \frac{2L}{\lambda_0^2}n^*(\lambda_0, i), \qquad (8)$$

$$c(i) = -\frac{2L}{\lambda_0^3}\left(n^*(\lambda_0, i) + \frac{\lambda_0^2}{2}\left(\frac{\partial^2 n}{\partial\lambda^2}\right)_{\lambda_{0,i}}\right). \qquad (9)$$

The approximation of the experimental dependence $m - m_0 = f(\Delta\lambda_m)$ with the quadratic trinomial allowed us to determine the coefficient $a(i)$, which was the sought-for change in the refractive index. The curves of the spectral dependence $\partial n/\partial j$ were then obtained by numerical differentiation.

The variation in the effective refractive index with the pumping current occurs as a result of the changes in

the density of the injected charge carriers and diode temperature:

$$\frac{dn}{di} = \left(\frac{\partial n}{\partial N}\right)_T\left(\frac{\partial N}{\partial i}\right) + \left(\frac{\partial n}{\partial T}\right)_N\left(\frac{\partial T}{\partial i}\right), \qquad (10)$$

where N is the charge-carrier density and T is the diode temperature. The temperature and concentration effects can easily be separated from each other, since the corresponding changes in the refractive index n have unlike signs. Actually, the charge carrier density is stabilized above the lasing threshold and Δn is determined only by the heating. As a result, it depends linearly on the pumping current. The temperature contribution to the change in the refractive index both above the lasing threshold and in the subthreshold mode can be evaluated from the slope of the curve $\Delta n = f(i)$ above the lasing threshold. On the assumption that below the lasing threshold all the power supplied goes into diode heating, we obtain $\left(\frac{\partial T}{\partial i}\right)\Big|_{\text{sp}} = RU$, where R is the thermal resistance of the diode and U is the voltage across the diode. In view of the fact that, above the lasing threshold, the diode loses some power by radiation, we have $\left(\frac{\partial T}{\partial i}\right)\Big|_{\text{las}} = R(U - \eta)$, where η is the external differential efficiency from both mirrors (expressed in W/A). Then the relation between the derivatives $\frac{\partial T}{\partial i}$ in the subthreshold mode and above the lasing threshold is defined by the expression $\left(\frac{\partial T}{\partial i}\right)\Big|_{\text{sp}} = \left(\frac{U}{U-\eta}\right)\left(\frac{\partial T}{\partial i}\right)\Big|_{\text{las}}$. It follows from this relationship and Eq. (10) that

$$\left(\frac{\partial n}{\partial N}\right)\left(\frac{\partial N}{\partial i}\right)\Big|_{\text{sp}} = \frac{dn}{di}\Big|_{\text{sp}} - \left(\frac{U}{U-\eta}\right)\frac{dn}{di}\Big|_{\text{las}}. \qquad (11)$$

The most extensively employed method for measuring the mode gain is based on determination of the modulation depth in the laser spectrum in the subthreshold mode (the Hakki–Paoli method) [16, 22]. However, with this method, a major contribution to measurement error comes from the background radiation in the spectral range between the Fabry–Perot resonances, which is due to the "wings" of the spread function. There are a number of modifications of this method, which permit the effect of the spread function to be accounted for to a certain extent [23, 24]. We use an unconventional procedure for determining the gain from the superluminescence spectra, which consists in expressing the gain in terms of the distance between the Fabry–Perot resonances $\Delta\lambda$ and the width of the resonance $\delta\lambda_\beta$ at some level β. If $I_{\max}$ is the intensity in the maximum of the resonance peak and $I_{\min}$ is the intensity in its minimum, then the intensity at the level β is expressed as

$$I_\beta = I_{\min} + \beta(I_{\max} - I_{\min}), \quad 0 \le \beta \le 1. \qquad (12)$$

It is assumed that the spectrum of the amplified radiation in the region of the mth resonance is described by the function

$$I(\lambda) = \frac{A}{\left(\frac{1+F^2}{2F}\right) - \cos\left(2\pi\frac{\lambda_m - \lambda}{\Delta\lambda_m}\right)}. \qquad (13)$$

Here, A is the amplitude, $\Delta\lambda_m = \frac{\lambda_m^2}{2n^*L}$ is the intermode spacing, $F = \exp(GL)$, $G = \Gamma g - \alpha - \frac{1}{L}\ln\frac{1}{R}$ is the net mode gain, n^* is the group refractive index, and L is the diode length. We can now obtain the relation between $\delta\lambda_\beta/\Delta\lambda$ and F from formulas (12) and (13):

$$\cos\left(\pi\frac{\delta\lambda_\beta}{\Delta\lambda_m}\right) = \frac{(1+F^2)(2\beta-1) + 2F}{(1+F^2) + 2F(2\beta-1)}. \qquad (14)$$

The spread function in the above procedure is taken into account in the following manner. The relationship $\delta\lambda_\beta = 0$ corresponds to the lasing threshold. However, the mode width $\delta\lambda_\beta^r$ at some level β of the measured spectrum appears to be larger than $\delta\lambda_\beta$ due to the broadening caused by the spread function. Because of this, it is assumed that the following relationship holds for β close to unity:

$$(\delta\lambda_\beta^r)^2 \approx (\delta\lambda_\beta)^2 + (\delta\lambda_\beta^a)^2, \qquad (15)$$

where $\delta\lambda_\beta^a$ is the width of the spread function "at the level β." This is due to the fact that, close to the maximum, the spectra and spread function can be approximated by Gaussians, in which case relationship (15) holds exactly. In this case, at the lasing threshold we have

$$\delta\lambda_\beta^r \approx \delta\lambda_\beta^a. \qquad (16)$$

The curves of the mode gain were first determined with expression (14) without regard for the spread function. For the current corresponding to the lasing threshold (when the gain spectrum ceased to vary), the width of the spread function "at the level β" (β was taken to be 0.8) was evaluated from the mode width at the gain maximum. Then the true width of each mode for all spectra was determined using expression (15). The parameter $\delta\lambda_\beta^a$ for the spread function was 0.011 nm in our experiment, which corresponded to the spectral resolution at the 0.03-nm level according to the Rayleigh criterion. The spectral dependence of the differen-

tial gain for various pumping current densities was thereafter determined from the gain curves obtained.

Thus, the advantages of the procedure are twofold. First, it allows simultaneous detection and accumulation of the signal, as well as data approximation in a wide spectral range when the instrument is used as a polychromator. Because of this, a more precise analysis of the experimental data is possible compared to the conventional method when the spectral instrument is used as a monochromator, with successive detection of the intensities of the separate modes. Second, in the proposed procedure, the gain is in fact determined from the ratio of the spectral width of the resonance to the distance between the resonances rather than from the ratio between the intensities in the maximum and minimum of the Fabry–Perot resonance. This procedure minimizes the error associated with the "wings" of the spread function of the spectral instrument.

RESULTS AND DISCUSSION

The spectral dependences of the group refractive index n^* and $d^2n/d\lambda^2$ were obtained using the procedure for spectrum processing discussed above. Typical curves for these dependences are shown in Fig. 3. The dependences for the sample with the resonator length L = 400 μm (the current density is 857 A/cm^2) are shown. The dependences for the other samples and different pumping levels differ little from each other, being within the accuracy of the measurements (about 20%).

One can see from the dependences shown in the figure that the group refractive index n^* (see formula (8) in the text) varies from 3.8 to 3.9 in the range of wavelengths corresponding to the emission from the active layer. It is worth noting that the values obtained for n^* prove to be distinctly smaller than those for lasers with a bulk active region rather than a QW layer. For such lasers, n^* is about 4.5–4.8 [25]. The reason for this difference is presumably the rather small optical confinement factor (1.7%) for the QW lasers. Actually, in the case under consideration, the major portion of the optical flux propagates in the layers of the structure where the fundamental absorption edge is well away from the emission wavelength from the active layer. As a result, the dispersion of the effective refractive index, which is characterized by the derivative $dn/d\lambda$, turns out to be smaller than in a bulk active medium. In the latter case, the emission wavelength corresponds to the interband transitions for the layer where the major portion of the optical flux propagates. The term $-\lambda(dn/d\lambda)$ in expression (8) for the group refractive index is correspondingly smaller for the QW lasers than for the lasers with a bulk active region.

The deviation of the dispersion of the effective refractive index from linearity is characterized by the parameter $d^2n/d\lambda^2$, whose value for the lasers being studied varies in the range 1.2×10^{-6}–3.5×10^{-6} nm^2 according to our results. These values are three to seven times less than the corresponding parameter for lasers with a bulk active region [25]. A nonzero value of this parameter results in dispersion of the group velocity and hence in distortion of the shape of radiation pulse during its propagation. The pulse duration τ and the maximum distance z_D that it propagates without distortion are related by the expression [26]

$$z_D \approx (c\tau)^2\left(\frac{\partial^2 n}{\partial\lambda^2}\lambda^3\right)^{-1}. \quad (17)$$

For example, for $\tau = 10^{-13}$ s, which corresponds to a wave packet of spectrum-matched pulses with the spec-

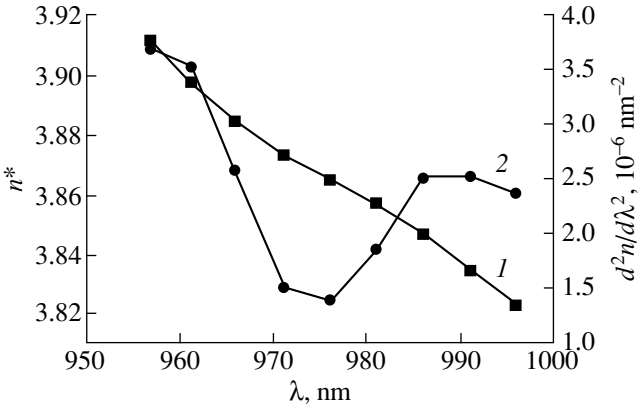

Fig. 3. Spectral dependences of (*1*) the group refractive index n^* and (*2*) $d^2n/d\lambda^2$ for the diode with the cavity length L = 400 μm for a pumping-current density of 857.14 A/cm^2. The maximum of the gain occurs at 983.6 nm.

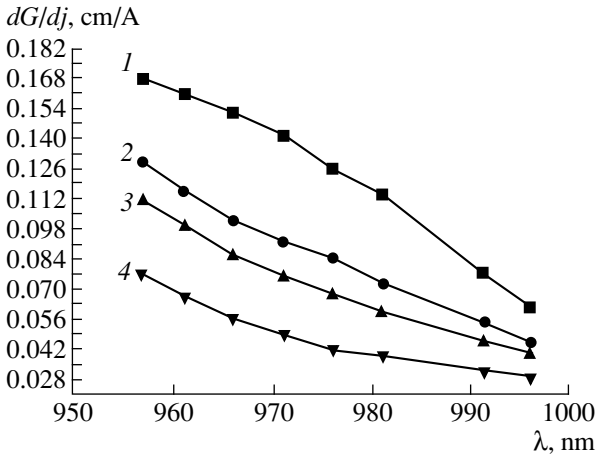

Fig. 4. Wavelength dependence of the differential gain of the diode with the cavity length L = 400 μm for the pumping-current densities of (*1*) 428.57 (maximum of gain is at the wavelength 989.7 nm); (*2*) 571.43 (the maximum of the gain is at the wavelength 987.1 nm); (*3*) 642.86 (maximum of gain is at the wavelength 986.5 nm); and (*4*) 857.14 A/cm^2 (maximum of gain is at the wavelength of 983.6 nm).

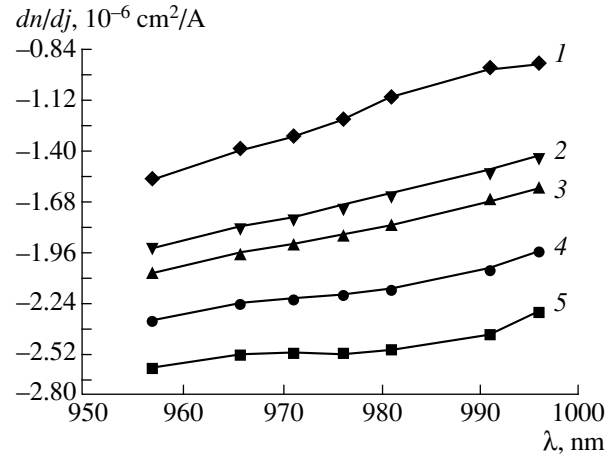

Fig. 5. Spectral dependences of $\partial n/\partial j$ for the diode with the cavity length L = 400 μm for the pumping current densities of (*1*) 857.14 (maximum of gain is at the wavelength 983.6 nm); (*2*) 642.86 (maximum of gain is at the wavelength 986.5 nm); (*3*) 571.43 (maximum of gain is at the wavelength 987.1 nm); (*4*) 428.57 (maximum of gain is at the wavelength 989.7 nm); and (*5*) 285.7 A/cm^2 (maximum of gain is at the wavelength 999.5 nm).

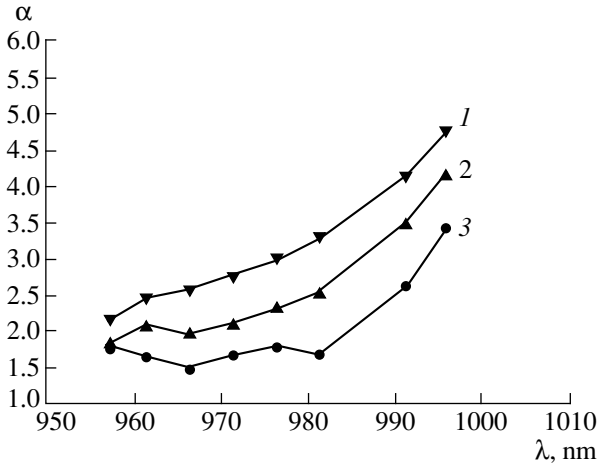

Fig. 6. Dispersion of the α-factor for the diode with the cavity length L = 400 μm for the pumping-current densities: (*1*) 571.43 (maximum of gain is at the wavelength 987.1 nm); (*2*) 428.57 (maximum of gain is at the wavelength 989.7 nm); and (*3*) 285.7 A/cm^2 (maximum of gain is at the wavelength 999.5 nm).

trum width $\Delta\lambda \approx 30$ nm and wavelength $\lambda = 1$ μm, the value of z_D will be in the range of 7×10^{-2}–2.5×10^{-2} cm. This distance corresponds to one or two passes of the pulse between the mirrors of the cavity in a typical laser diode. In other words, the values found for $d^2n/d\lambda^2$ are such that the possibility of generating and amplifying ultrashort light pulses is limited by the pulse duration at the level of 10^{-13} s. We note as a favorable condition that the spectral minimum of $d^2n/d\lambda^2$ is close to the wavelength corresponding to the gain maximum.

The typical experimental wavelength dependence of the differential gain at various pumping-current densities is shown in Fig. 4. This dependence was obtained for a diode with a cavity length of 400 μm. As can be seen from this figure, this dependence is quite regular. The parameter dG/dj decreases as the pumping-current density increases, which is the result of gain saturation at a fixed wavelength due to the restricted density of the electron states for the QW layer. Furthermore, the drop in the differential gain occurs with increasing wavelength for each value of the pumping current. This is due to the fact that the gain of the long-wavelength radiation is due to the transitions from the lowest level in the QW, while, for radiation with a shorter wavelength, a contribution to the gain can also be made by the transitions from the second level if the finiteness of the "homogeneous" linewidth of the transition is taken into account. The spectral range of 965–995 nm spans the electronic transitions from both the first and second levels of the QW [18].

The experimental curves of the wavelength dependence of dn/dj in the same spectral range, which characterize the anomalous dispersion, are shown in Fig. 5. Some of the curves obtained for the diode with the cavity length of 400 μm for different pumping-current densities are shown. In accordance with the expected behavior in the case of anomalous dispersion, the addition to the refractive index associated with the charge carriers increases with the wavelength in the spectral region where optical amplification occurs. It should also be stated that the total dispersion, which includes the variance of GaAs spacer layers and AlGaAs waveguide layers, will have normal behavior; i.e., the refractive index decreases with increasing wavelength.

The α-factor for the samples we studied was calculated using the data on the pumping-current dependences of the change in the effective refractive index and mode gain. The wavelength dependence of the α-factor obtained for one of the laser diodes is shown in Fig. 6. In the wavelength range from 956 to 997 nm, the α-factor shows nearly monotonic behavior for all values of the pumping current in the subthreshold mode. The values obtained for the parameter α fall within the range from 1 to 4.5, which is consistent with previously published data on the concentration dependence of the α-factor [8]. We notice that α increases with the wavelength. Referring to formula (1) for the sake of illustration we note that the denominator dG/dN decreases with increasing λ. It approaches zero as the long-wavelength edge of the line where gain saturation occurs is approached, whereas the numerator dn/dN does not tend to zero due to the contribution of the free carriers.

The behavior of the α-factor is quite regular. With the increase in the pumping-current density for the particular wavelength, α increases, which is also associ-

ated with saturation of the gain in the material at a fixed wavelength.

The scatter in the experimental values of α is not associated with the accuracy of the measurements but is a consequence of the observed behavior of α. It should be borne in mind that this parameter is the ratio of the derivatives. Because of this, it is more sensitive to the variation in the charge-carrier density than initial parameters, such as the refractive index or gain. The estimates show that the error in determining the α-factor can be as large as 10%.

CONCLUSION

Thus, a new procedure for experimental determination of the amplitude–phase coupling coefficient of semiconductor lasers was implemented in this paper. The results of measurements carried out with this technique for InGaAs lasers confirmed the currently available data on the α-factor values and provided new data on the spectral dependence of this coefficient in the wavelength region corresponding to the electron transitions from both the first and second levels in QW. Knowledge of the spectral dependence of the amplitude–phase coupling coefficient is of particular importance in the simulation and prediction of the characteristics of lasers operating at a fixed wavelength, for example, distributed-feedback lasers and α-distributed-feedback lasers.

The parameter $d^2n/d\lambda^2$ was experimentally determined for InGaAs lasers for the first time. This parameter is a measure of the dispersion "spread" of the pulse as it propagates inside the laser cavity. The estimates showed that the minimum practicable duration of the radiation pulse for lasing and amplification in these lasers is restricted by a value of about 10^{-13} s.

ACKNOWLEDGMENTS

This study was carried out within the framework of the Program "Physics of Solid-State Nanostructures" and supported in part by the Federal Special Program "Integration" (Educational-Scientific Centers "Basic Optoelectronics of the Quantum-Scale Semiconductor Structures" and "Basic Optics and Spectroscopy").

REFERENCES

1. H. Henry, IEEE J. Quantum Electron. **QE-18**, 259 (1982).
2. K. Vahala and A. Yariv, IEEE J. Quantum Electron. **QE-19**, 1096 (1983).
3. K. Vahala, L. C. Chiu, S. Margalit, and A. Yariv, Appl. Phys. Lett. **42**, 631 (1983).
4. R. J. Lang, D. Mehuys, D. F. Welch, and L. Golgberg, IEEE J. Quantum Electron. **QE-30**, 685 (1994).
5. A. Bogatov, Proc. SPIE–Int. Soc. Opt. Eng. **2399**, 456 (1995).
6. T. L. Koch and J. E. Bowers, Electron. Lett. **20**, 1038 (1984).
7. N. K. Dutta and G. P. Agrawal, *Long-Wavelength Semiconductor Lasers* (Van Nostrand Reinhold, New York, 1986), p. 264.
8. J. Hader, D. Bosset, J. Stohs, *et al.*, Appl. Phys. Lett. **74**, 2277 (1999).
9. S. A. Anson, J. T. Olesbereg, Michael E. Flatte, *et al.*, J. Appl. Phys. **86**, 713 (1999).
10. H. Wenzel, G. Erbert, and P. M. Enders, IEEE J. Sel. Top. Quantum Electron. **5**, 637 (1999).
11. N. K. Dutta, J. Wynn, D. L. Sivco, and A. Y. Cho, Appl. Phys. Lett. **56**, 2293 (1990).
12. N. K. Dutta, H. Temkin, T. Tanbun-Ek, and R. Logan, Appl. Phys. Lett. **57**, 1390 (1990).
13. R. Raghuraman, N. Yu, R. Engelmann, *et al.*, IEEE J. Quantum Electron. **QE-29**, 69 (1993).
14. K. Kikuchi, M. Amano, C. E. Zah, and T. P. Lee, IEEE J. Quantum Electron. **QE-30**, 571 (1994).
15. O. V. Danilina and A. S. Logginov, Kvantovaya Élektron. (Moscow) **22**, 1079 (1995).
16. V. P. Konyaev, V. D. Kurnosov, V. N. Luk'yanov, *et al.*, Kvantovaya Élektron. (Moscow) **21**, 1137 (1994).
17. T. C. Newell, D. J. Bossert, A. Stintz, *et al.*, IEEE Photonics Technol. Lett. **11**, 1527 (1999).
18. A. P. Bogatov, A. E. Boltaseva, A. E. Drakin, *et al.*, Kvantovaya Élektron. (Moscow) **30** (2000) (in press).
19. N. C. Casey, Jr. and M. B. Panish, *Heterostructure Lasers* (Academic, New York, 1978; Mir, Moscow, 1981).
20. W. X. Zou, J. L. Merz, and L. A. Coldren, J. Appl. Phys. **72**, 5047 (1992).
21. V. V. Bezotosnyĭ, A. P. Bogatov, L. M. Dolginov, *et al.*, Tr. Fiz. Inst. Akad. Nauk SSSR **141**, 18 (1983).
22. T. Paoli and B. Hakki, J. Appl. Phys. **44**, 4113 (1973).
23. D. T. Cassidy, J. Appl. Phys. **56**, 3096 (1984).
24. L. D. Westbrook, IEE Proc. **133**, 135 (1986).
25. J. P. van der Ziel and R. A. Logan, IEEE J. Quantum Electron. **19**, 164 (1983).
26. S. A. Akhmanov and S. Yu. Nikitin, *Physical Optics* (Mosk. Gos. Univ., Moscow, 1998).

Translated by Yu. Aleshchenko

Semiconductors, Vol. 34, No. 10, 2000, pp. 1214–1218. Translated from Fizika i Tekhnika Poluprovodnikov, Vol. 34, No. 10, 2000, pp. 1265–1269.

PHYSICS OF SEMICONDUCTOR DEVICES

An Artificially Anisotropic Thermoelectric Material with Semiconducting and Superconducting Layers

D. A. Pshenaĭ-Severin*, Yu. I. Ravich*, and M. V. Vedernikov**

** St. Petersburg State Technical University, ul. Politekhnicheskaya 29, St. Petersburg, 195251 Russia*

*** Ioffe Physicotechnical Institute, Russian Academy of Sciences, ul. Politekhnicheskaya 26, St. Petersburg, 194021 Russia*

Submitted April 3, 2000; accepted for publication April 3, 2000

Abstract—The thermoelectric parameters of an artificially anisotropic material composed of semiconducting and superconducting layers are considered. The transverse thermoelectric figure of merit and the sensitivity of a sensor responding to small heat fluxes are calculated. The use of high-temperature superconductor layers appreciably changes the optimal geometry of the layered structure (layer inclination angle and thickness ratio) compared with normal conductors. The figure of merit and the sensitivity of a thermoelectric element with superconducting layers exceed the respective parameters of a structure with metallic layers by a factor of 2–3. *© 2000 MAIK "Nauka/Interperiodica".*

1. INTRODUCTION

The operation of transverse thermoelectric devices based on anisotropic materials relies upon the nondiagonal component of the thermal emf tensor. The transverse voltage depends substantially not only on the thermoelectric parameters of a material, but also on the element geometry and, consequently, may be rather high. However, single crystals with anisotropic thermal emf have a comparatively low figure of merit, which stimulated the authors of [1] to propose artificially anisotropic heterophase materials comprising alternating parallel layers with different parameters and good transverse thermoelectric characteristics.

Calculations [1] have shown that the best starting components for such a layered material are high-quality *n*- and *p*-type semiconductors with very different electrical and thermal conductivities. For low temperatures (50–120 K), *n*-type semiconductor materials with a high thermoelectric figure of merit have been developed: in $Bi_{1-x}Sb_x$ alloys, the dimensionless figure of merit Z_1T is close to unity. However, the figure of merit for all the available *p*-type semiconductors is significantly lower than that for *n*-$Bi_{1-x}Sb_x$. The use of a low-efficiency *p*-type material in an artificially anisotropic layered structure impairs the system characteristics, similarly to what occurs in a conventional longitudinal thermoelement. For this reason, metallic layers are employed instead of a *p*-type semiconductor [2] as the passive metallic leg of a thermoelement. The figure of merit for a conventional thermoelement with a passive metallic leg is several times lower than that for a thermoelement fabricated from high-efficiency *n*- and *p*-type semiconductors.

As a solution for the case of a longitudinal thermoelement, the authors of [3] used a high-temperature superconductor (HTSC) characterized at zero thermal emf by an infinite ratio of electrical to thermal conductivities as a passive leg. Owing to this property, an HTSC appears to be a valid substitute for a semiconducting *p*-leg. Thus, we can expect that an artificial anisotropic structure with HTSC layers will have noticeably better thermoelectric parameters than a structure with metal interlayers.

In this study, the effective thermoelectric parameters of a heterophase structure consisting of semiconducting and superconducting layers are calculated. The parameters of a layered material with a superconductor as the second component are compared with those of an artificial anisotropic thermoelectric material containing metallic interlayers. It appears that the zero resistivity of the superconductor fundamentally changes the optimization conditions for the composite material parameters, compared with the previously discussed case of normal-conduction layers.

2. STARTING RELATIONS

Let us consider a sample consisting of alternating layers of two different isotropic materials brought into ideal contact with one another (Fig. 1). For definiteness, we assume that layers *1* are made of an *n*-type semiconductor with thermoelectric power α_1, thermal conductivity κ_1, resistivity ρ_1, and a high thermoelectric figure of merit

$$Z_1 = \frac{\alpha_1^2}{\rho_1\kappa_1}. \quad (1)$$

1063-7826/00/3410-1214$20.00 © 2000 MAIK "Nauka/Interperiodica"

Layers *2* with kinetic coefficients α_2, κ_2, and ρ_2 can be made of a *p*-type semiconductor, metal, or superconductor. If the layer thicknesses δ_1 and δ_2 are small compared with the sample dimensions, the heterogeneous material can be regarded as homogeneous with anisotropic effective thermoelectric parameters. In the (x_0, y_0) coordinate system associated with the layer orientations (Fig. 1), the effective thermal emf tensor is diagonal and has the components α_x and α_y; the components of the other tensors are denoted by κ_x, κ_y and ρ_x, ρ_y.

In order to use an anisotropic material in transverse thermoelectric devices, the *x* and *y* axes associated with the sample faces must be different from the main tensor axes. Assuming that the *x* and *y* axes are rotated by an angle ϕ with respect to the main tensor axes, we obtain the effective kinetic-coefficient tensors α_{ik}, κ_{ik}, and ρ_{ik} in the nondiagonal form. The expressions for all the kinetic coefficients mentioned above are given elsewhere [1]. The transverse thermoelectric figure of merit for an anisotropic medium is given by

$$Z_a = \frac{\alpha_{xy}^2}{\rho_{xx}\kappa_{yy}} = \frac{(\alpha_x - \alpha_y)^2\omega}{(\rho_x + \omega\rho_y)(\omega\kappa_x + \kappa_y)}, \quad (2)$$

where $\omega = \tan^2\phi$. The calculation of this function [1] yields general relations in the form of a product of functions:

$$Z_a = Z_1 F(n)\Phi(n, \omega), \quad (3)$$

where the geometric parameter *n* is given by

$$n = \frac{\delta_2}{\delta_1}. \quad (4)$$

The dimensionless function $F(n)$ is independent of the angle ϕ and is given by[1]

$$F = \frac{(\rho^* + n\alpha^*)^2(n+1)^2}{(\rho^* + n)^2(1 + n\kappa^*)(1 + n\rho^*)(1 + Z_0T)}, \quad (5)$$

where the parameters with an asterisk denote the relative quantities

$$\alpha^* = \frac{\alpha_2}{\alpha_1}, \quad \kappa^* = \frac{\kappa_2}{\kappa_1}, \quad \rho^* = \frac{\rho_2}{\rho_1}, \quad (6)$$

and Z_0 is the figure of merit for a conventional Peltier thermoelement with legs made of isotropic materials *1* and *2*, for which the ratio of the leg cross sections *n* is nonoptimized:

$$Z_0 = \frac{(\alpha_1 - \alpha_2)^2}{(\kappa_1 + n\kappa_2)(\rho_1 + \rho_2 n^{-1})}. \quad (7)$$

[1] Some discrepancies between formulas (5), (9), and (10) below and corresponding expressions in [1] (and handbook [4]) are due to misprints in [1], which have no effect on the final results of the calculations.

The function

$$\Phi(n, \omega) = \frac{(K_\alpha - 1)\omega}{(\omega K_\rho + 1)(\omega K_\kappa + 1)} \quad (8)$$

depends on ϕ via ω and implicitly on *n* via the relative quantities

$$K_\alpha = \frac{\alpha_x}{\alpha_y}, \quad K_\kappa = \frac{\kappa_x}{\kappa_y}, \quad K_\rho = \frac{\rho_y}{\rho_x}. \quad (9)$$

The angle ϕ can be optimized from the condition for maximizing Z_a taking into account that it appears in the term Φ:

$$\tan\phi_0 = \frac{[(1 + n\kappa^*)(\kappa^* + n)(1 + n\rho^*)(\rho^* + n)(1 + Z_0T)]^{1/4}}{(n+1)(\kappa^*\rho^*)^{1/4}}. \quad (10)$$

3. TRANSVERSE THERMOELECTRIC FIGURE OF MERIT FOR A SEMICONDUCTOR WITH METAL INTERLAYERS

An analysis of the general relations presented above shows that the best material for layers *2* is a high-efficiency *p*-type semiconductor, but, as mentioned in the Introduction, no good material has been found for the positive legs of low-temperature thermoelements. Therefore, the semiconductor–metal system is commonly discussed [1], for which, owing to the high electrical and thermal conductivities of the metal, it can be assumed that

$$\rho^* \ll 1, \quad \kappa^* \gg 1. \quad (11)$$

In addition, the thermoelectric figure of merit Z_0 of a semiconductor–metal couple is several times lower than the Z_1 value of a semiconductor. Since $Z_1T \simeq 1$ for the best semiconductor materials, we can assume that $Z_0T \ll 1$. As a result, we use (10) to obtain

$$\tan\phi_0 = \frac{n^{1/2}}{n+1}\left(\frac{\kappa^*}{\rho^*}\right)^{1/4}. \quad (12)$$

If $\phi = \phi_0$, the value Z_a/Z_1 is nearly independent of *n*, being equal to

$$\frac{Z_a}{Z_1} = \frac{1}{(\sqrt{\rho^*\kappa^*} + 1)^2} \quad (13)$$

for a wide range of *n* values

$$\rho^* \ll n \ll \kappa^*, \quad (\rho^*)^{-1}, \quad (14)$$

including the value $n = 1$; i.e., we have a very broad peak at $n \simeq 1$. Therefore, we may assume that $n \simeq 1$ for the optimal ϕ. Owing to the high values of κ^*/ρ^*, the optimal angle ϕ_0 is fairly close to 90°.

As an example, let us evaluate the couple that consists of a $Bi_{0.88}Sb_{0.12}$ semiconductor and Ag metal at

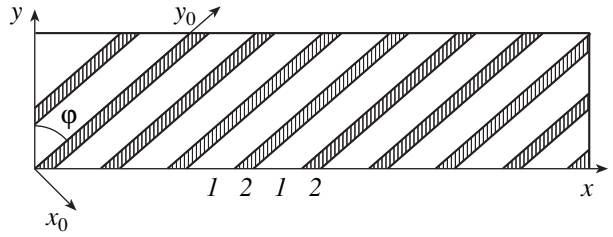

Fig. 1. Artificial anisotropic material consisting of (*1*) semiconductor layers and (*2*) layers with another type of conduction (*2*).

$T = 80$ K. The parameters of $Bi_{0.88}Sb_{0.12}$ are the following [5]:

$$\alpha_1 = -165\ \mu B/K,\ \rho_1 = 1.63 \times 10^{-6}\ \Omega\ m,$$

$$\kappa_1 = 3\ W/(m\ K)\ (Z_1 = 5.5 \times 10^{-3}\ K).$$

For the metal, the thermoelectric power α_2 can be neglected, $\rho_2 = 0.30 \times 10^{-8}\ \Omega$ m, and $\kappa_2 = 430$ W/(m K) [4, 6]. Hence, $\rho^* = 1.8 \times 10^{-3}$ and $\kappa^* = 0.14 \times 10^3$. For $n = 1$, the optimal angle ϕ_0 is 83°.

For such a small deviation of ϕ_0 from 90° ($\phi' = 90° - \phi_0 = 7°$), the sample dimension along the *x* axis should exceed the *y* dimension by at least two orders of magnitude; otherwise, the edge effects are pronounced. On reducing the *n* value to 0.1, no noticeable decrease in Z_a is observed and the angle ϕ_0 remains large: $\phi_0 = 78°$, $\phi' = 12°$. Therefore, it is of interest to consider angles ϕ differing from the optimal value.

Calculations by the above formulas showed that, when the value of ϕ departs from ϕ_0, the trend of the $Z_a(n)$ dependence changes radically: for $n \simeq 1$, a minimum is observed instead of maximum, with two peaks appearing at $n > 1$ and $n < 1$. For $\phi \le 70°$, these peaks are very far from unity; i.e., the first peak is located at $n \ll 1$ (Fig. 2). Values of *n* that are too small may be inconvenient in practice, and, therefore, all further numerical calculations were performed for a nonoptimized value $n = 0.1$, except for the case of $\phi = \phi_0$.

Relative transverse thermoelectric figure of merit Z_a/Z_1 for an artificial anisotropic material consisting of *n*-$Bi_{0.88}Sb_{0.12}$ layers and metallic or superconducting interlayers; $T = 80$ K. The layer thickness ratio $n = 1$ for $\phi = 83°$ for metallic layers and $n = 0.1$ otherwise

φ, deg	Material of layers *2*		
	Metal (Ag)	Bismuth-based HTSC	Yttrium-based HTSC
83	0.41	0.76	0.92
78	0.41	0.73	0.89
70	0.30	0.64	0.79
60	0.17	0.51	0.64
45	0.07	0.30	0.39

The table presents the transverse thermoelectric figures of merit, which are related to the semiconductor figure of merit Z_1, for silver interlayers of relative thickness *n* at various angles ϕ. Further on, we discuss how these results are modified by replacing a metal with superconducting layers.

4. THERMOELECTRIC FIGURE OF MERIT FOR A MATERIAL WITH SUPERCONDUCTING INTERLAYERS

When superconducting layers are used instead of a *p*-type semiconductor, it should be assumed that $\rho_2 = 0$ and $\alpha_2 = 0$ in the above relations. The thermal conductivity of HTSC materials is of the same order of magnitude as that of semiconducting thermoelectric materials; i.e., $\kappa^* \simeq 1$.

The calculations by formulas (3), (5), and (8) derived in [1] for normal-conduction layers lead to uncertainties; therefore, the starting relation (2) should be used to calculate the thermoelectric figure of merit. For a thermal emf and resistivity of the superconducting interlayers equal to zero, $\alpha_y = 0$ and $\rho_y = 0$. We again obtain equation (3) from (2), but now the expressions for the functions $F(n)$ and $\Phi(n, \omega)$ differ from (5) and (8):

$$F = \frac{\kappa^*}{\kappa^* + n}, \tag{15}$$

$$\Phi = \left[1 + \frac{(1 + n\kappa^*)(\kappa^* + n)(1 + Z_0 T)}{(n+1)^2 \kappa^* \omega}\right]^{-1}, \tag{16}$$

$$Z_0 = \frac{Z_1}{1 + n\kappa^*}. \tag{17}$$

For $n \ll 1$ and $\omega \gg 1$, the functions *F* and Φ tend to unity and the Z_a and Z_0 values approach the thermoelectric figure of merit of the semiconductor material Z_1. In this case, there are no optimal values of the geometric factors *n* and ω, since the dependence of Z_a on *n* and ω has no maximum: the closer the angle ϕ to 90° and the lower the *n* value, the closer Z_a is to the indicated limiting value. A constraint on the value of ω (angle ϕ) is imposed by edge effects associated with the finite sample size.

Using the expressions obtained above, we numerically calculated the relative transverse thermoelectric figure of merit Z_a/Z_1 for a material consisting of *n*-$Bi_{1-x}Sb_x$ semiconductor layers with the parameters given above and superconducting interlayers with thermal conductivities of bismuth-($BiSrCaCu_2O_y$) and yttrium-based ($YBa_2Cu_3O_y$) HTSCs. The thermal conductivity of an HTSC in the superconducting state depends on temperature, composition, defects, poros-

ity, etc. [7]. For evaluation purposes, we chose κ_2 = 1 W/(m K), corresponding to the thermal conductivity of the bismuth-based HTSC Bi–Sr–Ca–Cu–O at T = 80 K, and a severalfold higher value κ_2 = 4 W/(m K) of the same order of magnitude as the thermal conductivity of the yttrium-based HTSC $YBa_2Cu_3O_y$ at the same temperature. For the n-$Bi_{1-x}Sb_x$ semiconductor layers, κ^* was 0.3 and 1.3, respectively. The parameter n was taken to be 0.1, and the ϕ angles were varied, similarly to the case of a material with metallic layers. The calculated results are listed in the table. Comparison of the data for superconducting and metallic interlayers shows that the use of an HTSC in artificial anisotropic materials allows the transverse thermoelectric figure of merit Z_a to be increased substantially (two- to threefold), thus making it close to the semiconductor figure of merit Z_1, which is the maximum feasible value for the given type of material.

5. SENSITIVITY OF THE TRANSVERSE ELEMENT

When a thermoelement made of anisotropic material serves as a sensor of small heat fluxes, along with a high figure of merit, it must have high sensitivity proportional to

$$W = \frac{\alpha_{xy}}{\kappa_{yy}}. \tag{18}$$

The system optimization with respect to the angle ϕ yields for this case [8]

$$\tan^2\phi_0 = \frac{1}{K_\kappa}, \tag{19}$$

where the parameter K_κ is defined by (9). Expressing K_κ in terms of the quantities (6), we obtain

$$\tan^2\phi_0 = \frac{(1+n\kappa^*)(\kappa^*+n)(1+Z_0T)}{(n+1)^2\kappa^*}, \tag{20}$$

and an expression for the sensitivity optimized with respect to the angle ϕ:

$$W_{\max} = \frac{\alpha_1}{2\kappa_1} \times \frac{(\rho^*-\kappa^*)(\alpha^*-1)n}{[\kappa^*(\rho^*+n)^2(\kappa^*+n)(1+n\kappa^*)(1+Z_0T)]^{1/2}}. \tag{21}$$

For metallic interlayers, inequalities (11) hold; in addition, we can assume that $Z_0T \ll 1$. Analysis of the dependence of expression (21) on the layer thickness ratio n shows that W peaks for $n \ll 1$, so that expression (21) can be simplified. Then, calculating the optimal value for n, we have

$$n_0 = \frac{1}{2}(\rho^* + \sqrt{(\rho^*)^2 + 8(\kappa^*)^{-1}}), \tag{22}$$

which yields a very small value n_0 = 0.006 for n-$Bi_{1-x}Sb_x$ with Ag interlayers. In this case, the optimal angle ϕ_0 is 54° and $W_{\max} = 0.54(\alpha_1/2\kappa_1)$. If the parameter n is not optimized and n = 0.1, then ϕ_0 = 81° and $W_{\max} = 0.26(\alpha_1/2\kappa_1)$.

If metallic interlayers are replaced with those composed of a superconductor, the optimal angle is still expressed by (20) for $Z_0T \ll 1$, and we obtain for the sensitivity W

$$W = \frac{\alpha_1}{2\kappa_1}\frac{(\kappa^*)^{1/2}}{[(\kappa^*+n)(1+n\kappa^*)]^{1/2}}. \tag{23}$$

As in the consideration of Z_a, the use of HTSC layers changes the dependence of the sensitivity on n: the smaller the value of n, the closer W to its limiting value $\alpha_1/2\kappa_1$. Therefore, as was done above, we evaluate W for n = 0.1. Taking the thermal conductivities from the preceding section, we obtain ϕ_0 = 47° and $W = 0.85(\alpha_1/2\kappa_1)$ for the bismuth-based HTSC. For the yttrium-based HTSC, the sensitivity is even closer to the limit: $W = 0.91(\alpha_1/2\kappa_1)$ at ϕ_0 = 45°. Comparison of these values with the relevant data for metallic interlayers shows that the use of superconducting interlayers causes the sensitivity of sensors of small heat fluxes to increase by more than three times.

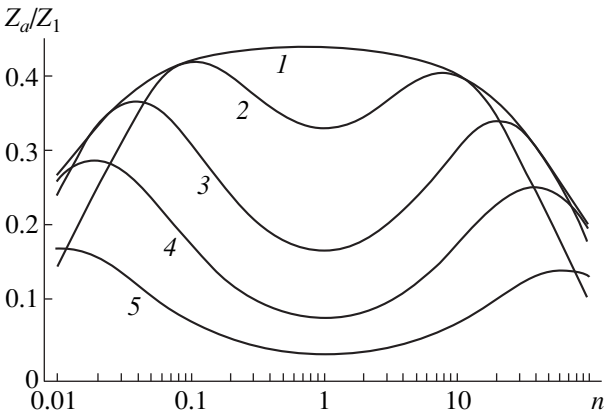

Fig. 2. Transverse thermoelectric figure of merit at T = 80 K for a heterophase material consisting of n-$Bi_{0.88}Sb_{0.12}$ semiconductor alloy layers and metallic silver interlayers as a function of the layer thickness ratio n for different layer tilt angles ϕ: (*1*) 83° (optimal angle), (*2*) 78°, (*3*) 70°, (*4*) 60°, and (*5*) 45°.

ACKNOWLEDGMENTS

The work was supported by the "Integration" Program, project no. 75.

REFERENCES

1. V. P. Babin, T. S. Gudkin, Z. M. Dashevskiĭ, *et al.*, Fiz. Tekh. Poluprovodn. (Leningrad) **8**, 748 (1974) [Sov. Phys. Semicond. **8**, 478 (1974)].
2. D. M. Gel'fgat, Z. M. Dashevskiĭ, L. D. Dudkin, *et al.*, Izv. Akad. Nauk SSSR, Neorg. Mater. **12**, 1932 (1976).
3. V. L. Kuznetsov, M. V. Vedernikov, P. Yandl', and U. Birkhol'ts, Pis'ma Zh. Tekh. Fiz. **20** (18), 75 (1994) [Tech. Phys. Lett. **20**, 757 (1994)].
4. L. I. Anatychuk, *Thermal Converters and Thermoelectric Devices* (Naukova Dumka, Kiev, 1979).
5. É. V. Osipov, *Solid-State Cryogenics* (Naukova Dumka, Kiev, 1977).
6. *Handbook for Chemists* (Khimiya, Leningrad, 1971), Vol. 1.
7. Yu. A. Kirichenko, K. V. Rusanov, and E. G. Tyurina, Sverkhprovodimost: Fiz., Khim., Tekh. **3**, 1385 (1990).
8. O. A. Gerashchenko, *Foundations of Thermometry* (Naukova Dumka, Kiev, 1971).

Translated by D. Mashovets

Semiconductors, Vol. 34, No. 10, 2000, pp. 1219–1223. Translated from Fizika i Tekhnika Poluprovodnikov, Vol. 34, No. 10, 2000, pp. 1270–1274.

PHYSICS OF SEMICONDUCTOR DEVICES

Injection Currents in Silicon Structures with Blocked Hopping Conduction

D. G. Esaev* and S. P. Sinitsa

Institute of Semiconductor Physics, Siberian Division, Russian Academy of Sciences, pr. Akademika Lavrent'eva 13, Novosibirsk, 630090 Russia

** e-mail: esaev@thermo.isp.nsc.ru*

Submitted April 4, 2000; accepted for publication April 14, 2000

Abstract—It is shown that injection currents in structures with blocked hopping conduction (the so-called BIB structures) may be interpreted as Richardson thermionic currents flowing through potential barriers. The latter are governed by the electron chemical potential in the N^{++}–N^{+} (N^{++}–I) regions. It is also shown that measurement of the injection potential is a convenient method for determining the degree of compensation in silicon structures with "ohmic" contacts. © *2000 MAIK "Nauka/Interperiodica".*

1. INTRODUCTION

It is known that, as the temperature decreases, the conductance of semiconductor structures (including silicon structures), for impurity concentration lower than that corresponding to the Mott transition, is sequentially controlled in weak electric fields by the following mechanisms: by intrinsic conduction, impurity conduction over the majority-carrier band, and hopping conduction over the impurity band.

In view of the activation-related behavior of all these mechanisms, the conductance of the structure in the ohmic region decreases with decreasing temperature to unmeasurably small values and the structure becomes insulating rather than semiconducting. Such behavior of the conductance is observed in experiments with resistor structures [1], *p–i–n* diodes [2], and photodetector structures with blocked hopping conduction (BIB structures) [3]. However, as the voltage applied to these structure increases, the structures again become conducting, with the current often being controlled by the contact injection. Without going into details of the injection-current theory [4], we will just mention the main assumptions that are important for further consideration here. The model of monopolar injection is based on the following assumptions:

(i) In steady-state conditions, there exists a thermodynamic equilibrium between the free and localized charge carriers.

(ii) The electric field at the injecting contact is equal to zero for any current through the contact.

Since in actual semiconductors there inevitably exists an uncontrolled compensating impurity with concentration N_{com} (in addition to the main doping impurity), the concentration of positively and negatively charged centers tends to a finite value $N^+ = N^- = N_{com}$ with decreasing temperature.

The injection-current theory makes it possible to determine the limiting voltage U_0 for which the charge at the second (drain) electrode in a structure with the length L can still be compensated by recharging the ionized centers; i.e.,

$$U_0 = qN_{com}L^2/(2\varepsilon\varepsilon_0),$$

where ε is the relative permittivity of the semiconductor and ε_0 is the permittivity of free space. As the voltage increases further, the theory predicts an abrupt increase in current [4, 5]. However, the dependences of the injection current on voltage and temperature cannot be accurately predicted by the theory in view of the second of the aforementioned assumptions. Because of this, there have been several attempts to consider the nature of the potential barrier at the injecting contact and the dependence of the barrier height on external voltage.

Thus, in resistor structures [1], the potential barrier is related [1] to the phenomenological effect of narrowing of the band gap in the case of heavy doping [6]. For *p–i–n* diodes, it is assumed [2] that narrowing of the band gap as the doping level increases is due to broadening of the upper Hubbard band that consists of D^- donor-impurity states for an *n*-type semiconductor. The origin and height of the potential barrier at a homojunction of heavily and lightly doped silicon were considered previously [7, 8] from the standpoint of using it to detect far-infrared radiation (λ = 100–1000 μm). It is believed [7, 8] that the barrier height for electrons in *n*-Si is governed by narrowing of the band gap, whereas the shape of the potential distribution is controlled by the image forces and the Pool–Frenkel effect.

The objective of this study was to show that, for both polarities of the applied voltage, the injection currents in a BIB structure are controlled by diffusion-related potential barriers which are formed at the boundaries of a BIB structure with the N^{++} contact

1063-7826/00/3410-1219$20.00

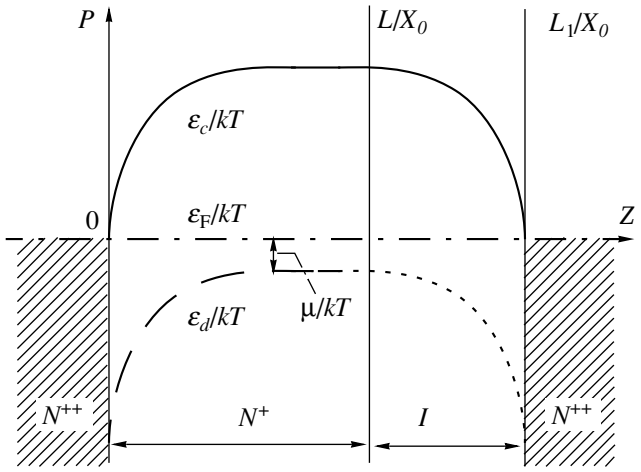

Fig. 1. Schematic representation of potential distribution in a BIB for zero bias.

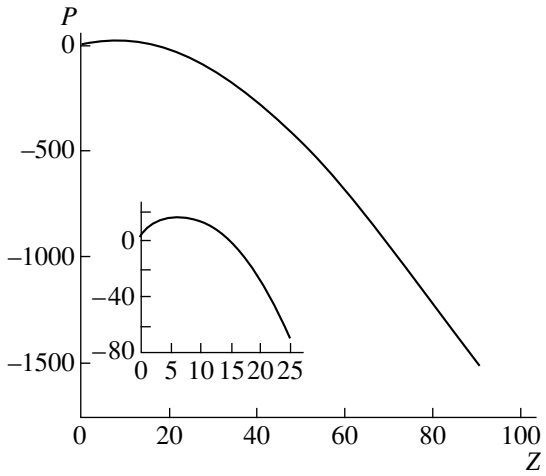

Fig. 2. The calculated potential distribution in a BIB structure for positive bias applied to the N^{++}–I contact. The following values of the parameters were used in the calculations: $N_a = 10^{13}$ cm^{-3}, $L = 10$ μm, $L_1 = 15$ μm, and $T = 10$ K.

regions as a result of the difference between the chemical potentials for electrons in the N^{++} and N^+ (or N^{++} and I) regions.

2. A MODEL OF A BIB STRUCTURE

For the sake of definiteness, we consider a BIB structure based on silicon doped with arsenic. The spatial distribution of arsenic in such a structure was reported elsewhere [3]. According to this distribution, experimental data on the conductance of an N^{++}–N^+–N^{++} structure obtained from a BIB structure after etching off the blocking layer [9] and the above assumptions, we can draw the diagram for the potential in such a structure (Fig. 1).

We use the following assumptions. It is assumed that both the embedded epitaxial contact to the photosensitive operating N^+ layer and the external diffused contact to the blocking layer are abrupt and that the transition layers are not considered. The impurity concentration is constant in the photosensitive layer. The Fermi-level position in the photosensitive layer, according to the measurements of the corresponding conductance, is governed by the impurity-band statistics [10]. The compensating acceptor impurity with constant background concentration N_a is present in the photosensitive layer in addition to the main doping impurity. We ignore the change in the potential between the N^+ and I layers, because this difference is small. Electrons in the conduction band and "holes" in the impurity band obey the Boltzmann statistics in the temperature range of 6–20 K that is important for the problem under consideration.

The dependence of the potential P on the coordinate Z in this model is described by the Poisson equation in the range of $0 \le Z \le Z_m$, where Z_m is the position of the potential maximum $P = P_m$ for positive bias at the outer electrode of the structure; thus, we have

$$\frac{d}{dP}\left(\frac{dP}{dZ}\right)^2 = [P_C \exp P - N_C \exp(-P) - 1]. \qquad (1)$$

Here, $P = -(qU/kT)$ is the dimensionless potential, $Z = X/X_0$ is the dimensionless coordinate, $X_0 = (\varepsilon\varepsilon_0 kT/q^2 N_a)^{1/2}$ is the screening length,

$$N_C = (N_c/N_a)\exp[-(E_c - E_d - \mu)/kT],$$

$$P_C = \exp[-(E_c - E_d)/kT],$$

where N_c is the effective density of states in the conduction band. In the range of $Z_m \le Z \le L/X_0$, only the charge density of ionized acceptors is taken into account on the right-hand side of Eq. (1). In the region of the blocking layer $L/X_0 \le Z \le L_1/X_0$, the right-hand side is assumed to be equal to zero. The boundary conditions have the following form: $P = 0$ for $Z = 0$, and $P = P_b$ for $Z = L_1/X_0$; here, P_b is the dimensionless potential at the outer electrode of the structure. In the case of negative bias applied to the outer electrode and a low current, the problem of calculating the barrier parameters for electron injection from the outer N^{++} contact into the blocking I layer is somewhat simplified, because almost all bias voltage drops across the blocking layer.

Equation (1) is first integrated analytically and then numerically. The constant appearing after the first integration is determined from the condition $Z(P_b) - Z(0) = L_1/X_0$ using an iteration procedure. The results of calculating the potential $P(Z)$ for the model of a BIB structure that is biased with $V = 1.29$ V at $T = 10$ K are shown in Fig. 2. It follows from the results that there are three distinctive portions in the dependence $P(Z)$. For small values of Z, the trend of the potential is controlled by free electrons that have diffused from the N^{++} contact

into the N^+ region, so that the dependence $P(Z)$ is logarithmic. As Z increases, the behavior of the potential is controlled by the charge of ionized acceptors N_a^- and $P(Z)$ is a quadratic function. In the region of the blocking layer ($Z \geq 60$), $P(Z)$ is a linear function according to the assumptions adopted.

Figure 3 shows the external-bias dependence of potential at the maximum (P_m). It can be seen that, for low bias voltages, P_m is equal to its equilibrium value in the neutral portion of the N^+ photosensitive layer. For larger values of P_b, the potential P_m decreases rapidly until the coordinate Z_m approaches the region where the behavior of $P(Z)$ is controlled by free electrons. Further on, $P_m(P_b)$ varies more slowly.

3. THE INJECTION VOLTAGE

According to [5], the injection current in an n-type BIB structure arises at the voltage V_i for which the space-charge region reaches the N^{++} contact. The quantity V_i is defined by the expression

$$V_i = \frac{qN_a}{2\varepsilon\varepsilon_0}(2L_xL_{1x} - L_x^2), \qquad (2)$$

where N_a is the concentration of compensating acceptors and L_x and L_{1x} are the thicknesses of the N^+ photosensitive layer and the BIB structure. In model [5], the existence of a potential barrier at the injecting contact is disregarded. For $V > V_i$, the injection current $J(V)$ is calculated as a drift current

$$J = qn\mu_n E - \text{const},$$

which satisfies the equation

$$\text{div}E + (q/\varepsilon\varepsilon_0)(-n - N_a^-)$$

with the boundary condition $E = 0$ at the contact $Z = 0$. An obvious disadvantage of this model is the absence of temperature dependence of the injection current and an unlimited increase in the injected-electron concentration at the contact.

An analysis of the behavior of the potential P_m obtained by solving Eq. (1) shows (Fig. 3) that, as V increases, the potential-barrier height tends to the value $(kT/q)\ln(N_c/N_a)$ rather than to zero. This behavior should be expected because, for $V \longrightarrow V_i$, the depletion layers merge in a BIB structure and further variation in the external bias is screened by free electrons in the N^+ layer near the N^{++} contact, rather than by ionized acceptors. Taking into account this screening, we may represent the injection voltage as

$$V_1^* = V_i - 2\left(V_i\frac{kT}{q}\ln\frac{N_c}{N_a}\right)^{1/2}, \qquad (3)$$

where V_i is defined by expression (2).

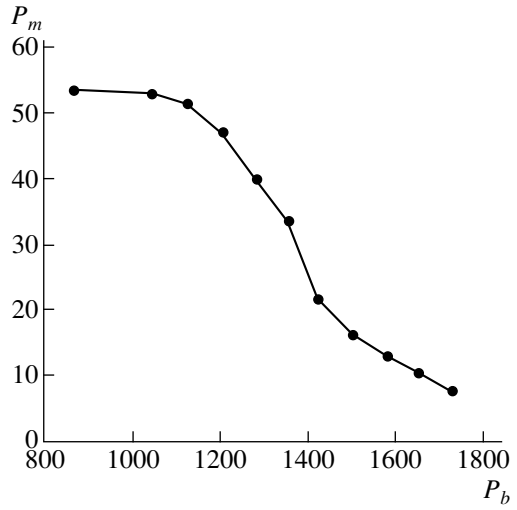

Fig. 3. The maximum of the potential as a function of positive bias applied to a BIB structure; $N_a = 10^{13}$ cm^{-3}, L_x = 10 μm, L_{1x} = 15 μm, and T = 10 K.

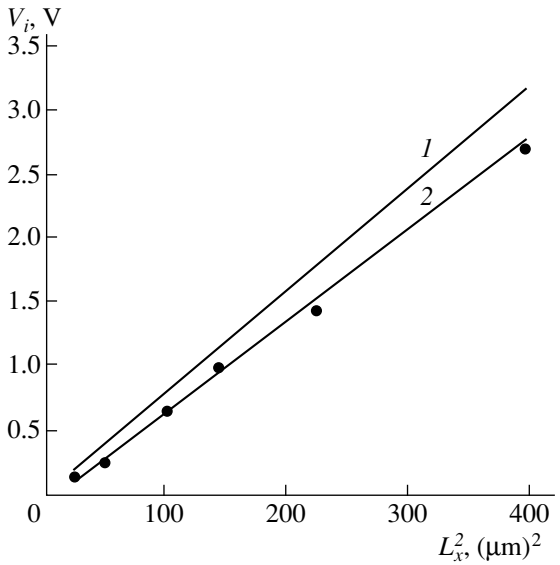

Fig. 4. The calculated dependence of the injection voltage on the thickness of a BIB structure: (*1*) according to [5] and (*2*) according to expression (3). The points were obtained using Eq. (1).

Figure 4 shows the results of calculating the injection voltage in relation to L_x^2 for $L_{1x} = L_x$. The straight lines *1* and *2* correspond to the results obtained by formulas (2) and (3), respectively. In addition, the results obtained by the procedure for calculating the quantity P_m, with a voltage at the outer boundary of the structure equal to V_1^*, are also shown. The maximum of the potential P for $V = V_1^*$ was found to be equal to P_m = 15.8–0.8 V. The scatter in the results is related to the assumptions adopted in the calculations.

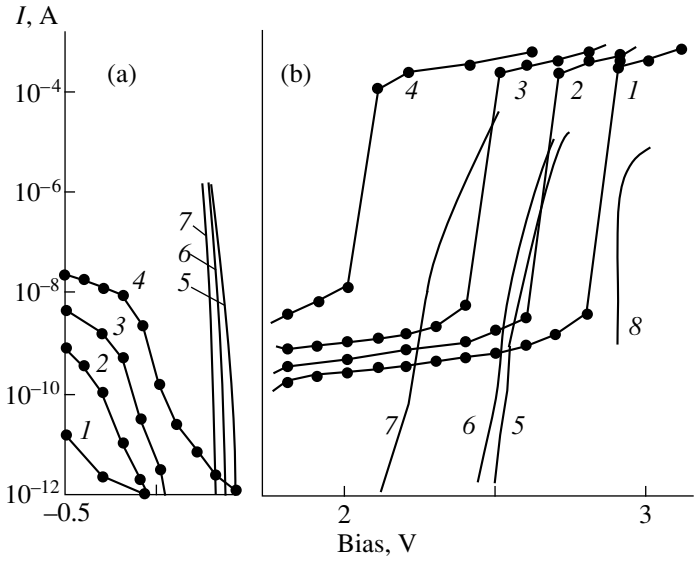

Fig. 5. The field dependence of the current through a BIB structure for (a) negative and (b) positive voltage polarities; (*1–4*) are experimental data [3], (*5–7*) are the calculated injection dependences, and (*8*) corresponds to the results reported previously [5]. The temperature T = (*1*) 7.4, (*2*) 9.7, (*3*) 11.6, (*4*) 14.9, (*5*) 6, (*6*) 10, and (*7*) 15 K.

4. INJECTION CURRENTS IN A BIB STRUCTURE

Injection currents in a BIB structure can be interpreted in terms of Richardson thermionic emission from the heavily doped N^{++} contacts into the bulk of the N^+ or I layers through the potential barrier P_m related to the chemical-potential jump. The latter is determined independently from the position of the As donor level in Si [11] and from measurements of the chemical potential in the bulk of the N^+ layer [9]. The dependence of P_m on the voltage at the outer electrode is controlled by three parameters, namely, L_x, L_{1x}, and N_a; these are determined independently by measuring the spreading resistance at the spherical section and the bias dependence of the BIB-structure capacitance [3].

The Richardson emission current is given by

$$J(V) = A^*T^2\exp[-P_m(V, T)], \qquad (4)$$

where A^* is the effective Richardson constant $A^* = AM$. Here, $A = 120$ A/(cm^2 K^2) is the Richardson constant for emission into vacuum and M is a factor equal to 2.1 for emission along the ⟨100⟩ direction in silicon [12].

Figure 5 shows the dependences of injection current on the applied voltage, which were calculated using the procedure described above for determining the quantity $P_m(V, T)$. Experimental data [3] and the results of calculations reported previously [5] are also shown. It can be seen that the suggested model correctly predicts the value of the injection voltage for both positive and negative biases (in the latter case, the model adopted previously [5] is inapplicable). The direction of the shift of the injection voltage with temperature is also correctly predicted. However, there is no satisfactory quantitative agreement between the results of calculations and experimental data. Apparently, the main cause of the discrepancy between theory and experiment is related to the fact that, in calculating the potential in the vicinity of the contact, we ignored the actual spread in the impurity concentration, which caused the dependence $P_m(V)$ to become stronger for $V < 0$. The temperature shift of the experimental current–voltage characteristics to larger V_i^* with decreasing temperature is larger than is predicted by the theory; this is true for both $V > 0$ and $V < 0$. This shift was previously related [9] to the electron capture by the As^+ center. This relation is confirmed by observation of hysteresis in measurements of the current–voltage characteristics at temperatures below 7 K. In this case, the injection potential depends on the current for $V < V_i^*$.

5. CONCLUSION

(i) It is shown that the injection currents in a BIB structure, which control the basic behavior of the current–voltage characteristics, may be interpreted in terms of Richardson thermionic emission through the potential contact barriers.

(ii) The expression defining the injection potential was refined.

(iii) It is ascertained that measurement of the injection potential at low temperatures may constitute a convenient and precise method for determining the compensating-impurity concentration (in particular, for low degrees of compensation $K \le 10^{-4}$) in silicon structures with “ohmic” contacts.

REFERENCES

1. E. Simoen, B. Dierickx, L. Deferm, *et al.*, J. Appl. Phys. **68**, 4091 (1990).
2. Y. Yang, D. D. Coon, and P. F. Shepard, Appl. Phys. Lett. **45**, 752 (1984).
3. D. G. Esaev, S. P. Sinitsa, and E. V. Chernyavskiĭ, Fiz. Tekh. Poluprovodn. (St. Petersburg) **33**, 614 (1999) [Semiconductors **33**, 574 (1999)].
4. M. A. Lampert and P. Mark, *Current Injection in Solids* (Academic, New York, 1970; Mir, Moscow, 1973).
5. B. G. Martin, Solid-State Electron. **33**, 427 (1990).
6. D. D. Coon and S. D. Gunapala, J. Appl. Phys. **57**, 5525 (1985).
7. A. G. U. Perera, H. X. Yuan, and M. H. Francombe, J. Appl. Phys. **77**, 915 (1995).
8. H. X. Yuan and A. G. U. Perera, Appl. Phys. Lett. **66**, 2262 (1995).
9. D. G. Esaev, S. P. Sinitsa, and E. V. Chernyavskiĭ, Fiz. Tekh. Poluprovodn. (St. Petersburg) **33**, 1005 (1999) [Semiconductors **33**, 915 (1999)].
10. B. I. Shklovskiĭ and A. L. Éfros, *Electronic Properties of Doped Semiconductors* (Nauka, Moscow, 1979; Springer-Verlag, New York, 1984).
11. N. Sclar, Prog. Quantum Electron. **9**, 214 (1984).
12. C. R. Crowell, Solid-State Electron. **8**, 395 (1965).

Translated by A. Spitsyn

Semiconductors, Vol. 34, No. 10, 2000, pp. 1224–1228. Translated from Fizika i Tekhnika Poluprovodnikov, Vol. 34, No. 10, 2000, pp. 1275–1279.

PHYSICS OF SEMICONDUCTOR DEVICES

Charge Transport Mechanism and Photoelectric Characteristics of n^+-Si–n-Si–Al_2O_3–Pd Diode Structures

S. V. Slobodchikov, Kh. M. Salikhov, and E. V. Russu

Ioffe Physicotechnical Institute, Russian Academy of Sciences, Politekhnicheskaya ul. 26, St. Petersburg, 194021 Russia

Submitted April 19, 2000; accepted for publication April 20, 2000

Abstract—Current–voltage characteristics at T = 100 and 300 K, the temperature dependence of the forward current and photocurrent, the influence of a magnetic field on the photocurrent, and the influence of hydrogen on the photovoltage and dark current were investigated. It was found that the mechanism of the charge transport is controlled by double injection in the diffusion approximation at both T = 100 K ($I \propto \exp(qV/4kT)$) and T = 300 K ($I \propto V^m$, m = 4–5.6). Diode structures enhance the photocurrent at a reverse bias. It was found that an increase in the photocurrent in the magnetic field H ($\Delta I_{ph} = \alpha \exp \beta H$) can be explained by tunneling of the photocarriers during resonance impurity scattering in terms of their exponential energy distribution. © *2000 MAIK "Nauka/Interperiodica".*

Our preliminary investigations of the electric and photoelectric properties of $n(p)$–Si–SiO_2–Pd diode structures with thin [1, 2] and thick [3] SiO_2 layers revealed two mechanisms of photocurrent increase and demonstrated that structures with a thin SiO_2 layer can be used as efficient sensors of hydrogen and hydrogen-containing gases. It was of interest to continue investigations of similar Si-based structures using, first, an n-Si substrate with a low electron density and, second, substituting an Al_2O_3 insulator film for the SiO_2 layer. It was expected that the resulting n^+-Si–n-Si–Al_2O_3–Pd diode structure should have another charge transport mechanism. Consequently, this structure should have another dependence of the dark current and photocurrent on external factors such as the applied voltage, magnetic field, and hydrogen-containing gas mixture. As a result of these investigations, we proposed to evaluate the advantages and drawbacks of these structures for possible practical applications.

1. EXPERIMENTAL

The substrates were Si(111) wafers with the electron density $n^+ = 6 \times 10^{17}$ cm^{-3}. The n-Si layers were grown on the thoroughly cleaned and etched wafers. The layer thickness was 30 μm, electron density was $n = 10^{14}$ cm^{-3}, and ρ = 40–60 Ω cm. The Al_2O_3 layer was deposited by electron-beam evaporation from a plate-shaped Al_2O_3 source. The Al_2O_3 layer was $d \lesssim 50$ Å thick. Al was used as the nonrectifying contact, and Pd was evaporated on the Al_2O_3 layer through a mask 0.1 cm in diameter. Deposition was carried out at a residual pressure of 10^{-5} Torr, and the Pd layer was 400 Å thick. A schematic diagram of the structure is shown in the insert in Fig. 1.

The current–voltage (I–V) characteristics at 100 and 300 K and the temperature dependence of the forward current and photocurrent were measured. In addition, the influence of the magnetic field on the photocurrent, as well as the influence of hydrogen on the photovoltage and I–V characteristics, were investigated.

2. CHARGE TRANSPORT MECHANISM

It is evident that the major components of the diode structure, which determine the charge transport mechanism, are the Al_2O_3 layer with the Schottky barrier and the depleted n-Si layer. Accordingly, the voltage drop across the structure is given by

$$V = V_1 + V_2, \quad (1)$$

where V_1 and V_2 are the voltage drops across the Schottky barrier and n-Si layer, respectively.

The I–V characteristics for a typical n^+-Si–n-Si–Al_2O_3–Pd structure, which were measured at T = 100 and 300 K, are shown in Fig. 2. Their characteristic features are as follows. At T = 100 K, the forward current (negative voltage on n^+-Si) varies exponentially with the voltage as $I \propto \exp\frac{qV}{nkT}$ (n = 4) up to V = 0.8 V (curve *1*). At room temperature, $I \propto V^m$. In this case, for various samples, m = 4–5.6 (curve *2*). Additional measurements of the I–V characteristics for structures without the Al_2O_3 layer demonstrated that the exponent m had the same values at T = 300 K. Thus, the I–V characteristic is conditioned mainly by the parameters of the n-Si layer; in this case, $V_2 \gg V_1$.

1063-7826/00/3410-1224$20.00

Taking into account these characteristics of the variation of the current with voltage, we can assume that charge transport is mainly due to double injection of the carriers into the *n*-Si layer (Fig. 1). Electrons are injected from the n–n^+ contact, and holes are injected from the Pd contact. In this case, the electron injection factor $K_{n-n^+} = I_n/I \cong 1$, while the hole injection factor $K_{\mathrm{Pd}} = I_p/I \neq 1$; i.e., the total current is mainly the electron current.

It is known that charge transport in the double injection regime is caused mainly by charge-carrier drift or by diffusion. In our case, there are grounds to believe that diffusion plays the major role. Drift transport is characterized by a power dependence with $m = 2$ or $m = 3$; and the values $m > 3$, which are observed in some experiments, are related to the diffusion current [4]. A decrease in temperature should not vary the analytical (power-low) form of the I–V characteristic, as was observed in our case, although a decrease in the equilibrium charge-carrier density in the *n*-Si layer should enhance the field component. The diffusion current can be represented as [5]

$$I = I_1 \exp\left(\frac{qV}{lkT}\right), \quad l = \cosh\frac{W}{L} \tag{2}$$

with the proviso that the thickness of the *n*-Si layer $W > L$, where

$$L = [D_p \tau 2b(\gamma + 1)/(b\gamma + b + 1)]^{1/2}$$

is the bipolar-diffusion length, γ is the hole-trapping coefficient, and other designations are conventional. Expression (2) is valid for a monotonic coordinate dependence of the injected carrier density in *n*-Si. In diffusion approximation (2), the current strongly depends on the bipolar-diffusion length. For this reason, variation of the current in the temperature range of 120–160 K (Fig. 3, curve *1*) is probably related to a sharp temperature dependence of the lifetime τ. The appearance of the power dependence with $m = 4$–5.6 at $T = 300$ K is caused by the variation of the carrier distribution in the *n*-Si layer, which becomes nonmonotonic. In this case, recombination in the high-resistivity layer dominates over recombination in the low-resistivity near-contact regions. An increase in the forward current with the activation energy $E_a = 0.08$ eV (Fig. 3, curve *1*) in a higher-temperature region is conducive to a nonmonotonic distribution of injected holes with a minimum close to the Al_2O_3–*n*-Si heterointerface due to an increase in the equilibrium electron density.

3. PHOTOVOLTAGE AND PHOTOCURRENT

At the peak in the spectral curve ($\lambda_{\max} = 0.98$ μm), the photovoltage of the n^+-Si–*n*-Si–Al_2O_3–Pd structures with thinner insulating layers at $T = 300$ K was larger by more than an order of magnitude compared to similar samples without Al_2O_3. The difference in the

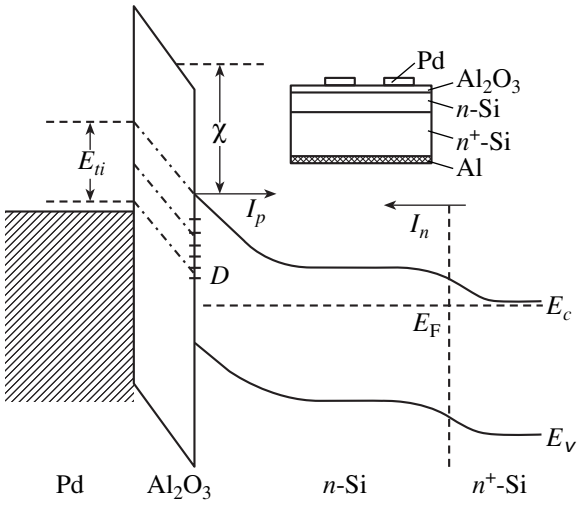

Fig. 1. Energy-band diagram of the n^+-Si–*n*-Si–Al_2O_3–Pd structure. The schematic diagram of the structure is shown in the insert.

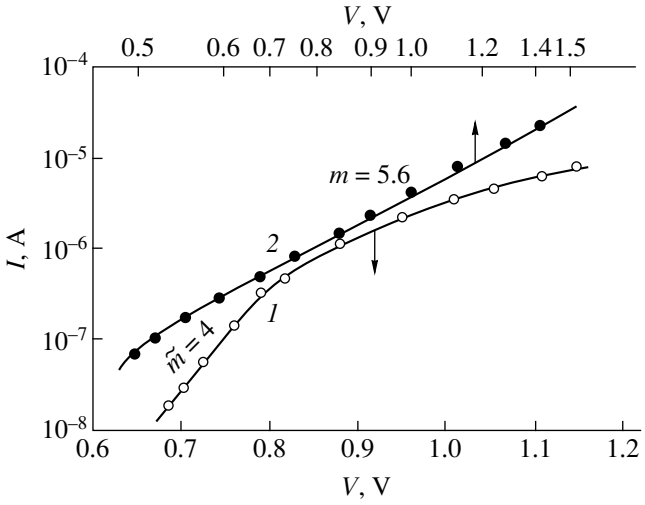

Fig. 2. Current–voltage characteristics of the n^+-Si–*n*-Si–Al_2O_3–Pd structure at T = (*1*) 100, (*2*) 300 K.

short-circuit photocurrents was much less; namely, it amounted to a factor of 2–3 and was apparently related to the distinction in the differential resistance R for both structures at zero bias. The temperature dependence of the photocurrent in the temperature range $T = 100$–300 K is shown in Fig. 3 (curve *2*). The photocurrent, which oscillates with temperature, has maxima and minima, which are in antiphase with the corresponding extrema of the forward dark current (curve *1*).

The photovoltage for the structure can be represented as

$$V_{\mathrm{ph}} = V_{\mathrm{ph0}} f(\chi, d, \sigma, D), \tag{3}$$

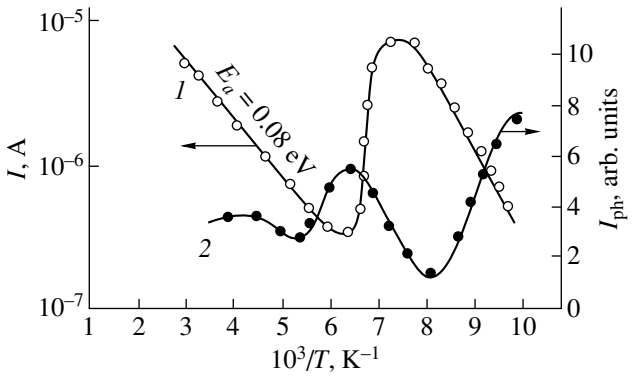

Fig. 3. Temperature dependence of the forward current (curve *1*, V = 0.8 V) and photocurrent (curve *2*) in the temperature range T = 100–300 K.

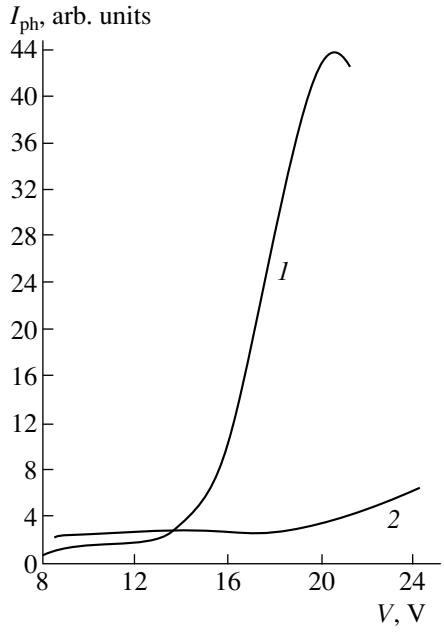

Fig. 4. Photocurrent as a function of reverse bias. (*1*) Corresponds to the n^+-Si–n-Si–Al_2O_3–Pd structure and (*2*) to the n^+-Si–n-Si–Pd structure.

where V_{ph0} is the photovoltage of an ideal Schottky diode and $f(\chi, d, \sigma, D)$ is a function of the barrier height χ (Fig. 1), thickness of the Al_2O_3 insulating film d, and the trapping cross sections σ and density D of the corresponding centers at the interface. This function $f \le 1$.

It is known that

$$V_{ph0} = \frac{kT}{q}\ln\left(\frac{I_{ph}}{I_0} + 1\right). \quad (4)$$

For low photovoltages, $V_{ph} \approx I_{ph}R$. The correlation of the oscillating curves of the photocurrent with those of dark current can be revealed by comparing the saturation current I_0 in (4) with the corresponding magnitude I_1 in expression (2). According to [5],

$$I_1 \approx \left(\frac{qD_n}{2L}\right)^2 \exp(2W/L). \quad (5)$$

In this case, a small decrease in the lifetime τ reduces the diffusion length L and exponentially increases the saturation current I_1 and, accordingly, I_0. As a result, both the photocurrent I_{ph} and the differential resistance R decrease. It is noteworthy that at $T \approx 130$ K the forward current varies by an order of magnitude, whereas the change in the photocurrent is approximately a factor of 3. This is an expected result, since, in formula (4), L does not appear in the exponent. The reverse-bias dependences of the photocurrent for two diode structures, with the Al_2O_3 layer (curve *1*) and without it (curve *2*), are shown in Fig. 4. It can be seen that the first structure amplifies the photocurrent at $V > 14$ V, with the gain being as high as 10^2. The second structure exhibits almost no gain. The amplification in Pd-layered diode structures with a SiO_2 insulator layer was investigated elsewhere [1]. For the structures with Al_2O_3, the shape of the photocurrent curves differs from those described previously, since the critical voltage of amplification onset is shifted to larger biases. This is related to a large voltage drop across the n-Si layer. The amplification mechanism, however, remains unchanged.

4. INFLUENCE OF A MAGNETIC FIELD ON THE PHOTOCURRENT

Interesting features of photocurrent variation in the absence of an applied bias are related to its dependence on the magnetic field H (Fig. 5). Instead of the expected photocurrent drop or its independence of H, an increase in photocurrent was observed for H = 1 – 18 kOe according to the law

$$I_{ph}^H - I_{ph}^0 = \Delta I_{ph} = \alpha\exp(\beta H). \quad (6)$$

It is evident that this dependence on H can be explained by the decisive influence of the Al_2O_3 insulator layer on photocarrier transport, since double-injection into the n-Si layer is impossible without applying the bias. In this connection, it is reasonable to suppose that tunneling through the Al_2O_3 layer should play the decisive role. It is known that the transparency of an insulator film with thickness d can be expressed by the relation $D_1 = D_0\exp(-2d/\alpha_1)$, where α_1 is the quantity that depends on the tunneling-photocarrier energy ε. The presence of impurities is disregarded in this relation, and the tunneling energy is counted downward from the conduction-band bottom. In the effective mass approximation, $\alpha_1 = \hbar/(2m\varepsilon)^{1/2}$. With regard for impurities, the tunneling mechanism varies due to scattering by impurity centers. In this connection, resonance and nonresonance subbarrier scattering of carriers are differenti-

ated. In the former case, the tunneling-carrier energy is close to the impurity energy level. In the latter case, impurity scattering affects the exponential factor $2d/\alpha_1$ only slightly. For a film containing no impurities, the magnetic field, which is parallel to the film surface, induces an additional potential that affects the tunneling carrier:

$$U(x) = (q^2H^2/2mc^2)(x - x_0)^2,$$

where x_0 is the center of the Landau oscillator. In this case, the wave function decaying normally to the surface is described by the dependence

$$\Psi(x) \propto \exp\left(-\frac{x^2}{2\lambda^2}\right) \quad (7)$$

for $x \gg \lambda^2/\alpha_1$, where λ is the magnetic length, and $\lambda = (c\hbar/qH)^{1/2}$. Correspondingly, the transparency is $D_1 \propto |\Psi(d)|^2$. In terms of the subbarrier nonresonance scattering in the magnetic field, it was found [6] that

$$D_1(d) \propto D_0 \exp(-2d/b_1),$$

where

$$b_1 = \alpha_1\left[1 - C\left(\frac{\alpha_1}{\lambda}\right)^{4/3}/\ln B\right],$$

C is a constant, and B is a dimensionless coefficient. In both cases of direct tunneling and nonresonance impurity scattering, one should thus expect a decrease in transparency with increasing magnetic field and, consequently, decrease in the photocurrent. In this connection, we believe that the observed experimental dependence (6) can be related to resonance scattering in the magnetic field. The problems of resonance tunneling were considered elsewhere [7]. In this paper, impurity tunneling through Schottky barriers was considered. It is our opinion that certain aspects of this analysis can be applied to tunneling through the insulator film. According to [7], the total rate of transition via impurity centers can be written as

$$R = \frac{R_1R_2}{R_1 + R_2}$$

$$= \frac{c_1c_2N_t\exp\left[-2\left(\int_{x_0}^{x_1} k\,dx + \int_{x_1}^{x_2} k\,dx\right)\right]}{c_1\exp\left(-\int_{x_0}^{x_1} k\,dx\right) + c_2\exp\left(-\int_{x_1}^{x_2} k\,dx\right)}, \quad (8)$$

where, with regard for our structure, R_1 and R_2 are the rates of transitions from the n-Si semiconductor to impurity centers in Al_2O_3 (R_1) and from these centers to the metal (R_2), respectively; c_1 and c_2 are slowly varying functions of voltage and temperature; N_t is the impurity-center density; and x_0, x_1, and x_2 are the turning points. The rate of the overall transition is proportional to the peak value (8). According to (8), the transmittance factor for the trap (impurity center) can be written as

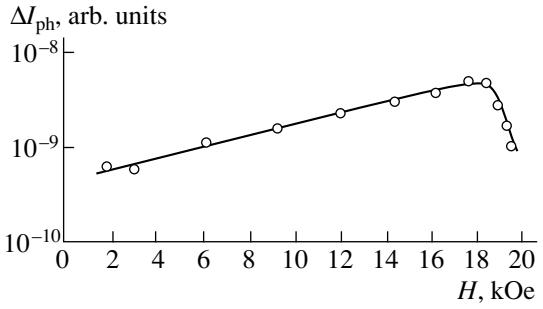

Fig. 5. Photocurrent increase $\Delta I_{ph} = I_{ph}^H - I_{ph}^0$ as a function of the magnetic field H in the range of 1–20 kOe.

$$T(E_x) \approx \exp\left(-2\int_{x_0}^{x_2} |k|\,dx\right), \quad (9)$$

where $k\hbar = \{2m^*[E_x - U'(x)]\}^{1/2}$, E_x is the tunneling-electron energy and $U'(x)$ is the average potential barrier in the trap-containing region.

Thus, the traps increase the tunneling current and the energy of most of the electrons tunneling through the barrier corresponds to the trap energy. There is a large probability that insulating films obtained by vacuum deposition contain various traps which are related to both chemical impurities and various defects. This should naturally be taken into account when analyzing the tunneling mechanism. A magnetic field directed parallel to the structure surface causes scattering of the photocarriers generated by the monochromatic light. We believe that not only elastic impurity scattering, but also nonelastic scattering with energy loss occurs both at the n-Si–Al_2O_3 heterointerface and within the insulating layer. The probability of scattering increases with increasing magnetic field, and the electron tunneling energy E_x should decrease. We can further assume that a certain potential $U'(x)$ corresponds to each type of trap. In this case, with an increase in the magnetic field, the transmittance factor (9), which should be largest for one type of trap, ceases to satisfy this condition and becomes largest for another type of trap. Here, the trap density N_t becomes important, as well as the trap energy distribution. We may assume that the trap energy distribution is exponential $N_t \propto \exp(-E/E_0)$. In this case, the total tunneling current through the set of traps should be defined by the sum $\sum_i R_i$. In this case, the tunneling-electron energy in expression (9) is $E_x = f(H)$.

The variation of the magnetic field causes weakening of one tunneling channel and enhancement of

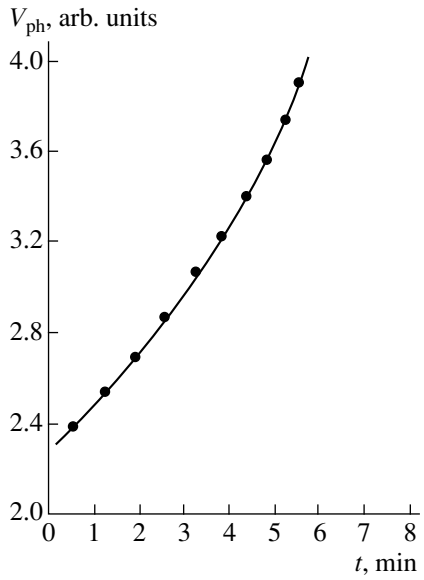

Fig. 6. Relaxation of the photovoltage V_{ph} subsequent to the hydrogen pulse effect.

another one. A possible verification of the suggested qualitative model of resonance tunneling in a magnetic field is the abrupt drop of the photocurrent at $H >$ 18 kOe (Fig. 5) due to the absence of both resonance $E_x(H)$ and the corresponding trap energy level.

5. INFLUENCE OF HYDROGEN ON THE PHOTOVOLTAGE AND DARK CURRENT

The following effects of the hydrogen pulse on heterostructrures with an Al_2O_3 layer were revealed. They are, first, a significantly lower sensitivity compared to structures obtained elsewhere [2] and, second, large relaxation times after shutoff of the hydrogen inlet. The photovoltage variation (drop) subsequent to the H_2 effect for various samples was from twofold to tenfold, and the relaxation time could be as large as 5–10 min. The typical relaxation curve of the photovoltage V_{ph} for one of the samples is shown in Fig. 6. Long relaxation times are caused by a number of factors, including the long times for initial H_2 diffusion through the Al_2O_3 layer and even more long times for rediffusion. The presence of deep traps in the Al_2O_3 layer and at the Al_2O_3–*n*-Si heterointerface, including temporary traps induced by the adsorbed H_2, also enhances photovoltage relaxation. The variation (increase) of the forward dark current under the influence of the H_2 pulse was 10%. This is evidently related to the fact that the charge transport mechanism is governed by the characteristics and parameters of the *n*-layer rather than the heterointerface, since the adsorption of H_2 enhances the carrier-injection factor only slightly.

Thus, in practice, the diode structures investigated lack the sensitivity and persistence necessary for H sensors. However, due to photocurrent enhancement and presence of the depletion *n*-Si layer (this decreases the persistence of the photoresponse), these structures are advantageous for photodetector applications.

REFERENCES

1. S. V. Slobodchikov, G. G. Kovalevskaya, A. V. Pentsov, and Kh. M. Salikhov, Fiz. Tekh. Poluprovodn. (St. Petersburg) **27** (7), 1213 (1993) [Semiconductors **27**, 669 (1993)].
2. G. G. Kovalevskaya, M. M. Meredov, E. V. Russu, *et al.*, Zh. Tekh. Fiz. **63** (2), 185 (1993) [Tech. Phys. **38**, 149 (1993)].
3. S. V. Slobodchikov, E. V. Russu, Kh. M. Salikhov, *et al.*, Fiz. Tekh. Poluprovodn. (St. Petersburg) **29** (8), 1517 (1995) [Semiconductors **29**, 791 (1995)].
4. R. Baron, Phys. Rev. A **137** (1), 272 (1965).
5. É. I. Adirovich, P. M. Karageorgiĭ-Alkalaev, and A. Yu. Leĭderman, *Double-Injection Currents in Semiconductors* (Sov. Radio, Moscow, 1978), Chap. 2, p. 73.
6. B. I. Shklovskiĭ and A. L. Éfros, Zh. Éksp. Teor. Fiz. **84** (2), 811 (1983) [Sov. Phys. JETP **57**, 470 (1983)].
7. G. N. Parker and C. A. Mead, Phys. Rev. **184** (3), 780 (1969).
8. J. C. Penley, Phys. Rev. **128** (2), 596 (1962).

Translated by N. Korovin